



# Dissertation

## Phase Behaviour of Colloidal Systems

ausgeführt zum Zwecke der Erlangung des akademischen  
Grades eines Doktors der technischen Wissenschaften unter der Leitung  
von

Ao. Univ.-Prof. Dr. Gerhard Kahl  
Institut für Theoretische Physik (136)  
Technische Universität Wien

eingereicht an der Technischen Universität Wien  
Fakultät für Physik  
von

Dipl.-Ing. Gernot J. Pauschenwein  
Matr.-Nr. 9725733  
Neuwaldeggerstraße 29/1/9, 1170 Wien

Wien, Oktober 2008

---



*Nothing shocks me. I'm a scientist.*  
Dr. Henry Walton Jones, Jr.



## Kurzfassung

Kolloidale Dispersionen zeigen, abhängig von den Wechselwirkungspotentialen der Systemteilchen (Kolloide), reichhaltiges Phasenverhalten. Eine wichtige Klasse kolloidaler Systeme sind solche, deren Paarpotentiale sich aus einer Abstoßung durch einen harten Kern und verschiedenen, additiven Potentialen außerhalb des Kerns zusammensetzen. Diese Gruppe von Modellsystemen wird in der vorliegenden Dissertation untersucht, wobei zwei Schwerpunkte gelegt werden.

Der erste liegt auf dem kritischen Verhalten von Systemen mit langreichweitigen Potentialen außerhalb des Kerns. Eine zuverlässige Flüssigkeitstheorie in der Region des kritischen Punktes ist die selbst-konsistente Ornstein-Zernike Näherung, die allerdings nicht direkt auf ionische Systeme anwendbar ist. Daher ändern wir diese Theorie auf eine Weise ab, welche sie für Modelle verwendbar macht deren Paarpotentiale aus Coulomb- und anderen, additiven Wechselwirkungen bestehen. Dadurch, und mittels weiterer numerischer Verbesserungen, sind wir in der Lage effektive kritische Exponenten mit einer bisher noch nie erreichten Genauigkeit zu bestimmen. Es zeigt sich ein Übergang zwischen dem kritischen Verhalten wie in der Molekularfeldnäherung und der üblichen Kritikalität im Rahmen der selbst-konsistenten Ornstein-Zernike Näherung bei geladenen Yukawa-, geladenen Kac- und Kac-Yukawasystemen. Des Weiteren kann eine neue Beziehung zur Bestimmung des kritischen Exponenten  $\gamma$ , die auf einer Störung des Wechselwirkungspotentials eines Referenzsystems durch ein Kac-Potential beruht, bestätigt werden.

Den zweiten Schwerpunkt stellt die Suche nach Gleichgewichtsstrukturen in der festen Phase verschiedener Modelle dar. Dafür setzen wir eine Suchstrategie ein, die auf einem genetischen Algorithmus basiert. Um eine zuverlässige Konvergenz des Algorithmus für harte Teilchen zu garantieren, führen wir die sogenannte *Parametrisierung mit kürzesten Abständen* für Kristallgitter ein. Außerdem entwickeln wir eine effiziente Methode zur Bestimmung aller Gleichgewichtsstrukturen des sogenannten Square-Shoulder-Modells (SSM) am absoluten Nullpunkt der Temperaturskala. Die erstaunlich große Vielfalt an Gleichgewichtsstrukturen im SSM kann in vier Gruppen unterteilt werden, in Cluster-, Säulen-, Lamellen- und kompakte Phasen, die sich mit steigendem Druck in dieser Reihenfolge einstellen. Die Abfolge, genauso wie die thermodynamischen Eigenschaften der jeweiligen Phasen, werden auch von der so genannten Kontinuumstheorie vorhergesagt. Diese Theorie beruht auf einer Mittelung von Teilchendichten und -energien und wird auf alle vier Strukturklassen im dreidimensionalen SSM angewandt. In der Folge erweitern wir, zumindest teilweise, unsere Methoden zur Aufspürung aller Gleichgewichtsstrukturen für das SSM mittels metrischer Skalierung auf bestimmte, stetige Potentiale außerhalb des Kerns. Dadurch wird z.B. eine neue, zentriert tetragonale Phase im Yukawa-Modell mit hartem Kern entdeckt.



## Abstract

Depending on the pair interactions of the constitutive system particles, colloidal dispersions display a rich phase behaviour. An important class of colloidal systems is characterised by pair potentials that contain a hard core in addition to versatile potential tails. This class of systems are investigated in the present thesis, focussing on two different aspects.

The first one is represented by the critical behaviour of long-range interaction systems, to which we apply the self-consistent Ornstein-Zernike approximation, a liquid state theory known to remain reliable in the critical region. We modify this theory in order to make it applicable to systems exhibiting Coulomb interactions in addition to other potential tails, and are able to calculate effective critical exponents with unprecedented accuracy. With the help of this technique we find a cross-over between mean-field and SCOZA critical behaviour of charged Yukawa, charged Kac, and Kac-Yukawa systems. Furthermore we verify a new relation for the ascertainment of the critical exponent  $\gamma$ , a relation which relies on the perturbation on the interaction of a reference system with a Kac-potential.

The second focus is laid on the search for solid equilibrium structures of hard core systems, for which we employ a search strategy based on a genetic algorithm. To ensure the convergence of the algorithm for hard core particles we introduce the *Minimum Distance Parametrisation* of crystal lattices. Additionally, we develop an efficient search strategy to detect all equilibrium structures of the square-shoulder model (SSM) at zero temperature, which can be extended to systems with certain continuous potential tails via metric scaling. In this way, we are able to distinguish, e.g., a new centred tetragonal phase for the hard core Yukawa model. The astonishingly large variety of the identified equilibrium structures for the SSM consist of cluster, columnar, lamellar, and compact phases, appearing in this sequence when increasing the pressure. The succession, as well as the thermodynamic properties of the respective structures, are predicted by the so called continuum theory. This theory relies on averaging the particle densities and energies and is applied to all four structural archetypes in the SSM.





# Contents

<b>1</b>	<b>Introduction</b>	<b>1</b>
<b>I</b>	<b>Fundamentals</b>	<b>5</b>
<b>2</b>	<b>Models</b>	<b>7</b>
2.1	Coulomb and Screened Coulomb Interactions . . . . .	7
2.2	Single Yukawa Interaction . . . . .	8
2.3	The Kac Limit . . . . .	8
2.4	Charged Yukawa and Kac–Yukawa Model . . . . .	9
2.5	Square–Shoulder Model . . . . .	10
2.6	Penetrable Sphere Model . . . . .	10
2.7	Interaction and Correlation Function Range . . . . .	10
2.8	Reduced Units . . . . .	11
<b>3</b>	<b>Concepts for Fluids</b>	<b>15</b>
3.1	Critical Point Properties . . . . .	16
3.2	Routes to Thermodynamics . . . . .	18
3.3	Integral Equation Theories . . . . .	22
3.3.1	Closure Relations . . . . .	24
3.3.2	Self–Consistent Ornstein–Zernike Approximation (SCOZA) . . . . .	25
<b>II</b>	<b>Methods</b>	<b>29</b>
<b>4</b>	<b>Application of SCOZA to Charged Yukawa Systems</b>	<b>31</b>
4.1	Separation of Coulomb and Yukawa Interactions . . . . .	31
4.1.1	Ornstein–Zernike Relation and MSA Closure . . . . .	31
4.1.2	Internal Energy and Compressibility . . . . .	33
4.2	Self–Consistency on the Entire System . . . . .	34
4.3	Solving the PDE for SCOZA . . . . .	35
4.3.1	Initial and Boundary Conditions . . . . .	36
4.3.2	The Inhomogeneity Term . . . . .	37

4.3.3	Predictor–Corrector Algorithm . . . . .	37
4.3.4	Critical Point Location and Coexistence Line . . . . .	39
<b>5</b>	<b>Equilibrium Structures in the Solid State</b>	<b>41</b>
5.1	Parametrisation of Three–Dimensional Crystals . . . . .	42
5.2	The Minimum Distance Parametrisation . . . . .	46
5.2.1	The <b>a–b</b> –Lattice Plane . . . . .	48
5.2.2	Constructing <b>c</b> as Shortest Lattice Vector . . . . .	49
5.2.3	Proof of the Completeness of the Description . . . . .	55
5.3	Identification of Bravais Lattices . . . . .	62
5.4	Basis Particles . . . . .	82
5.5	Close–Packed Structures . . . . .	83
5.6	Gibbs Free Energy . . . . .	87
5.7	Finding Equilibrium Crystal Structures . . . . .	88
5.7.1	Genetic Algorithm . . . . .	89
5.7.2	Powell Algorithm . . . . .	91
5.7.3	Cutoffs . . . . .	93
5.7.4	A Systematic Search Procedure for the Square–Shoulder Interaction . . . . .	93
5.7.5	Metric Crystal Scaling . . . . .	95
5.8	The Continuum Theory . . . . .	100
<b>III</b>	<b>Criticality of Hard Core Systems with Coulomb, Yukawa, and Kac Interactions</b>	<b>107</b>
<b>6</b>	<b>Charged Yukawa Model</b>	<b>109</b>
6.1	Spinodal and Binodal Lines . . . . .	109
6.2	Critical Exponents . . . . .	111
<b>7</b>	<b>Charged Kac Model</b>	<b>115</b>
7.1	Gas–Liquid Coexistence and Critical Point Location . . . . .	116
7.2	Critical Behaviour . . . . .	119
<b>8</b>	<b>Kac–Yukawa Model</b>	<b>121</b>
<b>IV</b>	<b>Ordered Phases of Systems with Hard Core Particles</b>	<b>127</b>
<b>9</b>	<b>Square–Shoulder Model</b>	<b>129</b>
9.1	Close–Packed Structures . . . . .	129
9.2	Minimum Enthalpy Configurations . . . . .	132
9.2.1	Short Shoulder Width ( $\lambda = 1.5\sigma$ ) . . . . .	133
9.2.2	Intermediate Shoulder Width ( $\lambda = 4.5\sigma$ ) . . . . .	137
9.2.3	Large Shoulder Width ( $\lambda = 10\sigma$ ) . . . . .	141

9.3	Application of the Continuum Theory . . . . .	143
9.3.1	Self–Energy . . . . .	143
9.3.2	Homogeneous Distribution . . . . .	147
9.3.3	Planar Lamellae . . . . .	148
9.3.4	Cylindrical Columns . . . . .	154
9.3.5	Spherical Clusters . . . . .	157
9.3.6	Summary and Comparison . . . . .	162
<b>10</b>	<b>Hard Core Yukawa Model</b>	<b>169</b>
<b>11</b>	<b>Conclusion and Outlook</b>	<b>177</b>
	<b>Acknowledgements</b>	<b>181</b>
<b>V</b>	<b>Appendix</b>	<b>183</b>
<b>A</b>	<b>Coulomb Part of the Charged Yukawa Model</b>	<b>185</b>
<b>B</b>	<b>2D Lattices</b>	<b>191</b>
B.1	Two Dimensional Minimum Distance Parametrisation . . . . .	191
B.2	Fractal Parameter Space . . . . .	192
<b>C</b>	<b>3D Symmetries in the MDP</b>	<b>197</b>
C.1	Mapping from the BCO MDP to the Conventional Parameters . . . . .	197
C.2	Minimum Distances in the SFCM Lattice . . . . .	198
<b>D</b>	<b>Complete List of MECs for the SSM with <math>\lambda = 4.5\sigma</math></b>	<b>205</b>
<b>E</b>	<b>Selected Analytic Expressions in Continuum Theory</b>	<b>217</b>
<b>F</b>	<b>Influence of a Cutoff on the Hard Core Yukawa Model</b>	<b>219</b>
<b>G</b>	<b>Tables</b>	<b>221</b>
	<b>Curriculum Vitae</b>	<b>245</b>



# Chapter 1

## Introduction

Soft matter has become a field of growing interest in the past twenty years, not only in physics, which will be the focus of this thesis, but also in chemistry and biology, thus representing an interdisciplinary topic [1,2]. One reason for this is the omnipresence of soft matter in our everyday life (blood, clay, plastics, DNA, proteins, toothpaste, mayonnaise, etc.). Another one is the fruitful interplay between theoreticians and experimentalists, arising because of the possibility to *tailor* the interaction between the building parts of soft matter systems nearly at will, as will be elucidated later. And, last but not least, soft matter has by now reached even technological relevance: For example in biotechnological or pharmaceutical applications, where specially designed soft matter particles can be used as drug delivery vehicles, in diagnostics, or represent a promising step towards the prevention of HIV and sexually transmitted infections [3,4]. In addition, for the assembly of photonic crystals, optical nano-structures that affect the motion of electromagnetic waves in the same way an electric semiconductor influences electrons, the growth of such crystals via self-assembling soft matter particles has become an attractive alternative [5].

Among the systems comprised in soft matter (liquids, gels, foams, polymers, granular materials, etc.), colloidal dispersions represent a large and prominent field. In colloidal dispersions a dispersed phase (the colloids or colloidal particles) is homogeneously mixed with a continuous phase, also called dispersion medium or solvent. Typical examples of colloidal dispersions appear e.g. in liquid and solid aerosols (clouds, smoke), sols (paint), emulsions (milk), or foams (whipped cream) [6].

Colloids are characterised by a variety of interesting features. The size of the particles (colloids), which can reach up to  $\simeq 1\mu\text{m}$ , simplifies their observation and handling in experiments, they can be virtually looked at via confocal microscopy [7] and manipulated by optical tweezers [8]. In addition, colloids can be assembled in various ways, giving rise to versatile *effective* interaction potentials: Via suitable coarse graining procedures [9], the influences of the particles constituting the dispersion medium on the colloids as well as the usually complicated architecture of the colloids themselves are integrated out. One obtains interaction potentials solely depending on the positions of the centres of mass of the comparatively large colloidal particles and, if necessary, a few other degrees of

freedom, describing e.g. the orientation of asymmetrical colloids like diblock copolymers [10]. The interactions of these effective particles exhibit energy scales of the order of room temperature thermal energies (i.e., of the order of  $k_B T$ ,  $T$  being the temperature and  $k_B \simeq 1.38 \cdot 10^{-23} \text{J/K}$  being the Boltzmann constant), which makes it possible to neglect quantum effects.

Through assembling appropriate colloids and varying the properties of the solvent into which the colloids are dispersed, one can therefore actually *tailor* the interaction potential between the system particles. Using this feature, it has been possible to experimentally design systems of hard spheres [11–13], which for a long time were only viewed as an academic model. Subsequently these systems of hard spheres could be altered to additionally exhibit other interactions, e.g. through attaching electric charges to the particles [14, 15], or covering them with grafted polymer chains [16, 17].

The goal of this thesis is to study such hard core systems theoretically. We intend to investigate the phase behaviour of typical model systems, where we focus on two different regions of phase space: First we investigate the vicinity and location of the gas–liquid critical point, and second we explore the region of solid phases, looking for yet unrecognised equilibrium crystal structures.

For the first task we scrutinise the *long–range critical behaviour* of three different model systems, one exhibiting a Coulomb and a Kac interaction, and two systems having either of the two in addition to a Yukawa interaction. After locating the critical point of the respective system, we investigate its critical behaviour through calculating three critical exponents:  $\beta$ , describing the shape of the gas–liquid coexistence curve in the critical region;  $\alpha$ , specifying how the specific heat at constant volume diverges at the critical point; and in particular  $\gamma$ , which gives information about the divergence of the isothermal compressibility, also at the critical point. The accuracies of the results for the location of the critical point and especially the critical exponents strongly depend on the level of sophistication of the applied liquid state theory. The self–consistent Ornstein–Zernike approximation (SCOZA) [18–20] is an integral equation theory that has proven to be reliable even in the critical region, which is why the application of SCOZA also to our model systems is a promising challenge to undertake. Since SCOZA has not been applicable to long–range interactions so far, we have to modify this concept to meet our requirements, approaching the limit of state–of–the–art numerical accuracy.

The other, main emphasis is put on the search for solid equilibrium structures at zero temperature in the hard core square–shoulder and hard core Yukawa models. Since the conventional approach to finding the equilibrium structures strongly depends on a preselection of candidate structures (relying on experience, intuition, or plausible arguments), a highly unsatisfactory approach that is likely to overlook possible candidates [21], we apply a search strategy based on a genetic algorithm (GA) [22]. In soft matter theory the usage of GAs, that incorporate key ideas of evolutionary processes such as survival of the fittest, recombination, or mutation, is still in its infancy. Nevertheless, it has been successfully

applied to soft systems (without hard core) [23–25] and monolayers of binary dipolar mixtures [26] recently. The central issue in the application of this highly stochastic algorithm to three-dimensional hard core systems is to find a parameter space which describes all possible crystal structures, excluding those structures exhibiting hard core overlaps *a priori*. We take care of this problem through the development of the so-called minimum distance parametrisation of crystal lattices.

To provide some more fundamental understanding of the emerging self-assembly strategies, we also extend the approach of averaging the particle densities and energies by Glaser *et al.* in two dimensions [27] to a three-dimensional, mean-field type “continuum theory”. We compare its predictions for the square-shoulder model with detailed investigations using the GA based search strategy.

This thesis is organised as follows.

The first part provides the prerequisites for our work. In chapter 2 the model systems of interest are introduced and the concepts of interaction range and reduced units are explained. Chapter 3 provides the basic background, both for the phenomenon of criticality, as well as for the theoretical tools suitable for the investigation of the fluids under consideration.

Part II elucidates the methods we developed for this thesis. In chapter 4 we explain how one can apply SCOZA to charged Yukawa systems, while chapter 5 is dedicated to the tasks one has to accomplish when looking for equilibrium crystal structures. These comprise in particular the development of the minimum distance parametrisation, a short discussion of possible close-packed structures, and the usage of these and other concepts (GA, metric crystal scaling, etc.) to establish a suitable search strategy for stable crystals. The last section of chapter 5 illustrates the mean-field type continuum theory.

Our results on criticality are presented in part III for the three chosen examples of the charged Yukawa (chapter 6), the charged Kac (chapter 7), and the Kac–Yukawa model (chapter 8). Part IV contains our findings concerning the equilibrium structures in the solid phase of the square-shoulder (chapter 9) and the hard core Yukawa model (chapter 10).

Finally, we give some concluding remarks in chapter 11.





**Part I**  
**Fundamentals**



# Chapter 2

## Models

The basic assumption needed for the description of a system of particles via *pair potentials* is the superposition principle, i.e., that the interaction between two particles does not depend on the degrees of freedom (position, orientation, ...) of any *other* particle. Especially in colloidal dispersions we usually deal with so called effective interactions (see introduction), where we obtain interactions depending only on the positions of the centres of mass of the comparatively large colloidal particles, which are also radially symmetric if no dipole-moments or extreme asymmetrical shapes of the colloids are involved. These simplified, effective interactions are in general also composed of 3-body and/or higher order interactions; however, (luckily) these multi-body interactions usually play a minor role and can be neglected, except at very high concentrations [9].

It is the aim of statistical mechanics, as will be outlined in chapter 3, to derive thermodynamic properties of a large ensemble of particles, like pressure in dependence on density and temperature (a so-called equation of state), starting from this pair potential.

In this chapter we introduce and justify the selection of pair interactions considered in this thesis, which will have one common feature: a hard core, reflecting the size of the rigid colloidal particles.

### 2.1 Coulomb and Screened Coulomb Interactions

The restricted primitive model (RPM) of electrolytes is a very popular model in statistical mechanics [28–30]. It is a binary mixture of size-symmetric hard particles having opposite electric charges, immersed in a dielectric background. Since this background carries no net charge, the electro-neutrality condition demands that the particle densities of the two constituting particle species have to be equal,  $\rho_+ = \rho_-$ . Using

$i, j = +, - \dots \dots \dots$  indices for different particle species,  
 $\rho = \rho_+ + \rho_- = 2\rho_i \dots$  overall particle density,  
 $\sigma_i \equiv \sigma \dots \dots \dots$  particle (hard core) diameter(s), and  
 $q_+ = -q_- \equiv q \dots \dots \dots$  electric charge(s),

the pair interaction in this system is given by

$$\phi_{ij}^{\text{RPM}}(r) = \begin{cases} \infty & r < \sigma \\ \phi_{ij}^{\text{C}}(r) & r \geq \sigma \end{cases}, \quad (2.1)$$

where  $\phi_{ij}^{\text{C}}(r) = \frac{q_i q_j}{\varepsilon r}$  is the Coulomb interaction with  $r = |\mathbf{r}_i - \mathbf{r}_j|$  being the distance between two particles positioned at  $\mathbf{r}_i$  and  $\mathbf{r}_j$ , and  $\varepsilon$  being the dielectric constant of the surrounding medium.

In colloidal dispersions one usually has to deal with a solution of the colloids in a salty solvent, which is necessary to prevent the colloidal particles from flocculating or sedimentation. If the colloids are charged, the salt ions in the solvent lead, according to the Derjaguin–Landau–Verwey–Overbeek (DLVO) theory [31, 32], to a screening of the Coulomb interaction yielding an effective interaction of

$$\phi_{ij}^{\text{DLVO}}(r) = \begin{cases} \infty & r < \sigma \\ \phi_{ij}^{\text{C}}(r) \frac{e^{-\alpha(r-\sigma)}}{(1+\alpha\sigma/2)^2} & r \geq \sigma \end{cases}, \quad (2.2)$$

usually called DLVO pair potential, with the screening parameter  $\alpha$ .  $1/\alpha$  has the dimension of a length and hence is usually called screening length. Sometimes the DLVO pair potential is also denoted as Yukawa restricted primitive model (YRPM), since the  $r$ -dependence has the typical form of a Yukawa interaction,  $\exp(-\kappa r)/r$ .

## 2.2 Single Yukawa Interaction

In salty, charged colloidal dispersions it is even possible for all the colloids to carry the *same charge* (all negative or positive, respectively), since the electro-neutrality condition is then satisfied through the salt counter-ions. In such a single component colloidal system the effective pair interaction between the colloids, with the solvent degrees of freedom integrated out, is then given by a single Yukawa interaction term in addition to the hard core interaction:

$$\phi^{\text{Y}}(r) = \begin{cases} \infty & r < \sigma \\ \frac{\varepsilon_Y \sigma}{r} e^{-\alpha(r-\sigma)} & r \geq \sigma \end{cases}, \quad (2.3)$$

with  $1/\alpha$  being again the screening length and  $\varepsilon_Y$  the interaction energy at contact.

## 2.3 The Kac Limit

The Yukawa interaction, equation (2.3), contains two relevant parameters,  $\varepsilon_Y$  and  $\alpha$  ( $\sigma$  is just a unit for the length scale, see section 2.8). If  $\alpha$  tends to zero, the exponential term becomes 1 and we end up with the RPM. If  $\varepsilon_Y$  vanishes (at constant  $\alpha$ ) the complete Yukawa term vanishes and the problem is reduced to plain hard spheres.

There is also a possibility for *both* parameters to tend to zero in a well-defined way, leading to a further, non-trivial interaction tail. This can be achieved by defining two quantities,  $\epsilon_K$  and  $n(> 0)$ , in a way to satisfy

$$\epsilon_Y e^{\alpha\sigma} = \epsilon_K \alpha^n . \quad (2.4)$$

Clearly,  $\epsilon_Y \rightarrow 0$  if  $\alpha \rightarrow 0$ . Thus we obtain for the Yukawa interaction

$$\phi(r; \alpha, n) = \epsilon_K \alpha^n \frac{e^{-\alpha r}}{r/\sigma} , \quad (2.5)$$

where the parametrical dependencies on  $\alpha$  and  $n$  are given explicitly. Now we calculate the field content of this interaction, which is usually the integral over the whole space of the interaction potential. For hard sphere particles this is just the integral over space except the volume of the central particle itself (which is a sphere of radius  $\sigma$  and centre at the origin, indicated by 0), i.e., the field content of the tail:

$$\int_{\mathbb{R}^3 - B_\sigma(0)} d^3r \phi(r; \alpha, n) = 4\pi\epsilon_K\sigma\alpha^n \int_\sigma^\infty dr r^2 \frac{e^{-\alpha r}}{r} = 4\pi\epsilon_K\sigma\alpha^{n-2} \left(1 + \mathcal{O}[(\alpha\sigma)^2]\right) . \quad (2.6)$$

If we now take the limit of  $\alpha \rightarrow 0$  there are three relevant possibilities:

- **$n > 2$ :** Not only the contact value but also the field content vanishes. We suspect that this interaction will not have any influence at all on the system, which is therefore again reduced to hard spheres.
- **$n = 2$ :** The field content attains the finite value of  $4\pi\epsilon_K\sigma$ .
- **$n < 2$ :** The field content diverges while the contact value of the potential still goes to zero.

Taking  $n = 2$  yields what is generally known as the Kac potential [33]:

$$\phi^{\text{Kac}}(r) = \epsilon_K \lim_{\alpha \rightarrow 0} \alpha^2 \frac{e^{-\alpha r}}{r/\sigma} , \quad (2.7)$$

which will be part of further considerations in this thesis.

## 2.4 Charged Yukawa and Kac–Yukawa Model

We will also consider a more general model, called *charged Yukawa model* [34], which is a *linear combination* of the hard core, the Coulomb, and the single Yukawa interactions, i.e.,

$$\phi_{ij}^{\text{CY}}(r) = \phi^{\text{Y}} + \phi_{ij}^{\text{C}} . \quad (2.8)$$

This pair interaction contains the RPM, equation (2.1), and the single Yukawa model, equation (2.3), as limiting cases, if either  $\epsilon_Y$  or  $q$  vanishes, respectively. Our considerations will also include the Yukawa part exhibiting the Kac limit.

Of course one can also combine just two Yukawa interactions with the hard core, one of which then gradually becomes a Kac potential. This kind of interaction will be termed *Kac–Yukawa model*:

$$\phi^{\text{KY}}(r) = \phi^{\text{Y}}(r) + \phi^{\text{Kac}}(r) . \quad (2.9)$$

## 2.5 Square–Shoulder Model

The square–shoulder model (SSM), also called hard core – soft shoulder interaction, is given by

$$\phi^{\text{SSM}}(r) = \begin{cases} \infty & r < \sigma \\ \epsilon & \sigma \leq r < \lambda \\ 0 & r \geq \lambda \end{cases} . \quad (2.10)$$

Due to its simple shape, it is easy to understand the arrangement of solid phases on geometric grounds (see the results presented in chapter 9) and hence this model is considered a “quintessential” [35] test system for solid–solid transitions. The SSM can also be a reasonable approximation for interactions between polymer–grafted colloidal particles [17] and has been extensively studied with Monte Carlo simulations and theoretical approaches in three and two dimensions in [27,36,37] and references therein, and using genetic algorithms in two dimensions [26,38].

## 2.6 Penetrable Sphere Model

The pair potential for the penetrable sphere model (PSM) is given by

$$\phi^{\text{PSM}}(r) = \begin{cases} \epsilon & r < \lambda \\ 0 & r \geq \lambda \end{cases} . \quad (2.11)$$

We will only use it for some approximate considerations of the SSM system in the continuum theory (see sections 5.8 and 9.3).

## 2.7 Interaction and Correlation Function Range

In discussing interactions it is useful to introduce a measure for the range of the interactions, that represents not just a criterion whether the interaction becomes exactly zero beyond some finite distance and above (SSM), or attains zero only asymptotically as  $r \rightarrow \infty$  (Yukawa, DLVO, Coulomb). Clearly it is important to distinguish between the different behaviour at long distances of the Yukawa and DLVO interactions compared to the Coulomb one. It is common to use the terms short and long range interactions, quantified as follows [39]:

An interaction potential  $\phi(r)$  is said to be long ranged if its field content outside the near-field region is infinite, i.e.,

$$4\pi \int_R^\infty \phi(r)r^2 dr = \infty \quad \forall R < \infty \quad \Rightarrow \quad \phi(r) \text{ is long ranged.} \quad (2.12)$$

In this sense the SSM, Yukawa and DLVO interactions are short ranged, while the Coulomb interaction has long range. We have to give some remarks here.

- The Kac interaction, which has a  $1/r$ -dependence like a Coulomb interaction but finite field content, is an exception to this rule; it is put into the set of long ranged interactions.
- If one replaces  $\phi(r)$  in equation (2.12) by a correlation function, which will be introduced in sections 3.2 and 3.3, we also obtain the common criterion for the (short or long) range of the corresponding correlation function.

## 2.8 Reduced Units

Comparing results of different theories, simulations, and experiments is an important task in scientific work. Historically various different systems of measurement have been established, including the appropriate conversion rules between them, and of course there is an ongoing debate about which system should be preferably used for the various physical phenomena.

There exists however a way to avoid this problem especially in theoretical considerations, that in addition can even clarify the underlying physical background. This way is to use for each problem its “natural” units, which correspond to characteristic scales of the model under consideration, as will be described in the following. In this thesis there will be only need of a few units of measurement, namely:

- **Length scale**

Since we are always dealing with equally sized hard spheres, the natural choice of length scale is the *hard core diameter*  $\sigma$ . It may happen that another characteristic length like the cutoff distance (the distance at which the interaction between two particles becomes negligible, i.e.  $\lambda$  for the square-shoulder potential) is describing the size of regions where interesting physical events appear more adequately. These cases will be pointed out explicitly in the appropriate sections.

- **Energy scale**

We use the previously defined length scale as an indication which energy is characteristic for the problem: The *interaction energy at contact* of two hard core particles, i.e., at a separation equal to the length scale, is the unit of choice.

To distinguish the reduced quantities from the original physical ones, we mark the quantities with stars, i.e., for the reduced length of the particle distance  $r$  we write

$$r^* = \frac{r}{[\text{length scale}]} = \frac{r}{\sigma}, \quad (2.13a)$$

and analogously any other length.

Similarly the inverse screening length  $\alpha$  is reduced through

$$\alpha^* = \alpha\sigma, \quad (2.13b)$$

and since the particle density  $\rho$  has dimension  $[\text{volume}]^{-1}$  we get

$$\rho^* = \rho\sigma^3. \quad (2.13c)$$

Thermodynamic potentials [(free) energies/enthalpies (per particle)] are simply reduced by the potential at contact. What will be used later are the energy per particle  $e$  and the enthalpy per particle  $h$  in the SSM system,

$$e^* = \frac{e}{\epsilon} = \frac{E/N}{\epsilon}, \quad (2.13d)$$

$$h^* = \frac{h}{\epsilon} = \frac{H/N}{\epsilon}. \quad (2.13e)$$

Capital letters  $E$  and  $H$  denote the total energy/enthalpy of the system under consideration, respectively, while  $N$  is the number of considered particles.

Quantities having dimension  $[\text{energy}] \times [\text{volume}]^{-1}$  are of course reduced by a factor of  $[\text{length scale}]^3 \times [\text{energy scale}]^{-1}$ . Among these we will use the internal energy per volume  $u = U/V$  reduced with the Yukawa energy at contact

$$u^* = \frac{u\sigma^3}{\epsilon_Y}, \quad (2.13f)$$

and the pressure  $P$ , both for Yukawa and SSM systems

$$P^* = \frac{P\sigma^3}{\epsilon_{(Y)}}. \quad (2.13g)$$

Occurring temperatures  $T$  always correspond to thermal energies of  $k_B T$ , where  $k_B$  is the famous Boltzmann constant ( $k_B = 1.3806504(24) \cdot 10^{-23} \text{J/K}$  in SI units). Thermal energies are more appropriate to describe the microscopic behaviour of a system than the arbitrary temperature scale of Kelvin, because  $k_B T$  is the order of magnitude of the energy of one single particle in an ensemble of particles at temperature  $T$ . This follows from the general *equipartition theorem*

$$\left\langle x_m \frac{\partial \mathcal{H}}{\partial x_n} \right\rangle = \delta_{mn} k_B T, \quad (2.13h)$$



which states that the thermodynamic average of  $x_m \frac{\partial \mathcal{H}}{\partial x_n}$ , with  $\mathcal{H}$  being the Hamiltonian of the system and  $x_m, x_n$  being any variables the Hamiltonian depends on [see equation (3.7)], is equal to  $k_B T$  if  $m = n$  (hence the Kronecker delta  $\delta_{mn}$ )<sup>1</sup>. E.g.,  $\frac{3}{2}k_B T$  is the average (translational) kinetic energy of one single particle in three dimensions. Therefore we define the reduced temperature as

$$T^* = \frac{k_B T}{[\text{energy at contact}]},$$

giving rise to the following quantities for the different models where temperature will be used:

$$T_Y^* = \frac{k_B T}{\epsilon_Y}, \quad (2.13i)$$

$$T_{\text{RPM}}^* = \frac{k_B T}{q^2/\epsilon\sigma}, \quad (2.13j)$$

$$T_{\text{CY}}^* = \frac{k_B T}{q^2/\epsilon\sigma + \epsilon_Y}. \quad (2.13k)$$

Sometimes it is also convenient to use the inverse thermal energy  $\beta = 1/(k_B T)$  in reduced units, i.e.,

$$\beta^* = \frac{1}{T^*}. \quad (2.13l)$$

In discussing the charged Yukawa model it is useful to introduce a parameter describing the relative importance of the two competing interactions:

$$q^* = \frac{q^2/\epsilon\sigma}{\epsilon_Y} = \frac{T_Y^*}{T_{\text{RPM}}^*} \quad (2.13m)$$

is the ratio of the two interaction contributions at contact and is called *reduced charge* [34].

---

<sup>1</sup>This theorem can easily be understood through an integration by parts of the complete phase-space integral of the canonical probability density equation (3.11), see [40, 41].



# Chapter 3

## Concepts for Fluids

When investigating the behaviour of a particular system, the *phase diagram* is of main interest. It depicts, in dependence on the appropriate thermodynamic variables (see section 3.2), the regions of the corresponding stable phases. A simple example for such a phase diagram of a one-component system is given in figure 3.1. In the  $P$ - $T$ -diagram [figure

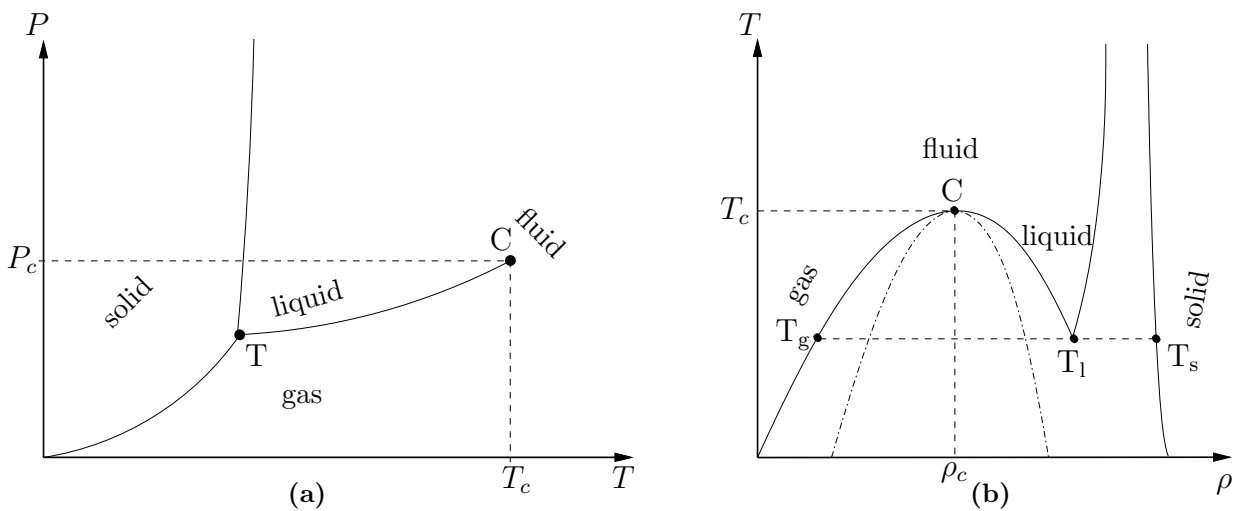


Figure 3.1: Sketch of a simple phase diagram in the  $P$ - $T$  and  $T$ - $\rho$  planes of a one-component system. The triple- and critical points are labelled  $T$  and  $C$ , respectively. In (b) the dash-dotted line is the spinodal line, delimiting the mechanically unstable region of the phase diagram, and the triple-“point” splits into three points, corresponding to the different densities of the coexisting phases.

3.1(a)] there appear, apart from the coexistence lines, two interesting phenomena. First there is the triple point, where all three phases, solid, liquid, and gaseous, coexist. Second, the gas-liquid coexistence line exhibits another endpoint, without intersecting any other coexistence lines. This means, that above a certain temperature  $T_c$  or pressure  $P_c$  the difference between the gas and the liquid phase disappears, and only one phase, usually

called fluid phase, exists. This state point is called the *critical point* of a substance, and will be a subject of our investigations in this thesis.

In the first section of this chapter we will explain how one can quantify the various critical phenomena. The sections 3.2 and 3.3 are then dedicated to the theoretical concepts that can be used to understand and predict the observed behaviour. In particular, we will describe how the self-consistent Ornstein–Zernike approximation (SCOZA, section 3.3.2) works, which we were able to apply to the charged Yukawa model, the topic of the next chapter. To facilitate comprehension we only deal with a one-component fluid throughout this chapter, the generalisation to two components will be given later on wherever needed.

For more background information see e.g. [40–43].

### 3.1 Critical Point Properties

Not only the location ( $T_c$ ,  $P_c$ , and  $\rho_c$ ) of the critical point is of interest, it is also characterised by the fact that certain thermodynamic quantities diverge or vanish there. In particular the difference in the densities of the liquid and gas phases, the so called order-parameter, vanishes at the critical point and is zero above it. On the other hand the correlation length, indicating the range of the influence of a disturbance at one position *diverges*, no matter whether the critical point is approached from the gas, liquid or fluid phase region.

For a more quantitative analysis one usually introduces the dimensionless temperature variable

$$\tau = \frac{T - T_c}{T_c}, \quad (3.1)$$

which measures the relative difference in temperature from the critical temperature. With the help of  $\tau$  we can quantify the behaviour of the thermodynamic quantities close to the critical point. For large groups of systems there appears a concordance in this quantitative behaviour, giving rise to the so called *universality classes* of systems, which exhibit the same critical behaviour. We quantify now this behaviour by the definition of the so called *critical exponent*  $e_Q$ , which is related to a thermodynamic property  $Q$  and characterises how  $Q$  behaves in the vicinity of the critical point via the generalised power series around  $\tau = 0$

$$Q(\tau) = \tau^{\pm e_Q} (q_1 + q_2\tau + q_3\tau^2 + \dots) \quad (3.2)$$

with the series coefficients  $q_i$ , or, in short notation,

$$Q(\tau) \sim \tau^{\pm e_Q}. \quad (3.3)$$

By convention the  $e_Q$  are assumed to be positive. Some of the critical exponents that are relevant for our work are presented together with their definitions in table 3.1. While the expansion coefficients  $q_i$  in equation (3.2) usually depend on all occurring system parameters, the critical exponents are more universal, i.e., belong to a so called *universality class*, characterised only by a few settings (class of model, applied theory; see table 3.2).

Exponent	Definition	valid range of $\tau$	Quantity
$\alpha$	$C_V \sim \tau^{-\alpha}$	$> 0$	specific heat at constant volume; along $V = V_c$
$\alpha'$	$C_V \sim (-\tau)^{-\alpha'}$	$< 0$	specific heat at constant volume; along the coexistence curve
$\beta$	$\rho_l - \rho_g \sim (-\tau)^\beta$	$< 0$	difference in the densities of the liquid and the gas phase, order parameter for fluids (shape of coexistence curve)
$\gamma$	$\chi_T \sim \tau^{-\gamma}$	$> 0$	isothermal compressibility; along critical isochore ( $V = V_c$ )
$\gamma'$	$\chi_T \sim (-\tau)^{-\gamma'}$	$< 0$	isothermal compressibility; along coexistence curve
$\delta$	$P - P_c \sim  \rho - \rho_c ^\delta \text{sgn}(\rho - \rho_c)$	$= 0$	variation of $P - P_c$ with $\rho - \rho_c$ along the critical isotherm

Table 3.1: Definitions of a selected set of critical exponents for fluid systems (from [42] p. 44).

Note that there are separate definitions for critical exponents when approaching the critical point from above ( $\tau > 0$ ) or below ( $\tau < 0$ ); however, static scaling theory predicts that these values should coincide [42, 44, 45]. The static scaling hypothesis follows from the argument of self-similarity in renormalisation group theory (see e.g. [46]) and can be formulated most easily for the Gibbs free energy  $G$  of a magnetic system. Instead of  $G(T, H)$  we use  $\tilde{G}(\tau, H)$ , where, in addition to the variable transformation from  $T$  to  $\tau$ , we also subtract all non-singular terms. The basic assumption, or *static scaling law*, is that there exist two parameters  $a_\tau$  and  $a_H$ , such that

$$\tilde{G}(\lambda^{a_\tau} \tau, \lambda^{a_H} H) = \lambda \tilde{G}(\tau, H) \quad (3.4)$$

for any value of  $\lambda$ . The parameters  $a_\tau$  and  $a_H$  are not specified, but all critical exponents can be derived to be simple expressions only involving these two parameters [42]. One major result from these derivations is, that primed and unprimed critical exponents are equal.

In the literature often the *effective critical exponents* are introduced via logarithmic derivatives, e.g.,

$$\gamma_{\text{eff}}(\tau) = \frac{\partial (\log \chi_T^{-1})}{\partial (\log \tau)} \quad (3.5)$$

for the isothermal compressibility [see equation (3.25)], which of course must satisfy

$$\lim_{\tau \rightarrow 0_+} \gamma_{\text{eff}}(\tau) = \gamma. \quad (3.6)$$

Theory/Model	$\alpha$	$\alpha'$	$\beta$	$\gamma$	$\gamma'$	$\delta$
mean field	$0_{\text{disc}}$	$0_{\text{disc}}$	$\frac{1}{2}$	1	1	3
$D=3$ spherical model	-1	—	$\frac{1}{2}$	2	—	5
$D=2$ Ising model	$0_{\text{log}}$	$0_{\text{log}}$	$\frac{1}{8}$	$\simeq \frac{7}{4}$	$\simeq \frac{7}{4}$	$\simeq 15$
$D=3$ Ising model	$\simeq \frac{1}{8}$	$\simeq \frac{1}{8}$	$\frac{5}{16}$	$\simeq \frac{5}{4}$	$\simeq \frac{5}{4}$	$\simeq 5$
$D=3$ SCOZA [47]	0	$-\frac{1}{10}$	$\frac{7}{20}$	2	$\frac{7}{5}$	5

Table 3.2: Values for critical exponents explained in table 3.1; if not mentioned otherwise taken from [42].  $0_{\text{disc}}$  means there is no divergence but a discontinuity in the quantity associated with the critical exponent,  $0_{\text{log}}$  accounts for a logarithmic divergence. The order parameter of the Ising model is the magnetisation.

Plotting the effective exponent versus  $\tau$  we can visualise how the limiting value is attained and therefore identify the temperature region in the vicinity of the critical point, where the critical exponent dominates the thermodynamic behaviour, i.e.,  $\gamma_{\text{eff}} \simeq \gamma$ .

To predict this macroscopic critical behaviour from the microscopic (pair) interactions, we need some theoretical background.

## 3.2 Routes to Thermodynamics

Most of the following can be found in detail in [40, 41, 43].

Statistical mechanics provides the means to understand and predict the macroscopic behaviour of a fluid on the basis of the behaviour of the particles on a microscopic scale. Let us consider a system of  $N$  particles which, through their positions  $\mathbf{r}_i$  and momenta  $\mathbf{p}_i$  ( $i = 1, 2, \dots, N$ ), constitute the  $6N$ -dimensional *phase space*. The Hamiltonian of the system is

$$\mathcal{H}(\mathbf{r}^N, \mathbf{p}^N) = \frac{1}{2m} \sum_{i=1}^N \mathbf{p}_i^2 + \frac{1}{2} \sum_{i \neq j}^N \phi(|\mathbf{r}_i - \mathbf{r}_j|), \quad (3.7)$$

where  $m$  is the mass of the particles and  $\phi(r)$  is the pair potential between them.

Gibbs' formulation of statistical mechanics uses the phase space *probability density*  $f^{(N)}(\mathbf{r}^N, \mathbf{p}^N)$ , which is time independent for equilibrium systems and normalised through

$$\int f^{(N)}(\mathbf{r}^N, \mathbf{p}^N) d^{3N}r d^{3N}p = 1. \quad (3.8)$$

We assume that our equilibrium systems are *ergodic*, i.e., the time average of an observable quantity  $\mathcal{A}(\mathbf{r}^N, \mathbf{p}^N)$  is assumed to be equal to its ensemble average, given by

$$\langle \mathcal{A} \rangle = \int \mathcal{A}(\mathbf{r}^N, \mathbf{p}^N) f^{(N)}(\mathbf{r}^N, \mathbf{p}^N) d^{3N}r d^{3N}p. \quad (3.9)$$

The explicit form of the probability density depends on the ensemble one uses, i.e., the ambient conditions that are kept fixed. There are four important kinds of ensembles [40, 41, 43].

- *Microcanonical ensemble*

The number of particles in the system  $N$  is constant, as well as the total volume  $V$  and the total energy  $E$ . The last condition directly enters the probability density,  $f_{\mathcal{M}}^{(N)}(\mathbf{r}^N, \mathbf{p}^N) = (Wh^{3N})^{-1} \delta(\mathcal{H}(\mathbf{r}^N, \mathbf{p}^N) - E)$ . The normalisation constant  $W$  is usually called *microcanonical partition function* and given by

$$W = \frac{1}{h^{3N}} \int \delta(\mathcal{H}(\mathbf{r}^N, \mathbf{p}^N) - E) d^{3N}r d^{3N}p, \quad (3.10)$$

where  $h$  is Planck's constant.

- *Canonical ensemble*

Instead of the energy the temperature is kept constant through establishing contact with a heat bath of fixed temperature  $T$ , which is why this ensemble is also called  $NVT$ -ensemble. In this case the probability density is

$$f_{\mathcal{C}}^{(N)}(\mathbf{r}^N, \mathbf{p}^N) = \frac{e^{-\beta\mathcal{H}(\mathbf{r}^N, \mathbf{p}^N)}}{N! h^{3N} Q_N(V, T)}, \quad (3.11)$$

where  $\beta = 1/k_{\text{B}}T$ ,  $N!$  takes care of the indistinguishability of the particles, and

$$Q_N(V, T) = \frac{1}{N! h^{3N}} \int e^{-\beta\mathcal{H}(\mathbf{r}^N, \mathbf{p}^N)} d^{3N}r d^{3N}p \quad (3.12)$$

is the *canonical partition function*.

- *Isothermal–isobaric ensemble*

The  $NPT$ -ensemble is kept under constant pressure  $P$  and in contact with a heat bath. The corresponding probability density

$$f_{\mathcal{I}}^{(N)}(\mathbf{r}^N, \mathbf{p}^N) = \frac{\beta P}{N! h^{3N}} \frac{e^{-\beta(\mathcal{H}(\mathbf{r}^N, \mathbf{p}^N) + PV)}}{\Delta_N(P, T)} \quad (3.13)$$

contains the *isothermal–isobaric partition function* [48]

$$\Delta_N(P, T) = \frac{\beta P}{N! h^{3N}} \int e^{-\beta(\mathcal{H}(\mathbf{r}^N, \mathbf{p}^N) + PV)} d^{3N}r d^{3N}p dV. \quad (3.14)$$

Note that, in addition to the integration over the  $6N$ -dimensional phase space, there appears now an integral over all possible volumes.

- *Grand canonical ensemble*

In this ensemble the exchange of particles and energy with a reservoir (characterised by constant temperature  $T$  and chemical potential  $\mu$ ) is considered while  $V$  is constant. The probability density is given by

$$f_{\mathcal{G}}(\mathbf{r}^N, \mathbf{p}^N; N) = \frac{e^{-\beta(\mathcal{H}(\mathbf{r}^N, \mathbf{p}^N) - \mu N)}}{N! h^{3N} \Xi(\mu, V, T)} \quad (3.15)$$

with the *grand partition function*

$$\Xi(\mu, V, T) = \sum_{N=0}^{\infty} \frac{e^{\beta\mu N}}{N! h^{3N}} \int e^{-\beta\mathcal{H}(\mathbf{r}^N, \mathbf{p}^N)} d^{3N}r d^{3N}p. \quad (3.16)$$

Note that there appears a sum over all possible particle numbers in the system.

The link between statistical mechanics (in terms of the partition functions) and thermodynamic potentials is given by the following expressions [40, 41, 43]:

$$S = k_{\text{B}} \ln W, \quad (3.17\text{a})$$

$$F = -k_{\text{B}}T \ln Q_N(V, T), \quad (3.17\text{b})$$

$$G = -k_{\text{B}}T \ln \Delta_N(P, T), \text{ and} \quad (3.17\text{c})$$

$$\Omega = -k_{\text{B}}T \ln \Xi(\mu, V, T), \quad (3.17\text{d})$$

where  $S$  is the entropy,  $F$  is the (Helmholtz) free energy,  $G$  is the Gibbs free energy, and  $\Omega$  is the grand potential. Together with the internal energy  $U = \langle \mathcal{H}(\mathbf{r}^N, \mathbf{p}^N) \rangle$  and the enthalpy  $H$  (accessible through a Legendre transformation, see the literature [40, 41, 43])  $U$ ,  $H$ ,  $F$ ,  $G$ , and  $\Omega$  are termed *thermodynamic potentials* (TDPs), while  $S$ ,  $V$ ,  $P$ ,  $T$ ,  $N$ , and  $\mu$  are called *thermodynamic variables* (TDVs). Each TDP depends on exactly three TDVs, the dependencies are  $U(S, V, N)$ ,  $H(S, P, N)$ ,  $F(T, V, N)$ ,  $G(T, P, N)$ , and  $\Omega(T, V, \mu)$ . Each TDP is said to be dependent on its *natural variables*, since the dependency is directly linked to the corresponding ensemble, e.g., the appropriate TDP for the isothermal–isobaric ensemble (NPT–ensemble) is the Gibbs free energy [see the link in equation (3.17c)]. For further details, e.g. about equations of state, Maxwell relations, the Gibbs–Duhem relation, etc., we refer to the literature [40, 41, 43].

We consider now the canonical ensemble. If we integrate the probability density over all momenta and all but  $n$  positions, which is equal to calculating the canonical ensemble average of a product of Dirac– $\delta$  functions

$$\int f_c^{(N)}(\mathbf{r}^N, \mathbf{p}^N) d^{3(N-n)}r d^{3N}p = \int \prod_{i=1}^n \delta(\mathbf{r}_i - \mathbf{r}'_i) f_c^{(N)}(\mathbf{r}'^N, \mathbf{p}^N) d^{3N}r' d^{3N}p = \left\langle \prod_{i=1}^n \delta(\mathbf{r}_i - \mathbf{r}'_i) \right\rangle_c, \quad (3.18)$$

---

<sup>1</sup>See Boltzmann's grave, Zentralfriedhof Vienna, Group 14C, Number 1.



we obtain, upon multiplication with  $N!/(N-n)!$ , the  $n$ -particle density

$$\rho_N^{(n)}(\mathbf{r}^n) = \frac{N!}{(N-n)!} \int f_C^{(N)}(\mathbf{r}^N, \mathbf{p}^N) d^{3(N-n)}r d^{3N}p. \quad (3.19)$$

Because of the normalisation [equation (3.8)] we have  $\int \rho_N^{(n)}(\mathbf{r}^n) d^{3n}r = N!/(N-n)!$ , in particular  $\int \rho_N^{(1)}(\mathbf{r}) d^3r = N$ . For homogeneous systems this implies  $\rho_N^{(1)}(\mathbf{r}) = N/V = \rho$ , independent of position  $\mathbf{r}$ .

With the use of the  $n$ -particle density we can define the  $n$ -particle distribution function

$$g_N^{(n)}(\mathbf{r}^n) = \frac{\rho_N^{(n)}(\mathbf{r}^n)}{\prod_{i=1}^n \rho_N^{(1)}(\mathbf{r}_i)}, \quad (3.20)$$

a measure for the deviation of the fluid from complete randomness. A special case is the two-particle or pair distribution function  $g_N^{(2)}(\mathbf{r}_1, \mathbf{r}_2)$ . For homogeneous, isotropic systems the pair distribution function only depends on the separation  $r = |\mathbf{r}_1 - \mathbf{r}_2|$  between the two particles, it is then called the *radial distribution function* and simply written as  $g(r)$ . If the distance between the particles becomes large,  $g(r)$  approaches its ideal gas limit, i.e.,

$$g(r) \xrightarrow{r \rightarrow \infty} 1 - \frac{1}{N}. \quad (3.21)$$

There are two main reasons for the usefulness of the radial distribution function. Firstly, via a Fourier transformation,  $g(r)$  (in the grand canonical ensemble) is related to the static structure factor

$$S(\mathbf{k}) = 1 + \rho \int e^{-i\mathbf{k}\cdot\mathbf{r}} [g(r) - 1] d^3r, \quad (3.22)$$

a quantity that is directly accessible in scattering experiments [49].

Secondly, if the particles interact via pair potentials, the thermodynamic properties of the fluid can be expressed through integrals over  $g(r)$ . Of course, these properties are also linked by thermodynamic relations [40, 41, 43], giving rise to multiple possibilities for the calculation of any property.

To keep track of this situation it is customary to define the way of calculation of any thermodynamic quantity by its so called “route”. The routes are identified by the quantity obtained directly from the distribution function, i.e., quantities derived from the internal energy obtained through

$$\frac{U}{N} = \underbrace{\frac{3}{2}k_B T}_{U^{\text{id}}/N} + \underbrace{2\pi\rho \int_0^\infty \phi(r)g(r)r^2 dr}_{U^{\text{ex}}/N}, \quad (3.23)$$

are said to be calculated through the *energy route*. In equation (3.23)  $U^{\text{id}}$  is the so called “ideal” contribution, because it is the only term present for an ideal gas ( $\phi(r) \equiv 0$ ). The

“excess” (over ideal) part, designated by  $U^{\text{ex}}$ , is due to the influence of the interaction potential and can be understood intuitively: The mean number of particles at a distance  $r$  from a reference particle P is  $n(r)dr = 4\pi r^2 \rho g(r)dr$ . The interaction energy of these particles with P is of course  $\phi(r)n(r)dr$ , which has to be divided by 2 in order not to count pairs of particles twice. Integrating this over the whole space yields  $U^{\text{ex}}/N$  as given in equation (3.23).

This thermodynamic potential can now be used to derive any other thermodynamic quantity, e.g. the pressure through  $\partial U/\partial V|_S = -P$ . Instead, one can also calculate the pressure directly from the radial distribution function via

$$\frac{\beta P}{\rho} = 1 - \frac{2}{3}\pi\beta\rho \int_0^\infty \phi'(r)g(r)r^3 dr, \quad (3.24)$$

which describes the pressure  $P$  as an integral of the derivative of the interaction potential and defines the *virial route*.

The isothermal compressibility, defined as

$$\chi_T = -\frac{1}{V} \left( \frac{\partial V}{\partial P} \right)_T = 1 / \rho \left( \frac{\partial P}{\partial \rho} \right)_T, \quad (3.25)$$

obeys (in the grand canonical ensemble)

$$\rho k_B T \chi_T = 1 + \rho \int \underbrace{(g(r) - 1)}_{=:h(r)} d^3r. \quad (3.26)$$

$h(r)$  is the *total correlation function* of an isotropic homogeneous fluid, its Fourier transformation (FT) being

$$\tilde{h}(\mathbf{k}) = \int e^{-i\mathbf{k}\cdot\mathbf{r}} h(r) d^3r. \quad (3.27)$$

Therefore we can write the formula for the *compressibility route* as

$$\chi^* := \frac{\chi_T}{\chi_T^{\text{id}}} = \rho k_B T \chi_T = 1 + \rho \tilde{h}(0), \quad (3.28)$$

where  $\chi_T^{\text{id}}$  is the isothermal compressibility of the ideal gas, for which  $g(r) \equiv 1$  holds.

### 3.3 Integral Equation Theories

As mentioned previously, a possibility to obtain thermodynamic quantities is to know the radial (or equivalently the total) distribution function. Integral equation theories calculate the distribution function through the famous *Ornstein–Zernike relation* (OZ) [50], which we only need for the isotropic, homogeneous case

$$h(r) = c(r) + \rho \int c(r')h(|\mathbf{r} - \mathbf{r}'|) d^3r'. \quad (3.29)$$

This equation can be understood as a defining equation for  $c(r)$ , the *direct correlation function*. So far we just introduced one integral equation and one unknown function. However, it is possible to generate an additional relation between the two correlation functions occurring in equation (3.29) and  $\phi(r)$  leading to the so called *closure relations*. But before going into more details about these closure relations, we provide a deeper understanding and justification for equation (3.29).

A hint to comprehension is already hidden in the names for  $h(r)$  and  $c(r)$ . Equation (3.29) can be read as follows:

The *total* correlation function between particles of a fluid separated by a distance  $r$  is given by the *direct* correlation function between these particles **plus** the indirect correlation conveyed through the *direct* correlation with all other particles which, on their part, are *totally* correlated to the second particle.

Note that via the transformation of the integration variable given by  $\mathbf{r}' \rightarrow \mathbf{r}'' = \mathbf{r}' - \mathbf{r}$ , the indirect correlation can also be interpreted as being conveyed through the *total* correlation with all other particles which, on their part, are *directly* correlated to the second particle. This symmetry in the OZ relation is best viewed if one iterates equation (3.29),

$$\begin{aligned} h_1(r) &= c(r) , \\ h_2(r) &= c(r) + \rho[c \otimes c](r) , \\ h_3(r) &= c(r) + \rho[c \otimes c](r) + \rho[c \otimes c \otimes c](r) , \\ &\vdots \\ h_m(r) &= \sum_{n=1}^m \left[ \bigotimes_{i=1}^n c \right] (r) , \\ &\vdots \end{aligned} \tag{3.30}$$

where the symbol  $\otimes$  is used as an abbreviation for the convolution integral. The total correlation function is obviously  $h(r) = h_\infty(r)$ .

A reason for the usefulness of  $c(r)$  is its property of being short ranged in the sense of equation (2.12) even at the critical point, in contrast to the total correlation function, which behaves like

$$h(r) \sim \frac{e^{-r/\xi}}{r^{d-2+\eta}} , \quad \xi \sim |\tau|^{-\nu} , \tag{3.31}$$

with the thus defined critical exponents  $\eta$  and  $\nu$  (mean field values  $\eta = 0$  and  $\nu = 1/2$ , see [42]), and the dimension  $d$ . The integral over all space of  $h(r)$  is hence proportional to

$$\int_{\mathbb{R}^3} h(r) d^3r \propto \xi^{5-d-\eta} \sim |\tau|^{-\nu(5-d-\eta)} \tag{3.32}$$

in the critical region and therefore diverges at the critical point —  $h(r)$  becomes infinitely long ranged. The fact that  $c(r)$  always exhibits short range behaviour can be seen by the following considerations.

The FT of the OZ relation (3.29) leads to

$$\tilde{h}(\mathbf{k}) = \tilde{c}(\mathbf{k}) + \rho\tilde{c}(\mathbf{k})\tilde{h}(\mathbf{k}) . \quad (3.33)$$

Solving for  $\tilde{h}(\mathbf{k})$  gives

$$\tilde{h}(\mathbf{k}) = \frac{\tilde{c}(\mathbf{k})}{1 - \rho\tilde{c}(\mathbf{k})} , \quad (3.34)$$

which, setting  $\mathbf{k} = 0$ , we insert into equation (3.28) and then solve for  $\tilde{c}(0)$ :

$$\rho\tilde{c}(0) = 1 - \frac{\chi_T^{\text{id}}}{\chi_T} . \quad (3.35)$$

The compressibility  $\chi_T$  is a positive, finite quantity except at the critical point, where it diverges with the critical exponent  $\gamma$  (see table 3.1 in section 3.1). As a consequence,  $\tilde{c}(0)$  is always finite, even at the critical point<sup>2</sup>. But

$$\tilde{c}(0) = \int_{\mathbb{R}^3} c(r) d^3r < \infty \quad (3.36)$$

is just the condition for  $c(r)$  to be of short range [see equation (2.12)].  $\square$

At the critical point we obtain

$$\chi_T \rightarrow \infty \quad \Rightarrow \quad \rho\tilde{c}(0) \rightarrow 1 \quad \Rightarrow \quad \tilde{h}(0) \rightarrow \infty , \quad (3.37)$$

in consistency with equation (3.32). Additionally, equation (3.35) represents a formula for the calculation of the reduced compressibility via the direct correlation function instead of the total one as in equation (3.28),

$$\frac{1}{\chi^*} = 1 - \rho\tilde{c}(0) . \quad (3.38)$$

### 3.3.1 Closure Relations

The above mentioned closure relations rely on the following exact expression [51]:

$$c(r) = -\beta\phi(r) + h(r) - \ln g(r) + B(r) , \quad (3.39)$$

introducing the so called bridge<sup>3</sup> function  $B(r)$ , yet another unknown function. Specific closure relations are based on approximate expressions assumed for  $B(r)$ . For detailed explanations and derivations of the various relations we refer to the literature and restrict ourselves to those relations relevant for this thesis.

<sup>2</sup>In the case where  $\rho \rightarrow 0$  we get the ideal gas properties, i.e.,  $\chi_T = \chi_T^{\text{id}}$  and  $\tilde{h}(k) = \tilde{c}(k) = 0$ .

<sup>3</sup>The term ‘‘bridge’’ stems from the shape of the related graphs, see [43] chapter 4.

$c(r)$  always has to satisfy [43]<sup>4</sup>

$$c(r) \xrightarrow{r \rightarrow \infty} -\beta\phi(r). \quad (3.40)$$

To ensure this limiting condition for large  $r$  one can simply set

$$c(r) = -\beta\phi(r), \quad (3.41)$$

known as the *linearised Debye–Hückel* approximation. If the potential is strongly repulsive at short range, this approximation is very poor, which is especially true for interactions exhibiting a hard core. However, one can apply the exact long range condition of equation (3.41) only to the region outside the hard core and combine it with the exact condition inside:

$$c(r) = -\beta\phi(r) \quad \text{for } r \geq \sigma \text{ and} \quad (3.42a)$$

$$g(r) = 0 \quad \text{for } r < \sigma, \quad (3.42b)$$

where  $\sigma$  is the hard sphere diameter. Equation (3.42) is known as the *mean spherical approximation* (MSA). It is also the starting point for the closure relation of main interest in this thesis, the topic of the following section.

### 3.3.2 Self-Consistent Ornstein–Zernike Approximation (SCOZA)

If any approximations are made during the calculation of the radial distribution function, like the usage of an approximate closure relation, the result for any thermodynamic quantity will depend on the route (see section 3.2) one chooses to calculate a specific quantity — the theory becomes inconsistent. It is a major task to minimise or even remove this error, achievable e.g. through SCOZA, as will be outlined now.

To overcome the inconsistency between the various routes, i.e., to make the theory *self-consistent*, several modifications to the known closure relations have been made. The general principle is to introduce additional parameters or unknown functions that can be adjusted to fit experimental or simulation data, or, the path also we will follow, to analytically impose thermodynamical consistency between the different routes.

An important example of such a modification is the generalised mean spherical approximation introduced by Waisman [53] to improve the MSA results for hard core particles. He changed the ansatz  $c(r) = 0$  outside the core to

$$c_{\text{HS}} = K_{\text{HS}}(\rho) \frac{e^{-\alpha_{\text{HS}}(r-\sigma)}}{r}, \quad (3.43)$$

i.e., to a Yukawa tail. After analytically solving the OZ relation with the exact core condition of equation (3.42b) and the closure equation (3.43) he chose the parameters

---

<sup>4</sup>To be exact, this limiting case equation concerns only long range parts of the interaction  $\phi(r)$ , which enter the Stillinger–Lovett sum–rules of ion correlation functions [52].

$K_{\text{HS}}(\rho)$  and  $\alpha_{\text{HS}}$  in a way to fit the Carnahan Starling equation of state [54]. Waisman's analytic solution was extended by Høye and Stell together with Waisman [55] to a linear combination of two Yukawa tails for  $c(r)$ .

Stell *et al.* [18, 56, 57] probably were the first to introduce the term *self-consistent Ornstein-Zernike approximation* (SCOZA). They used a similar scheme for ionic and dipolar fluids and fitted the available parameters to external data to obtain thermodynamical consistency. This first approach has been replaced later by a different approach, originally proposed by Høye and Stell [19, 58]. All versions of SCOZA are based on the MSA closure equation (3.42), where additional, state dependent functions are introduced and determined via demanding thermodynamic consistency, leading to partial differential equations (PDEs) for these unknown functions.

The version of SCOZA we will consider in this thesis is the one proposed in [20]. The closure relation is given by

$$c(r) = c_{\text{HS}}(r) + K(\beta, \rho)\phi(r) \quad \text{for } r \geq \sigma \text{ and} \quad (3.44a)$$

$$g(r) = 0 \quad \text{for } r < \sigma, \quad (3.44b)$$

where  $c_{\text{HS}}(r)$  is the hard sphere correction of Waisman given above in equation (3.43) and  $K(\beta, \rho)$  is the only state dependent function introduced here.

Since we have introduced only one function, thermodynamic consistency can only be imposed between two of the three routes, in this case between the energy and compressibility routes. To obtain a PDE for  $K(\beta, \rho)$  first consider the relations  $U = F + TS$  and  $S = -\left.\frac{\partial F}{\partial T}\right|_{V,N}$  [40, 41, 43]. Switching from  $T, V, N$  to  $\beta, \rho, N$  we get  $U = F + \beta\left.\frac{\partial F}{\partial \beta}\right|_{\rho,N}$  and hence  $u = \left.\frac{\partial}{\partial \beta}\right|_{\rho,N}(\beta f)$  for the quantities per volume, indicated by the lower case letters. On the other hand, from  $P = -\left.\frac{\partial F}{\partial V}\right|_{T,N}$ , we obtain  $\beta P = -\beta f + \rho\left.\frac{\partial}{\partial \rho}\right|_{\beta,N}(\beta f)$ , resulting in  $\left.\frac{\partial}{\partial \rho}\right|_{\beta,N}(\beta P) = \rho\left.\frac{\partial^2}{\partial \rho^2}\right|_{\beta,N}(\beta f)$ . Under the (common) assumption that the differentiations w.r.t.  $\beta$  and  $\rho$  commute (and dropping the  $N$  subscript since it will be always constant here), we arrive at

$$\rho\left.\frac{\partial^2}{\partial \rho^2}\right|_{\beta} u = \left.\frac{\partial}{\partial \beta}\right|_{\rho} \left(\frac{1}{\chi^*}\right), \quad (3.45)$$

where we used equation (3.25) and equation (3.28) to introduce the reduced compressibility. Note, that since the second derivative of the ideal part of  $u$  w.r.t. the density vanishes [see equation (3.23)], we can write  $u^{\text{ex}}$  instead of  $u$  on the l.h.s. of equation (3.45).  $u^{\text{ex}}$  and  $\chi^*$  can be replaced by expressions including only the correlation functions and eventually the known pair potential using equation (3.23) and equation (3.28). This finally results in three equations, (3.29), (3.44), and (3.45), for the three unknown functions  $g(r)$  [or  $h(r)$ ],  $c(r)$ , and  $K(\beta, \rho)$ .

It seems to be a difficult task to analytically reduce this set of equations to a single PDE for  $K(\beta, \rho)$ , and indeed this set of equations is usually solved directly with numerical methods. If however the pair potential happens to be a sum of Yukawa interactions, also

the ansatz for  $c(r)$ , equation (3.44a) consists only of Yukawa tails. In this case an analytical solution to the MSA closure ( $K(\beta, \rho) \equiv -\beta$ ) exists [59] and can be used, as derived by Schöll-Paschinger [60], to obtain a single SCOZA PDE for  $u(\beta, \rho)$ .

The reason why we are interested in extending the SCOZA to other than multi-Yukawa systems is, that the SCOZA has proven to give reliable results for thermodynamics even in the critical region. Also the critical exponents, especially below the critical temperature, show remarkable agreement with the exact ones [47]. In chapter 4 we will show how one can apply the SCOZA to the charged Yukawa system, while results from this theory are presented in part III.





# Part II

## Methods



# Chapter 4

## Application of SCOZA to Charged Yukawa Systems

The pair potential of the charged Yukawa model comprises a Yukawa and a Coulomb interaction [see equation (2.8)], the latter preventing a direct application of the SCOZA closure equation (3.44), because this would contradict equation (3.40) and hence violate the Stillinger–Lovett sum–rules [52,61]. Therefore we treated the two contributions separately, using a separation method introduced by Kristóf *et al.* [34], and developed a modified SCOZA (mSCOZA), where the SCOZA closure equation (3.44a) is only applied to the Yukawa part and thermodynamic consistency is still guaranteed for the entire system. This concept, together with its results and a detailed comparison to Monte Carlo simulations, was published in [62].

### 4.1 Separation of Coulomb and Yukawa Interactions

#### 4.1.1 Ornstein–Zernike Relation and MSA Closure

To describe the separation of Coulomb and Yukawa contributions to the charged Yukawa model we generalise the Ornstein–Zernike relation (3.29) to binary mixtures. We indicate the two particle species by indices + and – (like in section 2.1 for the RPM) and use the notation for the convolution integral already introduced in equation (3.30),

$$h_{++}(r) = c_{++}(r) + \rho_+ [h_{++} \otimes c_{++}](r) + \rho_- [h_{+-} \otimes c_{-+}](r), \quad (4.1a)$$

$$h_{+-}(r) = c_{+-}(r) + \rho_+ [h_{++} \otimes c_{+-}](r) + \rho_- [h_{+-} \otimes c_{--}](r). \quad (4.1b)$$

Due to symmetry  $c_{--}(r) = c_{++}(r)$  and  $c_{-+}(r) = c_{+-}(r)$  [and likewise for  $h_{--}(r)$  and  $h_{-+}(r)$ ]. The charge–neutrality condition demands  $\rho_+ = \rho_- \equiv \rho/2$  for the system, and introducing Yukawa and Coulomb total and direct correlation functions (indicated by the

respective superscripts) through

$$h^Y(r) = \frac{1}{2}(h_{++}(r) + h_{+-}(r)) , \quad (4.2a)$$

$$h^C(r) = \frac{1}{2}(h_{++}(r) - h_{+-}(r)) , \quad (4.2b)$$

$$c^Y(r) = \frac{1}{2}(c_{++}(r) + c_{+-}(r)) , \text{ and} \quad (4.2c)$$

$$c^C(r) = \frac{1}{2}(c_{++}(r) - c_{+-}(r)) \quad (4.2d)$$

the Ornstein–Zernike relations decouple:

$$h^Y(r) = c^Y(r) + \rho [h^Y \otimes c^Y](r) \quad \text{and} \quad (4.3a)$$

$$h^C(r) = c^C(r) + \rho [h^C \otimes c^C](r) . \quad (4.3b)$$

Next we define the radial Yukawa–distribution function through

$$g^Y(r) = h^Y(r) + 1 . \quad (4.4a)$$

In order to maintain the relation  $g_{++}(r) = g^Y(r) + g^C(r)$  (analogous to  $h_{++}(r) = h^Y(r) + h^C(r)$ ), the Coulomb–radial distribution function is given by

$$g^C(r) = h^C(r) . \quad (4.4b)$$

The complete decoupling of the OZ equations requires also a decoupling of the closure relations, not only w.r.t. the correlation functions but also the interaction potential contributions. Keeping in mind that we want to end up with the SCOZA closure similar to equation (3.44), we use, as a first step, a modified MSA closure where the Waisman hard sphere correction of equation (3.43) is included. Thus generalising equation (3.42) to binary symmetric mixtures the closure reads

$$c_{ij}(r) = c_{\text{HS}}(r) - \beta \phi_{ij}^{\text{CY}}(r) \quad \text{for } r \geq \sigma \text{ and} \quad (4.5a)$$

$$g_{ij}(r) = 0 \quad \text{for } r < \sigma . \quad (4.5b)$$

Using equation (4.2),  $g_{ij}(r) = h_{ij}(r) + 1$ , and equation (4.4) we finally obtain [34]

$$g^Y(r) = 0, \quad r < \sigma \quad (4.6a)$$

$$c^Y(r) = c^{\text{HS}}(r) - \beta \phi^Y(r), \quad r > \sigma \quad (4.6b)$$

$$g^C(r) = 0, \quad r < \sigma \quad (4.6c)$$

$$c^C(r) = -\frac{\beta q^2}{\varepsilon r}, \quad r > \sigma \quad (4.6d)$$

as closure relations. With equations (4.3a), (4.4a), (4.6a), and (4.6b) (and (3.43)) on the one hand and (4.3b), (4.4b), (4.6c), and (4.6d) on the other hand we have therefore two

completely separated sets of equations to solve for the Yukawa and Coulomb correlation functions, respectively.

Comparing equation (4.6b) with equation (3.44a) we recognise, that we can now impose a SCOZA closure on the Yukawa part alone by replacing equation (4.6b) with

$$c^Y(r) = c^{\text{HS}}(r) + K(\beta, \rho)\phi^Y(r), \quad r > \sigma, \quad (4.6e)$$

still satisfying equation (3.40) for the entire system. Equation (4.6a,c–e) represent the complete closure relation for our mSCOZA. While the Coulomb part is therefore completely solvable within MSA, the Yukawa part takes over the responsibility to satisfy thermodynamic consistency for the entire system. Consistency between the energy and compressibility routes is guaranteed through satisfying the PDE (3.45), for which we need the (excess) internal energy per volume and the reduced compressibility in dependence of the newly defined Yukawa and Coulomb correlation functions.

### 4.1.2 Internal Energy and Compressibility

To obtain the excess internal energy per volume we use the fact that we are dealing with a charge-neutral, symmetric binary mixture ( $\rho_+ = \rho_- \equiv \rho/2$ ) and insert  $g_{ij}(r) = h_{ij}(r) + 1$  and equation (4.2) into an expression analogous to equation (3.23) (for energy per volume instead of per particle) for a binary mixture

$$u^{\text{ex}} = 2\pi \int_0^\infty \sum_{i,j=+,-} \rho_i \rho_j g_{ij}(r) \phi_{ij}^{\text{CY}}(r) r^2 dr. \quad (4.7)$$

This quantity can be split into two contributions,

$$u^{\text{ex}} = \underbrace{2\pi\rho^2 \int_0^\infty g^Y(r) \phi^Y(r) r^2 dr}_{u^Y} + \underbrace{2\pi\rho^2 \int_0^\infty g^C(r) \frac{q^2}{\epsilon r} r^2 dr}_{u^C}, \quad (4.8)$$

a Yukawa and a Coulomb part, as indicated by the under-braces.

The generalisation of the compressibility equation (3.38) to binary mixtures reads

$$\frac{1}{\chi^*} = 1 - \frac{1}{\rho} \sum_{i,j=+,-} \rho_i \rho_j \tilde{c}_{ij}(0). \quad (4.9)$$

If we insert equation (4.2) and  $\rho_+ = \rho_- \equiv \rho/2$ , this results in

$$\frac{1}{\chi^*} = 1 - \rho \tilde{c}^Y(0) \equiv \frac{1}{\chi^Y}. \quad (4.10)$$

Obviously, only the hard-core Yukawa part of the interaction contributes to the compressibility, while the Coulomb interactions seem to have no influence! But this would only be true within an MSA framework, where equation (4.6a–d) is used as closure relation. Within SCOZA the Coulomb interaction also influences the Yukawa correlation function via the SCOZA PDE imposing thermodynamic consistency, leading to an indirect contribution to the compressibility.

## 4.2 Self-Consistency on the Entire System

It is not advisable to seek a PDE for  $K(\beta, \rho)$  by inserting the expressions for  $u^{\text{ex}}$  and  $\chi^*$  into equation (3.45). It is more convenient [60] to convert this equation rather into a PDE for the excess internal energy per volume via expressing  $\chi^*$  as a function of  $u^{\text{ex}}$ . The modifications necessary for the present case of the mSCOZA are described in the following.

Starting from equation (3.45) we obtain

$$\rho \frac{\partial^2 u^{\text{ex}}(\rho, \beta)}{\partial \rho^2} = \frac{\partial u^{\text{ex}}(\rho, \beta)}{\partial \beta} \frac{d}{du^{\text{ex}}} \left( \frac{1}{\chi^*} \right), \quad (4.11)$$

in short notation written as

$$C \frac{\partial^2 u^{\text{ex}}(\rho, \beta)}{\partial \rho^2} = B \frac{\partial u^{\text{ex}}(\rho, \beta)}{\partial \beta}, \quad (4.12a)$$

with

$$C = \rho \quad \text{and} \quad (4.12b)$$

$$B = \frac{d}{du^{\text{ex}}} \left( \frac{1}{\chi^*} \right). \quad (4.12c)$$

Now we use  $u^{\text{ex}} = u^{\text{Y}} + u^{\text{C}}$  and  $\chi^* \equiv \chi^{\text{Y}}$  from equation (4.10), and obtain

$$\rho \frac{\partial^2 u^{\text{Y}}(\rho, \beta)}{\partial \rho^2} + \rho \frac{\partial^2 u^{\text{C}}(\rho, \beta)}{\partial \rho^2} = \frac{\partial u^{\text{Y}}(\rho, \beta)}{\partial \beta} \frac{d}{du^{\text{Y}}} \left( \frac{1}{\chi^{\text{Y}}} \right), \quad (4.13)$$

since  $1/\chi^{\text{Y}}$  only depends on  $u^{\text{Y}}$ . Equation (4.13) can be written as

$$C \frac{\partial^2 u^{\text{Y}}(\rho, \beta)}{\partial \rho^2} = B \frac{\partial u^{\text{Y}}(\rho, \beta)}{\partial \beta} + f, \quad (4.14a)$$

with

$$C = \rho, \quad (4.14b)$$

$$B = \frac{d}{du^{\text{Y}}} \left( \frac{1}{\chi^{\text{Y}}} \right), \quad \text{and} \quad (4.14c)$$

$$f = -\rho \frac{\partial^2 u^{\text{C}}(\rho, \beta)}{\partial \rho^2}. \quad (4.14d)$$

Equation (4.14) has nearly the same form as equation (4.12), the only modification being the additional inhomogeneity  $f$ . Therefore the procedure to solve equation (4.12), explained for multi-Yukawa systems in [60], can be used to solve equation (4.14) after adding the proper expression for  $f$ . The only quantity we obviously require for  $f$  is the internal energy per volume of the Coulomb part,  $u^{\text{C}}$ , in dependence on  $\rho$  and  $\beta$  within the

MSA framework. This expression for  $u^C$  can be found in the literature [63, 64] and is also calculated in appendix A:

$$u^C = \frac{\kappa}{4\pi\beta\sigma^2} \left( -1 - \sigma\kappa + \sqrt{1 + 2\sigma\kappa} \right), \quad (4.15a)$$

with

$$\kappa = \sqrt{4\pi\beta\rho\frac{q^2}{\varepsilon}}. \quad (4.15b)$$

After some elementary calculation we obtain the second derivative of  $u^C$  w.r.t.  $\rho$ , resulting finally in

$$f = \frac{q^2/\varepsilon\sigma}{4\kappa\sigma} \left( \frac{1 + 3\kappa\sigma + 3\kappa^2\sigma^2}{(1 + 2\kappa\sigma)^{\frac{3}{2}}} - 1 \right). \quad (4.16)$$

### 4.3 Solving the PDE for SCOZA

To numerically solve the partial differential equation (4.14) we use the algorithm described in [60]: We just have to replace  $u$  with  $u^Y$  and add the inhomogeneity of equation (4.16)<sup>1</sup>. Then the predictor–corrector algorithm (see section 4.3.3), is applicable for the numerical calculation of  $u^Y$ . After having calculated  $u^Y$ ,  $u^C$  has to be added to get the total internal energy.

The numerical calculations have been performed in reduced quantities. We used the hard core diameter as length scale and the Yukawa energy at contact  $\epsilon_Y$  as energy scale (see section 2.8 for more information on units and reduced quantities) which are marked with star–superscripts. The PDE in reduced quantities reads

$$C^* \frac{\partial^2 u^{*Y}(\rho^*, \beta_Y^*)}{\partial \rho^{*2}} = B^* \frac{\partial u^{*Y}(\rho^*, \beta_Y^*)}{\partial \beta_Y^*} + f^*, \quad (4.17a)$$

with

$$C^* = \rho^*, \quad (4.17b)$$

$$B^* = \frac{d}{du^{*Y}} \left( \frac{1}{\chi^*} \right), \quad \text{and} \quad (4.17c)$$

$$f^* = \rho^* \frac{\partial^2 u^{*C}(\rho^*, \beta_Y^*)}{\partial \rho^{*2}}. \quad (4.17d)$$

The reduced Coulomb quantities are

$$u^{*C} = \frac{\kappa^*}{4\pi\beta^*} \left( -1 - \kappa^* + \sqrt{1 + 2\kappa^*} \right), \quad (4.17e)$$

---

<sup>1</sup>Compared to [60], our  $F_1(\rho, u^Y, G_2)$  is the same as equation (4.44)– [60] with  $u$  exchanged by  $u^Y$ , and  $F_2$ , which follows from the OZ relation (4.3a), is exactly the same. Our  $G_i$  are defined as in equation (4.22)– [60], just replace  $g$  with  $g^Y$ .

and

$$f^* = \frac{q^*}{4\kappa^*} \left( \frac{1 + 3\kappa^* + 3\kappa^{*2}}{(1 + 2\kappa^*)^{\frac{3}{2}}} - 1 \right), \quad (4.17f)$$

where

$$\kappa^* = \sqrt{4\pi\beta^*\rho^*q^*}. \quad (4.17g)$$

For notational convenience we will drop the star-superscripts from now on *in this section* (and its subsections). The only exception being  $q^*$ , to prevent confusion with the charge variable  $q$ .

To solve the equation (4.17), which is a diffusion equation where  $\beta$  plays the role of the time variable and  $f$  represents a “source”, we work on an  $\beta$ - $\rho$ -grid, starting at  $\beta = 0$  and proceeding to lower temperatures via increasing  $\beta$ . Of course, we also need initial and boundary conditions.

### 4.3.1 Initial and Boundary Conditions

At  $\rho = 0$  the internal energy per volume is of course zero,

$$u(\rho = 0, \beta) = 0 \quad \forall \beta. \quad (4.18)$$

For high densities the so-called high temperature approximation (HTA [60]) is used to determine the second derivative of  $u$  w.r.t.  $\rho$ . We chose  $\rho_{\max} = 1$  as a reasonable upper boundary (see [60]), resulting in the condition

$$\frac{\partial^2 u}{\partial \rho^2}(\rho = \rho_{\max}, \beta) = \frac{\partial^2 u}{\partial \rho^2}(\rho = \rho_{\max}, \beta = 0) \quad \forall \beta. \quad (4.19)$$

The value at the boundary,  $u(\rho = \rho_{\max}, \beta = 0)$  and its derivatives at this state-point, along with the complete initial condition  $u(\rho, \beta = 0)$ , can be determined using the fact, that for  $\beta = 0$  the direct correlation function  $c(r)$  coincides with that of the HS gas, since at *infinite* temperature all *finite* contributions of the interaction become negligible. Hence,  $c(r)$  reduces to  $c_{\text{HS}}(r)$  [equation (3.43)], reproducing the Carnahan Starling equation of state [54] for hard spheres.

There exists a so called “forbidden” region in the gas-liquid phase diagram, where the fluid becomes mechanically unstable. It is delimited by the so called spinodal line, which lies completely inside the gas-liquid coexistence curve (also called binodal line) and also culminates in the critical point (see figure 3.1). This forbidden region, where the PDE would become analytically instable, can be excluded by finding the limiting densities where  $1/\chi$  vanishes. At these loci we calculate the internal energy per volume (see [20, 60]) to obtain the bounding values for  $u$ . Thus we can restrict ourselves in the solution of the PDE to density values outside the spinodal.



### 4.3.2 The Inhomogeneity Term

We have to be cautious when calculating the inhomogeneity term of equation (4.17f) (which is now termed  $f$ ) of the PDE: if density and/or inverse temperature and/or reduced charge are small, then  $\kappa$  [see equation (4.17g)] can become small, too, introducing the risk of compensation error. This also applies to the evaluation of the Coulomb contribution to internal energy in equation (4.17e), although in this case numerical accuracy is not as critical, since it does not affect the PDE.

To overcome this problem we expand the equations (4.17f) and (4.17e) in power series. In order to guarantee numerical accuracy in at least 20 significant digits we use the following truncated power series:

$$\frac{C}{q^*} = \frac{3\kappa}{8} - \kappa^2 + \frac{75\kappa^3}{32} - \frac{21\kappa^4}{4} + \frac{735\kappa^5}{64} - \frac{99\kappa^6}{4} + \frac{27027\kappa^7}{512} - \frac{3575\kappa^8}{32} + \frac{240669\kappa^9}{1024}, \quad (4.20)$$

valid for

$$\kappa \leq 2.7 \cdot 10^{-3}, \quad (4.21)$$

and

$$\frac{4\pi\beta u^C}{\kappa} = -\frac{\kappa^2}{2} + \frac{\kappa^3}{2} - \frac{5\kappa^4}{8} + \frac{7\kappa^5}{8} - \frac{21\kappa^6}{16} + \frac{33\kappa^7}{16} - \frac{429\kappa^8}{128} + \frac{715\kappa^9}{128}, \quad (4.22)$$

valid for

$$\kappa \leq 2.2 \cdot 10^{-3}. \quad (4.23)$$

### 4.3.3 Predictor–Corrector Algorithm

The predictor–corrector algorithm is an unconditionally stable, implicit finite–difference algorithm [65], the application to our purpose is discussed in detail in [66]. Essentially, the algorithm introduces an intermediate temperature step, and the values of the unknown function are calculated in a way, that we always only have to solve a set of linear equations of tridiagonal type.

For the predictor–corrector algorithm we have to discretise. The increment of the  $\rho$ -grid is called  $\Delta\rho$  and will be kept fixed throughout the evolution of the algorithm. The increment in inverse temperature  $\beta$  is  $\Delta\beta$ , which will decrease continually as we approach the critical point. In this way we guarantee a highly accurate determination of the critical point.

We use the index  $j = 0, 1, 2, \dots, J$  to label the density values of the  $\rho$ -grid and  $n = 0, 1, 2, \dots$  is the index for the  $\beta$  values, with  $\rho_0 = 0$ ,  $\rho_J = \rho_{\max}$ , and  $\beta_0 = 0$ . To simplify the notation we use the following abbreviation for a quantity that depends on both density and (inverse) temperature,

$$Q(\rho_j, \beta_n) \longrightarrow Q_j^n, \quad (4.24)$$

which we apply to the PDE coefficients as well as to the unknown function  $u$ .

As indicated above, the predictor–corrector algorithm introduces an intermediate (inverse) temperature step, indicated by half–integer  $n$ –indices. The so called predictor equation reads

$$C_j \frac{u_{j+1}^{n+1/2} - 2u_j^{n+1/2} + u_{j-1}^{n+1/2}}{(\Delta\rho)^2} = B_j^n \frac{u_j^{n+1/2} - u_j^n}{\Delta\beta/2} + f_j^n, \quad (4.25)$$

while the corrector equation is

$$\frac{1}{2}C_j \left( \frac{u_{j+1}^{n+1} - 2u_j^{n+1} + u_{j-1}^{n+1}}{(\Delta\rho)^2} + \frac{u_{j+1}^n - 2u_j^n + u_{j-1}^n}{(\Delta\rho)^2} \right) = B_j^{n+1/2} \frac{u_j^{n+1} - u_j^n}{\Delta\beta} + f_j^{n+1/2}. \quad (4.26)$$

We multiply equation (4.25) by  $(\Delta\rho)^2$ , define  $\alpha = (\Delta\rho)^2 / \Delta\beta$  and rearrange the terms, leading to

$$C_j u_{j+1}^{n+1/2} + (-2C_j - 2\alpha B_j^n) u_j^{n+1/2} + C_j u_{j-1}^{n+1/2} = -2\alpha B_j^n u_j^n + (\Delta\rho)^2 f_j^n. \quad (4.27)$$

For zero density the internal energy per volume is always zero, i.e.,  $u_0^n = 0 \forall n$ . For high densities the HTA approximation of equation (4.19) is used, therefore the upper boundary condition for this system of linear equations reads

$$-2\alpha B_J^n u_J^{n+1/2} = -2\alpha B_J^n u_J^n + (\Delta\rho)^2 f_J^n - C_J (\Delta\rho)^2 \frac{\partial^2 u_{\text{HTA}}}{\partial \rho^2}(\rho_J), \quad (4.28)$$

where we explicitly indicate that the second derivative is evaluated at  $\rho_J \equiv \rho_{\max}$  after taking the derivative. We obtain a tridiagonal system of linear equations for the  $u_j^{n+1/2}$ ,

$$\begin{pmatrix} -2(C_1 + \alpha B_1^n) & C_1 & 0 & \cdots & \cdots & \cdots & 0 \\ C_2 & -2(C_2 + \alpha B_2^n) & C_2 & & & & \vdots \\ 0 & \ddots & \ddots & \ddots & & & \vdots \\ \vdots & & C_j & -2(C_j + \alpha B_j^n) & C_j & & \vdots \\ \vdots & & & \ddots & \ddots & \ddots & 0 \\ \vdots & & & & C_{J-1} & -2(C_{J-1} + \alpha B_{J-1}^n) & C_{J-1} \\ 0 & \cdots & \cdots & \cdots & \cdots & 0 & -2\alpha B_J^n \end{pmatrix} \times \begin{pmatrix} u_1^{n+1/2} \\ \vdots \\ \vdots \\ u_j^{n+1/2} \\ \vdots \\ \vdots \\ u_J^{n+1/2} \end{pmatrix} = \begin{pmatrix} -2\alpha B_1^n u_1^n + (\Delta\rho)^2 f_1^n \\ \vdots \\ \vdots \\ -2\alpha B_j^n u_j^n + (\Delta\rho)^2 f_j^n \\ \vdots \\ \vdots \\ -2\alpha B_J^n u_J^n + (\Delta\rho)^2 f_J^n - C_J (\Delta\rho)^2 \frac{\partial^2 u_{\text{HTA}}}{\partial \rho^2}(\rho_J) \end{pmatrix}, \quad (4.29)$$

that can be solved for the values  $u_j^{n+1/2}$  at the intermediate grid points.

Next we multiply equation (4.26) by  $2(\Delta\rho)^2$  and rearrange the terms,

$$\begin{aligned} C_j u_{j+1}^{n+1} + \left(-2C_j - 2\alpha B_j^{n+1/2}\right) u_j^{n+1} + C_j u_{j-1}^{n+1} = \\ = -C_j \left(u_{j+1}^n - 2u_j^n + u_{j-1}^n\right) - 2\alpha B_j^{n+1/2} u_j^n + 2(\Delta\rho)^2 f_j^{n+1/2}. \end{aligned} \quad (4.30)$$

Again, at zero density the internal energy is always zero. For high density ( $\rho_J$ ) the HTA internal energy is used for both, the old ( $n$ ) and the new ( $n+1$ ) grid points (the terms in parenthesis in equation (4.26), transformed back to differential expressions, just give two times the HTA result). Therefore the upper bound for the linear equation system is

$$-2\alpha B_J^{n+1/2} u_J^{n+1} = -2\alpha B_J^{n+1/2} u_J^n + 2(\Delta\rho)^2 f_J^{n+1/2} - 2C_J (\Delta\rho)^2 \frac{\partial^2 u_{\text{HTA}}}{\partial \rho^2}(\rho_J). \quad (4.31)$$

The tridiagonal linear equation system for the  $u_j^{n+1}$  in matrix form is thus

$$\begin{pmatrix} -2(C_1 + \alpha B_1^{n+1/2}) & C_1 & 0 & \cdots & \cdots & \cdots & 0 \\ C_2 & -2(C_2 + \alpha B_2^{n+1/2}) & C_2 & & & & \vdots \\ 0 & \ddots & \ddots & \ddots & & & \vdots \\ \vdots & & C_j & -2(C_j + \alpha B_j^{n+1/2}) & C_j & & \vdots \\ \vdots & & & \ddots & \ddots & \ddots & 0 \\ \vdots & & & & C_{J-1} & -2(C_{J-1} + \alpha B_{J-1}^{n+1/2}) & C_{J-1} \\ 0 & \cdots & \cdots & \cdots & \cdots & 0 & -2\alpha B_J^{n+1/2} \end{pmatrix} \times \\ \times \begin{pmatrix} u_1^{n+1} \\ \vdots \\ \vdots \\ u_j^{n+1} \\ \vdots \\ \vdots \\ u_J^{n+1} \end{pmatrix} = \begin{pmatrix} -C_1 (u_2^n - 2u_1^n + 0) - 2\alpha B_1^{n+1/2} u_1^n + 2(\Delta\rho)^2 f_1^{n+1/2} \\ \vdots \\ \vdots \\ -C_j (u_{j+1}^n - 2u_j^n + u_{j-1}^n) - 2\alpha B_j^{n+1/2} u_j^n + 2(\Delta\rho)^2 f_j^{n+1/2} \\ \vdots \\ \vdots \\ -2\alpha B_J^{n+1/2} u_J^n + 2(\Delta\rho)^2 f_J^{n+1/2} - 2C_J (\Delta\rho)^2 \frac{\partial^2 u_{\text{HTA}}}{\partial \rho^2}(\rho_J) \end{pmatrix}. \quad (4.32)$$

#### 4.3.4 Critical Point Location and Coexistence Line

Due to the discretisation described in the previous section, the location of the critical point is only possible with an uncertainty of  $\Delta\rho$  in density, the fixed width of the density grid. This density–uncertainty then also influences the precise knowledge of the critical temperature: Even if the temperature grid becomes arbitrarily fine approaching the critical point, the temperature uncertainty remains much larger than the minimum temperature step–size, because the result for the critical point will be a point on the  $\rho$ –grid — the one of largest temperature that lies on the spinodal line.

As a consequence we devise the following method for a more accurate location of the critical point, approaching this point from higher temperatures, i.e., lower  $\beta$ . First, we

locate the minimum value of  $1/\chi$  on the  $\rho$ -grid for given temperature and call it  $1/\chi_k$ ,  $k$  being the corresponding index of the  $\rho$ -grid. Then, take the values of the two neighbouring density grid-points on either side and interpolate a fourth order polynomial function through these five points. This function has an easily computable minimum in the considered density region which we call  $(1/\chi)_{\min}$ , attained at  $\rho_{\min}$ . As soon as we reach the point where  $(1/\chi)_{\min} = 0$ , we have located the critical point.

In this way, the accuracy for the location of the critical point is only limited by the minimum temperature step-size, by numerical precision, and of course by the numerical issue discussed in section 4.3.2.

Once  $u(\beta, \rho)$  has been determined, the pressure  $P$  and the chemical potential  $\mu$  are obtained via integration of  $\partial(\beta P)/\partial\beta$  and  $\partial(\beta\mu)/\partial\beta$  from

$$\frac{\partial(\beta P)}{\partial\beta} = -u + \rho \frac{\partial u}{\partial\rho} \quad (4.33a)$$

and

$$\frac{\partial(\beta\mu)}{\partial\beta} = \frac{\partial u}{\partial\rho}. \quad (4.33b)$$

The coexisting state points with the corresponding densities  $\rho_l$  and  $\rho_g$  of the liquid and gaseous phases at given temperature (below the critical temperature) are then obtained from the conditions that  $P$  and  $\mu$  are equal for the coexisting phases. For a better location of these state points, i.e., for not being restricted to the used  $\rho$ -grid, we use a linear interpolation scheme between grid-points. Finally, the coexistence lines are obtained by connecting the state points of the respective phases, which of course have to coincide at the critical point.

## Chapter 5

# Equilibrium Structures in the Solid State

The ordered equilibrium structures of the solid state are known to be in general crystals, which can be described via lattices and sets of basis particles [67]. Usually a crystal is not built in a perfect way, i.e., there occur lattice defects, grain boundaries, phase boundaries between different solid phases and also fluid phases, surface effects, lattice vibrations, etc. All these deviations from the perfect crystal are either linked to surface effects due to the finite size of real substances, to long-lived metastable phases, or to a finite temperature. However, under certain circumstances, considering infinitely extended perfect crystals is a valid approach to finding the equilibrium solid structures: Surface effects can be neglected by focussing on bulk properties, a common strategy which we will hence also adopt to, and metastable phases can simply be dropped when one is just looking for the real equilibrium structures. To rule out the influence of a finite temperature we restrict ourselves to the case of zero temperature,  $T = 0$ , where the entropic contribution to the thermodynamic potentials vanishes, thus

$$E = F \quad \text{and} \quad H = G . \quad (5.1)$$

$E$  reduces to the lattice sum, determined only by the pair potential and the static arrangement of the particles.

Although it is practically impossible to establish these requirements in real experimental setups, it is nevertheless interesting which crystals are the most stable ones at zero temperature, because these structures will most probably also appear when looking for stable crystal structures at finite temperatures.

In this thesis we will therefore consider infinitely extended perfect crystals at  $T = 0$  as the solid equilibrium structures. Before we can explain how to calculate  $E$  and  $H$  via lattice sums, we have to introduce the parametrisation of a general three-dimensional (3D) crystal.

## 5.1 Parametrisation of Three–Dimensional Crystals

A perfect crystal consists of a periodic arrangement of the so called unit cell. The periodic arrangement is called the *lattice*, while the so called *basis* of the crystal is the set of at least one basis particle, positioned inside the unit cell in a well–defined way [67]. We will try to make the basis as small as possible, i.e., to have the smallest possible number of basis particles inside the unit cell, and hence put as much information about the crystal as possible into the description of the lattice. In such a case of minimal basis the lattice is called *primitive lattice*.

To be more specific, every lattice can be described through three pairwise linearly independent vectors, the *primitive vectors*, which we call  $\mathbf{a}$ ,  $\mathbf{b}$ , and  $\mathbf{c}$ . The primitive vectors are used to construct the *lattice vectors*

$$\mathbf{L}_{ijk} = i\mathbf{a} + j\mathbf{b} + k\mathbf{c} , \quad (5.2)$$

with  $i$ ,  $j$ , and  $k$  being arbitrary integers. Taken as position vectors, these vectors correspond to positions which are called *lattice points*, each of them being the origin of one of the periodically arranged unit cells. This situation is visualised in figure 5.1 for a two–dimensional (2D) crystal where the smallest possible basis consists of two equal particles. Given the lattice points, the primitive vectors and the shape of the unit cell (along with the basis particle arrangement inside the cell) are not uniquely defined. In the figures 5.1(b,d–f) four different possible unit cells are drawn. Figures 5.1(b,d) depict unit cells that are parallelograms, defined by possible choices of the two primitive vectors (there is a countable, infinite number of possible parallelograms). Figure 5.1(e) shows, that the border of the unit cell can be nearly arbitrarily shaped, as long as the 2D space can be completely tiled with identical unit cells placed at each lattice point. The above arguments are directly transferable to 3D, parallelograms in 2D convert to parallelepipeds in 3D.<sup>1</sup>

Another, important example of a unit cell is the *Wigner–Seitz* unit cell [WSC, in the example of figure 5.1 depicted in panel (f)], which is constructed the following way: Take all lattice vectors  $\mathbf{L}_{ijk}$  (with their shafts at the origin) and construct a plane perpendicular to each vector that contains the point half–way from the origin,  $\frac{1}{2}\mathbf{L}_{ijk}$ . Then, the intersection of all half–spaces created by these planes that contain the origin represents the WSC. We will use this concept in section 5.3.

For a general parametrisation of all crystals we want to get rid of as many of the ambiguities in the choice of the primitive vectors and the shape of the unit cell as possible. W.l.o.g. we therefore demand (see also [68, 69]):

- The three primitive vectors shall be ordered according to their length, so that, using  $|\mathbf{a}| = a$ ,  $|\mathbf{b}| = b$ , and  $|\mathbf{c}| = c$ ,

$$c \leq b \leq a . \quad (5.3)$$

- $\mathbf{a}$  is always assumed to be parallel to the  $x$ –axis of the Cartesian coordinate system.

---

<sup>1</sup>It can be proven [67], that all primitive unit cells have the same volume.

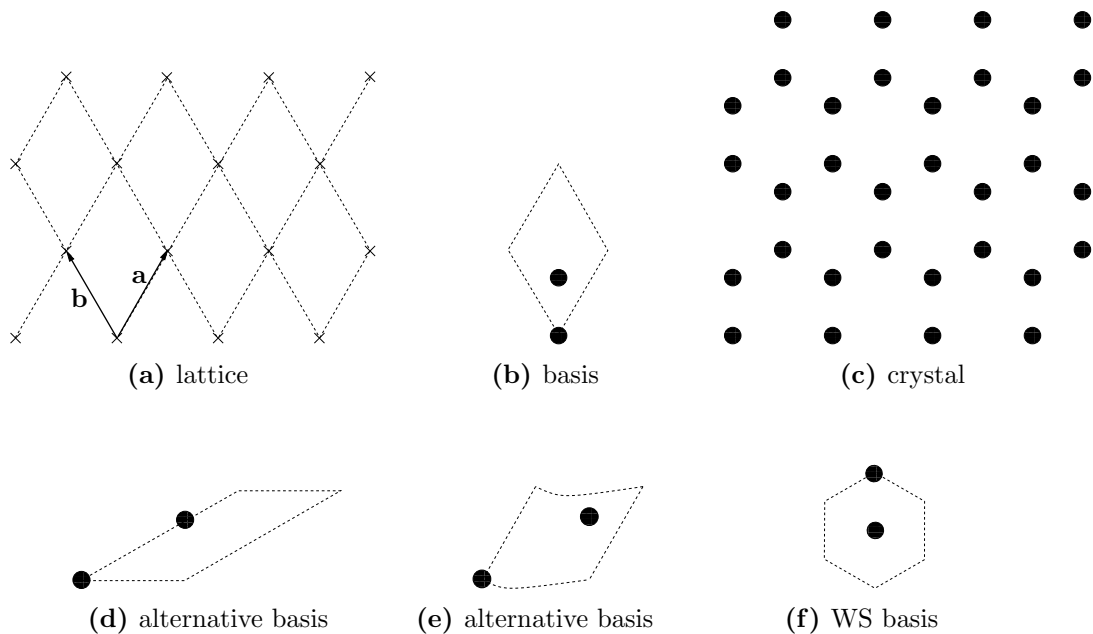


Figure 5.1: Decomposition of a 2D honeycomb crystal (c) into its lattice (a) and basis (b). In (a) each lattice point is marked with a cross; the two (example) primitive vectors are also drawn, as well as their periodic recurrence as dashed lines.

In (d–f) alternative unit cells with their corresponding basis particle arrangements are drawn, (f) is the so called Wigner–Seitz unit cell (see text).

- If  $\mathbf{a} \cdot \mathbf{b} < 0$ , transform  $\mathbf{b} \rightarrow -\mathbf{b}$  (the angle between  $\mathbf{a}$  and  $\mathbf{b}$  is assumed to be at maximum  $\pi/2$ ).
- The  $y$ -axis is chosen in such a way, so that  $\mathbf{b}$  lies in the first quadrant of the  $xy$ -plane.
- If the  $y$ -component of  $\mathbf{c}$  is negative, transform  $\mathbf{c} \rightarrow -\mathbf{c}$ .
- $\mathbf{c}$  has a positive  $z$ -component.
- The unit cell is chosen to be the parallelepiped spanned by the three primitive vectors.

Demanding the  $z$ -component of  $\mathbf{c}$  to be positive is in fact a constraint which cannot be made w.l.o.g. Obeying this constraint means, that out of each pair of crystals, defined by the condition that one crystal is obtained by mirroring the other, we only consider one crystal. However, since the considered pair potentials (see chapter 2) depend only on distances (i.e., are isotropic), all physical quantities (e.g., lattice sums) are the same for a crystal and its mirrored counterpart and we need not consider both of them.

The above conditions lead to the following parametrisation of  $\mathbf{a}$ ,  $\mathbf{b}$ , and  $\mathbf{c}$  [68, 69]:

$$\mathbf{a} = a \begin{pmatrix} 1 \\ 0 \\ 0 \end{pmatrix}, \quad \mathbf{b} = a \begin{pmatrix} x \cos \varphi \\ x \sin \varphi \\ 0 \end{pmatrix}, \quad \mathbf{c} = a \begin{pmatrix} xy \cos \psi \cos \vartheta \\ xy \sin \psi \cos \vartheta \\ xy \sin \vartheta \end{pmatrix}, \quad (5.4)$$

where

$$a > 0, \quad (5.5a)$$

$$0 < x \leq 1, \quad (5.5b)$$

$$0 < y \leq 1, \quad (5.5c)$$

$$0 < \varphi \leq \frac{\pi}{2}, \quad (5.5d)$$

$$0 \leq \psi < \pi, \quad \text{and} \quad (5.5e)$$

$$0 < \vartheta \leq \frac{\pi}{2}. \quad (5.5f)$$

Thus, we have a parametrisation for all possible primitive lattices in terms of their primitive vectors.

Taking basis particles into account we note, that w.l.o.g. we can always put the first basis particle at the origin of the unit cell. Since all other basis particles must also be located inside or at the edges of the unit cell, we can write for the positions of the basis particles

$$\mathbf{v}_i = v_{ia}\mathbf{a} + v_{ib}\mathbf{b} + v_{ic}\mathbf{c}, \quad i \in \mathbb{N} \wedge i \leq n_b (\in \mathbb{N}), \quad v_{ia}, v_{ib}, v_{ic} \in [0, 1) \forall i, \quad (5.6)$$

where  $n_b$  is the total number of basis particles, and

$$v_{1a} = v_{1b} = v_{1c} = 0. \quad (5.7)$$

We also impose an ordering scheme for the basis particles which reads

$$v_{(i-1)a} \leq v_{ia} \quad \forall i > 1, \quad (5.8a)$$

$$v_{(j-1)b} \leq v_{jb} \quad \forall j > 1 : v_{(j-1)a} = v_{ja}, \quad (5.8b)$$

$$v_{(k-1)c} \leq v_{kc} \quad \forall k > 1 : v_{(k-1)a} = v_{ka} \wedge v_{(k-1)b} = v_{kb}. \quad (5.8c)$$

Equation (5.5) together with equation (5.6) parametrises *all* possible crystal structures.

Of course, there remain ambiguities in the parametrisation, i.e., different sets of parameter-values can correspond to the same crystal structure. To return to our 2D example of figure 5.1, both subfigures (b) and (d) can represent valid [i.e., in accordance with equation (5.5) and equation (5.6)], different parametrisations of obviously the same crystal structure. Ambiguities in the parametrisation of the crystal structures can be a severe problem for any optimisation algorithm that searches for (periodic) particle arrangements that minimise a thermodynamic potential. Also, assuming our algorithm experiences no problems, being confronted with different solutions at the same conditions, we of course would like to



know whether we are just facing the same crystal with different parameter values or really different structures that happen to exhibit the same, minimum value of the thermodynamic potential under consideration — giving rise to distinct, coexisting phases.

One way to deal with this problem is to introduce a unification strategy that identifies equivalent parametrisations. It has become clear [68], that the only difficulty in this task is to unify the different primitive unit cells, the basis becomes unique by applying equation (5.6). A unification strategy presented by Gottwald *et al.* [68, 69] identifies the primitive unit cell with the smallest surface via an iterative algorithm, that works as follows:

1. Calculate the surface  $\Sigma^*$  of the primitive unit cell given by  $\mathbf{a}$ ,  $\mathbf{b}$ , and  $\mathbf{c}$ .
2. Calculate the surfaces of the 12 primitive unit cells defined through

$$\begin{aligned} & (\mathbf{a}, \mathbf{b} \pm \mathbf{a}, \mathbf{c}), & (\mathbf{a}, \mathbf{b}, \mathbf{c} \pm \mathbf{a}), \\ & (\mathbf{a} \pm \mathbf{b}, \mathbf{b}, \mathbf{c}), & (\mathbf{a}, \mathbf{b}, \mathbf{c} \pm \mathbf{b}), \\ & (\mathbf{a} \pm \mathbf{c}, \mathbf{b}, \mathbf{c}), & \text{and } (\mathbf{a}, \mathbf{b} \pm \mathbf{c}, \mathbf{c}), \end{aligned} \quad (5.9)$$

and denote the smallest among them by  $\tilde{\Sigma}$ .

3. If  $\tilde{\Sigma} < \Sigma^*$ , take the primitive vectors corresponding to  $\tilde{\Sigma}$  as the new values for  $\mathbf{a}$ ,  $\mathbf{b}$ , and  $\mathbf{c}$  and start over again, else stop.

Each triplet of primitive vectors that is *not changed* by this algorithm is called a *fixpoint*. There are, however, two disadvantages of this method:

- There exists no proof for the exact convergence of the algorithm to the triplet of primitive vectors that describe the unit cell with the smallest surface, and
- it only provides a recipe how to iteratively find the minimum surface unit cell for an arbitrary, given set of three primitive vectors (why this can pose a problem will become clear soon).

Nevertheless, this method proved to be sufficient to deal with the ambiguity–problem for soft core systems, i.e. systems that do not have a hard core but a finite interaction potential for all particle separations. The reason is, that — in principle — all parametrisations (i.e., all crystals) are allowed for such interaction potentials.

The situation is completely different when considering hard core particles. We have to argue a little more verbosely to clarify our point.

If one takes an arbitrary crystal structure parametrised via equations (5.5) and (5.6), it is very likely that there will be a hard core overlap, leading to an infinite potential energy — an unphysical situation. More figuratively speaking: The hard core condition cuts out regions of the  $(6 + 3(n_b - 1))$ -dimensional parameter space, leaving a highly porous regime of allowed structures. For the case of a simple 2D crystal we could prove, that the surface of the remaining regime even has a fractal form (see appendix B.2).

It is quite intuitive, that optimisation algorithms get in trouble when the parameter space is highly porous. For very many equilibrium structures, especially of the SSM [equation (2.10)], there occur touching hard cores (see chapter 9), i.e., the structure becomes stabilised by the hard core repulsion. If these touching particles would approach each other only a little bit, the hard cores would overlap, a situation that is excluded from parameter space — which means the parameters for the equilibrium structure lie, mathematically speaking, at the rim of parameter space, in a porous region! The only way to deal with this porosity problem is, to exclude the “forbidden” region from parameter space beforehand. To know whether a given parametrisation represents a forbidden crystal, we have to know the shortest distance between any particles in this crystal; this distance is of course shorter than the hard core diameter for forbidden structures, and larger (or equal) otherwise.

Now we return to the argument why the parametrisation of equations (5.5) and (5.6) together with the above unification strategy cannot deal with the requirement of an exclusion of all porous regions from parameter space: Even if a reduction of parameter space to those structures that represent fixpoints of the unification algorithm resulted in the exclusion of most of the porous parameter space (which could not be shown so far), it is not possible to parametrise only these fixpoint-structures, since the unification algorithm works only iteratively<sup>2</sup>.

As a consequence we were forced to find a new kind of parametrisation of 3D crystals, that excludes hard core overlaps *a priori*.

## 5.2 The Minimum Distance Parametrisation

In an effort to avoid hard core overlap it would obviously be most convenient to find a parametrisation of all crystals where one always *exactly* knows, which distance between particles is the *absolutely* smallest one occurring in the *whole* crystal. This distance has to be restricted to be larger than the hard core diameter to guarantee that no overlap will occur. The major task in finding this parametrisation was to solve this problem just for the lattice, i.e., to obtain a parametrisation where  $\mathbf{c}$  is always the shortest vector between any pairs of lattice points — the shortest lattice vector.

For a given lattice one can easily find such a smallest distance: Consider a sphere of radius  $\delta$  around a lattice point that is small enough to include no other lattice point. Then one gradually increases the radius until it just reaches another lattice point, its radius  $s$  being then the smallest distance between lattice points and the vector connecting these two points is the shortest lattice vector  $\mathbf{s}$ . While  $s$  is uniquely defined, there might be several vectors  $\mathbf{s}_i$  that satisfy  $|\mathbf{s}_i| = s$ . However, these ambiguities turned out to be no problem, as will be discussed later.

How can we find a parametrisation that always contains a vector of length  $s$  as a primitive vector?

---

<sup>2</sup>Note that both these arguments are not true in 2D, where the fixpoint-structures can be parametrised and do not incorporate any porous regime in parameter space, see the next section.

In 2D the above described unification algorithm of the unit cells minimises the circumference of the unit cells. This automatically leads to  $\mathbf{b}$ , the shorter one of the two unit cell vectors, being the shortest distance in the whole 2D lattice ( $b = s$ ), as is shown in appendix B.1. In addition, we only need one extra condition,  $\cos \varphi \leq x/2$  (see again appendix B.1 and section 5.2.1), to include only these fixpoints of the unification algorithm in parameter space, and this reduced parameter space has indeed no porous regions any more (see appendix B.2). We have to stress the fact, that this reduced parameter space of course still contains all possible lattices.

For 3D, relying on the above unification algorithm for primitive unit cells to find a suitable, reduced parameter space has two problems, also indicated in the previous section:

- It is not clear, whether in the primitive unit cell with the smallest surface, generated by the unification algorithm,  $\mathbf{c}$  is really the shortest lattice vector. In other words, there could still remain some porous region in the reduced parameter space.
- Up to now it was not possible to construct *a priori* a reduced parameter space, that contains only the fixpoints of the unification algorithm.

Therefore we decided to search for a new unification strategy for 3D lattices.

Let us go back to the picture of the sphere with growing diameter, centred at a lattice point. It provided us with the shortest distance in the lattice,  $s$ , and a finite number<sup>3</sup> of lattice vectors  $\mathbf{s}_i$  having length  $s$ . We choose one of the  $\mathbf{s}_i$  arbitrarily and call it  $\mathbf{c}$  (There are at least always two possibilities, since if  $\mathbf{c}$  is a lattice vector so is  $-\mathbf{c}$ .) If there exists another vector in the set of  $\mathbf{s}_i$  that is *linearly independent* of  $\mathbf{c}$  we call it  $\mathbf{b}$ . Else, we further increase the diameter of the sphere, until at least one other lattice point happens to lie on the spherical surface and the following condition is met: The lattice vector from the lattice point at the centre of the sphere to a lattice point at the surface is linearly independent of  $\mathbf{c}$ . Again, it is possible that several vectors of the same magnitude fulfil this requirement; one of them we call  $\mathbf{b}$ . In the same manner we can construct a third lattice vector  $\mathbf{a}$ , which of course must not lie in plane with  $\mathbf{b}$  and  $\mathbf{c}$ .

We conclude, that for *all* crystal lattices there exists a primitive unit cell where the primitive vectors  $\mathbf{c}$ ,  $\mathbf{b}$ , and  $\mathbf{a}$  are the three shortest possible, pairwise linearly independent lattice vectors, satisfying  $c \leq b \leq a$ . As a consequence it is sufficient for a general parametrisation of all lattices to find a parametrisation for all possible triplets of vectors that satisfy this condition.

We will describe now how one can construct this parametrisation, containing the shortest distance of the lattice as the length of  $\mathbf{c}$ , which we therefore call *minimum distance parametrisation* (MDP).

---

<sup>3</sup>At maximum 12, see below.

As a starting point we choose, w.l.o.g., the following representation for the three vectors in a Cartesian basis:

$$\mathbf{a} = a \begin{pmatrix} 1 \\ 0 \\ 0 \end{pmatrix}, \quad \mathbf{b} = ax \begin{pmatrix} \cos \varphi \\ \sin \varphi \\ 0 \end{pmatrix}, \quad \text{and} \quad \mathbf{c} = a \begin{pmatrix} \xi \\ \eta \\ \zeta \end{pmatrix}, \quad (5.10)$$

where we decided not to use the representation for  $\mathbf{c}$  as in equation (5.4). Of course we can still impose the analogous conditions to equation (5.5) for the present set of parameters, leading to

$$a > 0, \quad (5.11a)$$

$$0 < x \leq 1, \quad (5.11b)$$

$$0 < \varphi \leq \frac{\pi}{2}, \quad (5.11c)$$

$$\eta \begin{cases} \geq 0 & \xi \geq 0 \\ > 0 & \xi < 0 \end{cases}, \quad (5.11d)$$

$$\zeta > 0, \quad \text{and} \quad (5.11e)$$

$$x \geq \sqrt{\xi^2 + \eta^2 + \zeta^2}. \quad (5.11f)$$

From equation (5.10) we recognise, that  $a$  is a prefactor for all three primitive vectors, and hence represents just a scaling factor for the whole lattice. Therefore our aim is now to identify a subspace of the five parameters  $x$ ,  $\varphi$ ,  $\xi$ ,  $\eta$ , and  $\zeta$  in  $\mathbb{R}^5$ , so that  $\mathbf{c}$ ,  $\mathbf{b}$ , and  $\mathbf{a}$  represent the three shortest possible (i.e.,  $c \leq b \leq a$ ), linearly independent lattice vectors, monotonously ordered by magnitude. We will perform this task in two steps: first considering the plane spanned by  $\mathbf{a}$  and  $\mathbf{b}$ ; second, taking also the shortest vector,  $\mathbf{c}$ , into consideration.

### 5.2.1 The a–b–Lattice Plane

The two primitive vectors  $\mathbf{a}$  and  $\mathbf{b}$  define a 2D lattice, a so called *lattice plane* of the 3D lattice. We have to find all values of  $x$  and  $\varphi$  for which the two vectors  $\mathbf{a}$  and  $\mathbf{b}$  are the shortest, linearly independent 2D lattice vectors of this lattice plane.

Consider a lattice line parallel to  $\mathbf{b}$  and passing through a lattice point  $\mathbf{P}$  (see figure 5.2). The condition, that  $b$  is the shortest distance between lattice points in the 2D lattice demands, that there exists no lattice point having a distance shorter than  $b$  from  $\mathbf{P}$ . The second condition, that out of all lattice vectors in the 2D lattice that are linearly independent of  $\mathbf{b}$ ,  $\mathbf{a}$  is the shortest one, results in the even stronger restriction, that there must not be any lattice points having distance shorter than  $a$  from  $\mathbf{P}$ , with the possible exception of those at  $\mathbf{P} + n\mathbf{b}$ ,  $n \in \mathbb{Z}$ , lying on the same lattice line as  $\mathbf{P}$  ( $b$  is allowed to be shorter than  $a$ ). This has especially to hold for all points of the adjacent lattice line, which can be constructed by adding  $\mathbf{a}$  to each point of the lattice line that includes  $\mathbf{P}$  (see figure 5.2)<sup>4</sup>.

---

<sup>4</sup>If all distances to particles of the adjacent lattice line are greater than or equal to  $a$ , then the ones

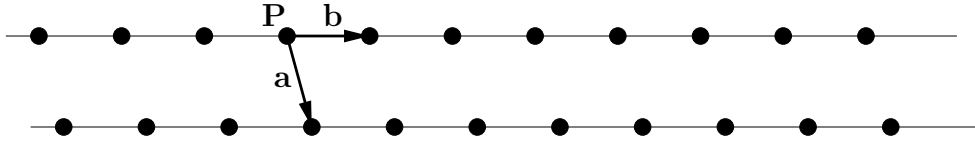


Figure 5.2: Two adjacent lattice lines in the  $\mathbf{b}$  direction.

We calculate now the distances between  $\mathbf{P}$  and the lattice points of this adjacent  $\mathbf{b}$ -line, giving  $\sqrt{a^2 - 2anb \cos \varphi + n^2b^2}$ ,  $n \in \mathbb{Z}$ . From  $\varphi \leq \pi/2$  it follows that  $\cos \varphi \geq 0$ , therefore only non-negative values of  $n$  have to be checked to guarantee that this distance is larger than or equal to  $a$ . For convenience we define a function  $f(n)$ , which is the square of the above expression, i.e., the square of the calculated distances,

$$f(n) = a^2 - 2anb \cos \varphi + n^2b^2, \quad (5.12)$$

which has to be larger than or equal to  $a^2$  for all values of  $n$ .  $f(n)$  is obviously a convex parabola with apex at  $n_{\min} = \frac{a}{b} \cos \varphi \geq 0$ , and of course  $f(0) = a^2$ . The condition  $f(1) \geq a^2$  leads to

$$\cos \varphi \leq \frac{b}{2a} = \frac{x}{2}, \quad (5.13)$$

which results in  $n_{\min} \leq \frac{1}{2}$ . Since the minimum of the parabola therefore lies between 0 and 1 (the two points where  $f(n) \geq a^2$  already holds), it immediately follows that  $f(n) > a^2$ ,  $\forall n > 1$ .

Therefore, equation (5.13) is the only necessary condition<sup>5</sup> to guarantee, that  $\mathbf{a}$  and  $\mathbf{b}$  are the shortest, linearly independent 2D lattice vectors with  $b \leq a$  (compare appendix B.1).

### 5.2.2 Constructing $\mathbf{c}$ as Shortest Lattice Vector

Now the third vector,  $\mathbf{c}$ , has to be added to describe the whole 3D lattice. This has to be done in a way, that it is not only the shortest lattice vector, but also there must not appear any other lattice vector that is

- shorter than  $b$  and not linearly dependent of  $\mathbf{c}$ , or
- shorter than  $a$  and cannot be described as  $i\mathbf{b} + j\mathbf{c}$  ( $i, j \in \mathbb{Z}$ );

---

to particles in lattice lines that are farther away are always greater than  $a$ : Assume the distance between the  $\mathbf{b}$ -lines is  $d$ , then the largest possible value for the shortest distance between points of adjacent lines is  $\sqrt{d^2 + b^2/4}$ , equal to  $a$ . The shortest possible distance to a lattice point at the next line is  $2d = a\sqrt{4 - b^2/a^2} \geq \sqrt{3}a > a$ .

<sup>5</sup>Note, that  $\sqrt{f(1)}$  is the length of the shorter diagonal of the parallelogram spanned by  $\mathbf{a}$  and  $\mathbf{b}$ , which is restricted to be greater than or equal to  $a$  by this condition.

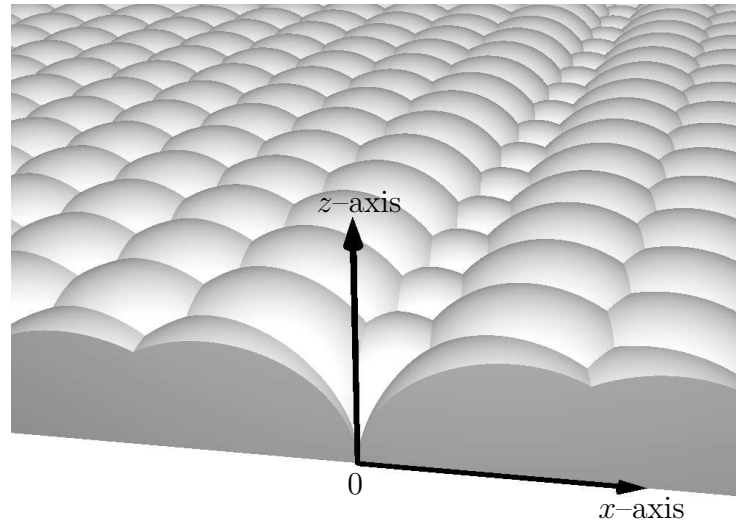


Figure 5.3: The “mogul slope”, above which all vectors from the origin  $0$  to  $k\mathbf{c}$  have to point. The  $y$ -axis, obtained via  $\hat{\mathbf{y}} = \hat{\mathbf{z}} \times \hat{\mathbf{x}}$ , cannot be seen (hats indicate unit vectors in the corresponding directions).

if this was the case, then this vector would substitute either  $\mathbf{b}$  or  $\mathbf{a}$  in the triple of the three shortest, linearly independent lattice vectors. Since the whole lattice can be described as a stacking of parallel  $\mathbf{a}$ - $\mathbf{b}$ -lattice planes, generated by shifting one plane by the vectors  $k\mathbf{c}$ ,  $k \in \mathbb{Z}$ , these two conditions can be visualised graphically: The vectors  $k\mathbf{c}$ ,  $k \in \mathbb{N}$  (only positive values due to symmetry have to be considered), have to point *above* the “mogul slope” drawn in figure 5.3, constructed in the following way.

1. Take the lattice plane spanned by the given primitive vectors  $\mathbf{a}$  and  $\mathbf{b}$  (starting from the origin) in the positive Cartesian  $y$ -direction (the lattice points  $i\mathbf{a} + j\mathbf{b}$  with  $i \in \mathbb{Z}$  and  $j \in \mathbb{N}_0$ ),
2. draw half-spheres of radius  $b$  around the points  $j\mathbf{b}$ ,  $j > 0$  and
3. draw half-spheres of radius  $a$  around all other points, except the origin.

Half-spheres extending to negative (Cartesian)  $y$ -values are truncated by the  $x$ - $z$ -plane, since  $\eta \geq 0$ .

### Conditions for $\mathbf{c}$

Let us first consider the case  $k = 1$ , i.e. the vector  $\mathbf{c}$  itself and not a multiple of it.

The condition  $c \leq b$  can be visualised as follows: draw a quarter-sphere centred at the origin of radius  $b$ , in the region where  $z, y \geq 0$ , the vector  $\mathbf{c}$  has to point this region, having its shaft at the origin (including the surface for  $c = b$ ). Combined with the mogul slope this gives a region looking like a kind of pendentive for the allowed  $\mathbf{c}$ -vectors (see figure 5.4).

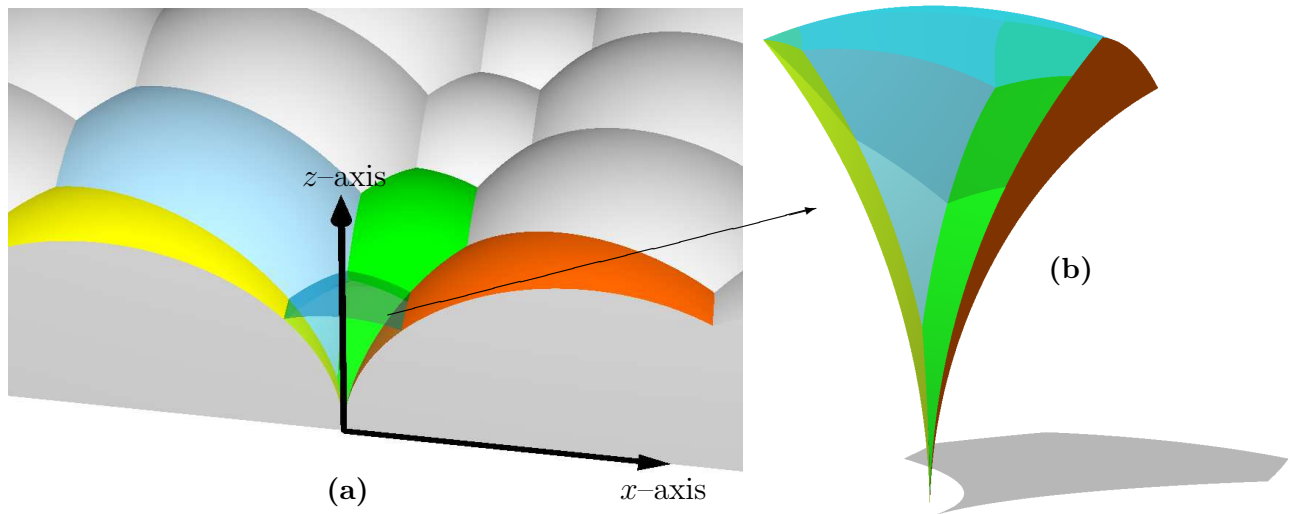


Figure 5.4: The mogul slope, similar to figure 5.3, is drawn, but with the four relevant moguls for the vector  $\mathbf{c}$  coloured yellow, blue, green, and red in (a). The allowed regime for  $\mathbf{c}$  is the transparent, pendentive like region, enlarged in (b).

We now formulate these conditions analytically. To describe the pendentive of figure 5.4(b) we need the intersections of the sphere centred at the origin (upper bound) with the other relevant spheres (lower bound). It turns out, that only the four spheres centred at  $\pm\mathbf{a}$ ,  $\mathbf{b}$ , and  $-\mathbf{a} + \mathbf{b}$  have to be considered<sup>6</sup>. A detailed proof follows at the end of this section.

The intersection of two of these spheres is a circle which has its centre somewhere on the straight line passing through the centres of the two spheres. Therefore, the intersection circle of two spheres having their centres in a plane, is always a straight line if projected onto this common plane. Since this is the case for our problem, and to simplify the visualisation, we rather consider the projection of our objects of interest onto the  $x$ - $y$ -plane from now on.

Including the restriction to non-negative  $y$ -values, we obtain the following straight lines

<sup>6</sup>This is similar to the question how many points have to be considered for the WSC of a 2D lattice; the answer is 4 (6 if negative  $y$ -values are included), see also [67], Chapter 4, Problem 4 (p. 82).

as the rim for the projection of the pendentive onto the  $x$ - $y$ -plane, our region of interest:

$$g_0 : \quad 0 = \eta , \quad (5.14a)$$

$$g_1 : \quad \xi = \frac{x^2}{2} , \quad (5.14b)$$

$$g_2 : \quad \eta \sin \varphi + \xi \cos \varphi = \frac{x}{2} , \quad (5.14c)$$

$$g_3 : \quad \eta \sin \varphi + \xi \left( \cos \varphi - \frac{1}{x} \right) = x - \cos \varphi , \quad (5.14d)$$

$$g_4 : \quad -\frac{x^2}{2} = \xi . \quad (5.14e)$$

If all equality signs are replaced with less-equal-signs ( $\leq$ ), the resulting five inequalities define the projection of the pendentive onto the  $x$ - $y$ -plane. The equalities (5.14) result in five intersection points at the rim of the region (they are given with their  $z$ -coordinates included for completeness, which can simply be calculated through  $\zeta = \sqrt{x^2 - \xi^2 - \eta^2}$ ):

$$g_0 \cap g_1 : \quad P_1 = a \frac{x}{2} (x, 0, \sqrt{4 - x^2}) , \quad (5.15a)$$

$$g_1 \cap g_2 : \quad P_2 = a \frac{x}{2} \left( x, \frac{1 - x \cos \varphi}{\sin \varphi}, \frac{\sqrt{3 - 4 \cos^2 \varphi + 2x \cos \varphi - x^2}}{\sin \varphi} \right) , \quad (5.15b)$$

$$g_2 \cap g_3 : \quad P_3 = a \frac{x}{2} \left( 2 \cos \varphi - x, \frac{1 - 2 \cos^2 \varphi + x \cos \varphi}{\sin \varphi}, \frac{\sqrt{3 - 4 \cos^2 \varphi + 2x \cos \varphi - x^2}}{\sin \varphi} \right) , \quad (5.15c)$$

$$g_3 \cap g_4 : \quad P_4 = a \frac{x}{2} \left( -x, \frac{1 - \frac{2}{x} \cos \varphi + x \cos \varphi}{\sin \varphi}, \frac{\sqrt{3 - x^2 - \frac{4}{x^2} \cos^2 \varphi + \frac{4}{x} \cos \varphi - 2x \cos \varphi}}{\sin \varphi} \right) , \quad (5.15d)$$

$$g_4 \cap g_0 : \quad P_5 = a \frac{x}{2} (-x, 0, \sqrt{4 - x^2}) . \quad (5.15e)$$

Figure 5.5 shows the projection of the pendentive and hence of the allowed region for  $\mathbf{c}$  onto the  $x$ - $y$ -plane, which is the resulting allowed region for the  $x$ - and  $y$ -coordinates of  $\mathbf{c}$  ( $a\xi$  and  $a\eta$ ). The lower bound for the  $z$ -coordinate for given  $\xi$  and  $\eta$  is determined by the surface of one of the four coloured moguls in figure 5.4, the corresponding regimes in the projection are coloured as the corresponding spheres in figure 5.4 and are labelled with uppercase letters. The intersections between these four moguls are again lines in the  $x$ - $y$ -projection given by

$$g_5 : \quad \eta x \sin \varphi = \xi (1 - x \cos \varphi) \quad (A|B), \quad (5.16a)$$

$$g_6 : \quad \xi = x \cos \varphi - \frac{x^2}{2} \quad (B|C), \quad (5.16b)$$

$$g_7 : \quad \xi(1 + x \cos \varphi) + \eta x \sin \varphi = 0 \quad (B|D), \quad (5.16c)$$

$$g_8 : \quad \xi \cos \varphi + \eta \sin \varphi = \frac{x}{2} - \cos \varphi \quad (C|D). \quad (5.16d)$$

Note that  $\mathbf{C}$  vanishes completely if  $\mathbf{a}$  and  $\mathbf{b}$  are perpendicular, i.e., if  $\cos \varphi = 0$ . The only additional intersection points in the region of interest, due to these additional lines, are



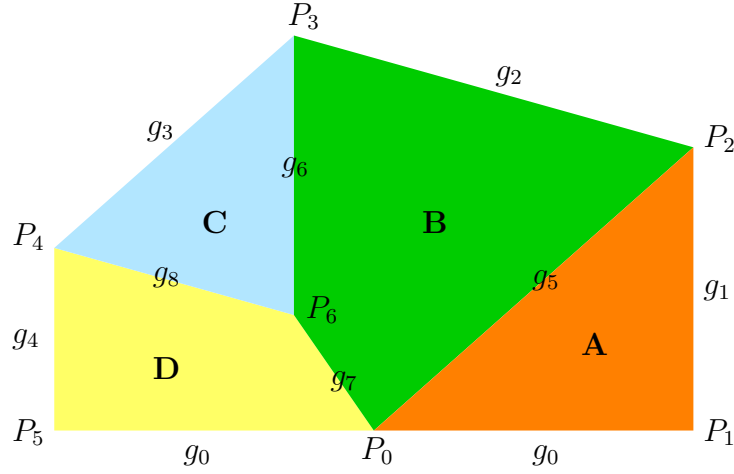


Figure 5.5: Projection of the pendentive [the allowed region for  $\mathbf{c}$ , see figure 5.4(b)] onto the  $x$ - $y$ -plane. Regions with different lower bound of  $\zeta$  for given  $\xi$  and  $\eta$  are coloured corresponding to the delimiting spheres in figure 5.4 and are labelled in bold, uppercase letters (**A**, **B**, **C**, and **D**). The limiting straight lines are labelled  $g_i$ , their intersection points, indicating the corners of the four 2D regions, are the  $P_i$ .

the origin ( $P_0$ ) and the intersection of  $g_6$ ,  $g_7$ , and  $g_8$ :

$$g_0 \cap g_5 \cap g_7 : P_0 = (0, 0, 0), \quad (5.17a)$$

$$g_6 \cap g_7 \cap g_8 : P_6 = a \frac{x}{2} \left( 2 \cos \varphi - x, \frac{1+x \cos \varphi - 2 \cos^2 \varphi - \frac{2}{x} \cos \varphi}{\sin \varphi}, \frac{\sqrt{3-x^2 - \frac{4}{x^2} \cos^2 \varphi - \frac{4}{x} \cos \varphi + 2x \cos \varphi}}{\sin \varphi} \right). \quad (5.17b)$$

With help of the boundary lines and corner points for the four different regions, it is straightforward to calculate the corresponding four sets of describing inequalities,

$$\mathbf{A} : 0 \leq \xi \leq \frac{x^2}{2} \wedge 0 \leq \eta \leq \frac{\xi}{x \sin \varphi} (1 - x \cos \varphi), \quad (5.18a)$$

$$\mathbf{B} : 0 \leq \xi \leq \frac{x^2}{2} \wedge \frac{\xi}{x \sin \varphi} (1 - x \cos \varphi) < \eta \leq \frac{x - 2\xi \cos \varphi}{2 \sin \varphi} \vee \vee -\frac{x^2}{2} + x \cos \varphi < \xi < 0 \wedge -\frac{\xi}{x \sin \varphi} (1 + x \cos \varphi) \leq \eta \leq \frac{x - 2\xi \cos \varphi}{2 \sin \varphi}, \quad (5.18b)$$

$$\mathbf{C} : -\frac{x^2}{2} \leq \xi \leq -\frac{x^2}{2} + x \cos \varphi \wedge \frac{x - 2(1 + \xi) \cos \varphi}{2 \sin \varphi} \leq \eta \leq \frac{x - \cos \varphi - \xi \cos \varphi - \xi/x}{\sin \varphi}, \quad (5.18c)$$

$$\mathbf{D} : -\frac{x^2}{2} + x \cos \varphi \leq \xi < 0 \wedge 0 \leq \eta < -\frac{\xi}{x \sin \varphi} (1 + x \cos \varphi) \vee \vee -\frac{x^2}{2} \leq \xi < -\frac{x^2}{2} + x \cos \varphi \wedge 0 \leq \eta < \frac{x - 2(1 + \xi) \cos \varphi}{2 \sin \varphi}. \quad (5.18d)$$

Note, that  $\mathbf{C}$  is reduced to a single point if  $\cos \varphi = 0$ .

Finally, we calculate the possible  $\zeta$ -values for given  $\xi$  and  $\eta$ . Obviously, the maximum value is given by  $\zeta_{\max} = \sqrt{x^2 - \xi^2 - \eta^2}$ , through the delimiting (quarter-)sphere around the origin. The minimum value  $\zeta_{\min}$  depends on the relevant spherical mogul. To obtain the corresponding  $\zeta_{\min,i}$  we have to solve the equation

$$\left[ a \begin{pmatrix} \xi \\ \eta \\ \zeta_{\min,i} \end{pmatrix} - \mathbf{M}_i \right]^2 = r_i^2 \quad (5.19)$$

for  $\zeta_{\min,i}$ , with the four pairs of centres and radii,

$$\mathbf{M}_1 = -\mathbf{a}, \quad r_1 = a, \quad (5.20a)$$

$$\mathbf{M}_2 = -\mathbf{a} + \mathbf{b}, \quad r_2 = a, \quad (5.20b)$$

$$\mathbf{M}_3 = \mathbf{b}, \quad r_3 = xa, \quad (5.20c)$$

$$\mathbf{M}_4 = \mathbf{a}, \quad r_4 = a, \quad (5.20d)$$

inserted. The result is given in the following summary for the region of the six dimensional parameter space for  $x$ ,  $\varphi$ ,  $\xi$ ,  $\eta$ ,  $\zeta$ , and  $a$ , describing all possible pendentives:

$$a \in \mathbb{R}^+, \quad (5.21a)$$

$$x \in (0, 1], \quad (5.21b)$$

$$\varphi \in \left[ \arccos\left(\frac{x}{2}\right), \frac{\pi}{2} \right], \quad (5.21c)$$

$$\xi \in \left[ -\frac{x^2}{2}, \frac{x^2}{2} \right], \quad (5.21d)$$

$$\eta \in \begin{cases} \left( 0, \frac{x^2 + \xi - (\xi + 1)x \cos \varphi}{x \sin \varphi} \right] & \xi < x \cos \varphi - \frac{x^2}{2} \\ \left( 0, \frac{x - 2\xi \cos \varphi}{2 \sin \varphi} \right] & x \cos \varphi - \frac{x^2}{2} \leq \xi < 0 \quad , \quad \text{and} \\ \left[ 0, \frac{x - 2\xi \cos \varphi}{2 \sin \varphi} \right] & 0 \leq \xi \end{cases} \quad (5.21e)$$

$$\zeta \in \begin{cases} \left[ \sqrt{2\xi - \xi^2 - \eta^2}, \sqrt{x^2 - \xi^2 - \eta^2} \right] & (\xi, \eta) \in \mathbf{A} \\ \left[ \sqrt{2x(\xi \cos \varphi + \eta \sin \varphi) - \xi^2 - \eta^2}, \sqrt{x^2 - \xi^2 - \eta^2} \right] & (\xi, \eta) \in \mathbf{B} \\ \left[ \sqrt{2x(\cos \varphi + \xi \cos \varphi + \eta \sin \varphi) - 2\xi - x^2 - \xi^2 - \eta^2}, \sqrt{x^2 - \xi^2 - \eta^2} \right] & (\xi, \eta) \in \mathbf{C} \\ \left[ \sqrt{-2\xi - \xi^2 - \eta^2}, \sqrt{x^2 - \xi^2 - \eta^2} \right] & (\xi, \eta) \in \mathbf{D} \end{cases}, \quad (5.21f)$$

where the regions **A**, **B**, **C**, and **D** are defined through 5.18, visualised in figure 5.5.

### 5.2.3 Proof of the Completeness of the Description

Now we proof that the conditions described in the previous section are already sufficient to guarantee that  $\mathbf{c}$ ,  $\mathbf{b}$ , and  $\mathbf{a}$  are the three shortest, linearly independent lattice vectors of the corresponding lattice for all 5-tuples  $x$ ,  $\varphi$ ,  $\xi$ ,  $\eta$ , and  $\zeta$ , defined by equation (5.21).

What remains to be shown is, that  $k\mathbf{c}$  indeed never lies inside the mogul slope for  $k > 1$ . To facilitate our analytical arguments, we consider the simpler problem, that the line generated by the equation  $\mathbf{x} = t\mathbf{c}$ ,  $t \in \mathbb{R}$  and  $t > 1$ , never touches or intersects any mogul, as long as  $\mathbf{c}$  itself lies inside the pendentive. Of course this includes the proof of the original problem.

The proof is performed in 3 steps:

**Theorem I:** *Only points at the rim of the pendentive, which is defined as the intersection of the sphere of radius  $b$  centred at the origin with the mogul slope, have to be considered.*

**Proof:** Let us temporarily change the parametrisation for  $\mathbf{c}$  to the one in [68, 69]:

$$\mathbf{c} = axy \begin{pmatrix} \cos \psi \cos \vartheta \\ \sin \psi \cos \vartheta \\ \sin \vartheta \end{pmatrix}, \quad (5.22)$$

where  $y$  is the fraction between  $c$  and  $b$ ,  $\psi$  is the angle of the projection of  $\mathbf{c}$  onto the  $x$ - $y$ -plane with the  $x$ -axis, and  $\vartheta$  is the angle between the vector  $\mathbf{c}$  and the  $x$ - $y$ -plane. Obviously, for given value of  $\psi$ , we only have to consider the vector with the smallest possible  $\vartheta$ ,  $\vartheta_{\min}$ , because if  $t\mathbf{c}_{\vartheta=\vartheta_{\min}}$  does not intersect the mogul slope for  $t > 1$ , neither will any other line with  $\vartheta > \vartheta_{\min}$ . Let us consider the lines starting at the origin, given by  $t\mathbf{c}$  with  $t \in \mathbb{R}^+$ , to find out for which  $\mathbf{c}$  the angle  $\vartheta$  is minimal, provided that  $\psi$  is fixed. To visualise the situation for fixed  $\psi$  we make a cut through the pendentive along the plane defined by the  $z$ -axis and  $\mathbf{c}$  (it is clear, that  $\mathbf{c}$  parallel to the  $z$ -axis needs not to be considered).

For the four important moguls, that define the lower bound (of  $\zeta$ ) for the pendentive, there appear two qualitatively different situations when performing this cut, visualised in figure 5.6.

- As depicted in figure 5.6(a), three of the four pendentive-defining moguls touch the origin, those representing the lower bound for  $\mathbf{c}$  in the regions **A**, **B**, and **D**. For given  $\psi$  only one of these moguls is relevant (see figure 5.5), therefore every line  $t\mathbf{c}$  will intersect the corresponding mogul exactly twice, at the origin and at one other point. As can be seen in figure 5.6(a) the  $\vartheta$ -value of  $\mathbf{c}$  is minimal in the above sense, for given  $\psi$  and length  $c$ , if this intersection point lies exactly at the intersection point of two circles, one representing the mogul and the other being defined as the set of points having distance  $c$  from the origin (visualised e.g. by the dotted circle centred at the origin). It is also obvious, that  $\vartheta$  decreases with increasing length  $c$ , being minimal at  $c = b = ax$ , the maximum value for  $c$  [see the dashed line and circle in figure 5.6(a)].

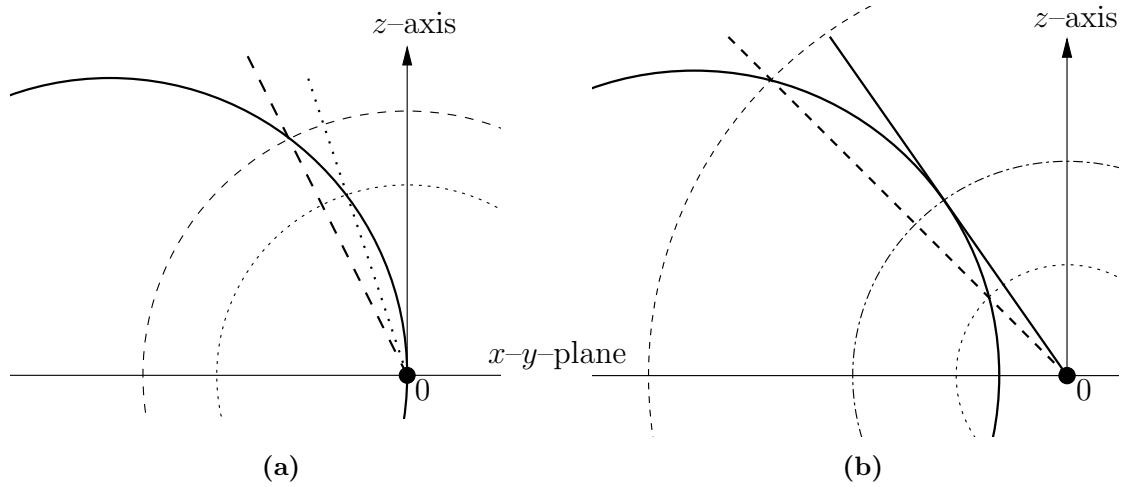


Figure 5.6: Cuts by a plane defined by  $\hat{\mathbf{z}}$  and  $\hat{\mathbf{c}}$ , i.e.,  $\psi = \text{const}$ . In (a) the solid circle represents one of the three moguls that touch the origin (denoted by 0), in (b) it corresponds to the fourth defining mogul for the pendentive, being the lower bound in the region **C** (see figure 5.5). The dashed circle indicates the maximum range for  $\mathbf{c}$ ,  $ax$ ; the dashed line is the corresponding line  $t\mathbf{c}$  of minimum  $\vartheta$ .

Hence, in the regions **A**, **B**, and **D**, minimum  $\vartheta$  for fixed  $\psi$  is obtained at the rim, where  $\sqrt{\xi^2 + \eta^2}$  becomes maximal.

- If the  $\mathbf{c}$ - $z$ -plane cuts through the mogul representing the lower bound in region **C**, the situation is slightly different, as depicted in figure 5.6(b). Although, for given  $c$  (and  $\psi$ ),  $\vartheta$  is still minimal for  $\mathbf{c}$  pointing at the surface of the mogul, the minimum with varying  $c$  is not obtained at the maximum value of  $c = b$ , visualised by the dashed circle (and line) in figure 5.6(b). The **C**-mogul does not touch the origin, therefore there exists an angle  $\vartheta_{\text{tan}}$  (for given  $\psi$ ), where the line  $t\mathbf{c}$  only touches the **C**-mogul, with the touching point having distance  $c_{\text{tan}}$  from the origin. Drawing the line that corresponds to the minimum  $\vartheta$ -value for the maximum value of  $c$  (dashed line), we recognise that there exists another, shorter vector  $\mathbf{c}$  pointing at the surface of the mogul, that generates the same line. Its length is indicated by the dotted line in figure 5.6(b). If we take even smaller values of  $c$  into account,  $\vartheta$  seems to be able to become arbitrarily small! Luckily, as we will show now, the region **C** only contains  $\mathbf{c}$ -vectors with  $c \geq c_{\text{tan}}$ , i.e., also in region **C** we obtain the minimum  $\vartheta$ -value at the rim.

To prove this last assertion we have to show that the touching points of all tangents starting at the origin to the sphere of radius  $a$  with centre at the point  $-\mathbf{a} + \mathbf{b}$  (the **C**-mogul) lie below the pendentive or even outside its  $x$ - $y$ -extent, i.e., their projections must not lie in **C**. Consider the set of tangents from the origin that touch

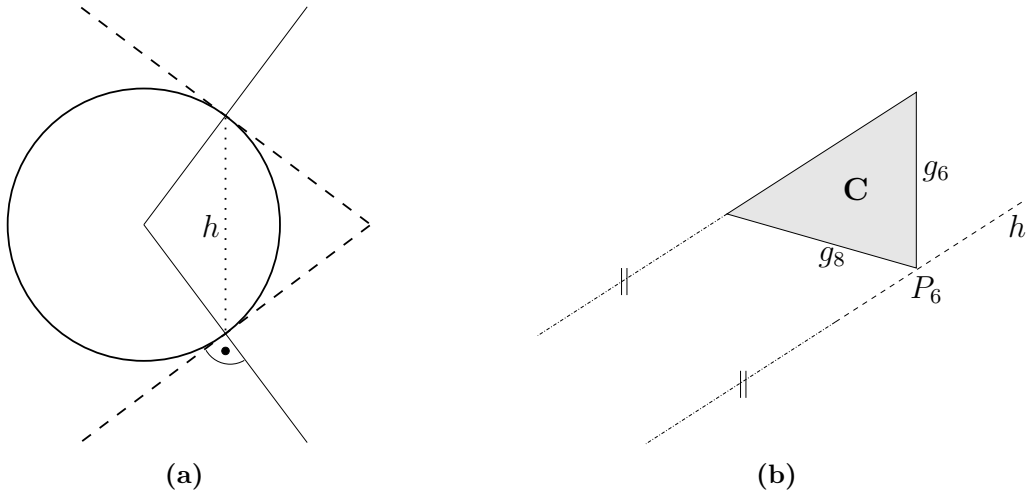


Figure 5.7: (a): Projection of a sphere (solid circle), a touching cone (dashed lines), and the intersection-circle (dotted line) onto a plane through the apex of the cone and the centre of the sphere.  
 (b): Region **C** and the projection of the intersection circle (dashed line, labelled  $h$ ) of the mogul at  $-\mathbf{a} + \mathbf{b}$  and its tangential cone with apex in the origin, onto the  $x$ - $y$ -plane.

this sphere. They form a cone that touches the sphere in a circle, which transforms into a straight line (called  $h$ ) when projected onto the  $x$ - $y$ -plane [see figure 5.7(a)]. The straight line representing this projection is perpendicular to the line from the origin to  $-\mathbf{a} + \mathbf{b}$ . Define the vector from the centre of the considered sphere to  $P_6$  as  $\mathbf{u} = P_6 - (-\mathbf{a} + \mathbf{b})$ . Since  $\mathbf{u} \cdot P_6 = 0$ ,  $P_6$  is one of the points where the cone touches the sphere, and  $h$  contains the projection of  $P_6$  onto the  $x$ - $y$ -plane.

Now

- $g_8$  has always a negative slope of  $-\cot \varphi$  [see equation (5.16d)],
- the slope of  $g_6$  is infinite [see equation (5.16b)],
- and  $h$  [as well as  $g_3$ , see equation (5.14d)] has a slope of  $(1 - x \cos \varphi)/x \sin \varphi$ , satisfying

$$\frac{1 - x \cos \varphi}{x \sin \varphi} \geq \frac{2 - x^2}{x \sqrt{4 - x^2}} \geq \frac{1}{\sqrt{3}} \quad \text{and} \quad (5.23a)$$

$$\frac{1 - x \cos \varphi}{x \sin \varphi} \leq \frac{1}{x} < \infty, \quad (5.23b)$$

since  $0 \leq \cos \varphi \leq \frac{x}{2}$  and  $0 < x \leq 1$ .

Therefore the tangential projection line never lies inside **C**, see figure 5.7(b).

We conclude: The larger  $c$  the smaller  $\vartheta$  can be, implying that the points at the rim of the pendentive are the ones having smallest  $\vartheta$  for each value of  $\psi$ .

□

Theorem II: *The 3 lines from the origin through the 3 points  $P_2$ ,  $P_3$ , and  $P_4$  never touch any mogul (and only intersect any of the 4 “important” moguls).*

**Proof:**<sup>7</sup> Let  $i, j \in \mathbb{Z}$ .

• **Line through  $P_2$**

The moguls centred at  $j\mathbf{b}$ ,  $j > 1$ , can never be touched, since the distance of the line  $tP_2$  ( $t \in \mathbb{R}^+$ ) from these points is  $\frac{\sqrt{3}}{2}axj$ , which is always larger than  $b = ax$  (the radius of these moguls) for  $j \geq 2$ .

From the points  $\mathbf{a} + j\mathbf{b}$  the line of interest has distance

$$d(j) = a\sqrt{1 + 2jx \cos \varphi - \frac{x^2}{4}(1 + 2j - 3j^2)}. \quad (5.24)$$

$d(0) = a\sqrt{1 - x^2/4} < a$  because the half sphere centred at  $\mathbf{a}$  is of course intersected. For  $j = 1$  we get  $d(1) = a\sqrt{1 + 2x \cos \varphi} > a$ , and with the general rule  $d(j) < d(j + 1)$ , true because  $0 < 2x \cos \varphi + x^2(1 + 6j)/4$ , we obtain through complete induction that  $d(j) > a$  for all  $j \geq 1$ .

Now we take the distance from the  $tP_2$ -line to all points of  $i\mathbf{a} + j\mathbf{b}$ , which gives

$$d(i, j) = \frac{a}{2}\sqrt{3j^2x^2 + i^2(4 - x^2) + 2ijx(-x + 4 \cos \varphi)}. \quad (5.25)$$

Only non-negative values of  $i, j$  have to be considered, since, when projected onto the  $x$ - $y$ -plane, the line  $t\mathbf{b}$  always has a steeper slope than  $tP_2$ . Demanding  $d(i, j)$  to be larger than  $a$  leads to

$$i^2(3 - x^2) - 4 + 8ijx \cos \varphi + 2j^2x^2 + (i - jx)^2 > 0, \quad (5.26)$$

where we just have to consider the first two terms (all other ones are at least non-negative): In the worst case (the smallest possible value for given  $i$ , obtained for  $x = 1$ ) they give  $2i^2 - 4$ , which is always positive for  $i > 1$ .  $i = 0, 1$  have been already considered above, therefore the line through the origin and  $P_2$  never touches the mogul slope outside the pendentive. □

• **Line through  $P_3$**

Analogous to above we check that the moguls centred at  $j\mathbf{b}$  ( $j > 1$ ) are never touched by the line  $tP_3$ ,  $t \in \mathbb{R}^+$ . Also similarly, we get for the distances from  $-\mathbf{a} + j\mathbf{b}$

$$d(j) = \frac{a}{2}\sqrt{4 - x^2 + 3j^2x^2 + 4x \cos \varphi - 4 \cos^2 \varphi - 2jx(x + 2 \cos \varphi)}. \quad (5.27)$$

<sup>7</sup>Elaborate calculations were done using *Mathematica* [70].

$j = 0$  and  $j = 1$  are already included in the set of pendentive-defining moguls, therefore the starting value for the complete induction is

$$d(2) = a\sqrt{1 - \cos^2 \varphi - x \cos \varphi + \frac{7}{4}x^2} \geq a\sqrt{1 + x^2} > a, \quad (5.28)$$

where we have used that the expression becomes minimal for maximal  $\cos \varphi$ .  $d(j) < d(j + 1)$  is again easily shown.

Now we take the distances to all the points  $i\mathbf{a} + j\mathbf{b}$  (with  $i < -1$ ), giving

$$d(i, j) = \frac{a}{2}\sqrt{3j^2x^2 + 2ijx(x + 2\cos \varphi) - i^2(-4 + x^2 - 4x\cos \varphi + 4\cos^2 \varphi)}. \quad (5.29)$$

To show that this is always larger than  $a$ , we just have to consider the smallest possible values for  $d(i, j)$ . Because of the negative prefactor of the  $\cos^2 \varphi$ -term, the expression under the square root (radicand) is a concave parabola in  $\cos \varphi$ , which has its minimum w.r.t.  $\cos \varphi$  at one of the two  $\cos \varphi$ -boundaries, 0 or  $x/2$  [see equation (5.21c)]. We consider both cases:

★  $\cos \varphi = 0$

$$d(i, j)|_{\cos \varphi=0} = \frac{a}{2}\sqrt{j^2x^2 + 2ijx^2 + i^2 + 2j^2x^2 + i^2(3 - x^2)}, \quad (5.30)$$

where

$$\underbrace{j^2x^2 + \underbrace{2ijx^2}_{\geq 2ijx} + i^2 + 2j^2x^2 + i^2(3 - x^2)}_{\geq (jx+i)^2} > 2i^2 \stackrel{(i < -1)}{>} 4. \quad (5.31)$$

★  $\cos \varphi = \frac{x}{2}$

$$d(i, j)|_{\cos \varphi=\frac{x}{2}} = \frac{a}{2}\sqrt{4i^2 + 4ijx^2 + 3j^2x^2}, \quad (5.32)$$

where the radicand is larger or equal to (again through  $ix^2 \geq ix$ , since  $i < -1$  and  $x \leq 1$ )

$$2i^2 + (jx)^2 + \left(\sqrt{2}i + \sqrt{2}jx\right)^2 > 2i^2 \stackrel{(i < -1)}{>} 4. \quad (5.33)$$

Therefore also the line through the origin and  $P_3$  never touches the mogul slope outside the pendentive.  $\square$

• **Line through  $P_4$**

Similar considerations like above lead to a distance of  $tP_4$  ( $t \in \mathbb{R}^+$ ) from the points  $i\mathbf{a} + j\mathbf{b}$  of

$$d(i, j) = \frac{a}{2}\sqrt{2ijx^2 + 3j^2x^2 - i^2(-4 + x^2) + (4ijx + 4j^2x)\cos \varphi - 4j^2\cos^2 \varphi}. \quad (5.34)$$

Again the  $\cos^2 \varphi$ -term has a negative prefactor and we check the  $\cos \varphi$ -boundaries:

★  $\cos \varphi = 0$  leads for the radicand to be

$$2ijx^2 + 3j^2x^2 + i^2(4 - x^2), \quad (5.35)$$

which is larger or equal to  $2j^2x^2 + (jx + i)^2 + i^2(3 - x^2)$ , due to  $ix^2 > ix$ . This expression is for sure larger than 4, if  $i < -1$ .

The case  $i = -1$  leads for the radicand to be equal to  $x^2(3j^2 - 2j - 1) + 4$ , which is larger than 4, if the term in brackets is larger than 0. This is the case for  $j > 1$ .

★ For  $\cos \varphi = \frac{x}{2}$  the radicand is

$$4ijx^2 + 4j^2x^2 + i^2(4 - x^2), \quad (5.36)$$

which is larger or equal to  $(i + 2jx)^2 + i^2(3 - x^2)$ , being larger than 4 for  $i < -1$ .

Again we check the case  $i = -1$  separately, leading to  $4j^2 - 4j - 1 > 0$ , fulfilled for  $j > 1$ .

Therefore equation (5.34) is always bigger than  $a$  and the line from the origin through  $P_4$  never touches the mogul slope outside the pendentive, too.  $\square$

$\square$

Theorem III: *If the lines through the “valleys” ( $P_2, P_3, P_4$ ) do not intersect the mogul slope, neither do lines through other points at the rim.*

**Proof:** Assume there exists an intersected mogul  $\mathcal{M}$  besides the four “important”, pendentive-defining ones. As a consequence, there has to exist a line  $\mathcal{L}$  from the origin through one of the four rims at the point  $\mathcal{P}$  (which cannot be one of the valley points,  $P_2, P_3$ , and  $P_4$ , see theorem II) that intersects  $\mathcal{M}$ . This rim of interest is of course a circular arc, a part of a circle with centre in the  $x$ - $y$ -plane, as described above.

Let us construct the following cones with apex in the origin and axis in the  $x$ - $y$ -plane:  $\mathcal{C}_r$ , containing the complete rim where  $\mathcal{P}$  is part of, and  $\mathcal{C}_i$ , which also contains  $\mathcal{L}$  and has its axis through the centre of  $\mathcal{M}$ . All straight lines lying in the surface of  $\mathcal{C}_i$  (and in the positive- $z$ -half-space) intersect  $\mathcal{M}$ . As a next step we consider the overlap between these two cones.

When considering the possible ways for two cones with common apex to overlap, it becomes clear, that there are only four possibilities:

- (i) The two cones only have one point, the apex, in common.
- (ii) The two cones touch each other, they have exactly one straight line in common which lies in plane with the two cone axes.
- (iii) One cone completely contains the other one.



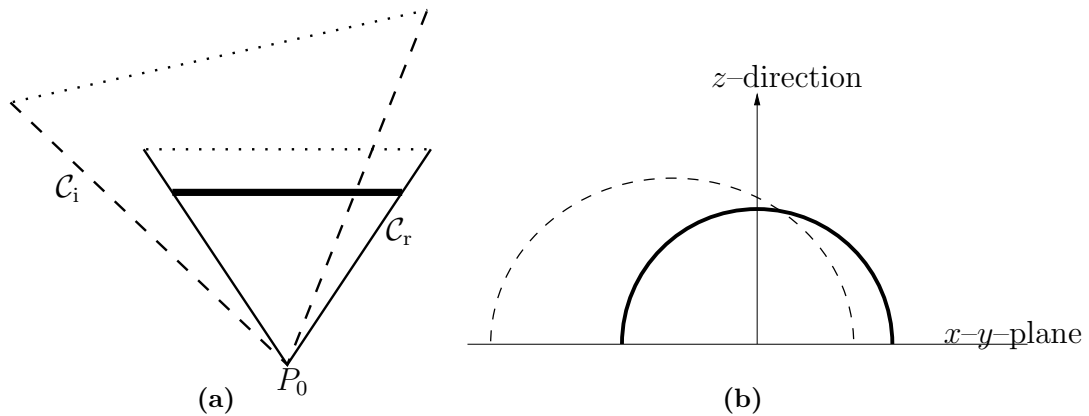


Figure 5.8: (a): Cut along the  $x$ - $y$ -plane through the cones  $\mathcal{C}_r$  (solid lines) and  $\mathcal{C}_i$  (dashed); since the infinitely extended cones have no base area, we assume some arbitrary cone heights (dotted lines), for a better visualisation. The projection of the considered rim-circle onto the  $x$ - $y$ -plane is drawn as a thick, solid line.

(b): Section through the same cones along the plane of the rim-circle in the positive- $z$ -half-plane.

- (iv) The cones only partially overlap, their surfaces intersect in two straight lines, that start at the common apex and are symmetrically arranged w.r.t. the plane defined by the two cone axes.

$\mathcal{C}_i$  and  $\mathcal{C}_r$  obviously overlap like in case (iv), since they intersect exactly along  $\mathcal{L}_i$ , a line which does not lie in the  $x$ - $y$ -plane — the plane containing on the other hand the axes of both cones. It becomes also clear, that, of the two lines where the cone surfaces intersect, only  $\mathcal{L}_i$  lies in the positive- $z$ -half-space, where the mogul-considerations take place. A visualisation of  $\mathcal{C}_r$  and  $\mathcal{C}_i$ , using a cross-section through the  $x$ - $y$ -plane, can be seen in figure 5.8(a).

In figure 5.8(b) we plot a cross section along the plane which contains the considered rim through the two cones, in the positive- $z$ -half-plane. The cross section of  $\mathcal{C}_r$  is of course a half-circle, while the one of  $\mathcal{C}_i$  is a half-ellipse (long axis along the base line), which partially lies above the half-circle of the rim. The intersection of these two lines is the point  $\mathcal{P}$ , lying between the two  $P_i$  points that delimit the considered rim.

As a consequence, one of the  $P_i$  has to lie inside the elliptic cross section of figure 5.8(b) and hence inside the cone  $\mathcal{C}_i$ . We can construct now a cone  $\mathcal{C}_p$  with the same axis and apex like  $\mathcal{C}_i$ , but smaller apex angle, in a way that the cone contains this  $P_i$ . By construction all straight lines (in the positive- $z$ -half-space) from the origin along the surface of  $\mathcal{C}_p$  intersect  $\mathcal{M}$ , in particular the line from  $P_0$  through  $P_i$ . Since this is a contradiction to theorem II, the original assumption of the existence of another intersected mogul was wrong.

□

This means:

Lines from the origin through any point inside the pendentive can never intersect any moguls except the four ones that constitute the lower boundary of the pendentive in  $z$ -direction.

Therefore, the introduced pendentive represents the region for the allowed  $\mathbf{c}$ -vectors for given  $a$ ,  $x$ , and  $\varphi$  is the only relevant region and includes all possibilities.

Before including the basis into consideration, necessary to build not only all lattices but all crystals, we discuss how one can identify the well known 14 Bravais lattices in the minimum distance parametrisation.

### 5.3 Identification of Bravais Lattices

Given the minimum distance parametrisation (MDP) lattice vectors  $\mathbf{a}$ ,  $\mathbf{b}$ , and  $\mathbf{c}$ , or equivalently the parameters  $a$ ,  $x$ ,  $\varphi$ ,  $\xi$ ,  $\eta$ , and  $\zeta$  [see equation (5.4) and equation (5.21)], we can proceed to the identification of the symmetries of the described lattice, i.e., to the categorisation in terms of Bravais lattices. In the following we show that it is indeed possible to find a one-to-one mapping of the minimum distance parameters and the usual parameters of the conventional unit cell of the corresponding Bravais lattice. We will denote the parameters used for describing the conventional Bravais lattice with tildes to prevent confusion with those of the MDP. The key problem that had to be solved was, to identify all possible choices for the three shortest, linearly independent lattice vectors for a given Bravais lattice.

As a first step we restrict ourselves to the possible symmetries of the 2D lattice spanned by  $\mathbf{a}$  and  $\mathbf{b}$ , parametrised by  $x \in (0, 1]$  and  $\varphi \in [\arccos(x/2), \pi/2]$  (the scaling factor  $a$  does not influence symmetry). This is not only done because the concepts are more easily grasped in 2D, but because it is necessary for the identification of the 3D symmetry to identify the symmetry of the underlying  $\mathbf{a}$ - $\mathbf{b}$ -lattice-plane first, before taking the third primitive vector,  $\mathbf{c}$ , into account.

There are five Bravais lattices in 2D: the hexagonal, the square, the rectangular, the centred rectangular, and the oblique lattice. Let us start with the centred rectangular lattice for a full explanation of the identification process, since it is the 2D lattice exhibiting the most versatile possibilities for the corresponding MDP (compared to the other four), as will be seen from the result. The centred rectangular lattice is characterised by the lengths of the two sides of the rectangular unit cell,  $\tilde{a}$  and  $\tilde{b}$ ; w.l.o.g. we assume  $\tilde{a} > \tilde{b}$ ,  $\tilde{a} = \tilde{b}$  would correspond to the square lattice.

Given a centred rectangular lattice we ask for the two shortest, linearly independent lattice vectors, that describe the same lattice if taken as the primitive vectors, i.e., for possible vectors  $\mathbf{a}$  and  $\mathbf{b}$ . To answer this question we consider three distances, namely  $\tilde{a}$ ,

$\tilde{b}$ , and the distance from the corner of the rectangle to the centred point, being half the diagonal  $\tilde{d}$ . Since  $\tilde{a} > \tilde{b}$  one immediately obtains

$$\frac{\tilde{d}}{2} = \frac{\sqrt{\tilde{a}^2 + \tilde{b}^2}}{2} < \frac{\tilde{a}}{\sqrt{2}} < \tilde{a}, \quad (5.37)$$

leaving only  $\tilde{b}$  and  $\tilde{d}/2$  as possible candidates for the lengths of  $\mathbf{a}$  and  $\mathbf{b}$ . We consider the three possible cases:

- $\tilde{d}/2 = \tilde{b}$  corresponds to a lattice of higher symmetry, i.e., a hexagonal one, since the side  $\tilde{b}$  and the two half-diagonals from the corners delimiting the side  $\tilde{b}$  to the centred point form an equilateral triangle.
- $\tilde{d}/2 > \tilde{b}$  leads via equation (5.37) to  $\tilde{a} > \sqrt{3}\tilde{b}$ .  $\tilde{b}$  is now the shortest and  $\tilde{d}/2$  is the second shortest distance, thus

$$\frac{|\mathbf{b}|}{|\mathbf{a}|} = x = \frac{\tilde{b}}{\tilde{d}/2} = \frac{2}{\sqrt{1 + (\tilde{a}/\tilde{b})^2}} < 1. \quad (5.38)$$

Since there is no upper limit for  $\tilde{a}/\tilde{b}$ ,  $x$  can become arbitrarily small. To determine  $\varphi$  we have to consider all angles between lattice vectors having the length  $\tilde{d}/2$  and those of length  $\tilde{b}$ . Obviously there are only two complementary values, of which we have to take the smaller one to obey  $\varphi \leq \pi/2$ . In the  $\tilde{a}$ - $\tilde{b}$ -rectangle this is just the angle between the diagonal and the side  $\tilde{b}$ , i.e.,  $\tilde{a}^2 = \tilde{b}^2 + \tilde{d}^2 - 2\tilde{b}\tilde{d}\cos\varphi$ . Inserting equation (5.37) and equation (5.38) leads to

$$\cos\varphi = \frac{x}{2}. \quad (5.39)$$

- $\tilde{d}/2 < \tilde{b}$  ( $\tilde{b} < \tilde{a} < \sqrt{3}\tilde{b}$ ) means, that  $\mathbf{a}$  and  $\mathbf{b}$  both have the length of the half-diagonal, since there are always two linearly independent lattice vectors of this length that describe the whole lattice. Vectors having the length of  $\tilde{b}$  are therefore too long to play a role in the MDP, obviously this leads to

$$x = 1. \quad (5.40)$$

Again there are two complementary angles as candidates for  $\varphi$ , the smaller one obeying  $2(\tilde{d}/2)^2 - 2(\tilde{d}/2)^2\cos\varphi = \tilde{b}^2$ . This leads, together with the boundary conditions  $\tilde{b} < \tilde{a} < \sqrt{3}\tilde{b}$  to

$$0 < \cos\varphi < \frac{1}{2}. \quad (5.41)$$

These and similar considerations for the other three non-oblique Bravais lattices lead to

$$x = 1 \wedge \cos \varphi = \frac{1}{2} \iff \text{hexagonal, } \tilde{a} = a, \quad (5.42a)$$

$$x = 1 \wedge \cos \varphi = 0 \iff \text{squared, } \tilde{a} = a, \quad (5.42b)$$

$$x = 1 \wedge 0 < \cos \varphi < \frac{1}{2} \iff \text{centred rectangular,} \quad (5.42c)$$

$$\tilde{a} = a\sqrt{2(1 + \cos \varphi)}, \tilde{b} = a\sqrt{2(1 - \cos \varphi)},$$

$$x < 1 \wedge \cos \varphi = \frac{x}{2} \iff \text{centred rectangular, } \tilde{a} = a\sqrt{4 - x^2}, \tilde{b} = ax, \quad (5.42d)$$

$$x < 1 \wedge \cos \varphi = 0 \iff \text{rectangular, } \tilde{a} = a, \tilde{b} = ax, \quad (5.42e)$$

the rest of the  $x$ - $\varphi$ -parameter space corresponds to oblique lattices,

$$x < 1 \wedge 0 < \cos \varphi < \frac{x}{2} \iff \text{oblique, } \tilde{a} = a, \tilde{b} = ax, \tilde{\alpha} = \varphi, \quad (5.42f)$$

where we can, w.l.o.g., choose the conventional parameters, the lengths  $\tilde{a}$  and  $\tilde{b}$  of the conventional primitive vectors and the angle  $\tilde{\alpha}$  between them, to be those of the 2D MDP. The correspondences of equation (5.42) are visualised in figure 5.9. The subequation letters

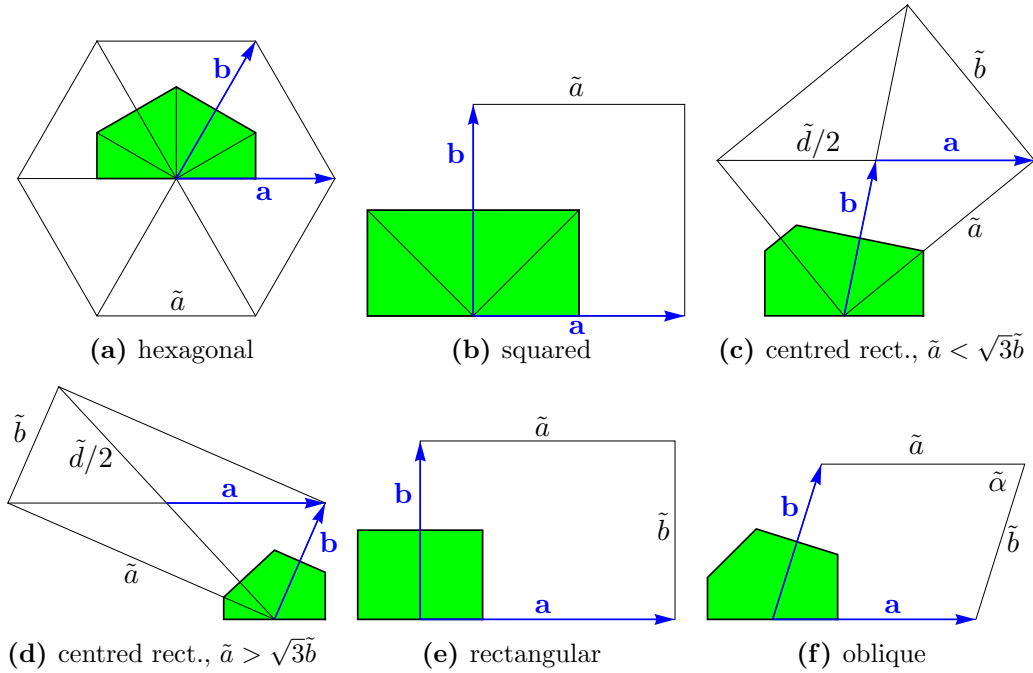


Figure 5.9: Allowed  $\xi$ - $\eta$ -regions (green) for the six different cases in equation (5.42), labelled with the same small letters as the equations. The region is obtained in the same way as in figure 5.5. Quantities describing the conventional 2D unit cell are marked with tildes, the corresponding MDP vectors  $\mathbf{a}$  and  $\mathbf{b}$  are blue. The origin is always at the initial point of the drawn vector  $\mathbf{b}$ , the  $x$ -axis is parallel to  $\mathbf{a}$ .

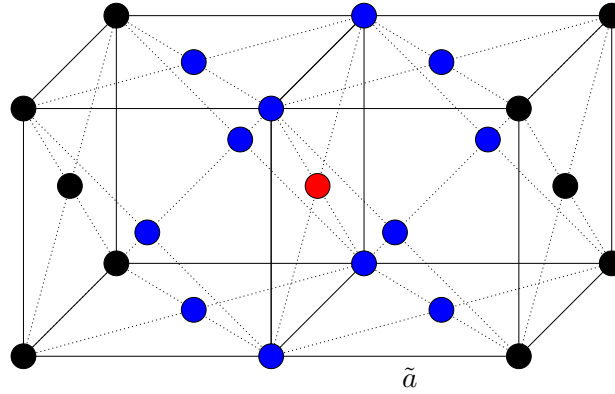


Figure 5.10: Two adjacent conventional fcc cells with edge length  $\tilde{a}$ . The distances from the red particle to the blue ones (the 12 nearest neighbours) are all the same and equal to  $\tilde{a}/\sqrt{2}$ .

in equation (5.42) are the same as the ones of the panels in figure 5.9, we will refer to these six cases of 2D symmetry just through the according letters.

In the figure we also visualise the allowed  $\xi$ - $\eta$ -region, i.e., the possible values for the  $x$ - and  $y$ -components of  $\mathbf{c}$ . It is determined by equation (5.21d) and equation (5.21e) for given values of  $x$  and  $\phi$ , and equivalent to the projection of the pendentive encompassing the allowed values for  $\mathbf{c}$  onto the  $x$ - $y$ -plane (which is also the  $\mathbf{a}$ - $\mathbf{b}$ -plane). Until now we always excluded points at the boundary with  $\eta = 0$  and  $\xi < 0$ , since they are identical (through mirroring) to the ones with inverted  $\xi$ . For the sake of simplicity we will consider all points of the pendentive, including the *whole* boundary (except the origin), as candidates for the MDP vector  $\mathbf{c}$ . The projections of this complete pendentive will be used for clarifying explanations in this section.

Proceeding to 3D, we also have to find all possibilities for describing the same lattice within the MDP, similarly to the 2D case. Let us discuss the fourteen 3D Bravais lattices of the seven crystal systems.

### 1. Cubic

- **Face Centred Cubic (fcc)**

In this Bravais lattice, the three shortest possible, linearly independent primitive lattice vectors have a length equal to the nearest neighbour distance  $\tilde{a}/\sqrt{2}$  (see figure 5.10). Obviously this results in  $a = \tilde{a}/\sqrt{2}$  and  $x = 1$ . Considering all angles between the 12 vectors from one particle to the nearest neighbours we recognise, that there are only two possibilities for  $\varphi$ , since we only take values less or equal  $\pi/2$  into account:  $\varphi = \pi/2$  and  $\varphi = \pi/3$  ( $\hat{=} \cos \varphi = 1/2 = x/2$ ).

The identification of the values for  $\xi$ ,  $\eta$ , and  $\zeta$  follows similarly from all possible third vectors, linearly independent of the previous two. In summary we get the restrictions for the minimum distance parameter values to describe an fcc

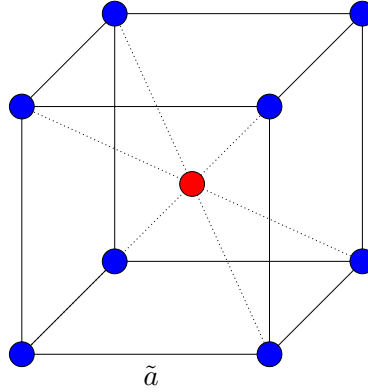


Figure 5.11: The conventional bcc cell with edge length  $\tilde{a}$ . The distances from the red particle to the blue ones (the 8 nearest neighbours) are all the same and equal to  $\tilde{a}\sqrt{3}/2$ .

lattice,

$$x = 1 \wedge \begin{cases} \varphi = \frac{\pi}{3} \wedge \zeta = \sqrt{\frac{2}{3}} \wedge \begin{cases} \eta = \frac{1}{2\sqrt{3}} \wedge \xi = \pm\frac{1}{2} \\ \eta = \frac{1}{\sqrt{3}} \wedge \xi = 0 \end{cases} \\ \varphi = \frac{\pi}{2} \wedge \zeta = \frac{1}{\sqrt{2}} \wedge \eta = \frac{1}{2} \wedge \xi = \pm\frac{1}{2} \end{cases}, \quad (5.43)$$

where the wedge  $\wedge$  is used as abbreviation for “and” and the curly bracket stands for an “or”-composition of the enclosed lines. As expected,  $\zeta$  always takes on the largest possible value compatible with the other parameters, to satisfy  $c = b(= a)$ . This result can be visualised in the following way. We first identify the 2D symmetry of the  $\mathbf{a}$ - $\mathbf{b}$  lattice plane described by  $x$  and  $\varphi$  [in this case either 2D-(a) or 2D-(b)], and draw the projection of the pendentive (describing the allowed  $\xi$ - $\eta$ -region) like in figure 5.9. There we mark the corresponding  $(\xi, \eta)$ -point(s), indicating whether  $\zeta$  takes on the largest (like in the fcc case) or smallest possible value or any value in between by a colour code, see figures 5.12(a) and 5.12(b), where the fcc identification is visualised in this way.

- **Body Centred Cubic (bcc)**

Again all three vectors  $\mathbf{a}$ ,  $\mathbf{b}$ , and  $\mathbf{c}$  are of equal length, which is the nearest neighbour distance  $\tilde{a}\sqrt{3}/2$  of the bcc lattice, see figure 5.11 (hence,  $a = \tilde{a}\sqrt{3}/2$  and  $x = 1$ ). Considering any pair of linearly independent vectors from a lattice point to the nearest neighbours, we find that the enclosed angles can only take on two complementary values. Obeying  $\varphi \leq \frac{\pi}{2}$  we therefore get  $\cos \varphi = 1/3$ . Of the remaining candidate vectors for  $\mathbf{c}$  only one is left after applying mirror and inversion symmetry ( $\eta, \zeta \geq 0$ ), giving

$$x = 1 \wedge \varphi = \arccos\left(\frac{1}{3}\right) \wedge \xi = -\frac{1}{3} \wedge \eta = \frac{\sqrt{2}}{3} \wedge \zeta = \sqrt{\frac{2}{3}}, \quad (5.44)$$

visualised in figure 5.12(c).

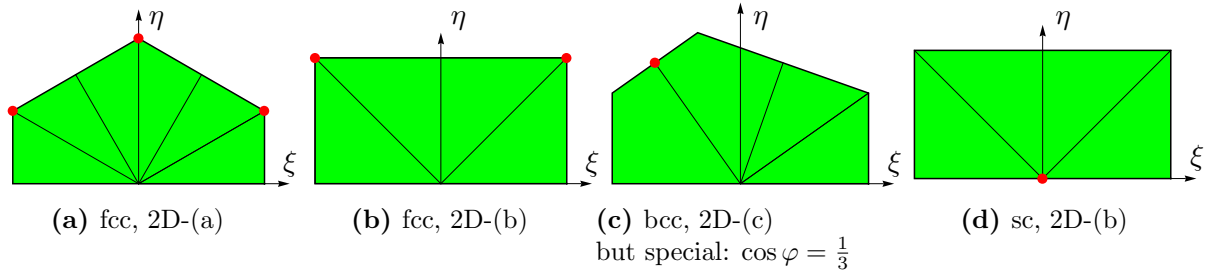


Figure 5.12: Projection of the pendentive (green) and the points for  $\mathbf{c}$  to describe the corresponding lattices as labelled in the subcaptions, where in addition the 2D symmetry of the  $\mathbf{a}$ – $\mathbf{b}$ –lattice plane is given in terms of the subfigure indices of figure 5.9 [or equivalently, subequation indices of equation (5.42)].

We use a colour code for the  $\mathbf{c}$ –points to give information about the  $\zeta$ –value: ● red means  $\zeta$  takes on its maximum value (corresponding to  $c = b$ ), ● yellow stands for the minimum value, and ● blue means any value in between. If only one value for  $\zeta$  is possible we use red, since this only happens for points at the rim where  $c = b$ .

- **Simple Cubic (sc)**

Considering the vectors to the 6 nearest neighbours it is easy to obtain

$$x = 1 \wedge \varphi = \frac{\pi}{2} \wedge \xi = \eta = 0 \wedge \zeta = 1, \quad (5.45)$$

depicted in figure 5.12(d).

The visualisation through the projections of the pendentive to the  $\mathbf{a}$ – $\mathbf{b}$ –plane gives no information about the total scaling of the lattice, given by  $a$ , which does not influence symmetry. Nevertheless we can extract the values of  $x$  and  $\varphi$  from such plots. In most cases they are just determined through the 2D symmetry and equation (5.42). For  $x < 1$ ,  $x$  is linked to the horizontal extent of the projected region, which is  $x^2$  [see equation (5.21d)]; for  $0 < \cos \varphi < x/2$  [2D-(c) and 2D-(f)]  $\varphi$  can be reconstructed if one draws the full 2D unit cell like in figure 5.5. If the values are not fixed by the 2D symmetry or other conditions, we usually take example values from within the allowed range for the drawn visualisations.

It is interesting to note, that the underlying 2D symmetry can provide some additional information. If only one of the  $(\xi, \eta)$ –points for  $\mathbf{c}$  in the  $\mathbf{a}$ – $\mathbf{b}$ –projections of figures 5.12 is given, the other ones (if any) can be obtained by applying the corresponding 2D symmetry transformation. All  $\zeta$ –values of these symmetry points hence are equal, too. This can be formulated in a more general way: Symmetry points in the 2D–projection indicate equivalent 3D–lattices if in addition the  $\zeta$ –values are equal (as mentioned before, mirrored lattices are considered to be equivalent).

2. *Hexagonal (hex)*

Let  $\tilde{a}$  be the edge length of the hexagon and  $\tilde{c}$  the distance between the hexagonal

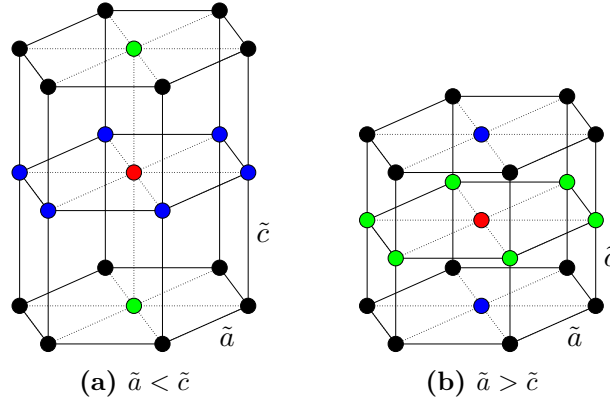


Figure 5.13: The two qualitatively different possibilities for the 3D hexagonal lattice.  $\tilde{a} = \tilde{c}$  is also possible but not shown. The nearest neighbours to the red particle are coloured blue, the next to nearest ones green.

lattice planes, see figure 5.13. We have to distinguish between the two cases where either  $\tilde{a} > \tilde{c}$  or  $\tilde{a} < \tilde{c}$ , the case of equality will be considered later.

$\tilde{a} > \tilde{c}$  implies that  $\tilde{c}$  is the shortest distance in the lattice and  $\mathbf{a}$  and  $\mathbf{b}$  build up the hexagonal lattice planes, having both length  $\tilde{a}$ . This means  $x = 1$ ,  $\varphi = \pi/3$ ,  $\xi = \eta = 0$ , and  $\zeta = \tilde{c}/\tilde{a}$  [see blue point in figure 5.14(a), which is partially covered by the red one].

$\tilde{a} < \tilde{c}$  results in both the shortest and second shortest linearly independent vector to have length  $\tilde{a}$  and lie in the hexagonal plane, while the longest of the MDP vectors has length  $a = \tilde{c}$ , i.e.,  $x = \tilde{a}/\tilde{c}$ ,  $\varphi = \pi/2$ ; it immediately follows  $\xi = 0$ ,  $\eta = 1/2$ , and  $\zeta = \sqrt{3}/2$  [see red point in figure 5.14(b)].

For  $\tilde{a} = \tilde{c}$  the limiting cases of both previously discussed choices for the MDP vectors are possible. From the first one we obtain the limiting case  $x = 1$ ,  $\phi = \pi/3$ ,  $\xi = \eta = 0$ , and  $\zeta = 1$  [red point in figure 5.14(a)], while the second one gives  $x = 1$ ,  $\varphi = \pi/2$ ,  $\xi = 0$ ,  $\eta = 1/2$ , and  $\zeta = \sqrt{3}/2$  [see upper red point in figure 5.14(c)]. However, since all three MDP vectors now have equal length, we a third possibility for their succession arises, i.e.,  $\mathbf{a}$  and  $\mathbf{c}$  lie in the hexagonal plane and  $\mathbf{b}$  is the vector perpendicular to it. This yields the additional identification of  $x = 1$ ,  $\varphi = \pi/2$ ,  $\xi = \pm 1/2$ ,  $\eta = 0$ , and  $\zeta = \sqrt{3}/2$  for the hexagonal symmetry [two lower red points in figure 5.14(c)]. These additional two points would have also followed from the above symmetry argument, since the three red points in the 2D projection of figure 5.14(c) are related to each other through applying the four-fold rotational symmetry of the square lattice [one of them is obtained through setting  $\tilde{c} = \tilde{a}$  in figure 5.14(b)].



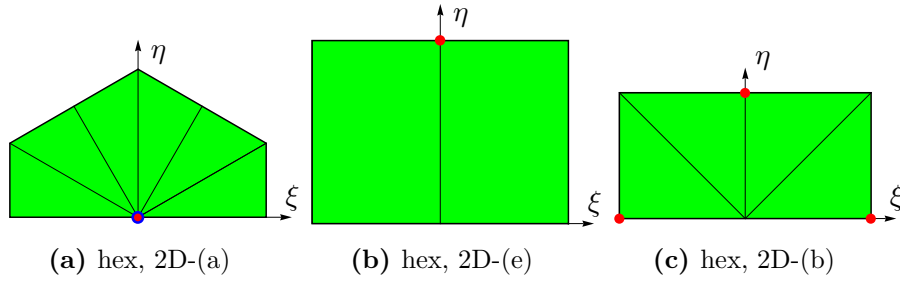


Figure 5.14: All possible parametrisations of the 3D hexagonal lattice; for symbols, labels, etc. see figure 5.12.

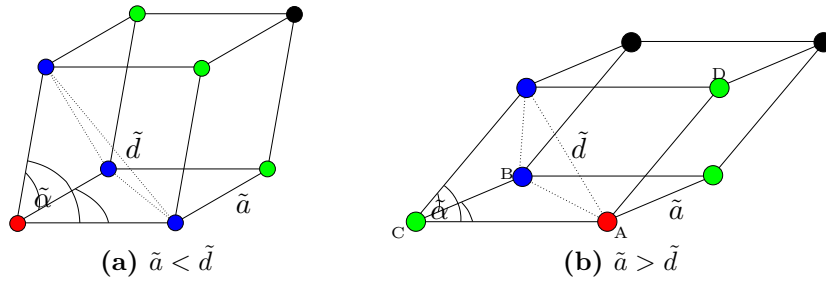


Figure 5.15: The two qualitatively different possibilities for the trigonal lattice. The nearest neighbours to the red particle are coloured blue, the next to nearest ones green. Solid lines all have equal length,  $\tilde{a}$ , chartered angles are all equal ( $\tilde{\alpha}$ ), and dotted lines have length  $\tilde{d}$ . In (b) we also label the points A to D, see text.

In summary we get

$$\begin{cases} x = 1 \wedge \begin{cases} \varphi = \frac{\pi}{3} \wedge \xi = \eta = 0 \wedge 0 < \zeta \leq 1 \\ \varphi = \frac{\pi}{2} \wedge \zeta = \frac{\sqrt{3}}{2} \wedge \begin{cases} \xi = 0 \wedge \eta = \frac{1}{2} \\ \xi = \pm \frac{1}{2} \wedge \eta = 0 \end{cases} \end{cases} \\ x < 1 \wedge \varphi = \frac{\pi}{2} \wedge \xi = 0 \wedge \eta = \frac{x}{2} \wedge \zeta = \frac{\sqrt{3}x}{2} \end{cases} \quad (5.46)$$

### 3. Trigonal (trig, also called rhombohedral)

The trigonal lattice can be formed from an sc lattice, which is stretched along a body diagonal (also called trigonal) while all edge-lengths remain constant. Therefore the three primitive vectors describing the conventional unit cell are of equal length,  $\tilde{a}$ , and enclose pairwise the same angle,  $\tilde{\alpha}$  (see figure 5.15), with  $\tilde{\alpha} < \pi/2$ . In a Cartesian coordinate system they can be given as

$$\tilde{\mathbf{a}} = \tilde{a} \begin{pmatrix} 1 \\ 0 \\ 0 \end{pmatrix}, \quad \tilde{\mathbf{b}} = \tilde{a} \begin{pmatrix} \cos \tilde{\alpha} \\ \sin \tilde{\alpha} \\ 0 \end{pmatrix}, \quad \tilde{\mathbf{c}} = \tilde{a} \begin{pmatrix} \cos \tilde{\alpha} \\ \cos \tilde{\alpha} \sqrt{\frac{1-\cos \tilde{\alpha}}{1+\cos \tilde{\alpha}}} \\ \sqrt{\frac{1+\cos \tilde{\alpha}-2\cos^2 \tilde{\alpha}}{1+\cos \tilde{\alpha}}} \end{pmatrix}. \quad (5.47)$$

The shorter diagonal of a face of the conventional unit cell is  $\tilde{d} = \tilde{a}\sqrt{2(1 - \cos \tilde{\alpha})}$ .

As long as  $\tilde{a} < \tilde{d}$  ( $\Leftrightarrow \cos \tilde{\alpha} < 1/2$ ) the MDP vectors are the same as those describing the conventional unit cell, i.e.,  $x = 1$ ,  $\varphi = \tilde{\alpha}$ , and  $\xi = \cos \varphi$ ,  $\eta = \cos \varphi(1 - \cos \varphi)/\sin \varphi$ , and  $\zeta = \sqrt{(1 + \cos \varphi - 2 \cos^2 \varphi)/(1 + \cos \varphi)}$ . If  $\tilde{a} = \tilde{d}$  ( $\Leftrightarrow \cos \tilde{\alpha} = 1/2$ ) the trigonal lattice is equivalent to an fcc lattice with a cubic lattice constant of  $\tilde{a}\sqrt{2}$ .

In the case of  $\tilde{a} > \tilde{d}$  ( $\Leftrightarrow \cos \tilde{\alpha} > 1/2$ ) the two shortest, linearly independent lattice vectors have length  $\tilde{d}$  and describe a 2D hexagonal lattice plane, which becomes obvious when recognising that the three dotted lines in each of the subfigures in figure 5.15 constitute an equilateral triangle. The third MDP vector,  $\mathbf{a}$ , has to point from one lattice point to one of its next to nearest neighbours [green in figure 5.15(b)], determining how to stack the hexagonal lattice planes to constitute the complete trigonal lattice<sup>8</sup>. As a consequence,  $x = \tilde{d}/\tilde{a} = \sqrt{2(1 - \cos \tilde{\alpha})} < 1$ . For the angle between the MDP vectors  $\mathbf{a}$  and  $\mathbf{b}$  there are two possibilities, to be described in the following: For both we take, w.l.o.g.,  $\mathbf{b} = \overrightarrow{AB}$  to be the vector from particle A to particle B in figure 5.15(b).

- If  $\mathbf{a} = \overrightarrow{AC}$  then the angle between  $\mathbf{a}$  and  $\mathbf{b}$  is given by<sup>9</sup>  $\cos \varphi = \frac{\tilde{d}}{2\tilde{a}} = x/2$ . There are two candidates for  $\mathbf{c}$  out of the six vectors to the nearest neighbours, their  $\xi$  and  $\eta$  coordinates are  $(\xi, \eta) = (0, x/\sqrt{4 - x^2})$  or  $(x^2/2, x(2 - x^2)/2\sqrt{4 - x^2})$ .  $\zeta$  always takes on its largest possible value, i.e.,  $\zeta = x\sqrt{(3 - x^2)/4 - x^2}$ .
- On the other hand if  $\mathbf{a} = \overrightarrow{AD}$  then the angle between  $\mathbf{a}$  and  $\mathbf{b}$  is  $\varphi = \pi/2$ , again leaving two possibilities for the  $\mathbf{c}$ -vector, parametrised by  $(\xi, \eta, \zeta) = (\pm x^2/2, x/2, x\sqrt{3 - x^2}/2)$ .

To summarise we write

$$\left\{ \begin{array}{l} x = 1 \wedge \frac{\pi}{3} < \varphi < \frac{\pi}{2} \wedge \xi = \cos \varphi \wedge \eta = \frac{\cos \varphi(1 - \cos \varphi)}{\sin \varphi} \wedge \zeta = \sqrt{\frac{1 + \cos \varphi - 2 \cos^2 \varphi}{1 + \cos \varphi}} \\ x < 1 \wedge \left\{ \begin{array}{l} \varphi = \frac{\pi}{2} \wedge \xi = \pm \frac{x^2}{2} \wedge \eta = \frac{x}{2} \wedge \zeta = \frac{x}{2}\sqrt{3 - x^2} \\ \cos \varphi = \frac{x}{2} \wedge \zeta = x\sqrt{\frac{3 - x^2}{4 - x^2}} \wedge \left\{ \begin{array}{l} \xi = 0 \wedge \eta = \frac{x}{\sqrt{4 - x^2}} \\ \xi = \frac{x^2}{2} \wedge \eta = \frac{x}{2}\sqrt{\frac{2 - x^2}{4 - x^2}} \end{array} \right. \end{array} \right. \end{array} \right. , \quad (5.48)$$

visualised in figure 5.16.

$\tilde{a}$  is always equal to the length  $a$  of the longest MDP vector  $\mathbf{a}$ , in the case  $x = 1$  we have  $\tilde{\alpha} = \varphi$ , and for  $x < 1$  we obtain  $\tilde{\alpha}$  through  $\cos \tilde{\alpha} = 1 - x^2/2$ .

#### 4. Tetragonal

The conventional unit cell of the tetragonal lattice is a rectangular prism with a square base ( $\tilde{a}$  by  $\tilde{a}$ ) and height  $\tilde{c}$  (which is different from  $\tilde{a}$ ). In principle there are, similar as for cubic lattices, simple, body centred, and face centred tetragonal

<sup>8</sup>This is similar to the stacking of the fcc lattice, see section 5.5.

<sup>9</sup>ABC constitute an isosceles triangle.

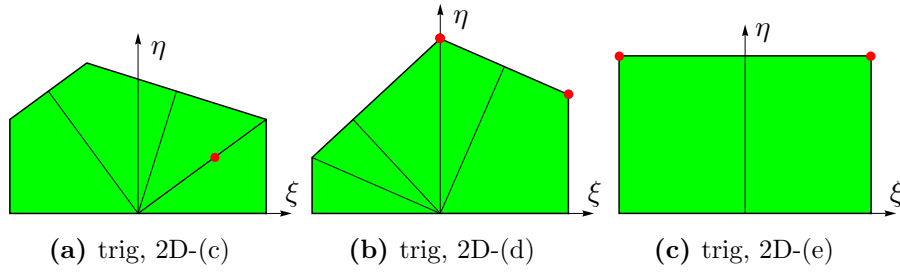


Figure 5.16: All possible parametrizations of the 3D trigonal lattice; for symbols, labels, etc. see figure 5.12.

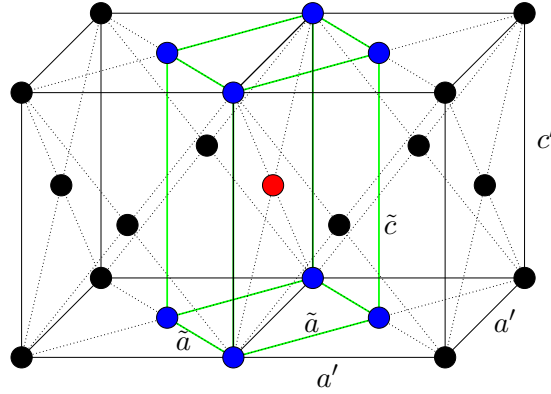


Figure 5.17: Equivalence of face centred tetragonal (fct) and body centred tetragonal (bct) lattices. The fct lattice with lattice constants  $a'$  and  $c'$  (the red particle is a face centred one) can also be described as a bct lattice with lattice constants  $\tilde{a} = a'/\sqrt{2}$  and  $\tilde{c} = c'$  (the red particle is located at the body centred position).

lattices. But since each face centred tetragonal lattice can also be described as a body centred tetragonal lattices, see figure 5.17, only one of them has to be considered. We chose the body centred one, but just call it “centred tetragonal” for the sake of simplicity. We analyse the three tetragonal lattices systematically:

- **Simple Tetragonal (st)**

We have to distinguish between the cases  $\tilde{a} < \tilde{c}$  and  $\tilde{a} > \tilde{c}$ , see figure 5.18. Whichever of these two lengths is smaller is also the length of the MDP vector  $\mathbf{c}$ , while the MDP vector  $\mathbf{a}$  has the other length. The second MDP vector,  $\mathbf{b}$ , always has the length of  $\tilde{a}$ . It is easy to find all possible parametrizations for the st lattice,

$$\varphi = \frac{\pi}{2} \wedge \xi = \eta = 0 \wedge \begin{cases} x = 1 \wedge 0 < \zeta < 1 \\ x < 1 \wedge \zeta = x \end{cases} . \quad (5.49)$$

- **Centred Tetragonal (ct)**

There are three candidate distances for the lengths of the MDP vectors:  $\tilde{a}$ ,  $\tilde{c}$ ,

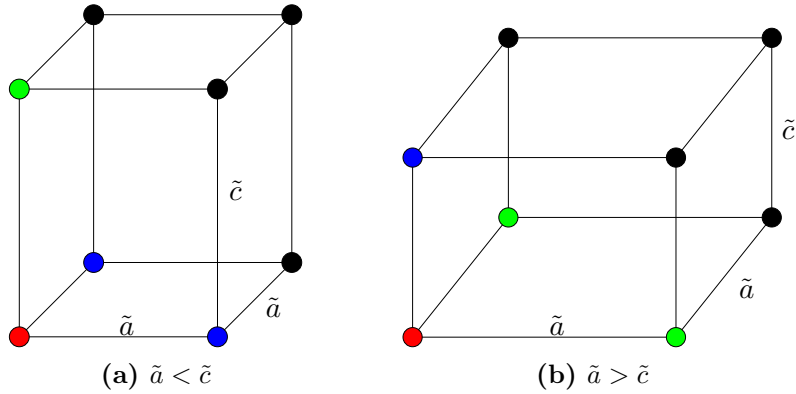


Figure 5.18: The two qualitatively different cases occurring for the st lattice. Nearest neighbours to the red particle are blue, next to nearest ones green.

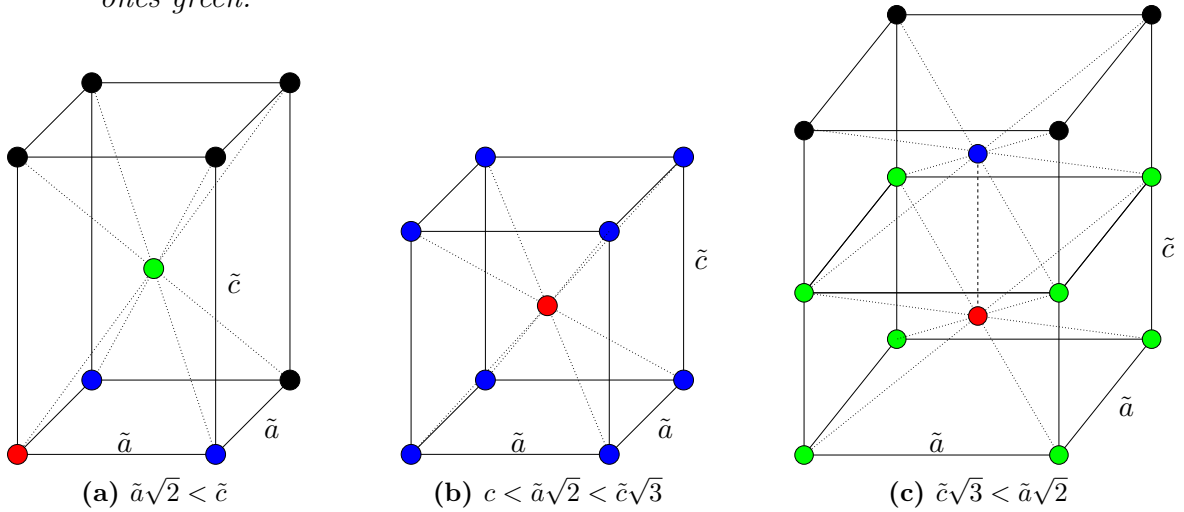


Figure 5.19: The three qualitatively different kinds of ct lattices. Nearest neighbours to the red particle are blue, next to nearest ones green.

and the distance from the body centred point to a corner of the conventional unit cell, which is half the trigonal  $\tilde{d} = \sqrt{2\tilde{a}^2 + \tilde{c}^2}$ . Since there are three linearly independent lattice vectors of length  $\tilde{d}/2$  and two linearly independent ones of length  $\tilde{a}$ , there remain only three different cases to be considered, visualised in figure 5.19.

- (i)  $\tilde{a} < \tilde{d}/2$ . It immediately follows that  $\tilde{d}/2 < \tilde{c}$  and  $\tilde{a}\sqrt{2} < \tilde{c}$ .  $\mathbf{c}$  and  $\mathbf{b}$  have length  $\tilde{a}$ , while the length of  $\mathbf{a}$  is  $\tilde{d}/2$  [see figure 5.19(a)].
- (ii)  $\tilde{d}/2 < \tilde{a}$  and  $\tilde{d}/2 < \tilde{c}$ . We obtain the conditions  $\tilde{a}\sqrt{2} < \tilde{c}\sqrt{3}$  and  $\tilde{c} < \tilde{a}\sqrt{2}$ . All three MDP vectors have the same length,  $\tilde{d}/2$  [see figure 5.19(b)].
- (iii)  $\tilde{c} < \tilde{d}/2$ . This implies  $\tilde{d}/2 < \tilde{a}$  and  $\tilde{c}\sqrt{3} < \tilde{a}\sqrt{2}$ , resulting in  $|\mathbf{c}| = \tilde{c}$  and  $|\mathbf{b}| = |\mathbf{a}| = \tilde{d}/2$  [see figure 5.19(c)].

The limiting case between (i) and (ii) (figures 5.19(a) and 5.19(b)), where  $\tilde{a}\sqrt{2} =$

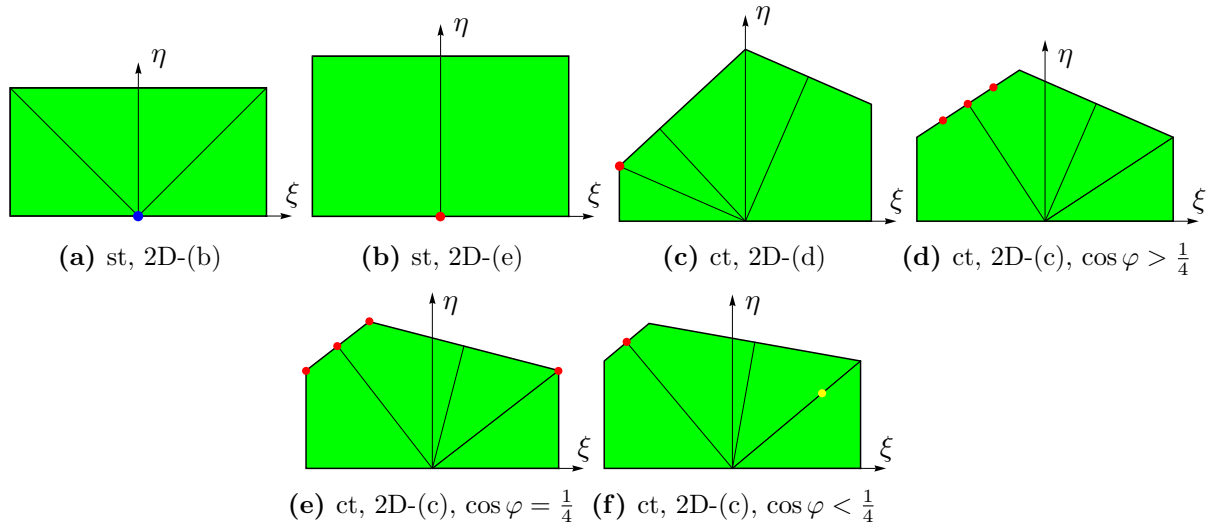


Figure 5.20: All possible parametrisations of the 3D tetragonal lattices; for symbols, labels, etc. see figure 5.12.

$\tilde{c}$ , is just an fcc lattice; and obviously  $\tilde{a} = \tilde{c}$ , covered in the second case, is a bcc lattice. Therefore both special cases have to be excluded from the general parametrisation for (true) ct lattices.

In case (i) we get  $x < 1$ , while in the cases (ii) and (iii) **a** and **b** are always of the length of  $\tilde{d}/2$ , resulting in  $x = 1$ . It is a time consuming but straightforward calculation to find all corresponding minimum distance parameters. In summary we obtain

$$\left\{ \begin{array}{l} x = 1 \wedge \left\{ \begin{array}{l} \cos \varphi \in (0, \frac{1}{2}) \setminus \{\frac{1}{3}\} \wedge \xi = \frac{\cos \varphi - 1}{2} \wedge \eta = \frac{\sin \varphi}{2} \wedge \zeta = \sqrt{\frac{1 + \cos \varphi}{2}} \\ \cos \varphi \in (0, \frac{1}{4}] \wedge \xi = 2 \cos \varphi \wedge \eta = \frac{2 \cos \varphi (1 - \cos \varphi)}{\sin \varphi} \wedge \zeta = \frac{2 \sqrt{\cos \varphi (1 - \cos \varphi)}}{\sin \varphi} \\ \cos \varphi \in [\frac{1}{4}, \frac{1}{2}) \setminus \{\frac{1}{3}\} \wedge \zeta = \frac{2 \sqrt{\cos \varphi (1 - \cos \varphi)}}{\sin \varphi} \wedge \left\{ \begin{array}{l} \left( \begin{array}{l} \xi = 2 \cos \varphi - 1 \wedge \\ \eta = \frac{2 \cos \varphi (1 - \cos \varphi)}{\sin \varphi} \end{array} \right) \\ \left( \begin{array}{l} \xi = -\cos \varphi \wedge \\ \eta = \frac{(1 - \cos \varphi)^2}{\sin \varphi} \end{array} \right) \end{array} \right. \end{array} \right. \\ x < 1 \wedge \cos \varphi = \frac{x}{2} \wedge \xi = -\frac{x^2}{2} \wedge \eta = \frac{x^3}{2\sqrt{4-x^2}} \wedge \zeta = x \sqrt{\frac{4-2x^2}{4-x^2}} \end{array} \right. \quad (5.50)$$

Figure 5.20(c) corresponds to case (i). The different points in the visualisations of figures 5.20(d-f) can be described in the following way: At  $\cos \varphi = 1/2$  all points corresponding to fcc lattices [figure 5.12(a)] are special cases of ct lattices, the points that half the lines  $\overline{P_2P_3}$  and  $\overline{P_3P_4}$  (see figure 5.5) correspond to true ct lattices. With decreasing  $\cos \varphi$  (i.e., increasing  $\varphi$ ) only the mid-point of  $\overline{P_3P_4}$  and two symmetrically assembled points on the  $\overline{P_3P_4}$ -line remain, they equally proceed “inwards” from the corner points  $P_3$  and  $P_4$  towards the mid-point with decreasing  $\cos \varphi$ . At  $\cos \varphi = 1/3$  all three points happen to lie on top of each other and hence represent the same lattice, a bcc lattice. Further decreasing

$\cos \varphi$  results again in a separation into three different points, similarly arranged on the  $\overline{P_3P_4}$ -line like above. At  $\cos \varphi = 1/4$  the symmetrically arranged points are again located at the corner points giving rise, due to symmetry, to the appearance of an extra ct point at  $P_2$  [see figure 5.20(e)]. For  $\cos \varphi < 1/4$  this extra point moves (with decreasing  $\cos \varphi$ ) along the  $\overline{P_0P_2}$ -line towards the origin, keeping at the lower rim of the 3D-pendentive, i.e.,  $\zeta$  takes on its minimum value for this point. The only other point to remain if  $\cos \varphi$  is less than  $1/4$  is the “bcc-like” one at the mid point of  $\overline{P_3P_4}$ , which turns into a representative of an fcc lattice at  $\cos \varphi = 0$  — the only remaining point then [which includes a second, similar one due to symmetry, see figure 5.12(b)].

### 5. Orthorhombic

The orthorhombic unit cell is a rectangular prism with a rectangular base, the three different edge lengths are labelled  $\tilde{a}$ ,  $\tilde{b}$ , and  $\tilde{c}$ . There are four different kinds of orthorhombic lattices, which will be discussed now.

- **Simple Orthorhombic** (so)

Only the corner points of the orthorhombic unit cell are lattice points for the so lattice. W.l.o.g. we can name the three edge lengths of the prismatic cell ordered by magnitude, i.e.,  $\tilde{a} > \tilde{b} > \tilde{c}$ . The MDP vectors are then the same as the conventional ones, i.e.,  $|\mathbf{a}| = a = \tilde{a}$ ,  $b = \tilde{b}$ , and  $c = \tilde{c}$ , corresponding to

$$x < 1 \wedge \varphi = \frac{\pi}{2} \wedge \xi = \eta = 0 \wedge \zeta < x, \quad (5.51)$$

visualised in figure 5.22(a).

- **Single Face Centred Orthorhombic** (sfco, also called base centred)

This lattice has, in addition to the corner points of the prismatic unit cell, one additional face centred lattice point on two opposing faces of the orthorhombic unit cell<sup>10</sup>. Putting the face centred point on the  $\tilde{a}$ - $\tilde{b}$ -face, w.l.o.g. we can only demand  $\tilde{a} > \tilde{b}$ , see figure 5.21. There are three candidates for the shortest lengths,  $\tilde{c}$ ,  $\tilde{b}$ , and half the  $\tilde{a}$ - $\tilde{b}$ -face diagonal,  $\tilde{d}$ . This results in five different possibilities for the corresponding MDP vectors.

(i)  $\tilde{c} \leq \tilde{b} < \tilde{d}/2$  results in  $c = \tilde{c}$ ,  $b = \tilde{b}$ , and  $a = \tilde{d}/2$ , and after some geometric considerations [see figure 5.21(a)] we arrive at

$$x < 1 \wedge \cos \varphi = \frac{x}{2} \wedge \xi = \eta = 0 \wedge \zeta \leq x, \quad (5.52a)$$

visualised in figure 5.22(b).  $x = 1$ , corresponding to  $\tilde{b} = \tilde{d}/2$ , would describe a st lattice. To obtain the conventional parameters from the MDP ones, use  $\tilde{c} = \zeta a$ ,  $\tilde{b} = xa$ , and  $\tilde{a} = \sqrt{4 - x^2}a$ .

<sup>10</sup>For a cubic cell this would be equivalent to a simple tetragonal lattice.

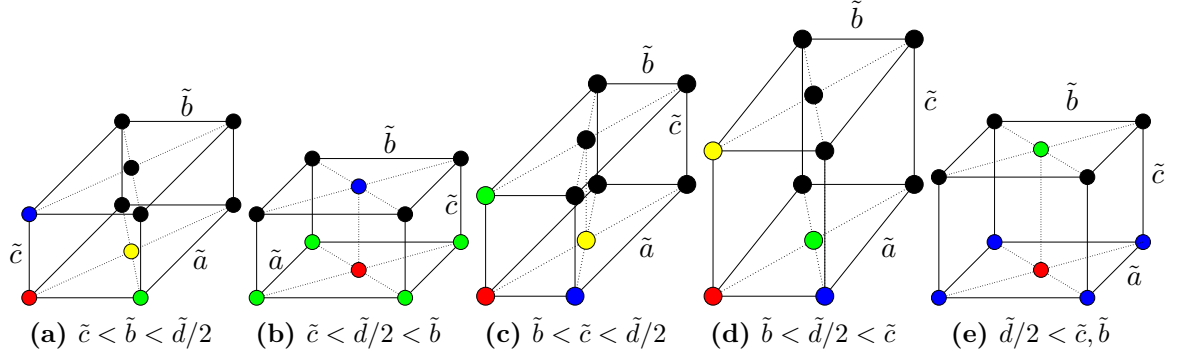


Figure 5.21: The five qualitatively different kinds of sfco lattices;  $\tilde{a} > \tilde{b}$  always holds. Nearest neighbours to the red particle are blue, next to nearest ones green, and third–next neighbours, if necessary for the MDP, are yellow.

- (ii)  $\tilde{c} \leq \tilde{d}/2 < \tilde{b}$  gives [see figure 5.21(b)]  $a = b = \tilde{d}/2$  and  $c = \tilde{c}$ , the possible ranges for  $x$ ,  $\varphi$ ,  $\xi$ ,  $\eta$ , and  $\zeta$  are

$$x = 1 \wedge \frac{\pi}{3} < \varphi < \frac{\pi}{2} \wedge \xi = \eta = 0 \wedge \zeta \leq 1, \quad (5.52b)$$

visualised in figure 5.22(c). The backwards transformation yields  $\tilde{c} = \zeta a$ ,  $\tilde{b} = xa$ , and  $\tilde{a} = \sqrt{4 - x^2}a$ .

- (iii)  $\tilde{b} \leq \tilde{c} < \tilde{d}/2$  [see figure 5.21(c)] means  $a = \tilde{d}/2$ ,  $b = \tilde{c}$ , and  $c = \tilde{b}$ , hence

$$x < 1 \wedge \varphi = \frac{\pi}{2} \wedge \xi \in \left[-\frac{x^2}{2}, \frac{x^2}{2}\right] \setminus \{0\} \wedge \eta = 0 \wedge \zeta = \sqrt{\xi(2 - \xi)}, \quad (5.52c)$$

where the negative  $\xi$ –values are only present because we include the whole boundary of the allowed region, as mentioned above. The  $\zeta$ –value is always the smallest one possible compatible with the other parameter values, hence the yellow colour in figure 5.22(d), where equation (5.52c) is visualised [only the points with  $\eta = 0$  correspond to equation (5.52c)].

This converts to  $\tilde{c} = xa$ ,  $\tilde{b} = a\sqrt{2\xi}$ , and  $\tilde{a} = a\sqrt{2(2 - \xi)}$ .

- (iv)  $\tilde{b} \leq \tilde{d}/2 < \tilde{c}$ , described in figure 5.21(d), corresponds to

$$x < 1 \wedge \varphi = \frac{\pi}{2} \wedge \xi = 0 \wedge \eta \in \left(0, \frac{x}{2}\right] \wedge \zeta = \sqrt{\eta(2x - \eta)}, \quad (5.52d)$$

also visualised in figure 5.22(d). Again,  $\zeta$  is as small as possible which we describe using the yellow colour (exactly below the red line which corresponds to the next item). Thus  $\tilde{c} = a$ ,  $\tilde{b} = a\sqrt{2x\eta}$ , and  $\tilde{a} = a\sqrt{2x(2 - \eta)}$ .

- (v)  $\tilde{d}/2 < \tilde{c}, \tilde{b}$  leads to  $a = \tilde{c}$  and  $b = c = \tilde{d}/2$  [see figure 5.21(e)] and we obtain

$$x < 1 \wedge \varphi = \frac{\pi}{2} \wedge \xi = 0 \wedge \eta \in \left(0, \frac{x}{2}\right) \wedge \zeta = \sqrt{x^2 - \eta^2}, \quad (5.52e)$$

which is described by the red line in figure 5.22(d). Thus  $\tilde{c} = a$ ,  $\tilde{b} = a\sqrt{2x(x - \eta)}$ , and  $\tilde{a} = a\sqrt{2x(x + \eta)}$ .

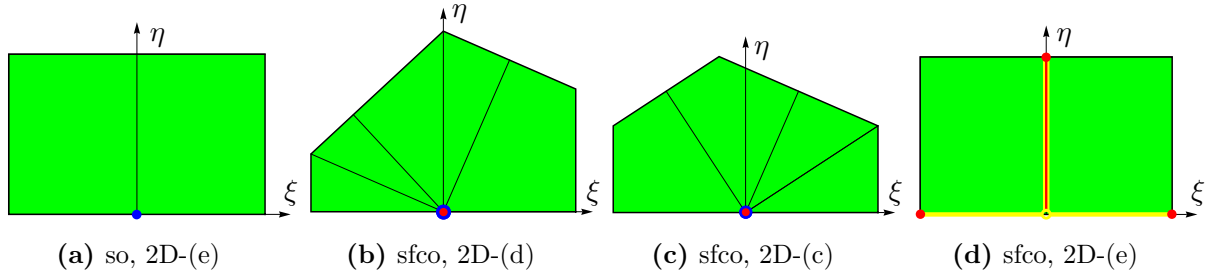


Figure 5.22: All possible parametrisations of the so and sfco lattices; for symbols, labels, etc. see figure 5.12.

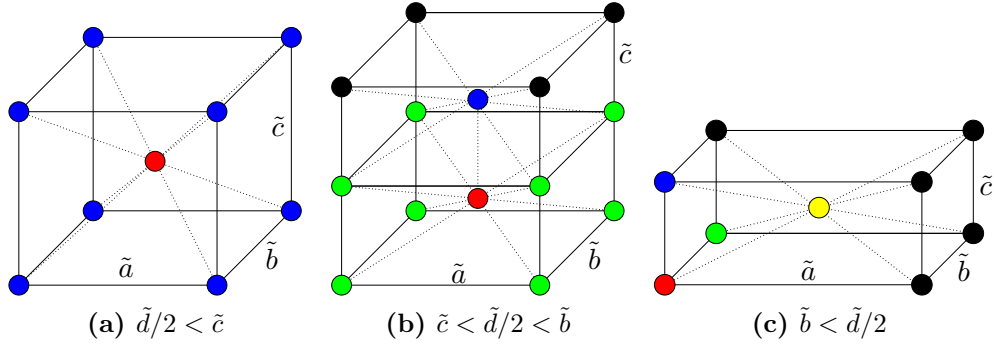


Figure 5.23: The three qualitatively different kinds of bco lattices. Nearest neighbours to the red particle are blue, next to nearest ones green, and third next ones (if necessary for the MDP) yellow.

If we replace the less than–sign ( $<$ ) in cases (iii)–(v) by a less equal–sign ( $\leq$ ) we include  $x = 1$  to the corresponding  $x$ –ranges, which of course has to be considered, too. The only difference for  $x = 1$  is, that all the endpoints of the corresponding  $\xi$  and  $\eta$  intervals have to be excluded, since for this case they correspond to higher symmetry lattices.

- **Body Centred Orthorhombic** (bco)

For the bco lattice we can again assume w.l.o.g.  $\tilde{a} > \tilde{b} > \tilde{c}$ , which means we only have to consider  $\tilde{b}$ ,  $\tilde{c}$ , and half the trigonal  $\tilde{d} = \sqrt{\tilde{a}^2 + \tilde{b}^2 + \tilde{c}^2}$  as candidates for the MDP vector lengths. This leaves us with three possibilities, visualised in figure 5.23.

- $\tilde{d}/2 \leq \tilde{c}$  results in all three MDP vectors to have the length of  $\tilde{d}/2$ , with the aid of figure 5.23(a) on can calculate all possible MDP parameters corresponding to such bco lattices,

$$x = 1 \wedge \frac{\pi}{3} < \varphi < \frac{\pi}{2} \wedge -\frac{1}{2} \leq \xi \leq -\frac{1}{2} + \cos \varphi \wedge \eta, \zeta \text{ maximal} . \quad (5.53a)$$

Of course, this also includes the bcc and some ct structures, therefore the corresponding points in the projection [figures 5.12(c), 5.20(d), 5.20(e), and 5.20(f)] have to be excluded. A typical case (assuming  $\cos \varphi = 0.3$ ) is visualised in figure 5.24(a). This parametrisation can of course also be converted back to the conventional parameters, but these rather lengthy



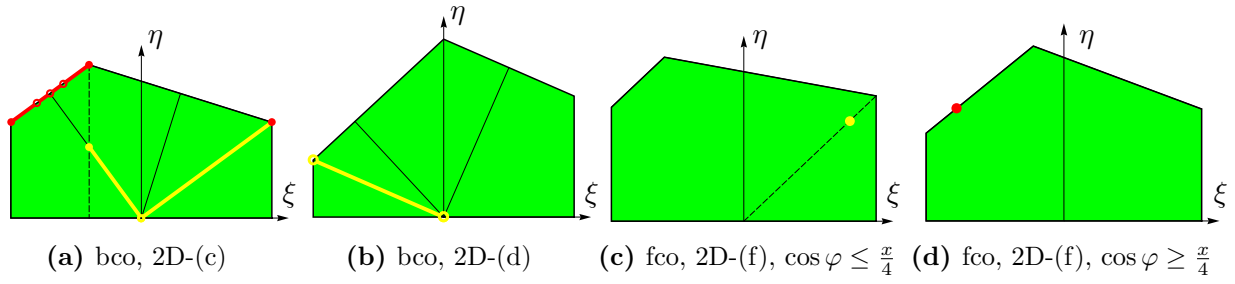


Figure 5.24: All possible parametrisations of the 3D bcc and 3D fcc lattices; for symbols, labels, etc. see figure 5.12. In (a) the ct points are excluded, see figure 5.20.

formulae are not very instructive and are hence only compiled in appendix C.1.

- (ii)  $\tilde{c} < \tilde{d}/2 < \tilde{b}$  gives  $a = b = \tilde{d}/2$  and  $c = \tilde{c}$ . After similar geometric considerations [see figure 5.23(b)] the resulting parameter ranges turn out to be

$$x = 1 \wedge \frac{\pi}{3} < \varphi < \frac{\pi}{2} \wedge \xi \in \left[-\frac{1}{2} + \cos \varphi, \frac{1}{2}\right] \setminus \{0\} \wedge \wedge \eta = \pm \xi \sqrt{\frac{1 \mp \cos \varphi}{1 \pm \cos \varphi}} \wedge \zeta = \sqrt{\frac{\pm 2\xi(1 \pm \cos \varphi \mp \xi)}{1 \pm \cos \varphi}}, \quad (5.53b)$$

visualised in yellow (smallest possible  $\zeta$ ) in figure 5.24(a). The red endpoint of the yellow line at  $\xi = 1/2$  also belongs to this case. For the back-transformation formulae see again appendix C.1.

- (iii) An example for  $\tilde{c} < \tilde{b} < \tilde{d}/2$  is depicted in figure 5.23(c); these conditions result in

$$x < 1 \wedge \cos \varphi = \frac{x}{2} \wedge \xi \in \left(-\frac{x^2}{2}, 0\right) \wedge \eta = -\frac{x\xi}{\sqrt{4-x^2}} \wedge \zeta = \sqrt{\frac{-2\xi(4-x^2+2\xi)}{4-x^2}}, \quad (5.53c)$$

visualised in 5.24(b). In this case it is easy to evaluate the back-transformation,  $\tilde{c} = a\sqrt{-2\xi}$ ,  $\tilde{b} = ax$ , and  $\tilde{a} = a\sqrt{4+2\xi-x^2}$ .

- **Face Centred Orthorhombic (fcc)**

W.l.o.g.  $\tilde{c} < \tilde{b} < \tilde{a}$ , therefore we also have for the three face diagonals  $d_{\tilde{a}\tilde{b}} > d_{\tilde{a}\tilde{c}} > d_{\tilde{b}\tilde{c}}$ , and of course also  $d_{\tilde{b}\tilde{c}}/2 < \tilde{b}$  holds. Hence, the only candidates for the shortest distance between lattice points are  $d_{\tilde{b}\tilde{c}}/2$  and  $\tilde{c}$ ;  $\mathbf{b}$  is *always* of length  $d_{\tilde{b}\tilde{c}}/2$ , because there always exist two linearly independent lattice vectors of this length. This means,  $\mathbf{c}$  and  $\mathbf{b}$  describe the lattice plane of the face with edges  $\tilde{c}$  and  $\tilde{b}$ .

The next shortest, linearly independent vector, representing  $\mathbf{a}$ , can then only

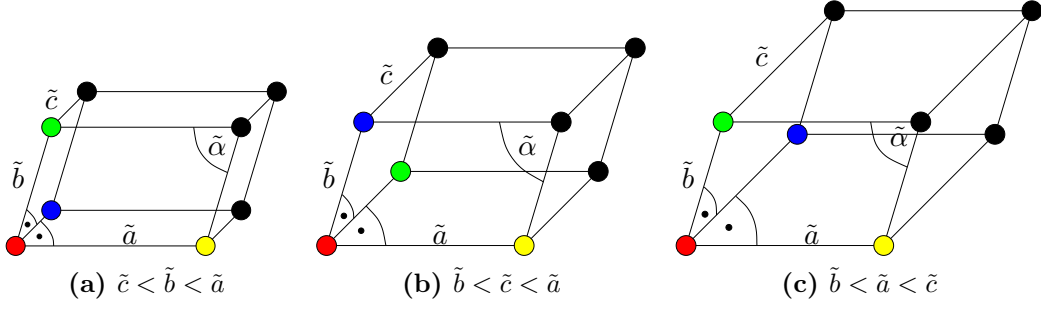


Figure 5.25: The three qualitatively different kinds of sm lattices. Nearest neighbours to the red particle are blue, next to nearest ones green, and third next ones yellow. Angles of  $\pi/2$  are indicated by dots.

have the length of  $d_{\tilde{a}\tilde{c}}/2$ . We obtain

$$x < 1 \wedge 0 < \cos \varphi \leq \frac{x}{4} \wedge \xi = 2x \cos \varphi \wedge \eta = \frac{2}{\sin \varphi} \cos \varphi (1 - x \cos \varphi) \wedge \zeta = \frac{2}{\sin \varphi} \sqrt{\cos \varphi (x - \cos \varphi) (1 - x \cos \varphi)}, \quad (5.54a)$$

$$x < 1 \wedge \frac{x}{4} \leq \cos \varphi < \frac{x}{2} \wedge \xi = -x \cos \varphi \wedge \eta = \frac{x + x \cos^2 \varphi - 2 \cos \varphi}{\sin \varphi} \wedge \zeta = \frac{2}{\sin \varphi} \sqrt{\cos \varphi (x - \cos \varphi) (1 - x \cos \varphi)}, \quad (5.54b)$$

and the back-transformations are given by  $\tilde{c} = 2a\sqrt{x \cos \varphi}$ ,  $\tilde{b} = 2a\sqrt{x(x - \cos \varphi)}$ , and  $\tilde{a} = 2a\sqrt{1 - x \cos \varphi}$ .

For all the orthorhombic cases, wherever there appears an inequality sign (e.g.  $<$ ) we can replace it by a sign that includes the limiting case (e.g.  $\leq$ ) and still have orthorhombic symmetry. But then it is of course possible to encounter even higher symmetries, see the Bravais lattices discussed before.

## 6. Monoclinic

### • Simple Monoclinic (sm)

In an sm lattice, one lattice vector,  $\tilde{\mathbf{c}}$ , is perpendicular to the other two,  $\tilde{\mathbf{a}}$  and  $\tilde{\mathbf{b}}$ , which, in turn, enclose an arbitrary angle. We call this angle  $\tilde{\alpha}$ , the length of the perpendicular vector is  $\tilde{c}$ , and the other two conventional lattice vectors have lengths  $\tilde{a}$  and  $\tilde{b}$ , see figure 5.25. W.l.o.g. we can set  $\tilde{b} \leq \tilde{a}$  and even demand, that these distances together with the angle  $\tilde{\alpha}$  are chosen in a way to satisfy the 2D MDP in their lattice plane, i.e.,  $\cos \tilde{\alpha} < \tilde{b}/2\tilde{a}$  (we have “ $<$ ” instead of “ $\leq$ ” to avoid the sfco symmetry). Therefore, there are three possibilities for the 3D MDP:

(i)  $\tilde{c} \leq \tilde{b} \leq \tilde{a}$ , depicted in figure 5.25(a) and resulting in

$$x \leq 1 \wedge 0 < \cos \varphi < \frac{x}{2} \wedge \xi = \eta = 0 \wedge 0 < \zeta \leq x, \quad (5.55a)$$

which corresponds to  $\tilde{a} = a$ ,  $\tilde{b} = ax$ ,  $\tilde{c} = \zeta a$ , and  $\tilde{\alpha} = \varphi$ .

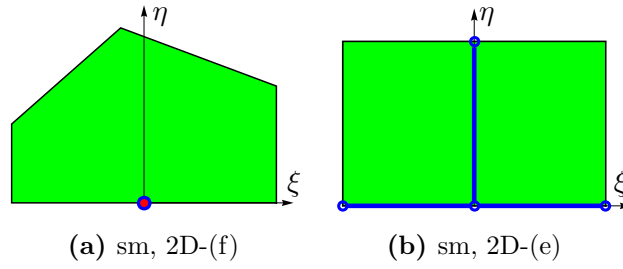


Figure 5.26: All possible parametrisations of the 3D sm lattices; for symbols, labels, etc. see figure 5.12.

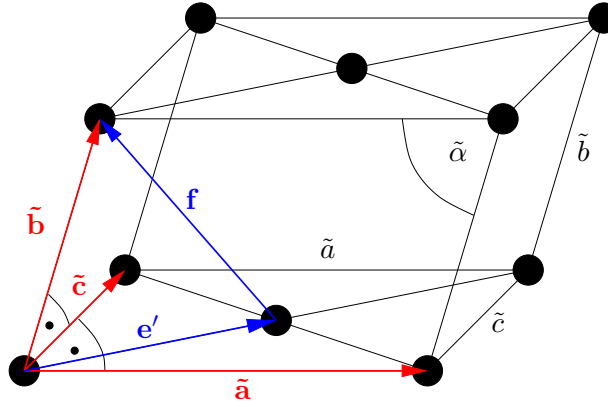


Figure 5.27: The sfcM lattice. *Italic symbols denote lengths; bold, upright ones denote vectors. Angles of  $\pi/2$  are indicated by dots.*

(ii)  $\tilde{b} \leq \tilde{c} \leq \tilde{a}$  [figure 5.25(b)], with

$$x \leq 1 \wedge \varphi = \frac{\pi}{2} \wedge \eta = 0 \wedge \xi \in \left[-\frac{x^2}{2}, \frac{x^2}{2}\right] \wedge \zeta \in [\zeta_{\min}, \zeta_{\max}] , \quad (5.55b)$$

back-transformed using  $\tilde{a} = a$ ,  $\tilde{b} = a\sqrt{\xi^2 + \zeta^2}$ ,  $\tilde{c} = xa$ , and  $\tan \tilde{\alpha} = |\zeta/\xi|$ .

(iii)  $\tilde{b} \leq \tilde{a} \leq \tilde{c}$  [figure 5.25(c)], giving

$$x \leq 1 \wedge \varphi = \frac{\pi}{2} \wedge \xi = 0 \wedge \eta \in \left[0, \frac{x}{2}\right] \wedge \zeta \in [\zeta_{\min}, \zeta_{\max}] , \quad (5.55c)$$

and  $\tilde{a} = xa$ ,  $\tilde{b} = a\sqrt{\xi^2 + \zeta^2}$ ,  $\tilde{c} = a$ , and  $\tan \tilde{\alpha} = \zeta/\eta$ .

Of course, the origin,  $(\xi, \eta, \zeta) = (0, 0, 0)$ , must be excluded. The corresponding 3D MDP parameter space is visualised in figure 5.26.

- **Single Face Centred Monoclinic (sfcM)**

The sfcM lattice has, compared to the sm lattice, an additional face centred point in one (and its opposite) of the rectangular faces of the monoclinic unit cell. W.l.o.g. we put it on the  $\tilde{a}$ - $\tilde{c}$ -face, see figure 5.27. In this case we *cannot* restrict  $\tilde{a} \geq \tilde{b}$  and also  $\tilde{\alpha}$  is now completely arbitrary. The way to find the three MDP vectors in dependence of the sfcM-parameters is rather complicated and will be performed in four steps.

First we switch to a description of the lattice through the primitive unit cell spanned by  $\tilde{\mathbf{a}}$ ,  $\tilde{\mathbf{b}}$  and the vector to one of the closest face centred points, which we call  $\mathbf{e}'$  (see figure 5.27). Its length is equal to half the length of the diagonal of the  $\tilde{a}$ - $\tilde{c}$ -face,  $e' = \tilde{d}/2$ .

Next, we consider the 2D lattice planes spanned by  $\tilde{\mathbf{a}}$  and  $\tilde{\mathbf{b}}$ , called  $(\tilde{\mathbf{a}}, \tilde{\mathbf{b}})$ : We can describe the same 2D lattice by its 2D MDP vectors, resulting in new vectors  $\mathbf{a}'$  and  $\mathbf{b}'$  of lengths  $a'$  and  $b'$  ( $b' \leq a'$ ), which enclose the angle  $\alpha'$ , satisfying  $\cos \alpha' \leq \frac{b'}{2a'}$ , i.e.,  $(\tilde{\mathbf{a}}, \tilde{\mathbf{b}}) = (\mathbf{a}', \mathbf{b}')$ . Now the question is: What is the relation between these new vectors  $\mathbf{a}'$  and  $\mathbf{b}'$  on the one hand, and the three vectors  $\tilde{\mathbf{a}}$ ,  $\tilde{\mathbf{b}}$ , and  $\mathbf{e}'$  on the other hand?

To answer this we first notice, that the projection of a point of a neighbouring (parallel)  $(\mathbf{a}', \mathbf{b}')$ -lattice plane, obtained by adding  $\mathbf{e}'$  to each point of the first lattice plane, of course always lies in a WSC<sup>11</sup> of the first lattice plane. The projection of the next but one neighbouring plane (obtained by adding  $2\mathbf{e}'$  to each point of the first lattice plane) onto the first plane lies exactly on top of the first lattice plane, since we have then moved along the whole diagonal of the  $\tilde{a}$ - $\tilde{c}$ -face and have hence reached a point also accessible through moving (from another lattice point) over a distance  $\tilde{c}$  *perpendicular* to the  $(\mathbf{a}', \mathbf{b}')$ -lattice (see again figure 5.27).

Calling the projection of  $\mathbf{e}'$  onto the  $(\mathbf{a}', \mathbf{b}')$ -lattice plane  $\mathbf{e}'_{\parallel}$ , this means, the point reached (from any lattice point) by  $\mathbf{e}'_{\parallel}$  in the  $(\mathbf{a}', \mathbf{b}')$ -lattice plane has to lie *exactly halfway* between two lattice points. In fact, for *any* 2D lattice point there exists another one in a way, that the position vector  $\mathbf{e}'_{\parallel}$  lies halfway between them. This is also true for the closest lattice point, which of course has a WSC, into which  $\mathbf{e}'_{\parallel}$  must point. We take the lattice vector from this closest point to  $\mathbf{e}'$  and call it  $\tilde{\mathbf{e}}$ . Now, w.l.o.g., we demand  $\tilde{a} = 2|\tilde{\mathbf{e}}_{\parallel}|$ , which just takes of all possible descriptions of a given sfc lattice the one with the smallest possible  $\tilde{a}$ ; but this condition also guarantees  $\tilde{\mathbf{e}} = \mathbf{e}'$ .

There are exactly six different points in a 2D-WSC lying halfway between two lattice points, due to symmetry this number is reduced to three. In our case of the  $(\mathbf{a}', \mathbf{b}')$ -lattice plane they are positioned at  $\mathbf{a}'/2$ ,  $\mathbf{b}'/2$  and  $(-\mathbf{a}' + \mathbf{b}')/2$ . For the sake of completeness we also define the vector  $\mathbf{c}' = 2\mathbf{e}'_{\perp}$  [with  $\mathbf{e}'_{\perp}$  being the component of  $\mathbf{e}'$  perpendicular to  $(\mathbf{a}', \mathbf{b}')$ ] which is of course equal to  $\tilde{\mathbf{c}}$ .

In each of these three cases there are five lengths which have to be considered when trying to find the 3D MDP vectors:

$$a', \quad b', \quad e' = \frac{\tilde{d}}{2}, \quad c', \quad \text{and } f, \quad (5.56)$$

where  $f$  is the length of the vector  $\tilde{\mathbf{e}} - \tilde{\mathbf{b}}$ , see figures 5.27 and 5.28. Of course, it can never be that  $a'$ ,  $b'$ , and  $c'$  are the lengths of the three MDP vectors, since

<sup>11</sup>Wigner-Seitz unit cell, see section 5.1.

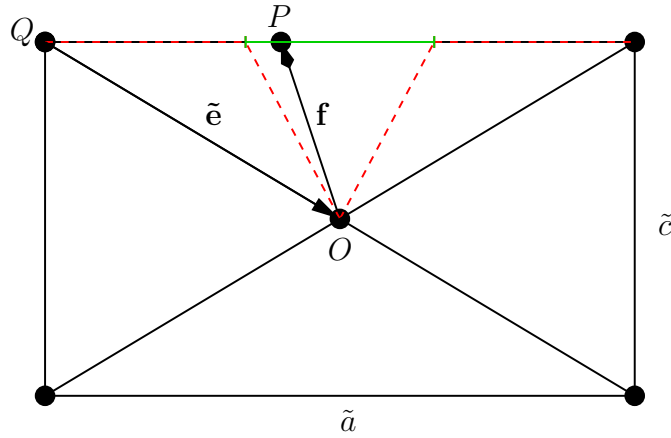


Figure 5.28: Visualisation why  $f$  can be one of the MDP vector lengths, i.e., smaller than  $b$ , using a projection of figure 5.27 onto the  $\tilde{a}$ - $\tilde{c}$ -plane. The vector  $\mathbf{f} = \tilde{\mathbf{b}} - \tilde{\mathbf{e}}$  has a different arrowhead indicating that it would point outside the plane, the projection of its apex is called  $P$ . The dashed red lines are all of equal length, indicating that if  $P$  lies on the green line (as depicted here), then  $OP \leq PQ$  and hence  $f \leq \tilde{b}$ . This can only happen if  $\tilde{a} > \tilde{c}$ .

this would lead to a sm lattice. Therefore  $\tilde{d}/2$  and/or  $f$  have to be the length(s) of at least one MDP vector.

As a third step we determine the extra length  $f$  introduced here. For this we treat the three cases separately.

- (i)  $\mathbf{e}'_{\parallel}$  points at  $\mathbf{a}'/2$ , i.e., tilde-quantities are equivalent to the corresponding primed ones. This results in

$$f^2 = \left( \mathbf{b}' - \frac{\mathbf{a}'}{2} + \frac{\mathbf{c}'}{2} \right)^2 = \frac{\tilde{d}^2}{4} + b'^2 - a'b' \cos \alpha' \geq \frac{\tilde{d}^2}{4} + \frac{b'^2}{2}, \quad (5.57)$$

where we used  $\cos \alpha' \leq b'/2a'$ . This obviously gives  $f > \tilde{d}/2$ , which means that  $\tilde{d}/2$  is *always* the length of a MDP vector in this case.

- (ii)  $\mathbf{e}'_{\parallel}$  points at  $\mathbf{b}'/2$ . This results in  $\tilde{a} = b'$  and

$$f^2 = \left( -\mathbf{a}' + \frac{\mathbf{b}'}{2} + \frac{\mathbf{c}'}{2} \right)^2 = \frac{\tilde{d}^2}{4} + a'^2 - a'b' \cos \alpha' \geq \frac{\tilde{d}^2}{4} + a'^2 - \frac{b'^2}{2}, \quad (5.58)$$

again  $f$  is bigger than  $\tilde{d}/2$ , since  $a' \geq b'$ .

(iii)  $\mathbf{e}'_{\parallel}$  points at  $(-\mathbf{a}' + \mathbf{b}')/2$ . In this case we obtain

$$\tilde{a} = |-\mathbf{a}' + \mathbf{b}'|, \quad (5.59)$$

$$\frac{\tilde{d}^2}{4} = \frac{a'^2 + b'^2 + c'^2}{4} - \frac{1}{2}a'b' \cos \alpha', \quad (5.60)$$

$$f^2 = \frac{\tilde{d}^2}{4} + a'b' \cos \alpha', \quad (5.61)$$

resulting similarly in  $f > \frac{\tilde{d}}{2}$ .

Finally, as a fourth step, we have to distinguish between all different possibilities for the MDP vectors, of which there are in total 56. They are listed in appendix C.2.

#### 7. *Triclinic* (tric)

This lattice has no symmetry (except inversion), all parametrisations not enclosed in the above discussion correspond to lattices of this kind of Bravais lattice. W.l.o.g. we can choose the MDP vectors as the conventional primitive vectors.

## 5.4 Basis Particles

We now return to the problem of finding the *shortest distance between particles* occurring in the whole crystal, *including* the basis particles. Therefore we consider an arbitrary basis consisting of (an arbitrary number of) equally sized hard spheres in addition to the MDP of equation (5.21) of the lattice. Note that, although the statements in this section are intuitive and strong evidence through billions of randomly generated crystals exists, they have not yet been proven analytically.

W.l.o.g. the first basis particle is always positioned at the lattice points, see equation (5.7). It is therefore easy to conclude, that in the case of only one basis particle, the shortest distance is just  $c$ .

For two basis particles we only have to check which distance between particles in and at the border of the unit cell is the shortest one. The vector indicating the position of the additional basis particle inside the unit cell is [see equation (5.6)]

$$\mathbf{v}_2 = v_{2a}\mathbf{a} + v_{2b}\mathbf{b} + v_{2c}\mathbf{c}, \quad (5.62)$$

with  $v_{2X} \in [0, 1)$ . The distances under consideration are the following:

$$\begin{array}{ll} |\mathbf{c}| & \\ |\mathbf{v}_2| & |\mathbf{v}_2 - \mathbf{c}| \\ |\mathbf{v}_2 - \mathbf{a}| & |\mathbf{v}_2 - \mathbf{a} - \mathbf{c}| \\ |\mathbf{v}_2 - \mathbf{b}| & |\mathbf{v}_2 - \mathbf{b} - \mathbf{c}| \\ |\mathbf{v}_2 - \mathbf{a} - \mathbf{b}| & |\mathbf{v}_2 - \mathbf{a} - \mathbf{b} - \mathbf{c}| \end{array} \quad (5.63)$$

One (or, in special cases, more) of these distances is the shortest one.

For more than two basis particles we have [see again equation (5.6)]

$$\mathbf{v}_i = v_{ia}\mathbf{a} + v_{ib}\mathbf{b} + v_{ic}\mathbf{c}, \quad i = 2, 3, \dots \quad (5.64)$$

In addition to equation (5.63) we have to check for each  $i$  the distances between the additional basis particle  $i$  and all the other ones. For this we also have to consider the basis particles in the  $3 \times 3 \times 3 - 1$  adjacent unit cells. We finally arrive at the minimum distance as a function of the crystal parameters

$$\frac{d_{\min}}{a} = d_{\min}^* = d_{\min}^*(x, \varphi, \xi, \eta, \zeta, \{v_{iX}\}) \quad (5.65)$$

We use a star superscript to indicate, that this is a dimensionless quantity, but note that this time we reduce with the length  $a$ , which is why we use a different kind of star (\*) in contrast to the one that indicates reduction with  $\sigma$  (\*).

The parameter  $a$  is just a factor that scales all the distances in the whole crystal. Therefore we can use  $a$  to finally satisfy the hard core condition. If there exists also a cutoff distance  $d_{\text{cut}}$  for the interaction potential (e.g.  $\lambda$  for the SSM), we can set

$$\sigma \leq ad_{\min}^* \leq d_{\text{cut}} \quad (5.66)$$

because values of  $a$  not satisfying the second inequality in equation (5.66) all result in lattices with zero energy<sup>12</sup>, of which only the one with the smallest volume fraction is of interest when looking for the minimal Gibbs free energy, see section 5.6.

There is still one issue to cover concerning crystal structures of hard-core particles, before we can finally turn towards to the calculation of Gibbs free energies.

## 5.5 Close-Packed Structures

In 2D there is exactly one possibility to arrange hard core particles in a close-packed way, *viz.* the hexagonal lattice with nearest neighbour distance equal to the hard core diameter  $\sigma$ . To construct the 3D close-packed structure we can use 2D hexagonally close-packed layers as building blocks, but their arrangement is not unambiguous, i.e., there are various, different possibilities to arrange them in a close-packed way.

Consider a primitive unit cell for one 2D hexagonal plane which is a rhombus with one diagonal being equal to the edge length of  $\sigma$ . This diagonal splits the unit cell into two equilateral triangles. If the adjacent layer has to be packed as closely as possible to the first one, the particles have to be positioned above the centroids of the equilateral triangles built by the particles of the first layer, thus minimising the distance between the layers to the height of a regular tetrahedron of edge length  $\sigma$ , which turns out to be  $\sqrt{\frac{2}{3}}\sigma$ .

Obviously, there are two possibilities for this positioning of the second layer. Iterating this procedure one finds out [67] that all layers can be classified into three different types,

<sup>12</sup>This will become more obvious with help of the formula for the lattice sum, equation (5.69).

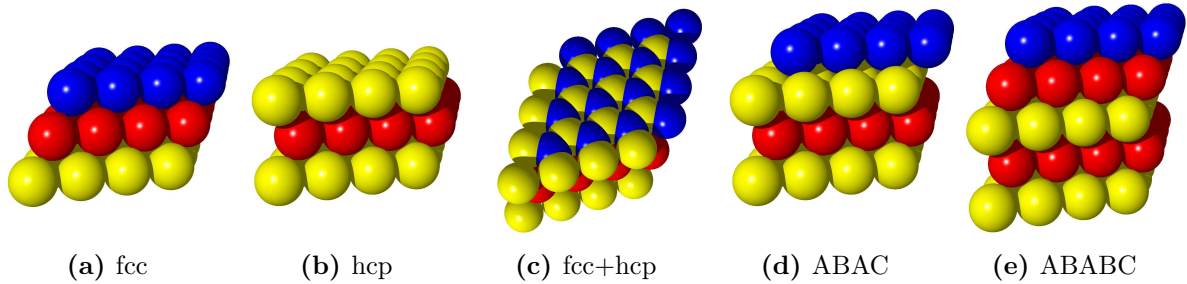


*Figure 5.29: Examples for different kinds of close-packed stackings; particles that are part of an A-plane are coloured yellow, B-plane particles are red, and those of the C-plane are blue. In (c) we put particles of A- and C-planes into the same (third) layer, thus visualising the difference between fcc and hcp.*

usually termed A, B, and C layers. They can be identified in the following way. We position a Cartesian coordinate system in a way that the  $x$ - $y$ -plane is parallel to the hexagonal layers and rotate it until the two primitive vectors of each hexagonal layer are  $\mathbf{a}_1 = \sigma \hat{\mathbf{x}}$  and  $\mathbf{a}_2 = \frac{\sigma}{2} \hat{\mathbf{x}} + \frac{\sigma\sqrt{3}}{2} \hat{\mathbf{y}}$ , where  $\hat{\mathbf{x}}$ ,  $\hat{\mathbf{y}}$ , and  $\hat{\mathbf{z}}$  are the unit vectors of the coordinate system. The A, B, and C layers can now be characterised by the  $x$  and  $y$  components of the particle which is closest to the  $z$ -axis (there can be three of equal distance), w.l.o.g. we choose  $A \leftrightarrow (0, 0)$ ,  $B \leftrightarrow \sigma \left( \frac{1}{2}, \frac{1}{2\sqrt{3}} \right)$ , and  $C \leftrightarrow \sigma \left( 0, \frac{1}{\sqrt{3}} \right)$ . Thus, each close-packed structure can be characterised by its stacking sequence, e.g. an fcc structure is represented by the stacking sequence ABC [see figure 5.29(a)], while the hexagonally close-packed structure (hcp) is simply represented by a stacking sequence AB [see figure 5.29(b)]; of course these sequences recur periodically, i.e., hcp is the stacking ...ABABAB..., and similar for any other stacking.

In this way one can represent all possible close-packed stackings by sequences of the letters A, B, and C. Of course the sequences are not completely arbitrary, as discussed above particles of consecutive layers occupy tetrahedral sites of the neighbouring layers, hence consecutive letters in stacking sequences always have to be different. This is also true for the first and last letters of any possible sequence, since they are also consecutive in the periodically recurring scheme. In the remaining pool of possible stacking sequences there are still many different sequences describing the *same* crystal, due to symmetry; of course we therefore reduce this pool further by symmetry considerations, to obtain a reduced pool where different sequences correspond to different crystals.

Since the labelling of the layers is strongly linked to the choice of the origin, we can always shift the coordinate system in a way to obtain a label of A for the first considered layer. In general there are three possibilities for this choice, we keep only one representative of them (this removes the redundancy that e.g. AB, AC, and BC all describe the same hcp structure). Of course we also exclude sequences that are multiples of shorter ones, or those that are obtained via cyclic permutation (of another one). Finally, we consider



the following transformation: inversion ( $\mathbf{r} \rightarrow -\mathbf{r}$ ) and subsequent mirroring<sup>13</sup> on the  $x$ - $y$ -plane ( $z \rightarrow -z$ ). While this transformation leaves the A layers unchanged, it exchanges the B and C ones, i.e., B $\rightarrow$ C and C $\rightarrow$ B. Again, we only select one representative from the corresponding equivalent structures.

The first couple of stacking sequences with increasing number of considered layers are given in table 5.1.

Having thus acquired the necessary tools for the description of crystals consisting of (equally sized) hard core particles, the MDP (along with a mapping procedure to conventional Bravais lattice parameters) with any possible basis, and the limiting cases for high densities, the possible close-packed stacking sequences, we are able to proceed to the next, major task: The minimisation of a thermodynamic potential to find the equilibrium structures.

---

<sup>13</sup>A crystal and its mirrored/inverted counterpart always have equal energies, see next section.

nr. of layers	different stacking(s)
1	—
2	AB (hcp)
3	ABC (fcc)
4	ABAC
5	ABABC
6	ABABAC, ABACBC
7	ABABABC, ABABCAC, ABACABC
8	ABABABAC, ABABACAC, ABABACBC, ABABCABC, ABABCBCAC, ABACBABC
9	ABABABABC, ABABABCAC, ABABABCBC, ABABACABC, ABABACBAC, ABABCABAC, ABABCACBC, ABABCBCAC, ABABCBCAC, ABACBACBC
10	ABABABABAC, ABABABACAC, ABABABACBC, ABABABCABC, ABABABCBCAC, ABABACABAC, ABABACACBC, ABABACBABC, ABABACBCAC, ABABACBCBC, ABABCABCAC, ABABCABCBC, ABABCACBAC, ABABCBCABC, ABABCBCBC, ABACABACBC, ABACABCABC, ABACBACABC
11	ABABABABABC, ABABABABCAC, ABABABABCBC, ABABABACABC, ABABABACBAC, ABABABCABAC, ABABABCACAC, ABABABCACBC, ABABABCBCABC, ABABABCBCAC, ABABACABABC, ABABACABCAC, ABABACABCBC, ABABACACABC, ABABACACBAC, ABABACBABC, ABABACBACBC, ABABACBCABC, ABABACBCBAC, ABABCABACBC, ABABCABCABC, ABABCABCBCAC, ABABCACABAC, ABABCACBABC, ABABCACBCAC, ABABCBCABCAC, ABABCBCACABC, ABABCBCBAC, ABACABACABC, ABACABCACBC, ABACBABCABC
12	ABABABABABAC, ABABABABACAC, ABABABABACBC, ABABABABCABC, ABABABABCBCAC, ABABABACABAC, ABABABACACAC, ABABABACACBC, ABABABACBABC, ABABABACBCAC, ABABABACBCBC, ABABABCABABC, ABABABCABCAC, ABABABCABCBC, ABABABCACABC, ABABABCACBAC, ABABABCBCABC, ABABABCBCBAC, ABABACABACAC, ABABACABACBC, ABABACABCABC, ABABACABCBCAC, ABABACACBABC, ABABACACBCAC, ABABACACBCBC, ABABACBABCABC, ABABACBABCAC, ABABACBABCBC, ABABACBACABC, ABABACBACBAC, ABABACBCABAC, ABABACBCACBC, ABABACBCBABC, ABABCABABCAC, ABABCABABCBC, ABABCABACABC, ABABCABACBAC, ABABCABCABAC, ABABCABCACBC, ABABCABCBCABC, ABABCABCBCAC, ABABCACABCBC, ABABCACBABC, ABABCACBACBC, ABABCACBCABC, ABABCACBCBAC, ABABCBCABCABC, ABABCBCABCBC, ABABCBCACABC, ABABCBCACBC, ABABCBCBABC, ABABCBCBAC, ABABCBCACBC, ABABCBCACBABC, ABABCBCACBCAC, ABACABACBABC, ABACABCBCABC, ABACBABCABC, ABACBABCBCABC

Table 5.1: The first 133 non-equivalent stacking sequences for close-packed particles, the number of layers ranging from 1 to 12. The first four stackings are visualised in figures 5.29(a,b,d,e).

## 5.6 Gibbs Free Energy

Our objective focuses on the quest to find all stable crystal structures at zero temperature. Since we consider infinitely extended, ideal crystals as candidate structures, we work in the thermodynamical limit, i.e., the number of particles  $N$  and the volume  $V$  tend to infinity, while their ratio, the number density  $\rho = N/V$  remains finite. At fixed  $T = 0$ , the number density is therefore the only relevant thermodynamic variable in the canonical ( $NVT$ ) ensemble, while in the isobaric ( $NPT$ ) ensemble only pressure remains relevant.

In applications of genetic algorithms to  $NVT$  ensembles of soft systems in references [68, 69] the density was optimised, hence the (free) energy was minimised. However there are three reasons why we chose to work in the  $NPT$  ensemble, minimising thus the Gibbs free energy (enthalpy).

- Firstly, in usual experimental setups it is much easier to work under constant (in general ambient) pressure.
- Secondly, when phase separation occurs, the coexisting phases have equal temperature and equal pressure, while density changes discontinuously from one phase to the other in a first order phase transition. Working in the  $NPT$  ensemble we avoid the occurrence of discontinuities in the thermodynamic variables.
- Thirdly, a reason related to technical issues of the parametrisation of the equilibrium structures: Keeping the density fixed imposes a constraint on the parameters describing all possible crystals. For given number of basis particles this is  $a^3 x \sin \varphi \zeta = \text{const.}$ , i.e., the volume of the unit cell has to be kept constant. Especially when considering a basis of more than one particle, this results in highly non-trivial alterations of equation (5.21), which can simply be avoided through letting density be optimised for given pressure.

Thus, in a first step we divide the zero temperature relation  $G = H = E + PV$  by the number of particles and obtain

$$g = h = e + \frac{P}{\rho}, \quad (5.67)$$

the Gibbs free energy or enthalpy per particle. The intensive *quantities per particle* are denoted by lowercase letters ( $e$ ,  $f$ ,  $h$ , and  $g$ ) in contrast to the extensive ones ( $E$ ,  $F$ ,  $H$ , and  $G$ ). Since  $g$  and  $h$  are equal at  $T = 0$ , we will from now on only use the term enthalpy and the corresponding symbol  $h$ , for the sake of simplicity.

To calculate the r.h.s. of equation (5.67) we need  $P$ ,  $\rho$ , and  $e$ . The pressure  $P$  is our independent thermodynamic variable, and the density  $\rho$  is easily derived for a given crystal,

$$\rho = \frac{n_b}{V_c} = \frac{n_b}{|(\mathbf{a} \times \mathbf{b}) \cdot \mathbf{c}|} = \frac{n_b}{a^3 x \sin \varphi \zeta}, \quad (5.68)$$

where  $n_b$  is the number of basis particles,  $V_c$  is the volume of the unit cell, and the other quantities have been defined in equation (5.10). At zero temperature, the energy

per particle in a crystal described by equations (5.10) and (5.6), is obtained through the following lattice sum (see [68])

$$e = \frac{1}{2} \sum_{\substack{(i,j,k) \in \\ \mathbb{Z}^3 \setminus (0,0,0)}} \phi(|\mathbf{L}_{ijk}|) + \frac{1}{n_b} \sum_{\substack{(i,j,k) \\ \in \mathbb{Z}^3}} \sum_{\substack{m,n=1 \\ m < n}}^{n_b} \phi(|\mathbf{L}_{ijk} + \mathbf{v}_m - \mathbf{v}_n|) , \quad (5.69)$$

where the lattice vectors  $\mathbf{L}_{ijk}$  are explained in equation (5.2), the basis vectors  $\mathbf{v}_i$  are defined in equation (5.6), and  $\phi(r)$  is the pair potential under consideration.

Taking a closer look at equations (5.69) and (5.68) we can easily understand what has already been stated previously: We recognise, that the density  $\rho$  as well as the *lengths* of the vectors occurring in equation (5.69) are unchanged under reflection of the crystal at a plane that contains the origin or under inversion at the origin, which is positioned at an arbitrary lattice point<sup>14</sup>. Equivalently one can state, that the energy and enthalpy per particle are the same irrespective of the handedness of the used Cartesian coordinate system, as long as the coordinates of all vectors are the same. This symmetry was used in section 5.1, where we could restrict the  $z$ -coordinate of  $\mathbf{c}$  to positive values as a consequence of this symmetry.

We can now aim at the task of minimising the enthalpy per particle, given by equation (5.67), w.r.t. all crystal parameters describing the primitive vectors and the number and positions of the basis particles.

## 5.7 Finding Equilibrium Crystal Structures

During the past decades several strategies have been proposed to find the energetically most favourable particle arrangements of a system. Apart from conventional approaches that rely on intuition, experience, or plausible arguments when selecting candidates for ordered equilibrium structures, there are more sophisticated approaches such as simulated annealing [71–74], basin hopping [75], or meta-dynamics [76–78]. However, all these strategies are affected by different sorts of deficiencies which can significantly reduce their success rates.

In recent years convincing evidence has been given that search strategies based on ideas of genetic algorithms (GAs) are able to provide a significant breakthrough to solve this problem. Generally speaking, GAs are strategies that use key ideas of evolutionary processes, such as survival of the fittest, recombination, or mutation, to find optimal solutions for a problem [22]. The wide spectrum of obviously successful applications in different fields of condensed matter physics unambiguously demonstrates their flexibility, reliability, and efficiency: among these are laser pulse control [79], protein folding [80], or cluster formation [81]. In contrast, attempts to apply GAs in the search for ordered equilibrium structures in condensed matter theory were realized considerably later. While the first

---

<sup>14</sup>Of course, lattice sum and density are also invariant under reflection or inversion at completely arbitrarily positioned planes or points, but by convention the origin is always positioned at a lattice point.

applications probably date back to 1999 [82] their widespread use in hard matter theory was pioneered by Oganov and co-workers [83, 84] only recently, where they have become meanwhile a standard tool: a wide spectrum of successful applications ranging from geophysical to technologically relevant problems give evidence of the power and the flexibility of this approach (for an overview see [83, 84]). In *soft* condensed matter theory the usage of these search strategies is still in its infancy. First applications to find minimum energy configurations of soft systems have, nevertheless, unambiguously documented the power of the algorithm: successful examples are the identification of exotic lattice structures and cluster phases for particular soft systems [23–25], or of complex, ordered arrangements of monolayers of binary dipolar mixtures [26]. Recently, we also successfully applied GAs to hard core systems in 3D [85–87], which will be discussed in part IV. All these investigations mentioned above give evidence that GA-based search strategies have an extremely high success rate.

### 5.7.1 Genetic Algorithm

In this thesis we use the GA pioneered by Dieter Gottwald (described in detail in his PhD thesis [68]), including some improvements from Julia Fornleitner (see also her PhD thesis [88]). We will briefly outline the basic principles of this algorithm, before describing our modifications in more detail.

Each crystal structure is represented by a so called individual  $\mathcal{I}$ , consisting of a sequence of integer numbers [which correspond one-to-one to values of the crystal structure parameters of equation (5.5) and equation (5.8)] encoded in the binary number system, resulting in a sequence of zeros and ones (the “genes”) and representing one candidate structure. This means, that we are working on a *grid* in parameter space, which is the reason why we will need a final refinement for the results proposed by the GA.

Another key feature for GAs is the so called fitness function  $F(\mathcal{I})$ , a value assigned to each individual which is the higher the “better” the individual. Since we want to find the minimum enthalpy configuration for given pressure  $P$ , we used as a fitness function

$$F(\mathcal{I}) = e^{-\frac{h(\mathcal{I})-h(\mathcal{I}_0)}{h(\mathcal{I}_0)}} , \quad (5.70)$$

where  $h(\mathcal{I})$  is the enthalpy per particle of the crystal structure represented by  $\mathcal{I}$ .  $\mathcal{I}_0$  is some reference structure, used to make the exponent both dimensionless and of the order of 1, useful for numerical reasons.

A pool of such (initially randomly generated) individuals is then “evolved” through mutation (random bit-flip at random positions), cross-over (cutting of two individuals, the parents, at the *same* position and putting first and second part from different parents together to build two new individuals), and selection by fitness, for further details concerning these processes cf. [68] or [88]. An optimisation also for the number of basis particles is not included so far, because of difficulties when crossing-over individuals of different lengths and when mutating the bits representing the number of particles. Therefore we have to apply our search strategy to a reasonable range of fixed particle numbers, which

turned out to be the larger the longer the range of the interaction potential (see chapter 9).

Of course the major modification of the GA presented in [68] is to include the MDP derived in section 5.2 into the encoding of the crystal structures. For a given number of basis particles  $n_b$  we have in total  $6 + 3(n_b - 1)$  independent parameters describing the crystal: six of them for the underlying lattice ( $x$ ,  $\varphi$ ,  $\xi$ ,  $\eta$ ,  $\zeta$ , and  $a$ ) and three for the position of each additional basis particle ( $v_{ia}$ ,  $v_{ib}$ , and  $v_{ic}$ , with  $2 \leq i \leq n_b$ ). Instead of  $a$  we use another parameter, which is strongly linked to  $a$  and which is obtained by the following considerations: By dividing inequality (5.66) by  $\sigma$  we obtain [cf. reduced quantities according to equation (2.13a)],

$$1 \leq a^* d_{\min}^* \leq d_{\text{cut}}^* . \quad (5.71)$$

Now further divide the left inequality by  $a^*$  and the right one by  $a^* d_{\text{cut}}^*$ ,

$$\frac{1}{a^*} \leq d_{\min}^* \quad \wedge \quad \frac{d_{\min}^*}{d_{\text{cut}}^*} \leq \frac{1}{a^*} . \quad (5.72)$$

By using  $1/a^*$  instead of  $a^*$  as the sixth parameter, we represent this parameter by an integer number on a grid of equal spacing of  $1/a^*$ -values — resulting in a grid for  $a^*$ , which becomes denser as one approaches the minimum value of  $a^*$ . This provides better convergence of the GA to the global minimum, since usually the equilibrium structure exhibits at least one instance of touching or very closely approaching hard spheres (see again chapter 9), a region of parameter space which is thus sampled with more care on a finer grid by the GA.

Introducing the (integer) precision parameter  $\varphi$ , we demand that the  $6 + 3(n_b - 1)$  integer numbers  $N_i$  are elements of  $\{0, 1, 2, \dots, N_{\max} - 1\}$ , with  $N_{\max} = 2^\varphi$ . The mapping from the  $N_i$  to the crystal parameters works as follows [compare with equation (5.21)]:

$$x = \frac{N_1 + 1}{N_{\max}} , \quad (5.73a)$$

$$\varphi = \arccos\left(\frac{x}{2}\right) + \frac{N_2}{N_{\max} - 1} \left(\frac{\pi}{2} - \arccos\left(\frac{x}{2}\right)\right) , \quad (5.73b)$$

$$\xi = -\frac{x^2}{2} + x^2 \frac{N_3}{N_{\max} - 1} , \quad (5.73c)$$

$$\eta = \eta_{\text{upper}} \frac{N_4}{N_{\max} - 1} , \quad \text{where } \eta_{\text{upper}} = \min\left(\frac{x^2 + \xi - (\xi + 1)x \cos \varphi}{x \sin \varphi}, \frac{x - 2\xi \cos \varphi}{2 \sin \varphi}\right) , \quad (5.73d)$$

(if  $\xi < 0$  then  $N_4 \neq 0$ ),

$$\zeta = \zeta_{\min} + \frac{N_5}{N_{\max} - 1} (\zeta_{\max} - \zeta_{\min}) , \quad \zeta_{\min, \max} \text{ according to eqs. (5.21f), (5.18)} , \quad (5.73e)$$

(if  $\xi = \eta = 0$  then  $N_5 \neq 0$ )

$$v_{jX} : \text{the mapping for the basis particle positions is unchanged compared} \quad (5.73f)$$

to [68]; it uses  $N_i$  with  $i > 6$  (i.e.  $v_{2a} = \frac{N_7}{N_{\max}}$ ,  $v_{2b} = \frac{N_8}{N_{\max}}$ ,  $\dots$ ,  $v_{4a} = \frac{N_{13}}{N_{\max}}$ ,  $\dots$ ),

$$\frac{1}{a^*} = d_{\min}^* (x, \varphi, \xi, \eta, \zeta, \{v_{jX}\}) \left( \frac{1}{d_{\text{cut}}^*} + \frac{N_6}{N_{\max} - 1} \left(1 - \frac{1}{d_{\text{cut}}^*}\right) \right) , \quad (5.73g)$$

(if  $d_{\text{cut}}^* = 1$  then  $N_6 = 0$ ).

The GA then finds the set  $\{N_i\}$  with the lowest enthalpy for given pressure. It converges, unsurprisingly, the faster the smaller the number of grid points, i.e., the smaller the binary precision  $\wp$ . Due to the exponential relation  $N_{\max} = 2^\wp$  the requirement in computational time grows very fast with growing  $\wp$ . Hence we cannot choose  $\wp$  to be arbitrarily large to obtain an exact location of the minimum enthalpy configuration. Therefore we select a reasonable value for  $\wp$  to obtain a good approximation of the minimum with the GA and subsequently apply a final refinement strategy. With this refinement we find the closest minimum of the enthalpy per particle, starting from the optimum structure proposed by the GA. The grid introduced through  $\wp$  then only needs to be fine enough for the GA to be able to bring us close to the global minimum. Usually  $\wp$  lies in the range of 4 – 6, only for structures with one basis particle already  $\wp = 2$  proved sufficient.

### 5.7.2 Powell Algorithm

The final refinement strategy of our choice is the so called Powell algorithm (PA) [89], an efficient method to find the minimum of a function of several variables, which does not rely on the evaluation of derivatives of the function w.r.t. these variables.

The reason why we have to avoid derivatives, as they are used, e.g., in the steepest descent method, is, that we want to investigate the square-shoulder model. For this model the energy per particle is calculated via a step-shaped interaction potential [see equation (2.10)], which means the energy per particle, defined by equation (5.69), is step-shaped, too, in dependence of all the crystal parameters  $(x, \varphi, \xi, \eta, \zeta, \{v_{jX}\}, a^*)$ . Optimisation of the energy per particle hence faces the problem of the derivative w.r.t. all these parameters being (a sum of) Dirac  $\delta$ -functionals and hence mostly zero, pathological for any minimisation using derivatives. Of course, our function to minimise, the enthalpy per particle, also depends on the density in a continuous way; but since the density only depends on the crystal parameters  $x, \varphi, \zeta$ , and  $a^*$  [see equation (5.68)], derivatives into directions of parameter space where these four parameters are constant are still zero<sup>15</sup>.

Therefore we choose the method of Powell described in detail in [90] and provided by [91]. This method selects in a sophisticated way the consecutive directions of minimisation in parameter space. The requirements for the PA are the following:

1. Independent variables in a well-defined parameter space. Since  $x, \varphi, \xi, \eta, \zeta, \{v_{iX}\}$ , and  $a^*$  are not independent variables due to the MDP, we use a mapping similar to

---

<sup>15</sup>For a steepest descent method, that searches the minimum into the direction of the gradient, this would result in an optimisation of just these four parameters.

the equations for the GA parameters, (5.73),

$$x = t_1 , \quad (5.74a)$$

$$\varphi = \arccos\left(\frac{x}{2}\right) + t_2 \left[\frac{\pi}{2} - \arccos\left(\frac{x}{2}\right)\right] , \quad (5.74b)$$

$$\xi = -\frac{x^2}{2} + t_3 x^2 , \quad (5.74c)$$

$$\eta = t_4 \eta_{\text{upper}} , \quad \text{where } \eta_{\text{upper}} = \min\left(\frac{x^2 + \xi - (\xi + 1)x \cos \varphi}{x \sin \varphi}, \frac{x - 2\xi \cos \varphi}{2 \sin \varphi}\right) , \quad (5.74d)$$

$$\zeta = \zeta_{\min} + t_5 (\zeta_{\max} - \zeta_{\min}) , \quad \zeta_{\min, \max} \text{ according to eqs. (5.21f), (5.18)} , \quad (5.74e)$$

$$v_{2a} = t_6 , \quad v_{2b} = t_7 , \quad v_{2c} = t_8 , \quad v_{3a} = t_9 , \quad \dots , \quad (5.74f)$$

$$a^* = [1 + t_{3(n_b+1)} (d_{\text{cut}}^* - 1)] / d_{\min}^*(x, \varphi, \xi, \eta, \zeta, \{v_{jX}\}) , \quad (5.74g)$$

which results in a  $[3(n_b + 1)]$ -dimensional unit cube as parameter space, i.e.,  $\mathbf{t} \equiv (t_1, t_2, \dots, t_{3(n_b+1)}) \in [0, 1]^{3(n_b+1)}$ .  $t_1 = 0$  must of course be excluded, but since the region of *arbitrarily* small  $x$  (i.e.,  $t_1$ ) usually turns out to be penalised with a high value of enthalpy per particle, this point will never be approached anyway.

2. A suitable line-minimisation method, i.e. a method used to find the minimum along a straight line in the multidimensional parameter-space. In principle one *can* take a method that relies on derivatives as a line-minimisation method, but of course this would be of no use in our problem (see discussion above). Our line-minimisation method is therefore based on a golden section search for the (local) minimum. We only had to add a prescription of what to do if the enthalpy per particle is a step-shaped function along the line of consideration in parameter space, where the minimum value is hence established for a whole segment: Take the midpoint of the segment as the point along the line that minimises the enthalpy per particle.

There is an ostensive motivation for this prescription. A constant enthalpy per particle for the square-shoulder model along a line in parameter space originates either from shearing the unit cell while keeping its volume constant, or from a movement of basis particles inside a fixed unit cell (or a combination of the two) — in a way that the number of shoulder overlaps does not change. The endpoints of the segment of equal, minimal enthalpy-values are hence arrangements where the shoulders of two particles touch each other. Of course, we want to find the structure with the highest density for given energy per particle. Therefore it is useful to arrange the basis particles in a way, that allows the unit cell to shrink (at least a bit) without causing any extra shoulder overlaps in subsequent minimisations into directions of parameter space that *change* the volume of the unit cell. This is most likely achieved by using the midpoint of the previously mentioned segment.

3. Boundary conditions. To prevent the line-minimisation from leading out of the unit cube there are various possibilities, the most commonly used are periodic boundary conditions or hard walls. We use the hard wall boundary, implemented as a kind of mirror-boundaries, i.e., when the line-minimisation shoots outside the unit cube, we



mirror the cube about the facet which the line just pierced instead of changing the line-direction according to the hard wall condition.

4. Starting point and direction. The starting point for the PA is of course provided by the GA. The starting directions — note that the PA needs  $3(n_b + 1)$  linearly independent ones — turned out to be most efficient if chosen exactly into the directions of the  $3(n_b + 1)$  variables  $t_i$ , i.e., the direction matrix is set to the unit matrix (or a matrix obtained via an arbitrary permutation of lines in a unit matrix).

### 5.7.3 Cutoffs

If a pair potential is gradually decaying ( $|\phi(x)| > |\phi(y)| \Leftrightarrow x < y$ ) but never attaining exactly the value of 0 (e.g., a Yukawa potential), a cutoff distance has to be introduced, above which the pair interaction is set to zero. We define the cutoff distance  $r_{\text{cut}}$  in dependence of a parameter  $\delta$  via

$$(1 - \delta) \int_{\sigma}^{\infty} d^3r \phi(r) = \int_{\sigma}^{r_{\text{cut}}} d^3r \phi(r), \quad (5.75)$$

similar to the definition in [68], with the alteration of the lower integration limit ( $\sigma$  instead of 0), to account for the hard core in our models. This definition guarantees, that the neglected contribution to energy is less than  $\delta$  times the total energy.

### 5.7.4 A Systematic Search Procedure for the Square-Shoulder Interaction

In this section we explain an efficient way to find all equilibrium crystal structures for particles interacting via the square-shoulder interaction [equation (2.10)] at  $T = 0$ .

For any energy per particle  $e$ , which just counts the mean number of shoulder overlaps per particle, there exists a configuration having the largest possible density  $\rho$  for this energy. This means if we minimise the enthalpy per particle  $h$  for different  $P$ , we can only obtain a certain number of pairs  $(e_i, \rho_i)$  which have to satisfy  $e_i \neq e_j \Leftrightarrow \rho_i \neq \rho_j$ .

Each of these pairs represents a straight line in the  $h$ - $P$ -diagram, namely  $h_i = e_i + P/\rho_i$ . Since for any  $P$  we only need the candidate with the smallest  $h_i$ , we even obtain

$$e_i > e_j \quad \Longrightarrow \quad \rho_i > \rho_j. \quad (5.76)$$

It is also obvious, that with increasing pressure, also density and energy per particle increase, hence:

$e$  versus  $P$  and  $\rho$  versus  $P$  are monotonously increasing, step shaped curves, where the discontinuities in these curves occur at exactly the same pressure values. The  $h$ - $P$ -curve is therefore the lower envelope of a sequence of intersecting straight lines, which intersect at the same pressure values where the energy/density curves change discontinuously.

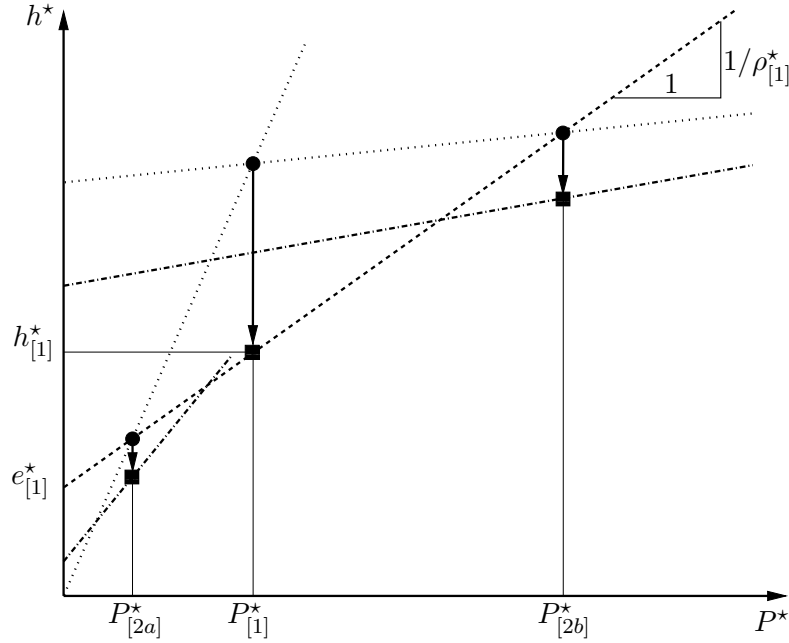


Figure 5.30: Schematic representation of our search strategy to identify MECs in the  $(h^*, P^*)$ -plane. The dotted lines represent  $h^*$  as a function of  $P^*$  for the limiting low and high pressure configurations: The vertical arrows represent GA-runs that identify, starting from an initial guess (dot), an energetically more favourable MEC (square). For details see text.

We introduce a recursive algorithm to find all of these pairs  $(e_i, \rho_i)$ , corresponding to the equilibrium configurations, also called minimum enthalpy configurations (MECs).

First we locate the two configurations with the lowest and highest energy- and density-values, respectively, being the equilibrium structures for very low or very high pressures. These are both close-packed structures (see section 5.5): one with nearest neighbour distance  $\lambda$  having hence  $e_{\min} = 0$  and  $\rho_{\min} = \sqrt{2}/\lambda^3$ , and the other one exhibiting touching hard cores, i.e.,  $\rho_{\max} = \sqrt{2}/\sigma^3$ . Calculating the corresponding  $e_{\max}$ , which means finding the close-packed structure with the lowest energy, is non-trivial but possible, see section 9.1. We therefore assume now that both pairs,  $(e_{\min}, \rho_{\min})$  and  $(e_{\max}, \rho_{\max})$ , are known. The corresponding  $h$ -lines are the dotted lines in figure 5.30.

We calculate the pressure  $P_{[1]}$  at the intersection point of the two corresponding  $h$ -lines and start a sufficient number of GA-runs with different number of basis particles and subsequent PA for this pressure. In general this will yield a different equilibrium structure with  $e_{[1]}$ - and  $\rho_{[1]}$ -values between the two limiting cases. The corresponding  $h$ -line is then intersected with the other two lines, giving two new intersection points at the pressure values  $P_{[2a]}$  and  $P_{[2b]}$  (and eliminating the old one).

For each of these pressure values we again look for the equilibrium structure, and iterating this procedure we cut off kinks from the  $h$ -curve thereby generating two new

ones. Of course, at some point this iteration will stop, when for all existing intersection pressures no better configuration can be found.

The advantages of this algorithm are:

- It is very efficient, since we keep the number of GA searches as low as possible.
- There is no risk to miss an equilibrium structure, which can happen when working on a finite  $P$ -grid.
- We avoid a GA search for pressure values with competing structures<sup>16</sup>, where the GA tends to fail. In fact, when we find a lower enthalpy at a given intersection pressure value, this happens at a pressure where the difference in enthalpy to the (two) competing structures is maximal.

### 5.7.5 Metric Crystal Scaling

The method described in section 5.7.4 is only applicable to the SSM. Energy and density of models exhibiting other pair potentials are in general continuous curves. It is however possible to develop a similar method for finding the whole  $h$ - $P$ -curve for pair potentials that exhibit a hard core and a repulsive potential tail  $\phi_t(r)$ , of which the first and second derivatives exist and satisfy

$$\phi_t'(r) < 0 \quad \wedge \quad \phi_t''(r) > 0 \quad (5.77)$$

for *all*  $r > 0$  [e.g. the hard core Yukawa interaction given by equation (2.3) with  $\epsilon_Y > 0$ ]. The key idea is, to consider equivalence classes of configurations, that enclose all configurations with the same shape through metric scaling [92], a concept we also present in [87]. Let us explain what we mean by “same shape”.

We call a crystal configuration, i.e. a set of the unit cell and basis vectors,  $\mathcal{K}$ . All other crystals in the equivalence class  $[\mathcal{K}]$  of crystals with the same shape are simply obtained by scaling the whole crystal  $\mathcal{K}$ , i.e., multiplying all vectors with the same scaling factor  $s$ ,

$$[\mathcal{K}] = \{s \cdot \mathcal{K} | 0 < s < \infty\} . \quad (5.78)$$

We will show, that for given pressure there is exactly one configuration out of this equivalence class that has the lowest enthalpy of its class. We will denote this configuration by  $\tilde{\mathcal{K}}([K], P)$ .

**Proof:** Let  $\mathcal{K}_0$  and  $P$  be given. The question is, how to find the scaling factor  $s$  for which the enthalpy takes on its minimum. To answer this we construct the function

$$h(\mathcal{K}_0, P, s) = e(\mathcal{K}_0, s) + \frac{P}{\rho(\mathcal{K}_0, s)} , \quad (5.79)$$

---

<sup>16</sup>Except at intersection pressures where no better structure is found, but the outcome of the GA search there does neither enter the list of minimum enthalpy configurations nor has any influence on subsequent calculations.

where  $e(\mathcal{K}_0, s)$  is the energy per particle and  $\rho(\mathcal{K}_0, s)$  is the particle density for the configuration  $\mathcal{K}_0$  scaled with the factor of  $s$ . Clearly,  $\rho(\mathcal{K}_0, 1) \equiv \rho_0$  is the density and  $e(\mathcal{K}_0, 1) \equiv e_0$  is the energy per particle of the configuration  $\mathcal{K}_0$ . Thus, the density term is simply given by

$$\rho(\mathcal{K}_0, s) = \rho_0/s^3 . \quad (5.80)$$

Of course the parameter  $s$  cannot adopt all positive real numbers. There exists a lower threshold  $s_{\text{low}}$  where the shortest distance in the crystal becomes equal to the hard core diameter, and an upper threshold  $s_{\text{high}}$  where the shortest distance is equal to the cutoff,  $r_{\text{cut}}$ . But for the following analytic calculations we consider a pair interaction that solely consists of the tail interaction, i.e.  $\phi(r) = \phi_t(r)$ , for *all* values of  $r$ . We will take the thresholds into account later on.

The energy per particle for this interaction is obtained via the lattice sum of equation (5.69) modified with the scaling parameter  $s$  by

$$e(\mathcal{K}_0, s) = \frac{1}{2} \sum_{\substack{(i,j,k) \in \\ \mathbb{Z}^3 \setminus (0,0,0)}} \phi_t(s |\mathbf{L}_{ijk}|) + \frac{1}{n_b} \sum_{\substack{(i,j,k) \\ \in \mathbb{Z}^3}} \sum_{\substack{m,n=1 \\ m < n}}^{n_b} \phi_t(s |\mathbf{L}_{ijk} + \mathbf{v}_m - \mathbf{v}_n|) , \quad (5.81)$$

where  $\mathbf{L}$  and  $\mathbf{v}$  are the lattice and basis vectors of  $\mathcal{K}_0$ , respectively. Of this energy function we can take both the first and second derivatives w.r.t.  $s$ ,

$$\frac{\partial e(\mathcal{K}_0, s)}{\partial s} = \frac{1}{2} \sum_{\substack{(i,j,k) \in \\ \mathbb{Z}^3 \setminus (0,0,0)}} \phi_t'(s |\mathbf{L}_{ijk}|) |\mathbf{L}_{ijk}| + \frac{1}{n_b} \sum_{\substack{(i,j,k) \\ \in \mathbb{Z}^3}} \sum_{\substack{m,n=1 \\ m < n}}^{n_b} \phi_t'(s |\mathbf{L}_{ijk} + \mathbf{v}_m - \mathbf{v}_n|) |\mathbf{L}_{ijk} + \mathbf{v}_m - \mathbf{v}_n| , \quad (5.82a)$$

$$\frac{\partial^2 e(\mathcal{K}_0, s)}{\partial s^2} = \frac{1}{2} \sum_{\substack{(i,j,k) \in \\ \mathbb{Z}^3 \setminus (0,0,0)}} \phi_t''(s |\mathbf{L}_{ijk}|) |\mathbf{L}_{ijk}|^2 + \frac{1}{n_b} \sum_{\substack{(i,j,k) \\ \in \mathbb{Z}^3}} \sum_{\substack{m,n=1 \\ m < n}}^{n_b} \phi_t''(s |\mathbf{L}_{ijk} + \mathbf{v}_m - \mathbf{v}_n|) |\mathbf{L}_{ijk} + \mathbf{v}_m - \mathbf{v}_n|^2 . \quad (5.82b)$$

Considering equation (5.77) we recognise that the addends in both equations (5.82) always have the same sign, resulting in

$$\frac{\partial e(\mathcal{K}_0, s)}{\partial s} < 0 \quad \wedge \quad \frac{\partial^2 e(\mathcal{K}_0, s)}{\partial s^2} > 0 \quad \forall s > 0 . \quad (5.83)$$

From the first derivative being always smaller than 0 we obtain, that  $e(\mathcal{K}_0, s)$  is strictly monotonously decreasing. Since we always have  $\phi(r) \xrightarrow{r \rightarrow \infty} 0$  also  $e(\mathcal{K}_0, s) \xrightarrow{s \rightarrow \infty} 0$ .

The pressure term of equation (5.79) on the other hand is zero for vanishing  $s$  and tends to infinity with  $s \rightarrow \infty$ . Hence we know for the enthalpy per particle  $h(\mathcal{K}_0, P, s) = e(\mathcal{K}_0, s) + Ps^3/\rho_0$

$$h(\mathcal{K}_0, P, s) \xrightarrow{s \rightarrow \infty} \infty , \quad (5.84)$$

and therefore the function  $h(\mathcal{K}_0, P, s)$  of  $s$  has to have at least one minimum. With help of equation (5.83) the second derivative of  $h$  w.r.t.  $s$  is

$$\frac{\partial^2 h(\mathcal{K}_0, P, s)}{\partial s^2} = \frac{\partial^2 e(\mathcal{K}_0, s)}{\partial s^2} + \frac{6Ps}{\rho_0} > 0 \quad \forall s > 0, \quad (5.85)$$

which means that there is exactly one minimum. To find this minimum we have to locate the value of  $s$ ,  $s_{\min}$ , where the first derivative vanishes,

$$\frac{\partial g(\mathcal{K}_0, P, s)}{\partial s} = \frac{\partial e(\mathcal{K}_0, s)}{\partial s} + \frac{3Ps^2}{\rho_0} \stackrel{!}{=} 0 \quad \Rightarrow s_{\min}. \quad (5.86)$$

It is obvious, that through setting

$$s_{\text{eq}} = \min(\max(s_{\min}, s_{\text{low}}), s_{\text{high}}) \quad (5.87)$$

we obtain the enthalpy per particle,  $h(\mathcal{K}_0, P, s_{\text{eq}})$ , of the equilibrium structure at pressure  $P$  with the hard core and cutoff constraints included, together with the corresponding configuration  $\tilde{\mathcal{K}}([\mathcal{K}_0], P)$ .

□

The aim is now, to find all occurring  $[\mathcal{K}_0]$  for the whole pressure regime.

Similar to the case of the square–shoulder potential in the previous section we begin considering close–packed structures, for simplicity we start with an fcc crystal. For very low pressures this is the simplest one (least number of basis particles) having minimum enthalpy, with the nearest neighbour distance being equal to the cutoff, sloppily written as  $\text{fcc}_{\text{cut}}$ . Of course this can be an unphysical result, e.g. for a Coulomb interaction which is known to freeze in a bcc crystal, due to the numerical error when introducing a cutoff to an infinitely ranged interaction potential. Nevertheless, within the chosen numerical accuracy,  $\text{fcc}_{\text{cut}}$  will always be the outcome for small enough pressure values.

Using the method described above we can now draw  $h([\text{fcc}], P)$  and locate the pressure threshold  $P_{\text{hc}}$  above which  $\tilde{\mathcal{K}}([\text{fcc}], P \geq P_{\text{hc}}) = \text{fcc}_{\sigma}$ , the close–packed fcc crystal where the hard spheres touch each other. At this pressure value we launch the first GA with subsequent PA, to find out whether fcc is really the optimum stacking for the close–packed spheres, for the Yukawa interaction it turns out to be the one (see chapter 10).

It is not completely clear, where to start looking for structures different than fcc, usually some random points distributed over the pressure regime from 0 to  $P_{\text{hc}}$  will yield a new minimum enthalpy structure  $\mathcal{K}_1$  at some point. Then we can calculate the intersection points of the curves  $h([\text{fcc}], P)$  and  $h([\mathcal{K}_1], P)$  (blue dots in figure 5.31), and we can apply the line–intersection–search like in the simpler square–shoulder case, now with curved lines. Still it is advisable to launch some additional runs also at pressure values not close to any intersection point, since it is possible now, that a curve just cuts another one twice, with no previous intersection point in between. This situation is clarified in figure 5.31: It is

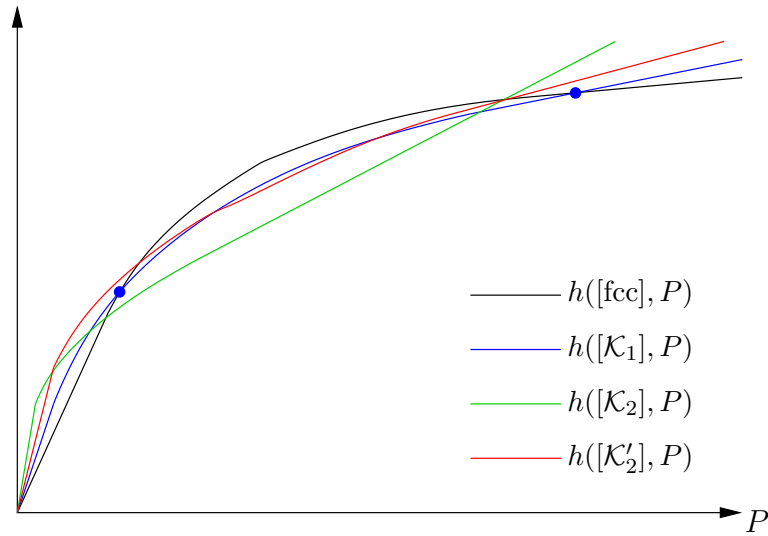


Figure 5.31: Sketch of possible enthalpy curves for configurations of four different equivalence classes as indicated in the legend. The intersection points of  $h([fcc], P)$  and  $h([K_1], P)$  are marked with blue dots, for details see text.

possible, after applying the GA based search strategy at the pressure values corresponding to the two intersection points marked as blue dots, that we find a better configuration class,  $[K_2]$ , whose enthalpy curve (green) cuts off one intersection point (in our example the one exhibiting lower pressure). However, it is also possible, that neither of the two intersection points lead to further MECs. Still, there can exist a configuration class,  $[K'_2]$ , which results in the minimum enthalpy curve at some intermediate pressure range, *between* the pressure values of the two previously calculated intersection points (red enthalpy curve).

The presented search strategy works perfectly well as long as the occurring crystals have cubic symmetry, since the cubic lattices only have one free parameter, the edge length  $\tilde{a}$  of the cubic unit cell. If however lower symmetry lattices occur, the method of an overall scaling factor will most probably not suffice to generate the entire enthalpy–pressure–curve. More parameters than just  $s$  have to be considered, leading to a higher dimensional minimisation problem.

For the case of a hard core Yukawa interaction, which we will investigate in more detail, there appears only one relevant non-cubic Bravais lattice, the centred tetragonal one, as will be shown in chapter 10. Therefore we extend the concept of metric scaling to this kind of lattice. A detailed explanation and visualisation of the ct lattice is given in section 5.3 (figure 5.19), where the identification of Bravais lattices was discussed. The ct lattice has two free parameters, e.g. the two different edge lengths  $\tilde{a}$  and  $\tilde{c}$ . Another possibility of parameters would be to use just one of the edge lengths (similar to a general scaling factor) and the ratio between them. We utilise even another parametrisation, using the general scaling factor  $s$  and a parameter  $f$ , describing the different possible ct lattices in the following way.

Let  $(s, f) = (1, 1)$  correspond to a bcc lattice (which is the special case of ct lattice)

where the nearest neighbours touch each other at the hard cores,  $bcc_\sigma$ . The conventional ct lattice parameters are in this case  $\tilde{a} = \tilde{c} = 2\sigma/\sqrt{3}$ . Keeping  $s = 1$  constant, we want to change the ct lattice via  $f$  in a way, that keeps the nearest neighbour distance constant at  $\sigma$ . If  $f$  is close enough<sup>17</sup> to 1, this is equivalent to the condition, that the triagonal of the ct unit cell is constant,  $2\sigma$ . As a first step we assume  $\tilde{c}$  to vary linearly with  $f$ , resulting in

$$\tilde{c}(f) = f \frac{2\sigma}{\sqrt{3}}, \quad \tilde{a}(f) = \sqrt{3 - f^2} \sqrt{\frac{2}{3}} \sigma. \quad (5.88)$$

The variation of  $f$  from 1 to  $\sqrt{3/2}$  covers a so-called Bain transformation [93] from bcc ( $f = 1$ ) to fcc ( $f = \sqrt{3/2}$ ).

A Bain transformation is a displacive phase transformation, which is characterised by a cooperative, homogeneous movement of the particles in a solid crystal. This movement can be described through the so called Bain strains, combined in a strain matrix that transforms a set of straight lines into a new set of straight lines [93, 94]. Among the most popular and extensively studied example of a phase transition describable through a Bain transformation is the  $bcc \leftrightarrow fcc$  transition [92, 95, 96], which is, for instance, found in iron [97–100]. Recently also computer simulations for iron [101] based on a tight-binding potential were able to reproduce this kind of phase transition. The consideration of Bain transformations in soft matter is a comparatively young issue, recent experimental observations of  $bcc \leftrightarrow fcc$  transitions of sphere-forming block copolymer/homopolymer blends were published in [102]. Another system that is able to solidify both in stable fcc as well as bcc phases, and represents therefore a suitable candidate for the investigation of such a transition, are charged colloids interacting via Yukawa potentials [103–105]. Therefore we will investigate the hard core Yukawa model in chapter 10, in an effort to find new stable crystal structures.

We further quantify our choice for the parametrisation of all ct lattices, comprising the Bain transformation from fcc to bcc. To obtain ct lattices with all possible ratios of  $\tilde{a}/\tilde{c}$  we also need to use values of  $f$  outside the interval  $[1, \sqrt{3/2}]$ . For  $f > \sqrt{3/2}$ ,  $\tilde{a}(f)$  becomes smaller than  $\sigma$ , which is not allowed. Since  $\tilde{a}$  thus represents the nearest neighbour distance in this  $f$ -regime, we restrict  $\tilde{a}$  to its minimum value of  $\sigma$  for  $f > \sqrt{3/2}$ , while  $\tilde{c}$  can be further increased linearly for large  $f$ , leading to arbitrarily small values of  $\tilde{a}/\tilde{c}$ . At  $f = \sqrt{3/2}$  a similar situation occurs for  $\tilde{c}$ , smaller  $f$ -values would result in  $\tilde{c} < \sigma$  according to equation (5.88). Analogously we demand  $\tilde{c} = \sigma$  for  $f < \sqrt{3/2}$ . But, to really cover all lattices (i.e. all arbitrarily large  $\tilde{a}/\tilde{c}$ -values) within  $f > 0$ , we also modify the formula for  $\tilde{a}$  to  $3\sigma/(2\sqrt{2}f)$  in this  $f$ -range. In summary we obtain, together with the overall scaling factor  $s$ ,

$$\tilde{c}(f, s) = s\sigma \begin{cases} 1, & 0 < f < \frac{\sqrt{3}}{2} \\ f \frac{2}{\sqrt{3}}, & f \geq \frac{\sqrt{3}}{2} \end{cases} \quad (5.89a)$$

---

<sup>17</sup>It will immediately become clear what we mean by “close enough”.

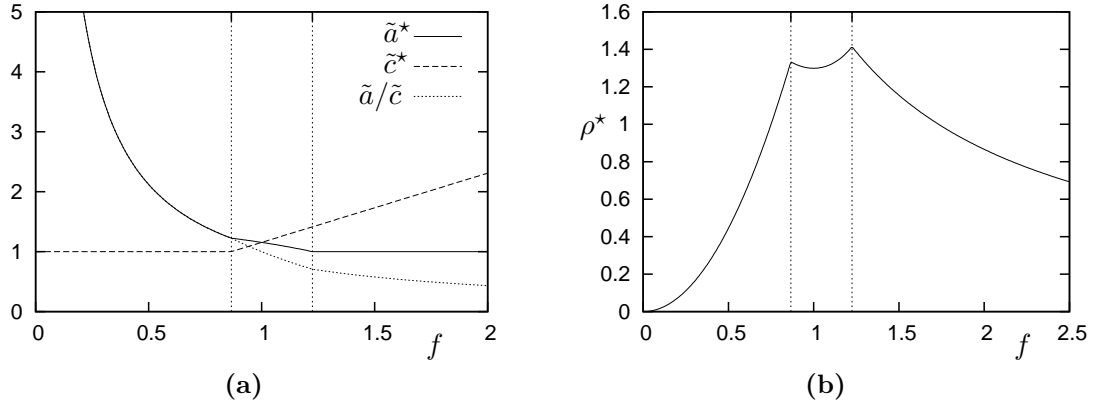


Figure 5.32: In (a) the functions of equations (5.89a) and (5.89b) for  $s = 1$  are visualised as indicated in the legend, together with the ratio  $\tilde{a}/\tilde{c}$  in dependence of the Bain parameter  $f$ . (b) shows the number density  $\rho$  (also for  $s = 1$ ) versus  $f$ . The vertical dotted lines indicate the values  $f = \sqrt{3}/2$  and  $f = \sqrt{3/2}$ .

and

$$\tilde{a}(f, s) = s\sigma \begin{cases} \frac{3}{2\sqrt{2}} \frac{1}{f}, & 0 < f < \frac{\sqrt{3}}{2} \\ \sqrt{3-f^2} \sqrt{\frac{2}{3}}, & \frac{\sqrt{3}}{2} \leq f \leq \sqrt{\frac{3}{2}} \\ 1, & f > \sqrt{\frac{3}{2}} \end{cases} . \quad (5.89b)$$

Both,  $\tilde{a}$  and  $\tilde{c}$ , are monotonous functions of  $f$ ,  $\tilde{a}$  is decreasing and  $\tilde{c}$  is increasing with  $f$ .  $\tilde{a}/\tilde{c}$  is strictly monotonously decreasing with  $f$  and covers all values from  $\infty$  to 0, all three functions are visualised in figure 5.32(a). In figure 5.32(b) we plot the number density in dependence of  $f$ , given by

$$\rho(f, s) = \frac{s}{\sigma^3} \begin{cases} \frac{16}{9} f^2, & 0 < f < \frac{\sqrt{3}}{2} \\ \frac{3\sqrt{3}}{2f(3-f^2)}, & \frac{\sqrt{3}}{2} \leq f \leq \sqrt{\frac{3}{2}} \\ \frac{\sqrt{3}}{f}, & f > \sqrt{\frac{3}{2}} \end{cases} . \quad (5.90)$$

It exhibits a maximum at  $f = \sqrt{3/2}$ , the fcc structure, and a local minimum at  $f = 1$ , corresponding to the bcc structure.

The reason why we introduced this special kind of Bain transformation parameter will become clear in the discussion of the hard core Yukawa model in chapter 10, where we will minimise the enthalpy per particle w.r.t. the two ct structure parameters  $s$  and  $f$ .

## 5.8 The Continuum Theory

Following the ideas of Glaser *et al.* [27] for 2D systems, we have developed a mean-field type theory where we assume that the solid structure is built up by aggregates in the shape of



spherical clusters, cylindrical columns, planar lamellae, or a distribution with “aggregation” of the particles over the whole space, corresponding to a compact phase. Within the aggregate, particles are distributed with a constant effective density,  $\rho_{\text{eff}}$ , interpretable as a kind of probability density for the discrete particles.

The next, quite drastic step is now, not just to consider a probability density for the discrete particles, but a *continuum* of matter (with the same constant density  $\rho_{\text{eff}}$ ) that assembles itself into shapes according to the aggregation of the formerly considered particles. The task to be performed is to calculate the analogon to the lattice sum of equation (5.69) in this continuum theory (CT).

Via the shape of the aggregates we can immediately define a position dependent density for the continuum matter, which we write as

$$\hat{\rho}(\mathbf{r}) = \rho_{\text{eff}}\theta_C(\mathbf{r}) , \quad (5.91)$$

where  $\theta_C(\mathbf{r})$  is assigned the value of 1 if  $\mathbf{r}$  lies within an aggregate and 0 otherwise.  $\theta_C(\mathbf{r})$  shall satisfy the following condition, which mathematically connects the particle picture with the continuum one: Consider an arbitrary, simply connected region  $\mathcal{R}$ . The number of particles inside this region is trivially given by

$$N = \sum_{\nu_i \in \mathcal{R}} 1, \quad (5.92)$$

where the sum is taken over all particles inside the region, positioned at  $\nu_i$  and indexed with  $i$ . The analogon in the CT is of course

$$N' = \int_{\mathcal{R}} \hat{\rho}(\mathbf{r}) d^3r , \quad (5.93)$$

and assuming that the continuum matter density  $\hat{\rho}(\mathbf{r})$  is a valid approximation for the arrangement of the real particles positioned at  $\nu_i$  it follows

$$N \simeq N' . \quad (5.94)$$

The reason why we use a “ $\simeq$ ”-sign instead of an exact “=”-sign is, that it is impossible to construct a continuum matter distribution  $\hat{\rho}(\mathbf{r})$  that fulfils  $N = N'$  for arbitrary regions  $\mathcal{R}$ . This is best explained via considering  $\mathcal{R}$  to be a sphere of radius  $R$  centred at an arbitrary point. The number of particles  $N$  inside  $\mathcal{R}$  as a function of  $R$  is obviously a (monotonously increasing) *step*-function, while  $N'$  is always a (monotonously increasing) *continuous* function of  $R$ .

Now we consider a particular particle, positioned at  $\mu$ . The energy of this particle is

$$e_{\mu} = \frac{1}{2} \sum_{\nu_i \neq \mu} \phi(|\nu_i - \mu|) . \quad (5.95)$$

Formally we can also write

$$e_{\boldsymbol{\mu}} = \frac{1}{2} \sum_{\forall \boldsymbol{\nu}_i} \phi(|\boldsymbol{\nu}_i - \boldsymbol{\mu}|) - \underbrace{\frac{1}{2} \phi(0)}_{e_{\text{self}}^{\text{disc}}}, \quad (5.96)$$

where we subtract the so called self-energy ( $e_{\text{self}}^{\text{disc}}$ ) in the discrete particle model from the sum over all particles. If  $\phi(r)$  diverges at  $r \rightarrow 0$  one either has to use equation (5.95) or find a suitable method to “renormalise” the energy according to equation (5.96). Switching to the CT, we need, analogously to the energy assigned to a particle, the *energy assigned to a continuum matter point*. Analogous to the case of particle number, we substitute the sum over particles by an integral over space of the continuum matter density  $\hat{\rho}(\mathbf{r})$ :

$$e_c(\boldsymbol{\mu}) = \frac{1}{2} \int_{\mathbb{R}^3} \hat{\rho}(\mathbf{r}) \phi(|\mathbf{r} - \boldsymbol{\mu}|) d^3r - e_{\text{self}}. \quad (5.97)$$

What remains to be determined is the self-energy term ( $e_{\text{self}}$ ), a problem that strongly depends on the particular interaction potential  $\phi(r)$ . For the moment we assume that we are able to determine this quantity, we will resume this task when applying the theory to the interaction of the square-shoulder model in section 9.3.1.

We are only one step away from the analogon to the average energy per particle in the CT. Consider equation (5.69), which is nothing else but a detailed formula for the calculation of this average energy for crystals. It is the specialisation to crystal structures of the more fundamental formula for the average energy per particle of an assembly of particles

$$e = \frac{1}{M} \sum_{\boldsymbol{\mu}_j \in \mathcal{M}} e_{\boldsymbol{\mu}_j}, \quad (5.98)$$

where  $e_{\boldsymbol{\mu}_j}$  is the energy of the particle positioned at  $\boldsymbol{\mu}_j$  [given by equation (5.95)].  $\mathcal{M}$  can be e.g. the set of all particle positions,  $M = |\mathcal{M}| = \sum_{\boldsymbol{\mu}_i \in \mathcal{M}} 1$  is the cardinal number of  $\mathcal{M}$ . Clearly, in particular for crystal structures, we can drop many elements from  $\mathcal{M}$  that lead to the same energy contributions as other elements, thus reducing equation (5.98) to equation (5.69). In other words,  $\mathcal{M}$  is the set of particle positions that result in different particle energies, points in  $\mathcal{M}$  are hence called *qualitatively* different.

The construction of the average energy in the CT also foos on a similar set  $\mathcal{N}$  of qualitatively different points in the continuum matter. We replace, in the same way like in the step from equation (5.92) to equation (5.93), the sums in equation (5.98) by integrals and define

$$e_c = \frac{1}{\int_{\mathcal{N}} \hat{\rho}(\mathbf{r}) d^n r} \int_{\mathcal{N}} \hat{\rho}(\mathbf{r}) e_c(\mathbf{r}) d^n r, \quad (5.99)$$

where  $n$  is the dimension of  $\mathcal{N}$ . This formula can be interpreted as the total energy of the continuum matter confined to  $\mathcal{N}$  divided by the number of particles in  $\mathcal{N}$ . In other words, the average energy per particle approximated by the CT.

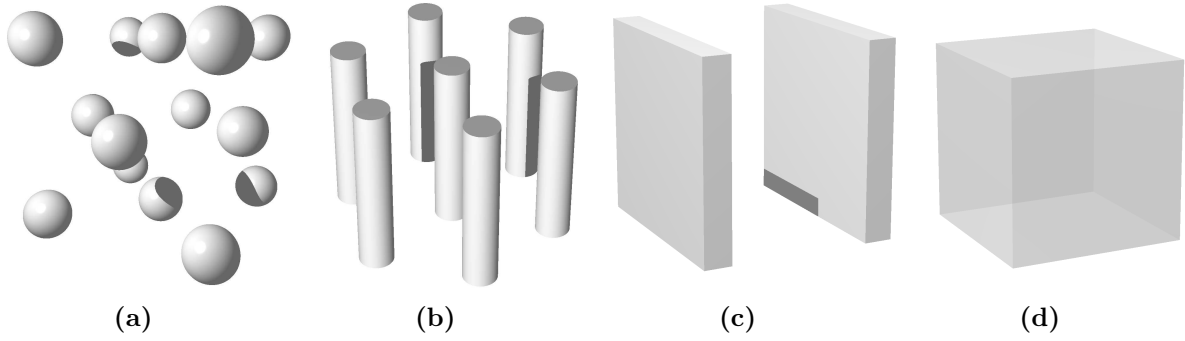


Figure 5.33: Considered aggregate shapes formed by the continuum matter: spherical clusters (a), cylindrical columns (b), planar lamellae (c), and a homogeneous distribution (d).

There is one simplification possible for equation (5.99):  $\mathcal{N}$  only contains points where the continuum matter is present, i.e.,  $\hat{\rho}(\mathbf{r}) = \rho_{\text{eff}} \forall \mathbf{r} \in \mathcal{N}$ . The constant factor  $\rho_{\text{eff}}$  can be pulled out of both integrals in equation (5.99) and cancelled, hence

$$e_c = \frac{1}{\int_{\mathcal{N}} d^n r} \int_{\mathcal{N}} e_c(\mathbf{r}) d^n r . \quad (5.100)$$

At last we have to construct the CT quantity which is equivalent to the enthalpy per particle given in equation (5.67). Therefore we need, besides the now calculated analogon for the energy per particle, the average density  $\rho_c$  in the CT, to calculate the pressure contribution. From equation (5.91) it is obvious, that  $\rho_c$  is equal to  $\rho_{\text{eff}}$  times the fraction of space filled by the continuum matter. We finally arrive at the CT approximation for the average enthalpy per particle,

$$h_c = e_c + \frac{P}{\rho_c} . \quad (5.101)$$

To be able to apply this CT to particular model systems, we have to restrict ourselves to special, simple shapes of the aggregates.

### Special Aggregate Shapes

Let us now discuss the shape and cardinality of  $\mathcal{N}$  for the four possible aggregate shapes of clusters, columns, lamellae, and compact phases, visualised in figure 5.33 and motivated by the results of the GA based search method for the square-shoulder model (see chapter 9).

- **Clusters**

The approximation for cluster shaped aggregates in the CT is to consider perfect spheres of matter, which are arranged on a crystal lattice. If we further restrict the arrangement to be one of the Bravais lattices and all spheres to have the same radius, we recognise that  $\mathcal{N}$  has to be contained in one of the equal spheres. The reason for

this is, that each arbitrary point  $\mathbf{r}$  inside a sphere is assigned the same energy as any other point  $\mathbf{r} + \mathbf{L}_{ijk}$ , where  $\mathbf{L}_{ijk}$  is an arbitrary lattice vector [see equation (5.2)].

The symmetry of the lattice reduces the region of  $\mathcal{N}$  even more. E.g. even for the lowest symmetry, a triclinic lattice, we always have inversion symmetry, reducing  $\mathcal{N}$  to a hemisphere. Higher symmetries lead to further reduction by planes through the centre point of the sphere, cutting it into equivalent pieces. Note however, that the average energy formula (5.100) still holds, if one integrates over a superset of  $\mathcal{N}$ .

Therefore, to keep equation (5.100) simple, we take the whole sphere corresponding to a cluster aggregate as integration region, which of course has a dimension  $n$  of 3 in this case.

For spheres of volume  $V_s$  placed on the lattice points of a Bravais lattice the ratio of filled to total space is the same as the one of  $V_s$  to the volume of a primitive unit cell  $V_c$ , resulting in the average continuum matter density of

$$\rho_c = \rho_{\text{eff}} \frac{V_s}{V_c} . \quad (5.102)$$

- **Columns**

A phase of columnar shaped aggregates is approximated by the continuum matter being distributed over infinitely long, parallel cylinders of equal radius. Since an *arbitrary* displacement of such a cylinder along its axis is a symmetry transformation, and hence does not change energy nor density, the only relevant information about the arrangement of the cylinders has to be given w.r.t. the two independent directions perpendicular to the parallel cylinder axes. We arrange the cylinders on a 2D Bravais lattice of which the basis vectors are perpendicular to the cylinder axes and recognise, that  $\mathcal{N}$  is contained in the 2D cross-section of one cylinder. The symmetries of the corresponding 2D Lattice have the same influence as in the cluster case,  $\mathcal{N}$  gets reduced from the circular cross-section to a sector of the disk. But, similar to the cluster case, we take the whole cylinder cross-section as integration regime  $\mathcal{N}$ . Clearly, in this case  $n = 2$ .

Parallel cylinders arranged on a 2D Bravais lattice fill space with the ratio of the (circular) cross section  $A_c$  of one cylinder to the area of a 2D primitive unit cell  $A_p$  of the lattice, leading to

$$\rho_c = \rho_{\text{eff}} \frac{A_c}{A_p} . \quad (5.103)$$

- **Lamellae**

Lamellar arrangements of the aggregate are treated as infinitely extended parallel planes of equal thickness in the CT. Because of the twofold continuous symmetry for plane shifts, the only relevant information left for their arrangement is the distance between them. Putting them on a “one-dimensional Bravais lattice” just means, that they all have equal distance to their neighbouring planes. Analogous to the previous

item, symmetry reduces  $\mathcal{N}$  to (half) a segment, obtained by the intersection of a straight line perpendicular to the planes and one of these planes, which also means  $n = 1$ . For convenience we will take the whole segment as integration region.

The average density for parallel planes of equal thickness  $D$  stacked with nearest-plane distance  $L$  (see also figure 9.8) is given by

$$\rho_C = \rho_{\text{eff}} \frac{D}{L} . \quad (5.104)$$

- **Compact phases**

As mentioned at the beginning of this section, a compact phase means, that the particles “aggregate” over the whole space, not forming any specially shaped aggregates. In CT this corresponds to  $\hat{\rho}(\mathbf{r}) = \rho_C = \rho_{\text{eff}} \forall \mathbf{r}$ , i.e., a completely homogeneous phase. Obviously, all points then get assigned the same energy, resulting in  $\mathcal{N}$  to contain only one single point. The zero-dimensional integrals reduce to a simple sum over this single point, which means  $e_C = e_C(\mathbf{r})$  with  $\mathbf{r}$  being completely arbitrary.

These four aggregate shapes will be considered in chapter 9, dedicated to the investigation of the square-shoulder model.



## Part III

# Criticality of Hard Core Systems with Coulomb, Yukawa, and Kac Interactions





# Chapter 6

## Charged Yukawa Model

In this chapter we will discuss the results obtained through the mSCOZA (see chapter 4) for the charged Yukawa model, introduced in section 2.4. Since there exist extensive investigations of this system using MSA (see section 3.3.1) and Monte Carlo simulations (MC) in [34], we study the system with the same parameters used there as a first step.

Therefore we restrict the inverse screening parameter to the value of  $\alpha^* = 1.8$ , a value for which the single Yukawa interaction gives results for the phase diagram comparable to the Lennard–Jones fluid [106]. The parameter  $q^*$ , controlling the relative strength of the two competing tails [see equation (2.13m)], is given the values 0, 2, 5, 10, 15, 100, and 300.

We use a  $\rho$ -grid of 100.000 points between  $\rho^* = 0$  and  $\rho_{\max}^* = 1$  and extended (also called quadruple) precision floating point variables, i.e., 16 bytes of storage are used for each real variable. This would give approximately  $34 [\simeq \log_{10}(2^{113})]$  significant digits, but due to the problem with the inhomogeneity term discussed in section 4.3.2 we can only guarantee for the leading 20 digits. We work in Yukawa–reduced units, i.e.,  $\sigma$  is the length scale and  $\epsilon_Y$  is the energy scale (see section 2.8), with the minimum inverse temperature step–size  $\Delta\beta_{Y,\min}^* = 10^{-15}$ , gradually attained when approaching the critical point. A complete determination of the critical point along with the bi- and spinodal lines for one  $q^*$ -value takes on the average one to two weeks on one node of the *Phoenix Linux Cluster* of the Vienna University of Technology.

### 6.1 Spinodal and Binodal Lines

We first take a look at the gas–liquid coexistence curve, also called binodal line. A comparison of the MSA, the mSCOZA and the MC data is visualised in figures 6.1 and 6.2 for the  $q^*$ -values specified above. We use the same reduced temperatures as in [34], where the MC data are taken from. The mSCOZA result for the location of the critical point are given in table 6.1.

At  $q^* = 0$  we obtain the single Yukawa model. Since in this case the inhomogeneity term of equation (4.17f) and the Coulomb contribution to internal energy per volume [equation (4.17e)] both vanish, our mSCOZA yields the same results as the usual SCOZA treatment

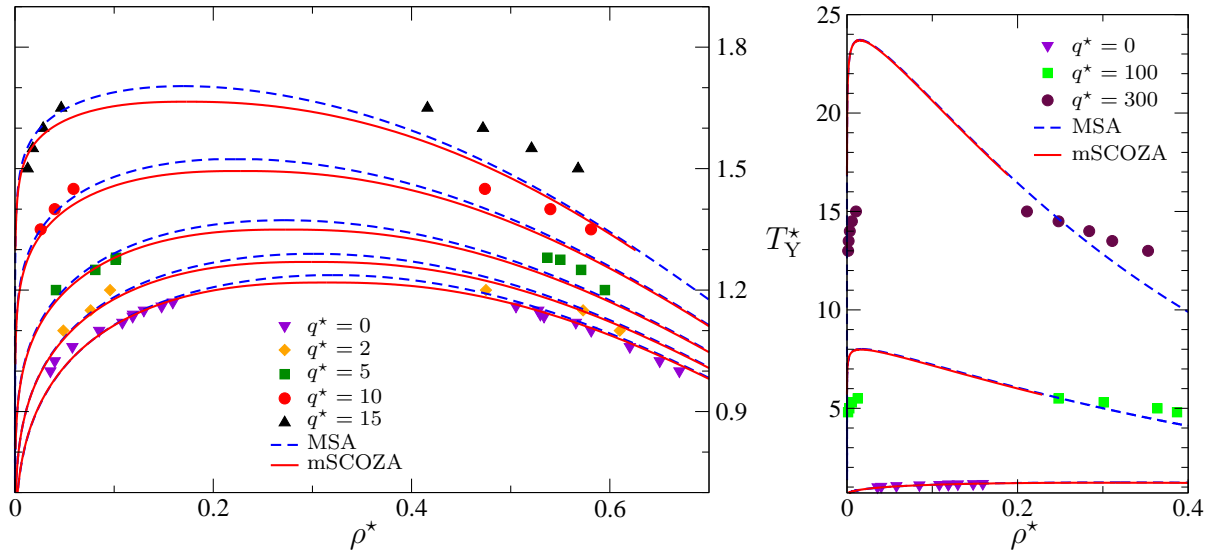


Figure 6.1: Coexistence curves of the Charged Yukawa model for various values of  $q^*$  obtained via the MSA (dashed blue lines), the mSCOZA (solid red lines), and the MC simulations (different symbols as indicated in the legend). We use the Yukawa-reduced temperature defined in equation (2.13i) as in [34], where the MC data are taken from.

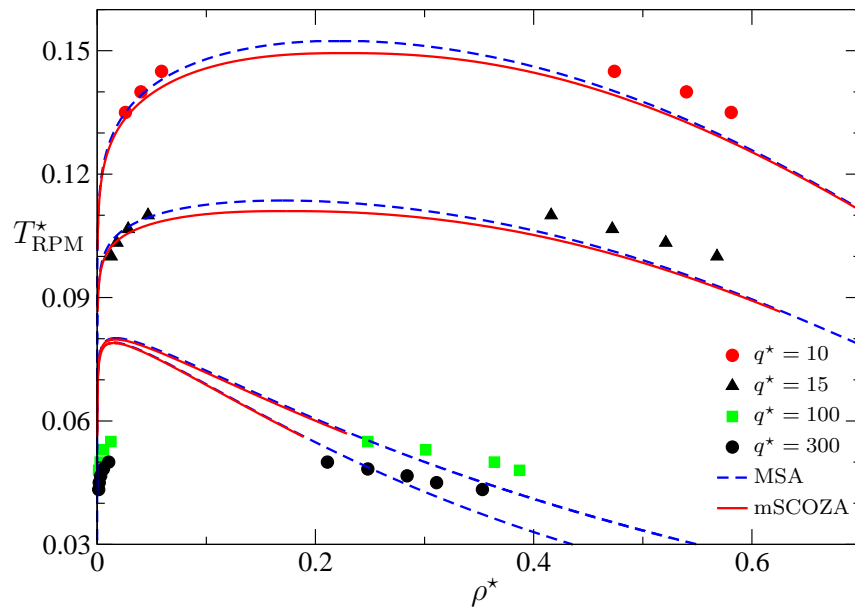


Figure 6.2: Coexistence curves of the Charged Yukawa model as in figure 6.1, but in terms of the RPM-reduced temperature  $T_{\text{RPM}}^*$  of equation (2.13j).

$q^*$	$\rho_c^*$	$T_{cY}^*$	$T_{cCY}^*$	$T_{cRPM}^*$
0	0.314495	1.21869	1.21869	—
2	0.298805	1.26954	0.423181	0.634772
5	0.273225	1.34942	0.224903	0.269884
10	0.227140	1.49412	0.135830	0.149412
15	0.173140	1.66520	0.104075	0.111013
100	0.016275	7.98089	0.0790187	0.0798089
300	0.014975	23.6829	0.0786806	0.0789428

Table 6.1: Critical point location of the Charged Yukawa model for various  $q^*$ -values with the mSCOZA; the reduced temperature is given for the three different possibilities of reduction, see equations (2.13i)–(2.13k).

of a single Yukawa model, given e.g. in [20]. For such a model the SCOZA is known to give better agreement with MC data than the MSA, which can also be seen in figure 6.1.

Several trends can be seen with varying  $q^*$ : Firstly, as is already well known, the MSA overestimates the critical temperature the closer we approach the RPM ( $q^* \rightarrow \infty$ ). Secondly, the mSCOZA has a lower critical temperature than MSA, the difference in absolute values of  $T_Y^*$  becoming larger as we approach the RPM. But unfortunately thirdly the relative difference, which is the more relevant quantity for describing the difference in the location of the critical point and the shape of the coexistence curve, becomes negligible for high values of  $q^*$ . This is best visualised using the RPM-reduced temperature as in figure 6.2.

In fact, the coexistence curves of the MSA and the mSCOZA become practically identical for large values of  $q^*$ , resulting also in the same underestimation of the critical density. To quantify this similarity of the MSA and the mSCOZA for large  $q^*$ -values, we also investigated several of the critical exponents.

## 6.2 Critical Exponents

As outlined in section 3.1, we can use the so called effective critical exponents to describe the critical behaviour of a system. For the seven different  $q^*$ -values under consideration we therefore calculate the effective critical exponents  $\gamma_{\text{eff}}$ ,  $\alpha_{\text{eff}}$ , and  $\beta_{\text{eff}}$  with the mSCOZA.

The critical properties obtained by an approach from above the critical point could be calculated with high accuracy due to the interpolation scheme described in section 4.3.4. This applies to the location of the critical point itself as well as to the critical exponents  $\gamma$  and  $\alpha$ . Therefore the abscissae in figure 6.3, where the temperature parameter  $\tau$  [see equation (3.1)] is given in the usual logarithmic scale, extend to  $-12$ , which means a relative approach to the critical point of  $10^{-10}\%$ .

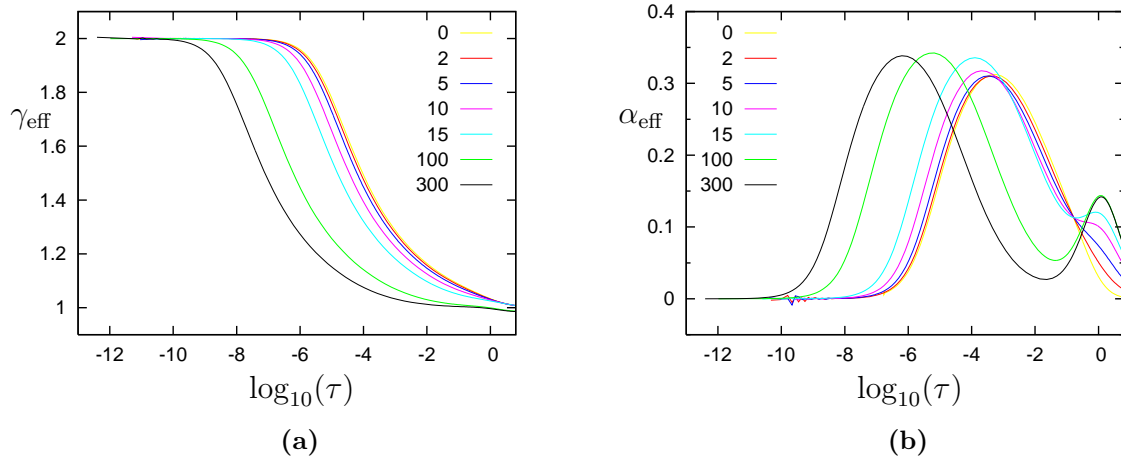


Figure 6.3: Effective critical exponents versus the common logarithm of  $\tau$  [see equation (3.1)], of the Charged Yukawa model for  $q^*$ -values indicated in the legends, obtained via the mSCOZA.

For both,  $\gamma_{\text{eff}}$  and  $\alpha_{\text{eff}}$ , visualised in figures 6.3(a) and 6.3(b), respectively, we could determine the values close to the critical point to be equal to the known SCOZA values  $\gamma_{\text{SCOZA}} = 2$  and  $\alpha_{\text{SCOZA}} = 0$  (compare table 3.2). But it is also clearly visible, that there appears a systematic change with increasing  $q^*$ . For  $\alpha_{\text{eff}}$  the characteristic global maximum in the curve  $\alpha_{\text{eff}}(\tau)$  shifts to lower values of  $\tau$ , and the final value of 0 is attained closer to the critical point. For  $\gamma_{\text{eff}}$  the transition from the mean-field critical exponent value of  $\gamma_{\text{MF}} = 1$  to the one of the SCOZA moves the closer to the critical point the larger  $q^*$ . This is another indication that the mSCOZA becomes similar to the MSA for large  $q^*$ -values, since the MSA always gives mean-field exponents.

$\beta_{\text{eff}}$  seems to behave strangely at first sight, see figure 6.4(a). It always attains a final value of 0, which should not happen within any theory (see table 3.2)! But the reason is a numerical issue resulting in a defective coexistence curve close to the critical point. As depicted in figure 6.4(c), the high and low density branches of the coexistence curve do not join at the critical point because of two numerical inaccuracies.

Firstly, the algorithm used to determine the points where chemical potential and pressure of the two phases are equal (i.e., the points of coexistence for given temperature) relies on linear interpolation between the points of the  $\rho$ -grid (see section 4.3.4).

Secondly, coexistence near the critical point occurs close to the region where the spinodal excludes the “forbidden region” and approximate boundary conditions are used (see section 4.3.1). The closer spinodal and binodal approach each other, the more this approximation will influence the determination of the binodal. Near the critical region this results in wrong data for the coexisting state-points.

Therefore we concentrate on calculating the location of the critical point and critical exponents obtained via an approach from above ( $\tau \rightarrow 0_+$ ) in subsequent considerations.

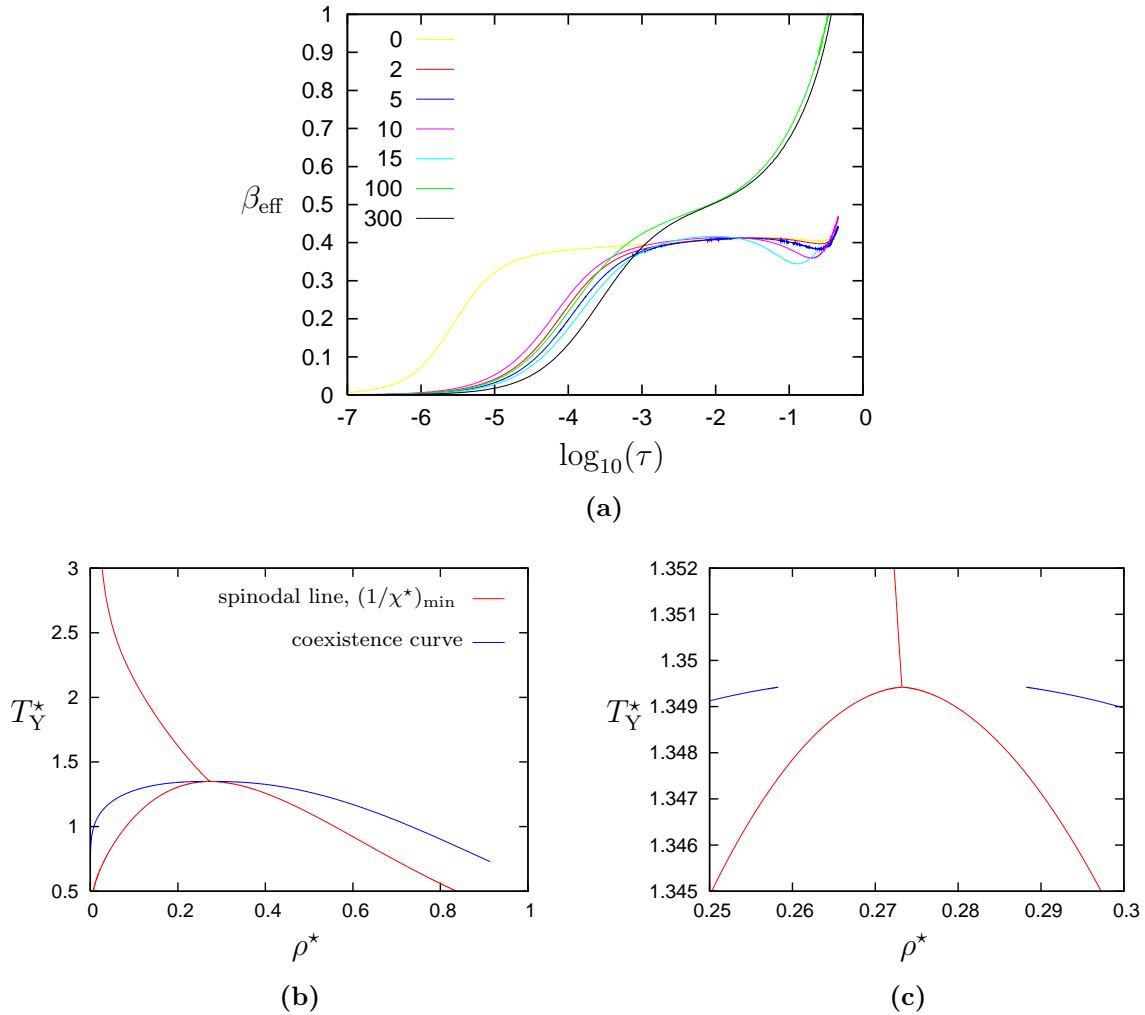


Figure 6.4: Effective critical exponent  $\beta_{\text{eff}}$  versus  $\log_{10} \tau$  of the Charged Yukawa model for  $q^*$ -values indicated in the legend in (a), obtained via the mSCOZA. The coexistence curve and spinodal line for  $q^* = 5$  are depicted in (b) and (c), the latter being a closeup of the critical region in (b). Above the critical point, we draw a line between the state points of minimal  $1/\chi^*$  for given temperature in (b) and (c), which splits into the two branches of the spinodal line below the CP.



# Chapter 7

## Charged Kac Model

The purpose of this chapter is to investigate the critical behaviour of a system where the pair-potential  $\phi(r)$  is a linear combination of two interactions, that are known to exhibit different critical behaviour individually.

It is well established, that the RPM (see section 2.1) belongs to the Ising 3D universality class [107, 108], while a system interacting via a Kac interaction (see section 2.3) exhibits mean field (MF) critical behaviour. In addition, the critical points (CPs) of these two systems differ significantly: for the RPM the critical point is located in the range  $T_{\text{RPM}}^* \simeq 0.0489 - 0.0492$ ,  $\rho^* \simeq 0.076 - 0.080$  [107–109], and the CP of a Kac system is defined by  $T^* \simeq 1.13052$ ,  $\rho^* \simeq 0.27$  [62] (for both system the respective natural units have been used for the reduced units, i.e., the hard core diameter  $\sigma$  for the densities of both systems and the respective interaction energy at contact for temperature, see section 2.8). Taking a linear combination of the two potentials results in the *charged Kac model*,

$$\phi_{ij}^{\text{CK}}(r) = \phi_{ij}^{\text{RPM}}(r) + \phi^{\text{Kac}}(r) , \quad (7.1)$$

with the two contributions given by equation (2.1) and equation (2.7).

If the limit  $\alpha \rightarrow 0$  in the Kac part is performed exactly, the SCOZA is not applicable to this system, even in our modified form (mSCOZA, chapter 4). Since we want to rely on the renowned reliability of the SCOZA in the critical region, we consider a slightly modified potential, where the parameter  $\alpha$  is kept finite:

$$\phi_{ij}(r) = \phi_{ij}^{\text{RPM}}(r) - \xi^2 \frac{q^2}{\sigma} (\alpha\sigma)^2 \frac{e^{-\alpha r}}{r/\sigma} , \quad (7.2)$$

where the strength parameter  $\epsilon_K$  of the Kac potential has been changed to  $\epsilon_K = -\xi^2 q^2 \sigma$ , which makes  $\xi^2$  the parameter of the *relative* strength of the two contributing potentials. We will approximate the potential of equation (7.1) by that of equation (7.2) numerically by making  $\alpha$  as small as possible. Comparing equation (7.2) with equation (2.8) we recognise, that we are now in fact dealing with a charged Yukawa system, where the Yukawa energy at contact is just  $\epsilon_Y = -\xi^2 \frac{q^2}{\sigma} (\alpha\sigma)^2 e^{-\alpha\sigma}$ . To this model the mSCOZA as described in chapter 4 is now applicable.

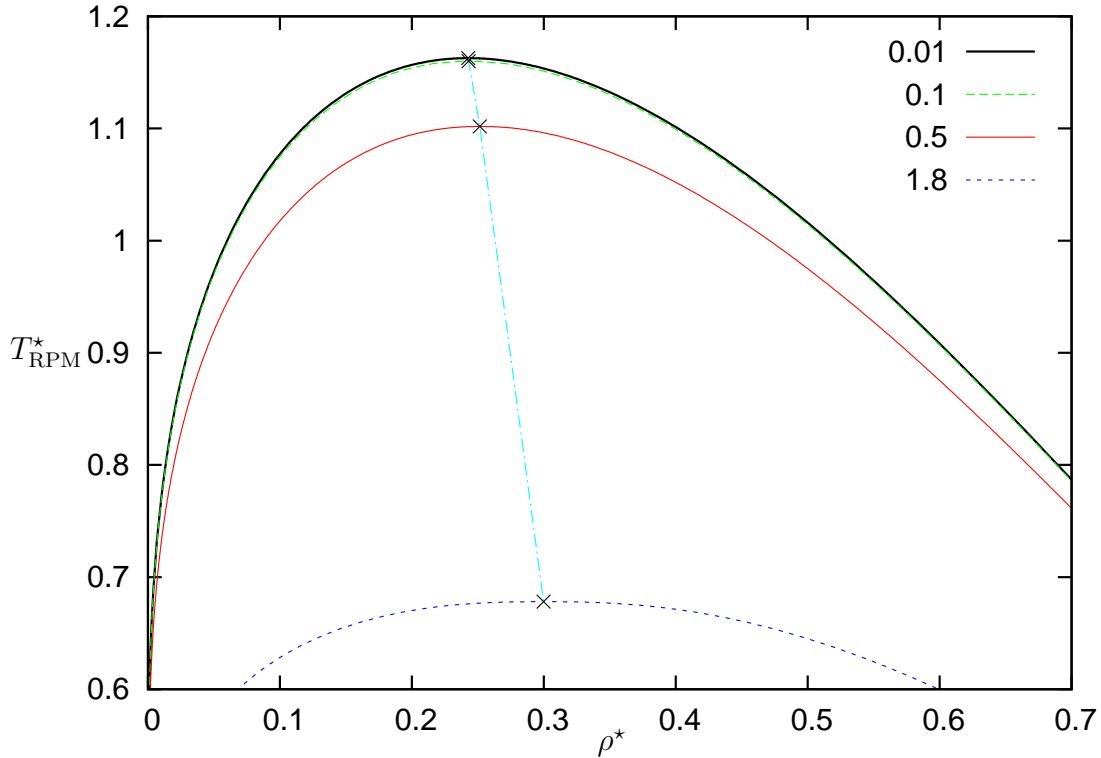


Figure 7.1: *mSCOZA* coexistence curves of the approximated charged Kac model for  $\xi^2 = 1$  and  $\alpha^*$  as indicated in the legend. The corresponding critical points are marked by crosses and connected by the dash-dotted light blue line.

## 7.1 Gas–Liquid Coexistence and Critical Point Location

First we take a look at the coexistence curve at fixed  $\xi^2$  and varying  $\alpha$ , where the latter will be specified in terms of the reduced quantity  $\alpha^* = \alpha\sigma$  (see section 2.8) from now on. We start at a value of  $\alpha^* = 1.8$ , which is the same as in the previous chapter, and then gradually decrease  $\alpha^*$ . In figure 7.1 we plot some coexistence curves for  $\xi^2 = 1$ . It is clearly visible that the coexistence curves, calculated for different  $\alpha^*$ -values within the *mSCOZA*, tend to a certain limiting curve. The difference between the curves for  $\alpha^* = 0.1$  and  $\alpha^* = 0.01$  is already very small, indicating that  $\alpha^* = 0.01$  is sufficiently small to represent a good approximation of the Kac limit. A combined plot of the *mSCOZA* coexistence curve for  $\alpha^* = 0.01$  and the MF curve calculated within the exact limit  $\alpha^* \rightarrow 0$  (performed by Caillol as described in [62]) results in the two curves to lie exactly on top of each other, which is why we did not plot an extra MF line in figure 7.1. In other words, for decreasing  $\alpha^*$  the *mSCOZA* converges to the MF results.



This coincidence is valid for any value of  $\xi^2$ , as the data of table G.1 in the appendix shows. We also include results for the critical exponent  $\beta$ , obtained via a simple fit of

$$\Delta\rho^*(T) = \frac{\rho_l(T) - \rho_g(T)}{\rho_c} = B|\tau|^\beta \quad (7.3)$$

to the coexistence curve data within a range of  $\tau \in (-0.1, 0)$  (see equation (3.1) for the definition of  $\tau$ ). The prefactor  $B$  and the exponent  $\beta$  are the fit parameters<sup>1</sup>,  $\rho_l$  and  $\rho_g$  are the liquid and gas phase densities at coexistence, respectively, and  $\rho_c$  is the critical density (see [110]). A clear tendency also for the fitted  $\beta$ -values to approach the MF value of  $1/2$  for decreasing  $\alpha^*$  is visible, especially in the results for  $\xi^2 = 0.16$ , since the systems with this  $\xi^2$ -value have been studied most intensely over many  $\alpha^*$ -values.

Second, we compare the mSCOZA results for  $\alpha^* = 0.01$  (representative of the Kac limit) with MC simulation data. Grand canonical MC simulations were successfully performed by our colleagues in Paris, Jean-Michel Caillol, Dominique Levesque, and Jean-Jacques Weis, for volumes of  $V^* = 1000, 4000$ , and  $8000$  of the simulation box ( $V^* = V/\sigma^3$ ); for details see [62]. In figure 7.2 we selected four representative values for  $\xi^2$  (given in the subcaptions) and plotted the data for the coexistence curves in the *vicinity* of the CP. The convergence of the simulation data with increasing volume is clearly visible, the result for  $V^* = 8000$  appears to be close to the infinite system limit. The approximate data for the CP from the simulations can be obtained by fitting the data for  $V^* = 8000$  to the universal MF distribution [equation (7.3) with  $\beta = 1/2$ ], the result is presented, along with the mSCOZA data for  $\alpha^* = 0.01$  in the following table:

$\xi^2$	simulation		mSCOZA	
	$T_{c,\text{RPM}}^*$	$\rho_c^*$	$T_{c,\text{RPM}}^*$	$\rho_c^*$
100.0	113.4	0.250	113.3	0.249
11.11	12.62	0.251	12.60	0.249
1.0	1.172	0.242	1.167	0.245
0.10	0.1599	0.190	0.1480	0.179
0.05	0.1062	0.151	0.09725	0.0959
0.02	0.0742	0.0758	0.08255	0.0225

Table 7.1: Critical point location ( $\rho_c^*$  and  $T_{c,\text{RPM}}^*$ ) from the MC simulation (exact Kac limit) and the mSCOZA calculations (approximated Kac limit, i.e.,  $\alpha^* = 0.01$ ) for the charged Kac model.

The comparison with the mSCOZA results shows good agreement for large and intermediate values of  $\xi^2$  ( $\gtrsim 1$ ), and an increasing discrepancy when decreasing  $\xi^2$  further. This

<sup>1</sup>Since we have the same issue with a non-closing coexistence curve as described in connection with figure 6.4, we also include the value of the critical temperature  $T_c$  into the set of fit parameters to get a better fit. However, the value for the critical temperature in table G.1 is the one from the original, high accuracy mSCOZA calculation.

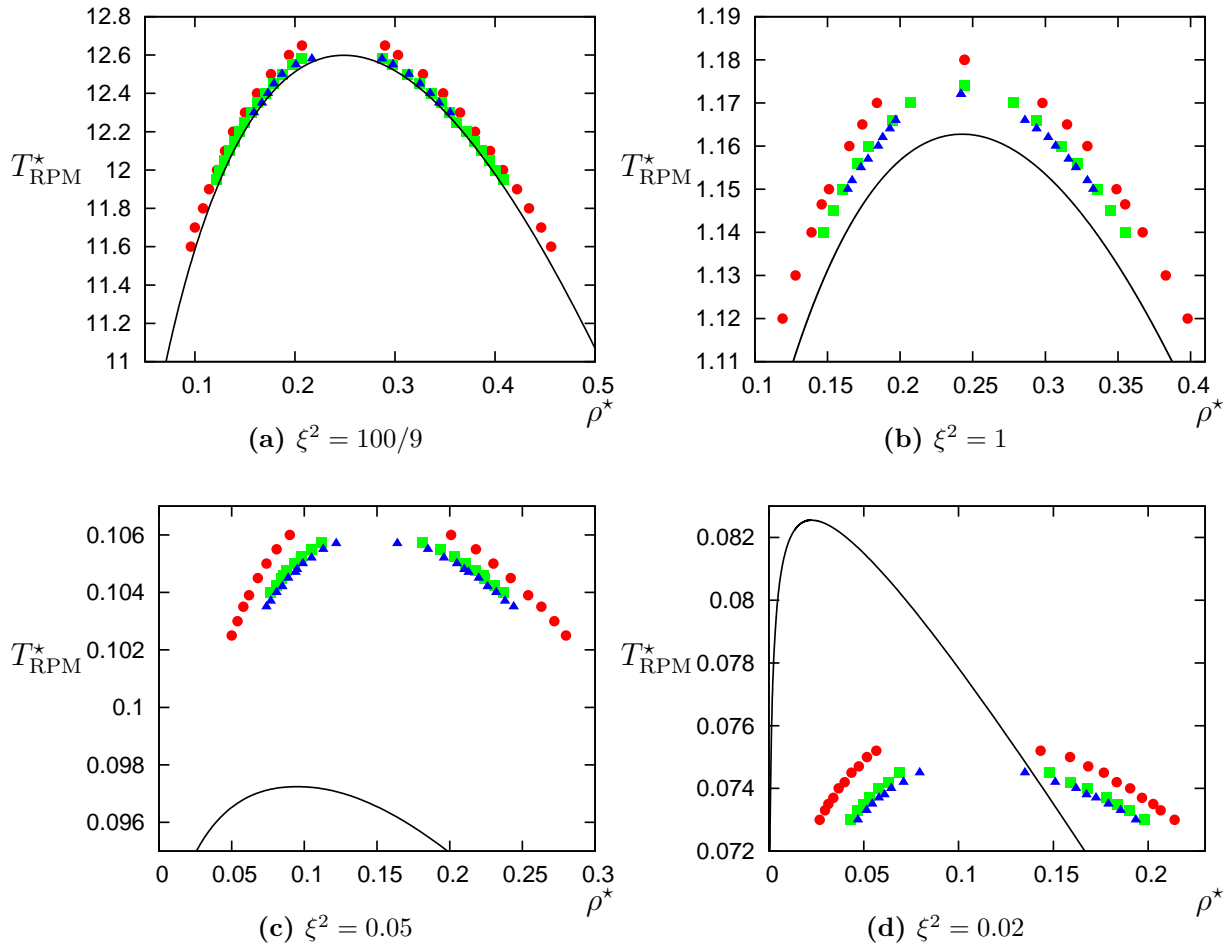


Figure 7.2: *mSCOZA* coexistence curves of the approximated charged Kac model ( $\alpha^* = 0.01$ , black lines) for selected values of  $\xi^2$  as indicated in the subcaptions. The symbols represent Monte Carlo simulation data of the exact charged Kac model for different sizes of the simulation box: red circles correspond to  $V^* = 1000$ , green squares to  $V^* = 4000$ , and blue triangles to  $V^* = 8000$ .

can be best visualised by plotting the data for the CP,  $T_{c,\text{RPM}}^*$  and  $\rho_c^*$ , versus  $\xi^2$  for small values of  $\xi^2$ , see figure 7.3. For  $\xi^2$  in the range from 0.06 to 1 the deviation is  $\simeq 10\%$  for the critical temperature and  $\simeq 30\%$  for the critical density. Below  $\xi^2 \lesssim 0.06$  the RPM contribution to the potential becomes dominant and we find, not surprisingly, that the theoretical data start to differ substantially from the simulation results; the critical temperature and density tend to the MSA values for the RPM ( $\xi^2 = 0$ ). The failure of the MSA to reproduce simulation data is well-known [30].

Despite this deficiency, the *mSCOZA* is able to provide further insight in the system's behaviour at the CP.

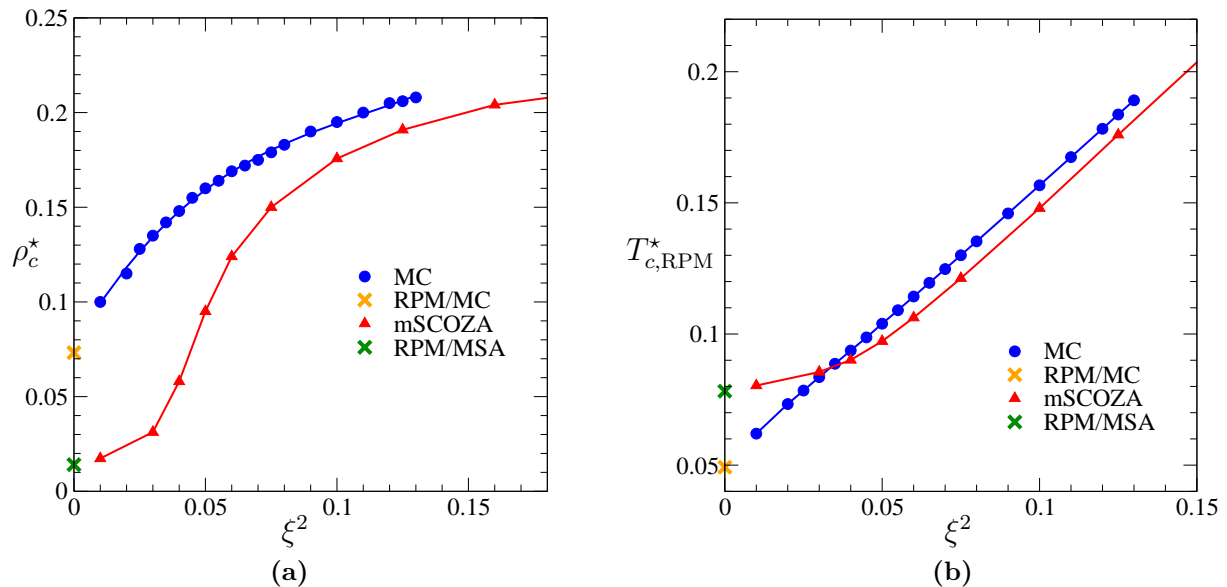


Figure 7.3: Location of the CP of the charged Kac model in dependence on the relative strength parameter  $\xi^2$  in the region of small  $\xi^2$ . Blue circles are Monte Carlo simulation data, red triangles are the mSCOZA data (approximated Kac limit, i.e.,  $\alpha^* = 0.01$ ), both sets are connected by lines as a guide to the eye. Orange and blue crosses mark the result for the pure RPM from the MC simulation and the MSA, respectively.

## 7.2 Critical Behaviour

As discussed in chapter 6, the data provided by the numerical solution of the mSCOZA in the vicinity of the CP is more reliable for  $T > T_c$  (i.e.,  $\tau > 0$ ). In addition, the critical exponent  $\gamma$ , describing the divergence of the isothermal compressibility at the CP, is known to have a value of 1 in the MF theory and 2 for the SCOZA (see table 3.2), which represents a substantial difference. Therefore we use the effective critical exponent  $\gamma_{\text{eff}}$  [see equation (3.5)] to characterise the critical behaviour of the charged Kac system.

The reason why we did not include our findings for  $\gamma$  in table G.1 is, that  $\gamma$  turns out to be *always* 2, no matter how small  $\alpha^*$  or  $\xi^2$  are chosen (both can of course never be exactly zero in practice). But, as can be seen in figure 7.4, the cross-over of  $\gamma_{\text{eff}}$  from the MF behaviour ( $\gamma = 1$ ) far away from the CP to the non-MF one in its vicinity ( $\gamma_{\text{SCOZA}} = 2$ ) appears the closer to the CP the smaller  $\alpha^*$ . The curves indicate that for  $\alpha^* = 0$  we would observe the MF value of  $\gamma_{\text{eff}} = 1$  over the *entire*  $\tau$ -range, reflecting the fact that in the Kac limit  $\alpha^* \rightarrow 0$  the MF behaviour becomes dominant. This pattern turns out to be the same for all  $\xi^2$ -values investigated.

The results from the mSCOZA therefore agree with the findings from the MC simulations [62], that a MF critical behaviour is observed for all  $\xi^2$ -values except for  $\xi^2 = 0$

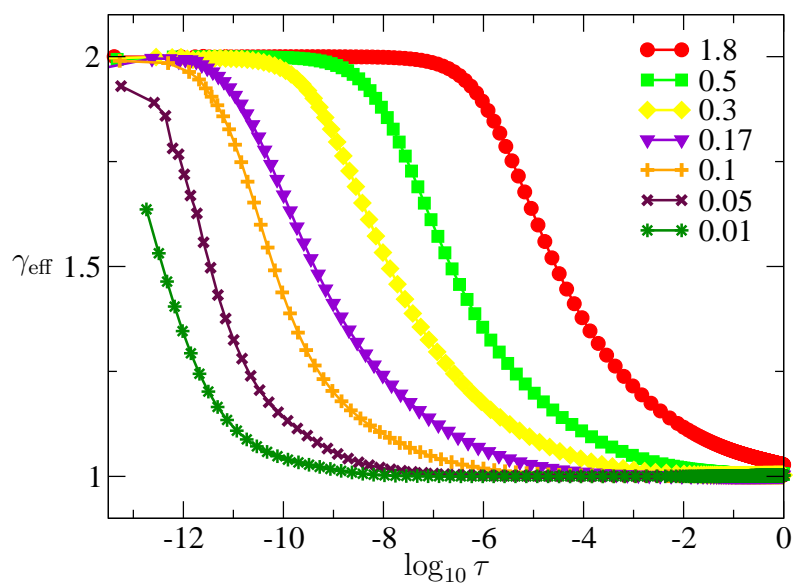


Figure 7.4: Effective critical exponent  $\gamma_{\text{eff}}$  versus the common logarithm of  $\tau$  for the charged Kac model for  $\xi^2 = 0.16$ , approximated with different  $\alpha^*$ -values as indicated in the legend.

exactly, i.e., when the system degenerates to the pure RPM. This is also in accordance with the predictions of the improved MF theory, also presented in [62].

# Chapter 8

## Kac–Yukawa Model

In the publication where we investigated the charged Kac model [62], we also stated a general rule concerning the critical exponent  $\gamma$  of a reference system and the parameter  $\xi^2$  for a system where the pair interaction has the form of

$$\phi(r) = \phi^{\text{ref}}(r) + \xi^2 \phi^{\text{Kac}}(r) . \quad (8.1)$$

Here  $\phi^{\text{Kac}}(r)$  is again the Kac–potential [equation (2.7)] and  $\phi^{\text{ref}}(r)$  is *any* reference potential. The rule connects the location of the CP of the perturbed system where the particles interact via the potential of equation (8.1) on the one hand, and the critical exponent  $\gamma$  of the reference system, where the particles interact solely via  $\phi^{\text{ref}}(r)$ , on the other hand.

To derive this rule we need the Landau function  $\mathcal{L}(\beta, \mu, \rho)$  [111, 112], in this case given by [62]

$$\mathcal{L}(\beta, \mu, \rho) = -\beta\mu\rho + \beta f^{\text{ref}}(\rho, \beta) + 2\pi\beta\sigma\epsilon_K \xi^2 \rho^2 . \quad (8.2)$$

$\mu$  is the chemical potential and  $f^{\text{ref}}(\rho, \beta)$  is the Helmholtz free energy per unit volume of the reference fluid. At low temperatures and arbitrary  $\mu$ ,  $\mathcal{L}(\beta, \mu, \rho)$  has in general two minima as a function of  $\rho$ , but there is only one value of  $\mu$  for given  $\beta$ , i.e.  $\mu_{\text{coex}}$ , for which the Landau function takes on identical values at the two minima. The corresponding minima then supply the parameters of the coexisting gas and liquid phases. At the CP these two minima coincide, which means the second derivative of the Landau function has to vanish there,

$$\frac{\partial^2 \mathcal{L}}{\partial \rho^2}(\beta_c, \mu, \rho_c) = 0 , \quad (8.3)$$

resulting in

$$-4\pi\sigma\epsilon_K \xi^2 = \frac{1}{\rho_c^2 \chi_T^{\text{ref}}(T_c, \rho_c)} , \quad (8.4)$$

where the general formula  $\frac{\partial^2}{\partial \rho^2} f(\beta, \rho) = 1/\rho^2 \chi_T(T, \rho)$  has been used. Note that  $\chi_T^{\text{ref}}(T_c, \rho_c)$  is the isothermal compressibility of the reference system, but evaluated at that state point in the temperature–density plane, where the CP of the perturbed system is located.

Of course, for  $\xi^2 \rightarrow 0$  the CP of the perturbed system approaches the CP of the reference one. Since we know how  $\chi_T^{\text{ref}}(T_c, \rho_c)$  diverges as  $T_c \rightarrow T_c^{\text{ref}}$ , namely  $\chi_T^{\text{ref}} \sim \tau^{-\gamma}$ , we obtain

$$\xi^2 \sim (T_c - T_c^{\text{ref}})^\gamma. \quad (8.5)$$

We tried to verify equation (8.4) and, subsequently, equation (8.5) for the Kac–Yukawa model, i.e., for a system with

$$\phi^{\text{ref}}(r) = \begin{cases} \infty & r < \sigma \\ \epsilon_Y \frac{\sigma}{r} e^{-\kappa r} & r \geq \sigma \end{cases}. \quad (8.6)$$

The reason for this choice is, that the reliable SCOZA for multi–Yukawa interactions (see section 3.3.2) is applicable in this case. We used  $\epsilon_Y = \epsilon_K/\sigma^2 \equiv -\epsilon < 0$  (i.e. an attractive tail to make the SCOZA diffusion equation stable) and the usual value of  $\kappa = 1.8/\sigma$ . Again, the Kac potential had to be approximated by using a small but finite  $\alpha$ , which directly explains the high numerical effort necessary for the calculations: Since the two terms making up the net interaction are treated on an equal footing within the SCOZA, the ration between the Kac and Yukawa contributions to the pair potential should stay well within the bounds on relative accuracy dictated by the specific representation of floating point numbers. (As a measure of this ration, the quantity  $\xi^2 \alpha^{*2} e^{\kappa^* - \alpha^*}$  may be used.) Thus, all calculations in the interesting parameter regime (small  $\alpha^*$  and  $\xi^2$ ) had to be done using extended precision (128 bit for one real variable), consuming about one CPU week to obtain the CP of a system characterised by a single pair of  $\alpha^*$  and  $\xi^2$  parameters.

We calculated the CP to high accuracy for a sequence of  $\xi^2$ – and  $\alpha^*$ –values, for a representative selection see table G.2 and figure 8.1. From the unexpected change in curvature of the  $\alpha^* = 0.0001$ –curve in figure 8.1(d) we assume that results for  $\xi^2$ –values below  $10^{-8}$  tend to be unreliable.

For all  $\alpha^*$  and  $\xi^2$  values studied, we also had to calculate the isothermal compressibility of the reference system at the CP of the corresponding Kac–Yukawa system. Thus, for given  $\alpha^*$  we obtain a mapping from  $\xi^2$  through the CP data of the perturbed system to the expression on the right hand side of equation (8.4),

$$\xi^2 \longrightarrow \frac{1}{[\rho_c(\xi^2)]^2 \chi_T^{\text{ref}}(T_c(\xi^2), \rho_c(\xi^2))}. \quad (8.7)$$

In figure 8.2 we compare the two sides of equation (8.4). We note that, the smaller  $\alpha^*$ , the better the data for the two sides coincide. The systematic deviation, visible for  $\alpha^* = 0.1$  and  $\alpha^* = 0.01$ , is to be expected for finite  $\alpha^*$ : When approaching the CP, as soon as the correlation length (which diverges at the CP) becomes larger than the range ( $1/\alpha$ ) of the Kac–like interaction, the system “becomes aware” of the non–Kac behaviour, and equation (8.2) [and hence equation (8.4)], which only holds for the mean field type behaviour of the exact (i.e., limiting) Kac potential, is no longer correct.

In the investigated region a value of  $\alpha^* = 0.0001$  proved to give an interaction that is sufficiently Kac–like, so that equation (8.4) indeed holds for our example reference interaction.

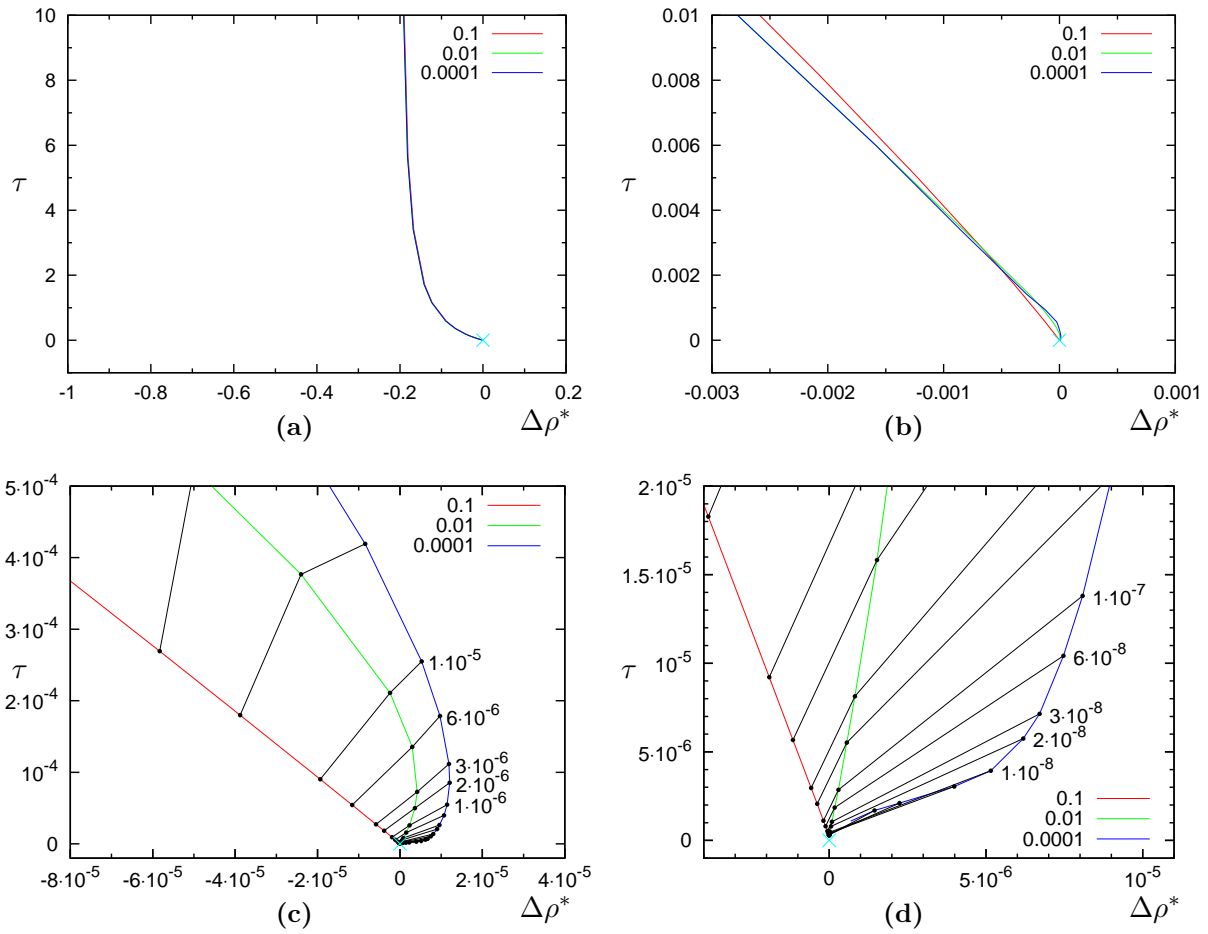


Figure 8.1: Lines of consecutive CPs for the approximated Kac–Yukawa system in relation to the CP of the reference system, i.e.,  $\tau = (T_c - T_c^{\text{ref}})/T_c^{\text{ref}}$  and  $\Delta\rho^* = (\rho_c - \rho_c^{\text{ref}})/\rho_c^{\text{ref}}$ , with decreasing  $\xi^2$  for three different values of  $\alpha^*$ , as indicated in the legends. From (a) to (d) we zoom into the critical region of the reference system; in (c) and (d) points corresponding to equal values of  $\xi^2$  are connected by black lines and labelled with the corresponding  $\xi^2$ -value (see table G.2). The CP of the reference system is indicated by a light-blue cross.

To check the validity of equation (8.5) directly we again use the concept of an effective critical exponent for  $\gamma$  [see equation (3.5)]. A quantity analogous to equation (8.5) can be defined as

$$\gamma_{\xi}^{\text{eff}} = \frac{\partial(\log \xi^2)}{\partial(\log \tau)}. \quad (8.8)$$

In figure 8.3 we find excellent agreement between  $\gamma_{\text{eff}}^{\text{ref}}$  (effective critical exponent  $\gamma$  of the reference system along the critical isochore) and  $\gamma_{\xi}^{\text{eff}}$  defined in equation (8.8), as long as

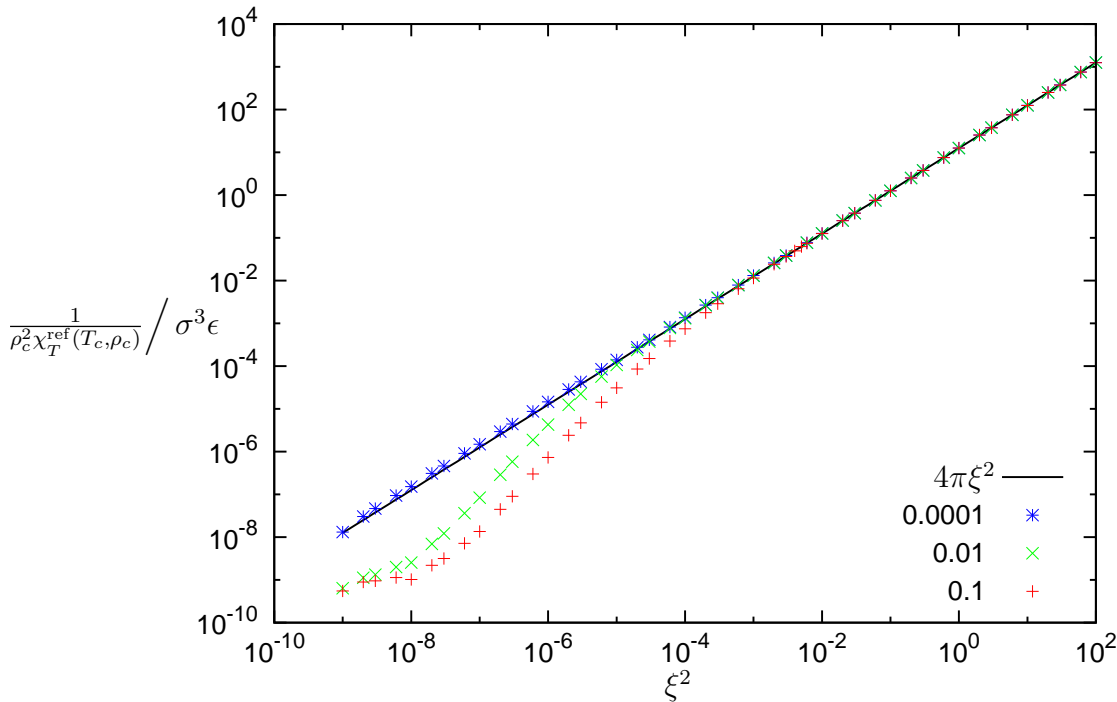


Figure 8.2:  $1/\rho_c^2\chi_T^{\text{ref}}(T_c, \rho_c)$  (in units of  $\sigma^3\epsilon$ ) versus  $\xi^2$  for different values of  $\alpha^*$  (cf. legend) on a double-logarithmic scale for the approximated Kac–Yukawa model, compared to  $4\pi\xi^2$  [see equation (8.4)].

equation (8.4) holds. For larger  $\alpha^*$ -values the onset of the strong deviation of  $\gamma_\xi^{\text{eff}}$  from  $\gamma_{\text{eff}}^{\text{ref}}$  happens exactly at the point where equation (8.4) is no longer correct, visualised in figure 8.2. The small right shift of the blue stars relative to the black line is due to the fact, that the line of consecutive CPs of the perturbed system does not coincide with the critical isochore (see figure 8.1).

It is also apparent, that  $\gamma = 2$ , the value of  $\gamma_{\text{eff}}^{\text{ref}}$  in the vicinity of the CP for SCOZA, is barely attained by  $\gamma_\xi^{\text{eff}}$  before the limit of numerical reliability is reached. Nevertheless we found strong evidence that the relation between the compressibility (and hence the critical exponent  $\gamma$ ) of a reference (hard core) Yukawa system and the parameter  $\xi^2$  (the strength of an added Kac potential), equation 8.5, indeed holds. On the other hand, for the relation to be a useful means to derive the critical exponent  $\gamma$  for the reference system, the numerical effort has still to be increased, going beyond extended precision calculations.<sup>1</sup>

The work presented in this chapter has been published in [114].

<sup>1</sup>An attempt to increase the numerical accuracy using FMLIB [113] pushed the amount of required CPU time beyond practicality.



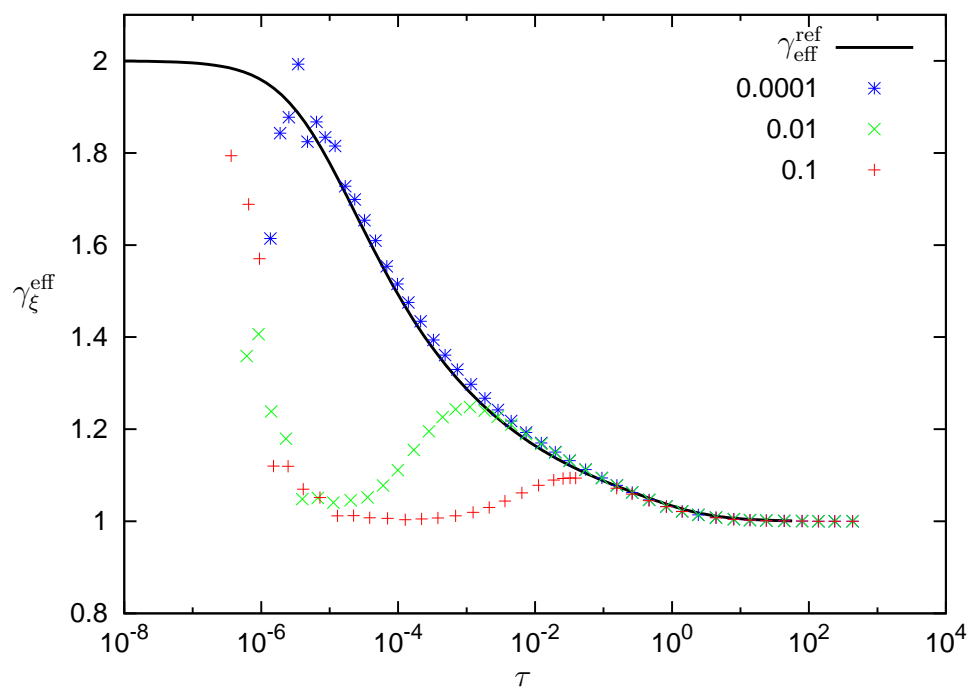


Figure 8.3:  $\gamma_{\xi}^{\text{eff}}$  versus  $\tau$  (symbols) for different values of  $\alpha^*$  (indicated in the legend) for the approximated Kac–Yukawa model.  $\gamma_{\text{eff}}^{\text{ref}}$  (solid line) of the reference hard core Yukawa model is added for comparison.



## Part IV

# Ordered Phases of Systems with Hard Core Particles



# Chapter 9

## Square–Shoulder Model

The topic of this chapter is to investigate in a systematic and thorough way the ordered particle arrangements of the square–shoulder model [equation (2.10)], introduced in section 2.5, in 3D<sup>1</sup>. Using the methods explained in chapter 5, we will work at  $T = 0$  in an NPT ensemble, i.e., we search for configurations that minimise the enthalpy (which is equal to the Gibbs free energy in the zero temperature case). These equilibrium configurations are therefore termed minimum enthalpy configurations (MECs).

To provide a deeper insight into the self–assembly strategies of the system we consider a short ( $\lambda = 1.5\sigma$ ), an intermediate ( $\lambda = 4.5\sigma$ ), and a large ( $\lambda = 10\sigma$ ) shoulder width. As a starting point for our systematic search strategy (see section 5.7.4) we need the close–packed structure of minimum energy for each value of  $\lambda$ .

### 9.1 Close–Packed Structures

Before looking for the close–packed structure (CPS) with the lowest energy, we introduce the following convention: If there is more than one CPS that exhibits the lowest occurring energy out of all CPSs, we only consider the CPS with the shortest stacking sequence as MEC (see section 5.5). An exception to this rule is that we favour fcc (ABC) to hcp (AB) in such a case, motivated by the fact that — although the stacking sequence for fcc is longer than the one for hcp — the crystallographic description (lattice plus basis) for the fcc structure requires only one basis particle, while for the hcp structure it is a non–simple one. In general, for all stackings but the ABC stacking, the minimum number of basis particles in a crystallographic description is equal to the length of the stacking sequence. This convention is necessary since it is possible that there are *infinitely many* stacking sequences of equal energy, e.g. for very short shoulder widths ( $\lambda < \sqrt{2}\sigma$ ), where only nearest neighbour interactions occur, *all* stacking sequences have an equal energy per particle of  $e = 6\epsilon$ .

An important question we need to answer in an effort to find the equilibrium CPS, i.e., the one exhibiting the lowest energy is: What length should the considered stacking

---

<sup>1</sup>Most of this work has been published in [85, 86].

sequences have? In particular, is there a maximum stacking sequence length  $n_{\max}$  such that including all stacking sequences up to this length into the set of candidate CPSs guarantees that all possible energies per particle for *all* CPSs are covered?<sup>2</sup> We will demonstrate that this question cannot be easily answered.

In an attempt to find  $n_{\max}$  for the square-shoulder interaction we recognise, that  $n_{\max}$ , if it exists, must depend on the inherent cutoff-distance which this interaction comprises, the shoulder range  $\lambda$ . Consider a particular layer  $\mathcal{L}_0$ , which is of course either an A, B, or C layer. The two neighbouring layers shall be called  $\mathcal{L}_1$  and  $\mathcal{L}_{-1}$ , next nearest neighbours are  $\mathcal{L}_2$  and  $\mathcal{L}_{-2}$ , etc. Then, the lower bound for the shortest possible distance of a particle in  $\mathcal{L}_0$  to a particle in a layer  $\mathcal{L}_n$  is given by the layer distance

$$d_n = \sqrt{\frac{2}{3}}\sigma|n|, \quad (9.1)$$

where the height of a regular tetrahedron of edge length  $\sigma$ ,  $\sqrt{2/3}\sigma$ , is used. If, for a particular, positive index  $i$ ,  $d_i \geq \lambda$ , then there will not appear any shoulder overlap between a particle of  $\mathcal{L}_0$  and any particle in one of the layers  $\mathcal{L}_n$  with  $|n| \geq i$ . An upper bound for the smallest such  $i$  is easy to calculate, it is given by

$$i = \left\lceil \frac{\lambda}{\sigma} \sqrt{\frac{3}{2}} \right\rceil, \quad (9.2)$$

where  $\lceil x \rceil$  denotes the ‘‘ceiling’’, the smallest integer number that is greater or equal to  $x$ . Thus, for the energy of each particle in  $\mathcal{L}_0$  we only have to consider overlaps with particles of the layers  $\mathcal{L}_k$  with  $-i + 1 \leq k \leq i - 1$ , i.e.,  $2i - 1$  layers in total.

One could thus assume that

$$n_{\max} = 2i - 1. \quad (9.3)$$

However, as will be shown, this is not true. The reason we suspect is, that for the calculation of  $e$ , the *average* energy per particle, one has to take the average of the particle energies over all layers (particles in the same layer have the same energy, due to symmetry). Equation (9.3) just represents the maximum number of layers to consider for the calculation of the energy of a particle in one particular layer. This energy per particle can, in general, differ from layer to layer of a stacking sequence.

In figure 9.1 we give an overview of the equilibrium close-packed structures for  $\lambda$ -values from  $\sigma$  to  $4.5\sigma$ . Stacking sequences of up to 12 layers have been considered, corresponding in total to 133 different stacking sequences (see table 5.1). We start at  $\lambda = \sigma$ , the pure hard sphere model, where fcc represents our favoured stacking. As already stated above, for  $\sigma \leq \lambda < \sqrt{2}\sigma$  only nearest neighbour overlaps occur, all stackings have the same energy of  $e = 6\epsilon$ , and fcc is still the structure of our choice. In the range of  $\sqrt{2}\sigma \leq \lambda < 2\sqrt{2/3}\sigma$ , second nearest neighbours start to overlap. Still, all considered stackings exhibit the same

---

<sup>2</sup>This would imply that there appears always at least one infinite set of stacking sequences of CPSs, all elements of which exhibit the same energy per particle.

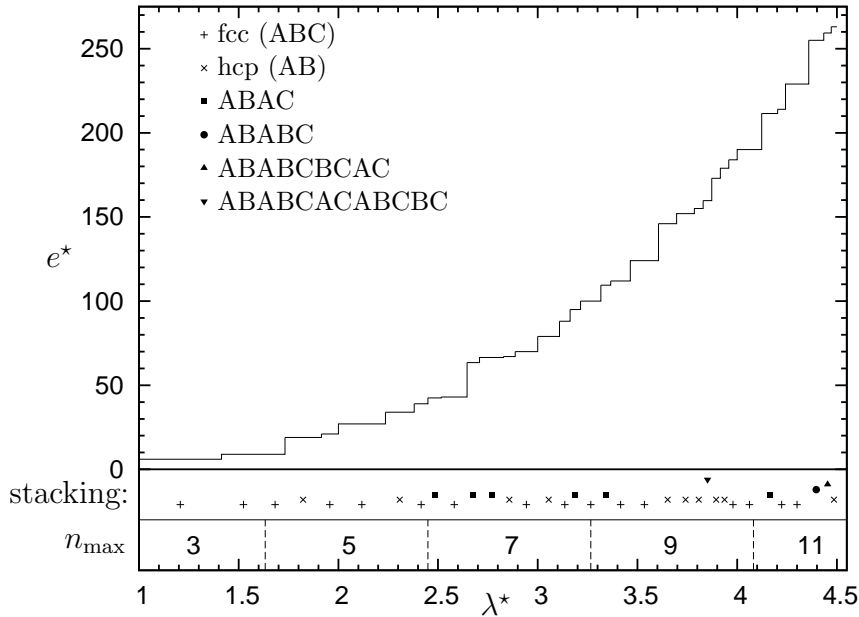


Figure 9.1: Reduced energy per particle  $e^*$ , for the energetically most favourable close-packed particle arrangement with the shortest stacking sequence, as a function of the reduced shoulder width  $\lambda^*$  of the SSM. Symbols indicate the corresponding stacking sequence, different symbols have different vertical offsets for a better distinction. The graph is accompanied by the number of layers to consider for the energy-calculation of one particle,  $n_{\max}$ , in dependence on  $\lambda^*$ .

energy per particle,  $e = 9\epsilon$ ; fcc is chosen as a representative. For  $2\sqrt{2/3}\sigma \leq \lambda < \sqrt{3}\sigma$  different stackings start to have different energies per particle, fcc exhibits the lowest value of (still)  $e = 9\epsilon$ . Hence, again fcc is the favoured structure. Only at  $\sqrt{3}\sigma \leq \lambda < \sqrt{11/9}\sigma$  another stacking starts to become the representing CPS: hcp (AB) has the minimum energy per particle of  $e = 19\epsilon$  in this range.

In table 9.1 we summarise the other findings visualised in figure 9.1. Two phenomena deserve to be mentioned: Firstly, the 12-layer structure appearing as equilibrium CPS between  $2\sqrt{11/3}\sigma \leq \lambda < \sqrt{15}\sigma$ . Clearly, this CPS represents an exception to the assumption that the largest number of layers necessary to consider is given through equation (9.3) by 9. Although being the only exception we found, one counter-example is sufficient to prove the assumption wrong. Secondly, while, considering up to 12 layers, above  $\lambda > 2\sqrt{2/3}\sigma$  usually only one CPS out of the pool of 133 stacking sequences exhibits the minimum energy per particle, in the interval  $\sqrt{19}\sigma \leq \lambda < \sqrt{59/3}\sigma$  two structures have equal, minimal energy.

Nevertheless, we are able to find with high reliability the CPS exhibiting the lowest energy per particle for given  $\lambda$ , which represents the equilibrium structure for our model at high pressure.

$\lambda^*$ -range		$e^*$	optimum stacking sequence(s)
analytic	numeric		
$1 - \sqrt{2}$	$\simeq 1.00 - 1.41$	6	fcc, hcp, ABAC, ...
$\sqrt{2} - 2\sqrt{2/3}$	$\simeq 1.41 - 1.63$	9	fcc, hcp, ABAC, ...
$2\sqrt{2/3} - \sqrt{3}$	$\simeq 1.63 - 1.73$	9	fcc
$\sqrt{3} - \sqrt{11/3}$	$\simeq 1.73 - 1.91$	19	hcp
$\sqrt{11/3} - 2$	$\simeq 1.91 - 2.00$	21	fcc
$2 - \sqrt{5}$	$\simeq 2.00 - 2.24$	27	fcc
$\sqrt{5} - \sqrt{17/3}$	$\simeq 2.24 - 2.38$	34	hcp
$\sqrt{17/3} - \sqrt{6}$	$\simeq 2.38 - 2.45$	39	fcc
$\sqrt{6} - \sqrt{19/3}$	$\simeq 2.45 - 2.52$	85/2	ABAC
$\sqrt{19/3} - \sqrt{7}$	$\simeq 2.52 - 2.65$	43	fcc
$\sqrt{7} - \sqrt{22/3}$	$\simeq 2.65 - 2.71$	127/2	ABAC
$\sqrt{22/3} - 2\sqrt{2}$	$\simeq 2.71 - 2.83$	133/2	ABAC
$2\sqrt{2} - 5/\sqrt{3}$	$\simeq 2.83 - 2.87$	67	hcp
$5/\sqrt{3} - 3$	$\simeq 2.87 - 3.00$	70	fcc
$3 - \sqrt{29/3}$	$\simeq 3.00 - 3.11$	79	hcp
$\sqrt{29/3} - \sqrt{10}$	$\simeq 3.11 - 3.16$	88	fcc
$\sqrt{10} - \sqrt{31/3}$	$\simeq 3.16 - 3.21$	95	ABAC
$\sqrt{31/3} - \sqrt{11}$	$\simeq 3.21 - 3.32$	100	fcc
$\sqrt{11} - \sqrt{34/3}$	$\simeq 3.32 - 3.37$	219/2	ABAC
$\sqrt{34/3} - 2\sqrt{3}$	$\simeq 3.37 - 3.46$	112	fcc
$2\sqrt{3} - \sqrt{13}$	$\simeq 3.46 - 3.61$	124	fcc
$\sqrt{13} - \sqrt{41/3}$	$\simeq 3.61 - 3.70$	146	hcp
$\sqrt{41/3} - \sqrt{43/3}$	$\simeq 3.70 - 3.79$	152	hcp
$\sqrt{43/3} - 2\sqrt{11/3}$	$\simeq 3.79 - 3.83$	155	hcp
$2\sqrt{11/3} - \sqrt{15}$	$\simeq 3.83 - 3.87$	639/4	ABABCACABCBC
$\sqrt{15} - \sqrt{46/3}$	$\simeq 3.87 - 3.92$	173	hcp
$\sqrt{46/3} - \sqrt{47/3}$	$\simeq 3.92 - 3.96$	179	hcp
$\sqrt{47/3} - 4$	$\simeq 3.96 - 4.00$	184	fcc
$4 - \sqrt{17}$	$\simeq 4.00 - 4.12$	190	fcc
$\sqrt{17} - \sqrt{53/3}$	$\simeq 4.12 - 4.20$	423/2	ABAC
$\sqrt{53/3} - 3\sqrt{2}$	$\simeq 4.20 - 4.24$	214	fcc
$3\sqrt{2} - \sqrt{19}$	$\simeq 4.24 - 4.36$	229	fcc
$\sqrt{19} - \sqrt{59/3}$	$\simeq 4.36 - 4.43$	255	ABABC, ABABCACABCBC
$\sqrt{59/3} - 2\sqrt{5}$	$\simeq 4.43 - 4.47$	778/3	ABABCBCAB
$2\sqrt{5} - 9/2$	$\simeq 4.47 - 4.50$	263	hcp

Table 9.1: The CPSs of minimum energy for the SSM (third column) for reduced shoulder width values ( $\lambda^*$ ) up to 4.5. The corresponding reduced energies ( $e^*$ ) are given in the second column.

## 9.2 Minimum Enthalpy Configurations

With the two limiting cases at hand, the fcc structure with touching shoulders ( $e = 0$ ) at low pressure and the CPS from the previous section at high pressure, we can now start the search strategy outlined in section 5.7.4. However, since the application of the GA



(section 5.7.1) proved to become significantly more expensive the more basis particles were considered, we used a modified search strategy: We first look for the MECs that contain just 1 basis particle over the whole pressure regime using our method of successively cutting lines (see section 5.7.4). The resulting  $h(P)$ -curve is then used as an initial sequence of straight lines for the search of two-particle MECs, the outcome is fed into three-particle considerations, and so on. Although this results in many more GA runs for a small number of basis particles, we achieve a significant reduction in runs for a large number of particles in the basis, which pays off in total CPU time.

Our choice for the short, intermediate, and large shoulder widths are  $\lambda = 1.5\sigma$ ,  $\lambda = 4.5\sigma$ , and  $\lambda = 10\sigma$ , respectively. Let us discuss these three cases in detail. We will use the abbreviations for the underlying Bravais lattices introduced in section 5.3 and summarised in table G.3, and reduced units as explained in section 2.8. Also, we will categorise the occurring MECs in four classes: clusters, columns, lamellae, and compact structures.

### 9.2.1 Short Shoulder Width ( $\lambda = 1.5\sigma$ )

The three quantities, enthalpy and energy per particle (i.e.,  $h$  and  $e$ ) and the number density ( $\rho$ ), in dependence of pressure  $P$ , characterise the complete phase diagram at  $T = 0$ . They are plotted, along with visualisations of the resulting MECs, in figure 9.2, while numerical details can be found in table 9.2. The MECs found can be analysed on

lattice	$n_b$	$e^*$	$\rho^*$
fcc	1	0	$\frac{8\sqrt{2}}{27} \simeq 0.419$
bco	1	1	$\frac{8}{3\sqrt{23}} \simeq 0.556$
fco	2	2	$\frac{16}{\sqrt{455}} \simeq 0.750$
hex	1	4	$\frac{4}{\sqrt{15}} \simeq 1.03$
sfco	2	5	$\frac{16}{2\sqrt{15+\sqrt{35}}} \simeq 1.17$
bco	1	7	$\frac{8}{\sqrt{35}} \simeq 1.35$
fcc	1	9	$\sqrt{2} \simeq 1.41$

*Table 9.2: Numerical details of the ordered equilibrium structures identified for the SSM with  $\lambda = 1.5\sigma$ : the underlying lattice is characterised by the appropriate abbreviation from Table G.3,  $n_b$  is the number of basis particles required to describe the MEC.  $e^*$  and  $\rho^*$  are the energy per particle and particle density, respectively. Since the MECs can be described on the basis of geometric considerations,  $\rho^*$  can be given in closed, analytic expressions.*

geometric grounds, resulting in closed, analytic expressions for all lattice parameters, as well as for related thermodynamic quantities (e.g., the density as given in table 9.2). We discuss the emerging seven MECs in detail, starting at the low pressure limiting MEC and

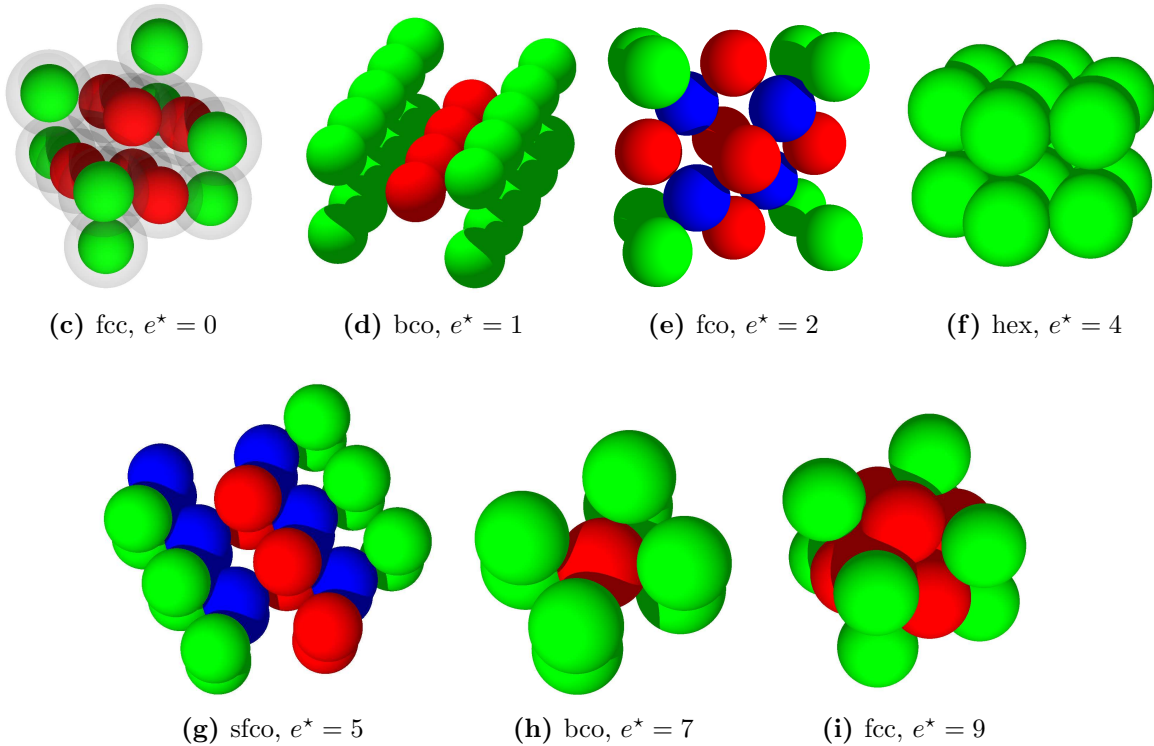
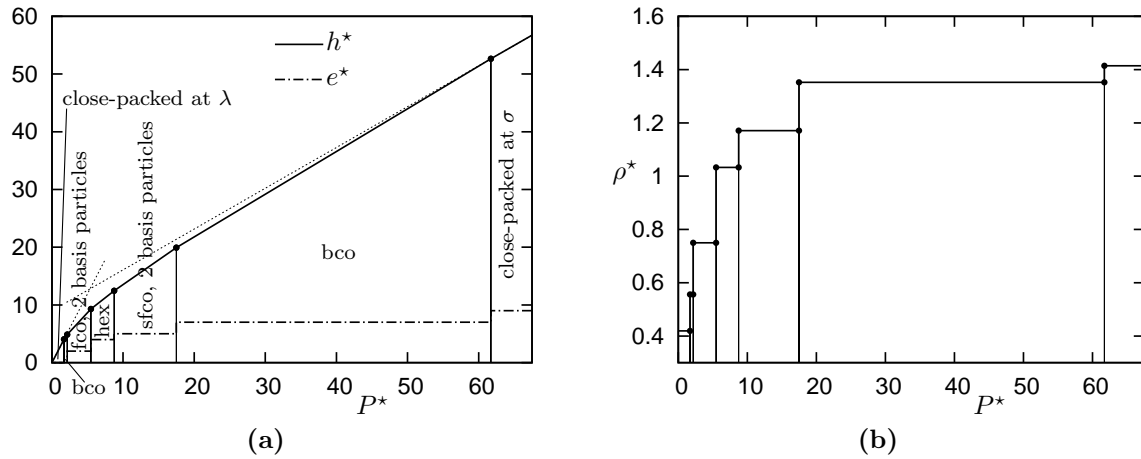


Figure 9.2: (a): Reduced enthalpy and energy per particle ( $h^*$  and  $e^*$ ) versus reduced pressure  $P^*$ , for the SSM with  $\lambda = 1.5\sigma$ . The dotted lines indicate the low and high pressure limiting cases, cf. text. The identified lattices are labelled with standard abbreviations (see table G.3) and with their number of basis particles (if different from one). In (b) the corresponding reduced density  $\rho^*$  is plotted. (c–i) are visualisations of the seven MECs found, where we use the following colourcode: green – particles at the corner positions of the conventional unit cell; red – particles at body or face centred positions; blue – additional basis particles; transparent corona – shoulder [only drawn in (c)].

labelling them with the unambiguous value for the energy per particle (numerical details on these seven MECs are given in table G.4):

- $e = 0$ . At very low pressure, as discussed in section 5.7.4, all “CPSs” with nearest neighbour distance equal to the shoulder width  $\lambda$  are MECs. We select (cf. the arguments put forward in section 9.1) the fcc structure as a representative, see figure 9.2(c). The edge length of the corresponding conventional unit cell is obviously given by  $\tilde{a} = \sqrt{2}\lambda$ .
- $e = \epsilon$ . When increasing the pressure, the first non-trivial structure we encounter is a bco structure, visualised in figure 9.2(d). The bco unit cell is determined through three conditions on distances between lattice points: Firstly, the shortest of the three edges of the conventional unit cell is equal to the hard core diameter,  $\tilde{c} = \sigma$ . Secondly, the second shortest edge has the length of the shoulder width,  $\tilde{b} = \lambda = 3\sigma/2$ . And thirdly, the body centred lattice point has an equal distance from all eight corner points of  $\lambda$ , too, i.e.,  $|\tilde{\mathbf{a}} + \tilde{\mathbf{b}} + \tilde{\mathbf{c}}|/2 = 3\sigma/2$ . This leads, through  $\tilde{\mathbf{a}} = \tilde{a}\hat{\mathbf{x}}$ ,  $\tilde{\mathbf{b}} = \tilde{b}\hat{\mathbf{y}}$ , and  $\tilde{\mathbf{c}} = \tilde{c}\hat{\mathbf{z}}$ , to  $\tilde{a} = \sqrt{23}/4\sigma \simeq 2.40\sigma$  and hence also  $\rho = 2/(\tilde{a}\tilde{b}\tilde{c}) = 8/(3\sqrt{23}\sigma^3)$ .

This bco structure can be viewed as a columnar structure: The particles form columns in the direction of  $\tilde{\mathbf{c}}$ , along which the hard cores of the particles are in contact. Therefore there appear two intra-columnar shoulder overlaps of a particle with the two neighbouring particles in a column. Any other overlap is avoided, resulting in  $e = \epsilon$ .

- $e = 2\epsilon$ . Further increasing the pressure leads to a rather compact, fco structure with two basis particles (in the primitive unit cell), see figure 9.2(e). Using for the location of the second basis particle the vector  $\tilde{\mathbf{v}}_2$ , and again  $\tilde{\mathbf{a}} = \tilde{a}\hat{\mathbf{x}}$ ,  $\tilde{\mathbf{b}} = \tilde{b}\hat{\mathbf{y}}$ , and  $\tilde{\mathbf{c}} = \tilde{c}\hat{\mathbf{z}}$ , this fco structure can be described in the following way:

The face centred particle at the smallest face touches the corresponding corner-particles at the shoulders, giving  $\tilde{c}^2 + \tilde{b}^2 = (2\lambda)^2$ . The extra basis particle has a distance of  $\sigma$  from one corner particle and the three closest face centred particles ( $|\tilde{\mathbf{v}}_2| = |\tilde{\mathbf{v}}_2 - (\tilde{\mathbf{a}} + \tilde{\mathbf{b}})/2| = |\tilde{\mathbf{v}}_2 - (\tilde{\mathbf{a}} + \tilde{\mathbf{c}})/2| = |\tilde{\mathbf{v}}_2 - (\tilde{\mathbf{b}} + \tilde{\mathbf{c}})/2| = \sigma$ ). The next nearest corner particle has a distance of  $\lambda$  from the extra particle,  $|\tilde{\mathbf{v}}_2 - \tilde{\mathbf{c}}| = \lambda$ . This results in

$$\tilde{\mathbf{a}} = 2\sqrt{4\sigma^2 - \lambda^2}\hat{\mathbf{x}} = \sqrt{7}\sigma\hat{\mathbf{x}} \simeq 2.65\sigma\hat{\mathbf{x}}, \quad (9.4a)$$

$$\tilde{\mathbf{b}} = \sqrt{2}\sqrt{\lambda^2 + \sigma^2}\hat{\mathbf{y}} = \sqrt{\frac{13}{2}}\sigma\hat{\mathbf{y}} \simeq 2.55\sigma\hat{\mathbf{y}}, \quad (9.4b)$$

$$\tilde{\mathbf{c}} = \sqrt{2}\sqrt{\lambda^2 - \sigma^2}\hat{\mathbf{z}} = \sqrt{\frac{5}{2}}\sigma\hat{\mathbf{z}} \simeq 1.58\sigma\hat{\mathbf{z}}, \quad (9.4c)$$

$$\begin{aligned} \mathbf{v}_2 &= \frac{1}{2\sqrt{2}} \left( \sqrt{2}\sqrt{4\sigma^2 - \lambda^2}\hat{\mathbf{x}} + \sqrt{\lambda^2 + \sigma^2}\hat{\mathbf{y}} + 3\sqrt{\lambda^2 - \sigma^2}\hat{\mathbf{z}} \right) = \\ &= \frac{\sigma}{4\sqrt{2}} \left( \sqrt{14}\hat{\mathbf{x}} + \sqrt{13}\hat{\mathbf{y}} + \sqrt{5}\hat{\mathbf{z}} \right) \simeq 0.66\hat{\mathbf{x}} + 0.64\hat{\mathbf{y}} + 0.40\hat{\mathbf{z}}. \end{aligned} \quad (9.4d)$$

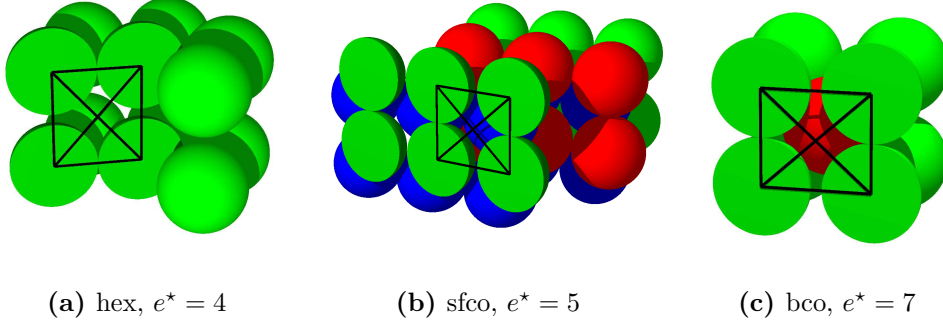


Figure 9.3: Visualisation of particle distances of selected MECs for  $\lambda = 1.5\sigma$  in the SSM, using similar subcaptions as in figure 9.2. The plotted rectangles are all equal, having diagonals  $\lambda$  and shorter edge length  $\sigma$ .

The particle density (see table 9.2) follows from  $\rho = 8/(\tilde{a}\tilde{b}\tilde{c})$ , since we have four basis particles in the conventional fco unit cell, each of which is accompanied by an extra particle shifted by  $\tilde{\mathbf{v}}_2$ .

- $e = 4\epsilon$ . Proceeding further in the pressure range we arrive at a lamellar structure, where each lamella is a hexagonally close-packed lattice plane. Using an appropriate coordinate system we can describe these lattice planes by  $\tilde{\mathbf{a}} = \sigma \hat{\mathbf{x}}$  and  $\tilde{\mathbf{b}} = \sigma/2 \hat{\mathbf{x}} + \sigma\sqrt{3}/2 \hat{\mathbf{y}}$ . The stacking of these hexagonal layers is determined by the shoulder width. The distance to the twelve *third* nearest neighbours of a particle, situated in the two adjacent layers, is equal to  $\lambda$ , e.g.,  $|\tilde{\mathbf{a}} + \tilde{\mathbf{c}}| = \lambda$ . This leads to a hexagonal 3D lattice with  $\tilde{\mathbf{c}} = \tilde{c} \hat{\mathbf{z}}$  and  $\tilde{c} = \sqrt{\lambda^2 - \sigma^2} = \sigma\sqrt{5}/2 \simeq 1.12\sigma$ . The geometry of this structure is illustrated in figure 9.3(a). The arrangement of particles in the rectangular arrangement indicated by black lines is quite typical for many MECs of this particular shoulder width.
- $e = 5\epsilon$ . At even higher pressure values only compact structures are encountered, the next one having the symmetry of an sfco lattice with one extra basis particle. The face centred particle is (w.l.o.g.) positioned at the  $\tilde{a}$ - $\tilde{b}$  face. The  $\tilde{b}$ - $\tilde{c}$  face is determined by the rectangle described in the previous item [see figure 9.3(b)],  $\tilde{\mathbf{c}} = \sigma \hat{\mathbf{z}}$  and  $\tilde{\mathbf{b}} = \sqrt{5}\sigma/2 \hat{\mathbf{y}}$ . The rest of the structure parameters are obtained by the fact that the extra basis particle touches the four particles of one  $\tilde{b}$ - $\tilde{c}$  face and the two adjacent face centred particles at the hard core, i.e.,  $|\tilde{\mathbf{v}}_2| = |\tilde{\mathbf{v}}_2 - \tilde{\mathbf{b}}| = |\tilde{\mathbf{v}}_2 - \tilde{\mathbf{c}}| = |\tilde{\mathbf{v}}_2 - (\tilde{\mathbf{b}} + \tilde{\mathbf{c}})| = |\tilde{\mathbf{v}}_2 - (\tilde{\mathbf{a}} + \tilde{\mathbf{b}})/2| = |\tilde{\mathbf{v}}_2 - [(\tilde{\mathbf{a}} + \tilde{\mathbf{b}})/2 + \tilde{\mathbf{c}}]| = \sigma$ . This gives

$$\tilde{\mathbf{a}} = \tilde{a} \hat{\mathbf{x}}, \quad \tilde{a} = \sqrt{3}\sigma + \sqrt{4\sigma^2 - \lambda^2} = \left(\sqrt{3} + \sqrt{7}/2\right)\sigma \simeq 3.05\sigma, \quad (9.5a)$$

$$\begin{aligned} \tilde{\mathbf{v}}_2 &= \frac{1}{2} \left( \sqrt{4\sigma^2 - \lambda^2} \hat{\mathbf{x}} + \sqrt{\lambda^2 - \sigma^2} \hat{\mathbf{y}} + \sigma \hat{\mathbf{z}} \right) = \\ &= \sqrt{7}\sigma/4 \hat{\mathbf{x}} + \sqrt{5}\sigma/4 \hat{\mathbf{y}} + \sigma/2 \hat{\mathbf{z}} \simeq \sigma(0.66 \hat{\mathbf{x}} + 0.56 \hat{\mathbf{y}} + 0.50 \hat{\mathbf{z}}). \end{aligned} \quad (9.5b)$$

It is interesting to note that in this structure  $|\tilde{\mathbf{v}}_2 + (\tilde{\mathbf{b}} - \tilde{\mathbf{a}})/2 (+\tilde{\mathbf{c}})| = \lambda$ , which means that e.g. the particles at  $\tilde{\mathbf{b}} + \tilde{\mathbf{v}}_2$  and  $(\tilde{\mathbf{a}} + \tilde{\mathbf{b}})/2$  touch each other at the shoulder.

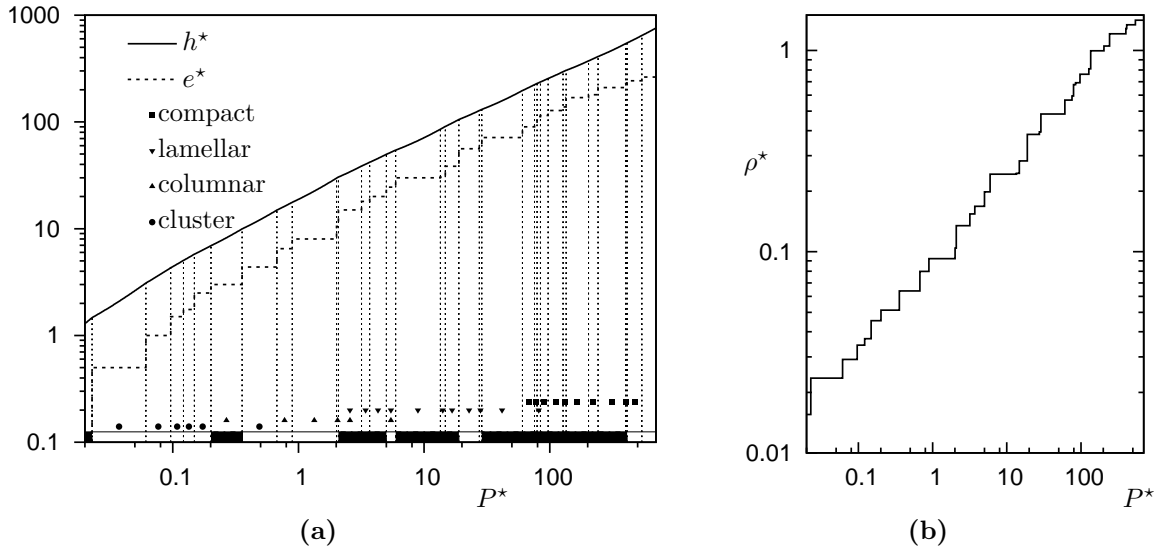


Figure 9.4: (a): Reduced enthalpy and energy per particle ( $h^*$  and  $e^*$ ) versus reduced pressure  $P^*$  on a double logarithmic scale, for the SSM with  $\lambda = 4.5\sigma$ . Symbols (cf. legend) specify to which archetype the corresponding MEC belongs, the horizontal bars at the bottom indicate that no hard core contacts occur in the respective MECs. In (b) the corresponding reduced density  $\rho^*$  is plotted, also on a double-logarithmic scale.

- $e = 7\epsilon$ . The last non-trivial compact structure is a bcc crystal, see figures 9.2(h) and 9.3(c). Again, one side face is characterised by the before mentioned rectangle ( $\tilde{c} = \sigma$  and  $b = \sqrt{5}\sigma/2$ ), while  $\tilde{a}$  is determined by the fact that the centred particle touches all eight particles at the corners of the unit cell, i.e.,  $\tilde{a} = \sqrt{4\sigma^2 - \lambda^2} = \sqrt{7}\sigma/2$ .
- $e = 9\epsilon$ . As discussed previously, the high-pressure limiting case MEC is in this case an fcc crystal with cubic edge length  $\tilde{a} = \sqrt{2}\sigma$ .

### 9.2.2 Intermediate Shoulder Width ( $\lambda = 4.5\sigma$ )

Much larger diversity in the MECs can be found for a shoulder width of  $\lambda = 4.5\sigma$ . The two limiting cases are now an hcp structure at high pressure values (see table 9.1) and, as always, an fcc structure at low pressure. Our search strategy revealed in total 33 MECs, where we considered up to 10 basis particles in the unit cell.

Besides the straightforward investigation concerning the lattice symmetry and conventional unit cell parameters, we will now be able to discern a clear ordering of the occurring MECs into four structural archetypes: at low pressure clusters are preferred, increasing the pressure favours columns, which then transform into lamellae and finally into compact structures. Figure 9.4 shows the phase diagram for our intermediate shoulder width, while numerical details can be found in tables 9.3 and G.5. A visualisation of all 33 MECs is given in figure 9.5.

From the collected data one can see, that at low pressure (i.e., up to  $P^* \sim 0.5$ ) the preferred MECs are clusters. We observe a gradually increasing number of particles in the cluster (usually equal to the number of basis particles) up to eight particles. In addition, a strong interplay between the shape of the cluster and the unit cell can be observed: the more aspherical the cluster, the lower the symmetry of the lattice. This trend stems from the tendency to avoid inter-cluster shoulder overlaps, i.e., for many clusters the energy per particle is just given by the number of overlaps inside a single cluster, where the particles are usually closely packed. Since the spatial extent of the clusters is always much smaller than the shoulder range  $\lambda$ , the energy per particle for many cluster phases is just given by the number of distinct particle pairs (overlaps) inside one cluster divided by the number of particles  $n$  forming that cluster, hence  $e^* = (n - 1)/2$ . A nice example for the complexity of the cluster phases is depicted in figure 9.5(4), where tetrahedral clusters populate the lattice points of a triclinic lattice, while another four-particle cluster is situated in the body of the unit cell in such as to avoid inter-cluster overlaps. It is therefore a cluster phase with four particles per cluster, hence the name *clu(4)* in table 9.3.

At the upper pressure limit of the cluster regime, the cluster MECs compete with structures of another archetype, the columnar ones. The transition from clusters to columns does not appear at a definite pressure value: After the first columnar structure occurs at  $P^* \sim 0.3$ , an eight-particle cluster MEC appears at even higher pressure ( $P^* \sim 0.5$ ), which exhibits a relatively large number of inter-cluster overlaps. Only above  $P^* \gtrsim 0.68$  a sequence of columnar structures represent the MECs. These MECs can form single or double stranded columns, which now in turn tend to avoid inter-columnar overlaps (particles of different strands of a double column always touch at the hard core).

The next transition, from the columnar to the lamellar structures, appears much smoother, since the columns approach each other in one preferred direction, at some point building lamellae that consist of parallel columns, see figures 9.5(12,15). Besides these intermediate transition stages, the lamellar MECs follow a clear pattern for their arrangement, while always tending to avoid inter-lamellar shoulder overlaps: Starting with single-layer lamellae (usually in a 2D hexagonal shape) the nearest neighbour distance decreases with increasing pressure. If the possibility to maximise the particle density inside a single layer is exhausted, double-layer lamellae are formed, where again the 2D particle density inside one layer increases with pressure. While neighbouring particles of different layers in the *same* lamella touch each other at the hard cores, the distance between the lamellae is ruled by two conditions: Firstly, that particles of layers that are part of adjacent lamellae and face each other, e.g. the blue particles of the leftmost lamella in figure 9.5(19) and the red ones, may overlap with their shoulders. Secondly, that particles of layers in adjacent lamellae that do *not* face each other, never overlap [e.g. the red particles and the green ones of the leftmost lamella in figure 9.5(19)]. There also appears one triple-layer lamellar structure [see figure 9.5(24)], at the transition regime to what we call compact phases.

Compact MECs are usually characterised by a large number of nearest neighbours and the absence of any hard core contact [see the horizontal bar in figure 9.4(a)], except at very high pressures, where of course finally a CPS appears, in this case an hcp one. A detailed, geometrical analysis of all 33 MECs is given in appendix D.

structure					stable up to	
lattice	$n_b$	shape	$e^*$	$\rho^*$	$h^*$	$P^*$
fcc	1	clu	0	0.0155	1.47	0.0228
sm	2	clu	1/2	0.0235	3.10	0.0612
sfcm	3	clu	1	0.0291	4.30	0.0963
tric	8	clu (4)	3/2	0.0343	5.05	0.122
tric	4	clu	7/4	0.0369	5.77	0.148
tric	6	clu	5/2	0.0454	6.93	0.201
bco	1	col	3	0.0512	9.95	0.356
bco	8	clu	35/8	0.0638	14.9	0.675
tric	2	col	13/2	0.0799	17.7	0.892
sm	2	col	8	0.0923	29.8	2.01
tric	2	col	21/2	0.104	30.5	2.08
bco	1	lam/col	15	0.135	38.6	3.17
trig	1	lam	18	0.154	41.9	3.69
tric	2	lam	20	0.168	49.7	5.00
tric	2	lam (col)	49/2	0.198	54.4	5.94
trig	2	lam	30	0.243	85.5	13.5
trig	2	lam	61/2	0.245	90.6	14.7
ct	2	lam	77/2	0.283	105.	18.9
sfcm	2	lam	56	0.383	127.	27.5
sm	2	lam	58	0.394	131.	28.8
fco	2	lam	143/2	0.484	197.	60.6
bcc	1	com	90	0.567	223.	75.6
ct	1	com	96	0.594	229.	79.1
tric	3	lam	337/3	0.677	237.	84.3
trig	1	com	115	0.692	255.	96.9
sc	1	com	128	0.763	295.	128.
hex	1	com	138	0.811	304.	135.
bcc	1	com	169	0.997	373.	203.
ct	1	com	180	1.05	410.	242.
sfcm	1	com	210	1.21	542.	403.
fcc	1	com	229	1.29	550.	413.
ct	1	com	243	1.34	645.	540.
hcp	2	com	263	1.41	$\infty$	$\infty$

Table 9.3: Stable crystal structures of the SSM for reduced shoulder width  $\lambda^* = 4.5$ .  $n_b$  is the number of particles in the basis, the general shape is indicated by the abbreviations for cluster, columnar, lamellar, and compact structures; additional information in the third column is explained in the text. Irrational numbers are given as floating point values.

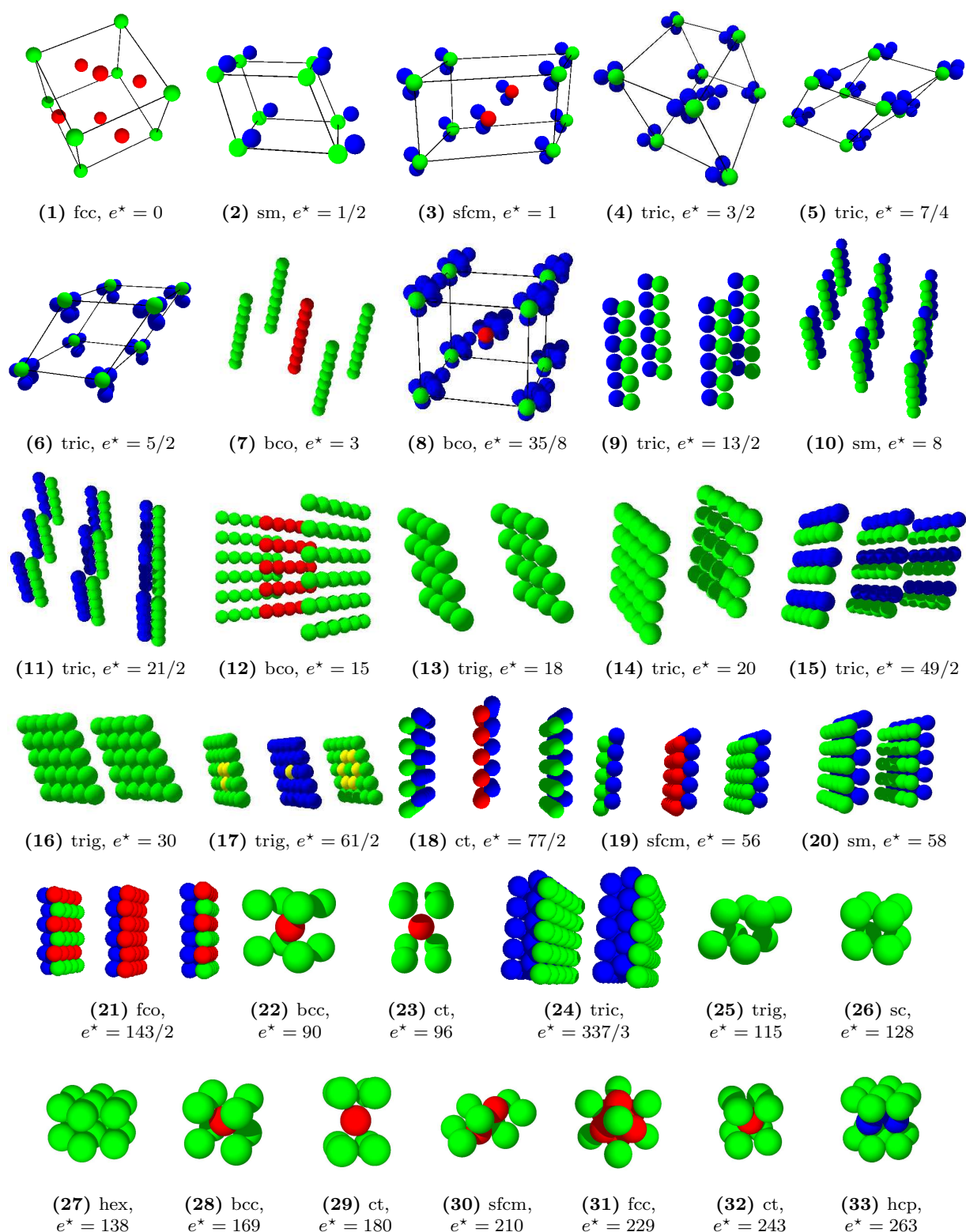


Figure 9.5: Visualisation of all 33 ordered equilibrium structures for the SSM with  $\lambda^* = 4.5$ . Structures are characterised by standard abbreviations (see table G.3) and their respective  $e^*$ -value. Colour code: green – particles at the corner positions of the conventional unit cell; red – particles at body or face centred positions; blue – additional basis particles. The shoulders of the yellow particles in panel (17) touch the ones of the other yellow particles, located in the neighbouring layers.



### 9.2.3 Large Shoulder Width ( $\lambda = 10\sigma$ )

Finally, we consider the case of a large shoulder width for which we have chosen a value of  $\lambda = 10\sigma$ . Since the hard core region is now relatively small compared to the shoulder range, at low pressures/densities the core plays a minor role and the system becomes closely related to the penetrable sphere model (PSM, see section 2.6) [115]. The PSM belongs to a class of soft matter systems where particles are able to solidify in so called cluster phases [116], i.e., where particles form stable clusters located at the positions of periodic lattices. Evidence for this particular phase behaviour has been found in density functional based investigations and in computer simulations, for the PSM [117] and via purely theoretical considerations, combined with computer simulations, for a closely related model potential, the generalised Gaussian core model [24, 25, 118, 119]. As we have already seen for intermediate shoulder width, such cluster phases are also stable for the square-shoulder system at low pressure values, where the particles' hard cores have a negligible effect on the properties of the system. We will show that, not surprisingly, this cluster region becomes more pronounced for large shoulder width.

Since the MECs are expected to be rather complex we have considered up to 29 basis particles in our GA based search strategy, with up to 22 being actually required for the resulting MECs. In total we have identified as many as 47 MECs, i.e., a relatively large number, for which we could not perform an exact, i.e. analytical, geometrical analysis, for practical reasons. Therefore, in figure 9.6, we cannot give information about exact hard core contacts using a horizontal bar at the bottom of the plot like we did for intermediate shoulder width in figure 9.4. Nevertheless the thermodynamic properties of all these MECs are displayed in figure 9.6 and given numerically in table G.6. We point out that the high pressure limiting configuration is an fcc lattice with  $e^* = 2947$ . For the case  $\lambda = 10\sigma$  the rule for the sequence of structural archetypes (cluster – columnar – lamellar – compact structures) is strictly obeyed (see symbols in figure 9.6).

As expected cluster structures emerge at low pressure values. A few examples of the ten cluster structures that have been identified are depicted in Figures 9.7(a–c). The clusters can contain as many as 22 particles [e.g., in the structure depicted in Figure 9.7(c)] and are arranged in various symmetry lattices (see table G.6). An example of a typical cluster is depicted in Figure 9.7(b); in general the intra-cluster arrangement of the particles turns out to be irregular.

At  $P^* \simeq 0.76$  the transition to columnar structures occurs. The relatively large shoulder width allows for much more complicated columnar morphologies than for short or intermediate shoulder widths, including multi-columnar arrangements or complex helical columns — cf. figures 9.7(d–f) — while the number of different columnar structures is significantly smaller than for intermediate shoulder width. In figure 9.7(e) a side view of a single column gives evidence of its complex internal structure: Ten basis particles are required to parameterise this columnar MEC, which can be viewed as a helical structure. We note that helical columns have also been observed in experiment for a particular class of colloidal particles [120]. The other two columnar structures are examples for multi-columnar arrangements: Triple columns form the MEC displayed in Figure 9.7(d), while

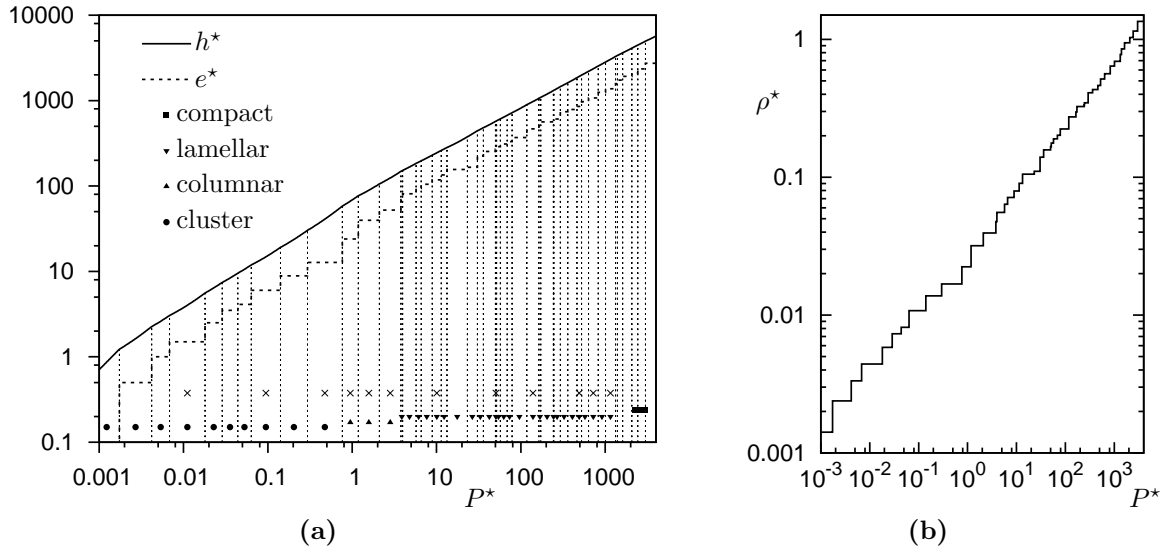


Figure 9.6: (a): Reduced enthalpy and energy per particle ( $h^*$  and  $e^*$ ) versus reduced pressure  $P^*$  on a double logarithmic scale, for the SSM with  $\lambda = 10\sigma$ . Symbols (cf. legend) specify to which structural archetype the corresponding MEC belongs, the crosses mark MECs that are visualised in figure 9.7. In (b) the corresponding reduced density  $\rho^*$  in dependence on reduced pressure is plotted, also on a double-logarithmic scale.

the MEC shown in Figure 9.7(f) can be described as six parallel single columns that are nearly in close contact and are aligned in parallel to form a sixfold column, as can be seen from the rightmost column, where the direction of projection is parallel to the columnar axis.

Most of the MECs identified for the case  $\lambda = 10\sigma$  have lamellar character: in total we have identified as many as 28 lamellar MECs. Again, we observe a strategy similar to that identified for  $\lambda = 4.5\sigma$ : First the particle arrangement within the single layer structures is optimised; then, if this possibility for closely packed arrangements is exhausted, multi-layer structures are formed. The large shoulder width is responsible both for the large inter-lamellar distance as well as the close contact within the lamellae: One has the impression that the large range of the shoulder compactifies adjacent layers, bringing them in direct contact, while maximising at the same time the distance between these groups of layers [cf. figures 9.7(g–l)].

Finally, we enter the regime of compact structures. Since they resemble very closely the MECs that have been identified for  $\lambda = 4.5\sigma$ , they need not be visualised explicitly, see table G.6 instead. The next section will provide a more fundamental understanding of the general rule for the MECs of the SSM to build first clusters, then columns, then lamellae, and finally compact structures with increasing pressure.

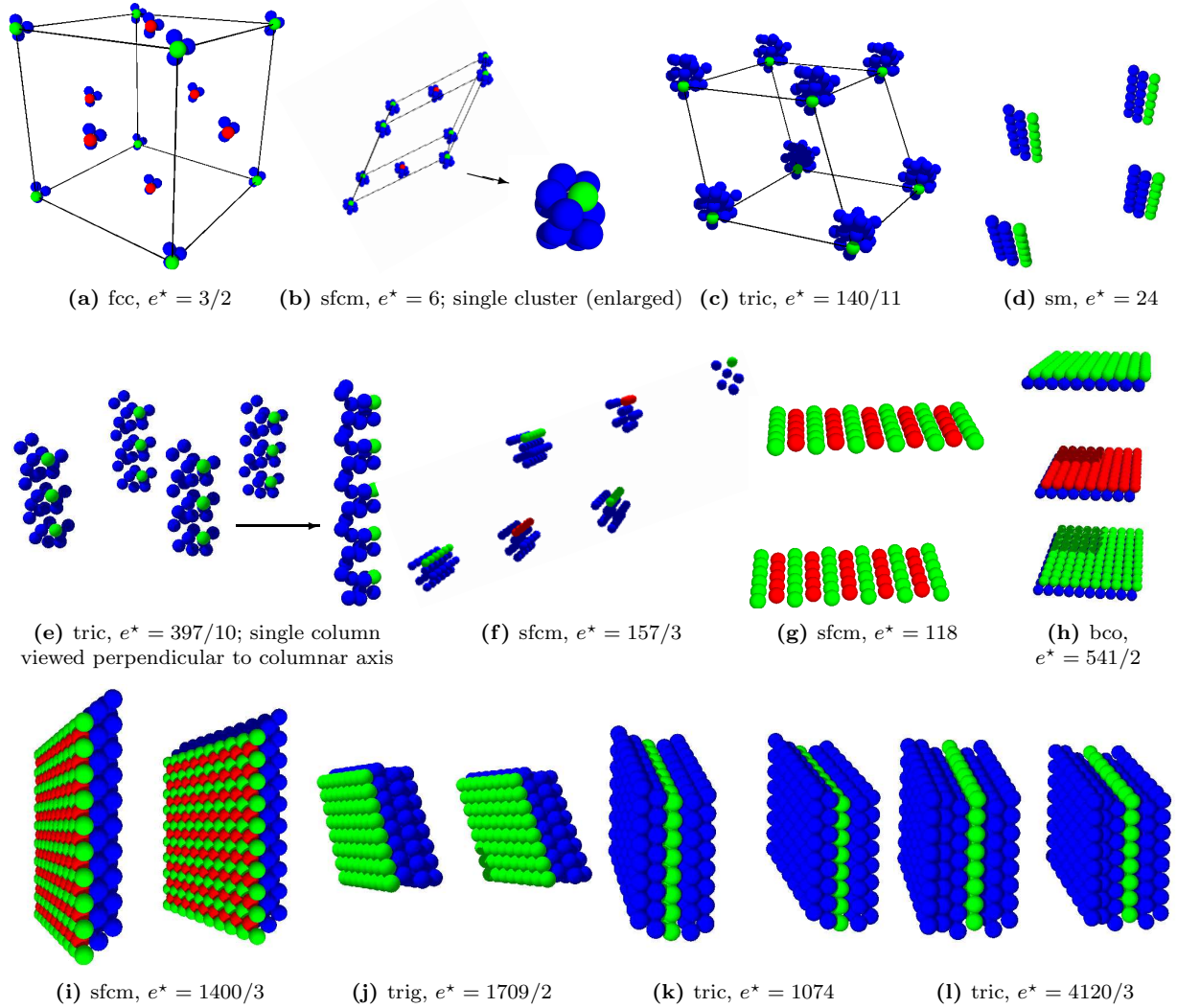


Figure 9.7: Visualisation of selected MECs for the SSM with  $\lambda = 10\sigma$  (see figure 9.6). Structures are characterised by standard abbreviations (see table G.3) and their respective  $e^*$ -value. Colour code: green – particles at the corner positions of the conventional unit cell; red – particles at body or face centred positions; blue – additional basis particles.

## 9.3 Application of the Continuum Theory

### 9.3.1 Self-Energy

As mentioned in section 5.8, the first step when applying the continuum theory (CT) to a certain interaction potential is, to ascertain the self-energy term in equation (5.97), i.e., to determine how the so-called “energy assigned to a continuum matter point” should be calculated. For hard core particles there is a rather intuitive way to solve this problem, also taken in [27]. It simply relies on the fact, that the only way to obtain a finite value

for the integral of the interaction potential over space is to exclude the hard core from the integration region,

$$e_{\mathcal{C}}^{\text{HC}}(\boldsymbol{\mu}) = \frac{1}{2} \int_{\mathbb{R}^3 \setminus B_{\sigma}(\boldsymbol{\mu})} \hat{\rho}(\mathbf{r}) \phi(|\mathbf{r} - \boldsymbol{\mu}|) d^3r, \quad (9.6)$$

in this way directly approximating equation (5.95) ( $B_{\sigma}(\boldsymbol{\mu})$  is a sphere of radius  $\sigma$  centred at  $\boldsymbol{\mu}$ ). But this definition does not only have the disadvantage of cutting a hole out of the integration regime which usually makes the evaluation of the integral more difficult, it also lacks the ability to reflect certain physical properties of the corresponding system of real hard core particles, as will be explained for the interaction of the SSM in the following.

First we insert the chosen potential together with the expression for the density of equation (5.91) into equation (9.6) and obtain

$$e_{\mathcal{C}}^{\text{HC}}(\boldsymbol{\mu}) = \frac{\epsilon \rho_{\text{eff}}}{2} \int_{\mathbb{R}^3 \setminus B_{\sigma}(\boldsymbol{\mu})} \theta_{\mathcal{C}}(\mathbf{r}) \theta(\lambda - |\mathbf{r} - \boldsymbol{\mu}|) d^3r = \frac{\epsilon \rho_{\text{eff}}}{2} \int_{B_{\lambda}(\boldsymbol{\mu}) \setminus B_{\sigma}(\boldsymbol{\mu})} \theta_{\mathcal{C}}(\mathbf{r}) d^3r, \quad (9.7)$$

where the conventional Heaviside step-function

$$\theta(r) = \begin{cases} 0, & r < 0 \\ 1, & r \geq 0 \end{cases} \quad (9.8)$$

was used.

Now consider a single cluster of  $N$  particles, approximated by a continuum matter sphere of radius  $R$  and centre at  $\mathbf{C}$ , that satisfies  $N = \frac{4}{3}\pi R^3 \rho_{\text{eff}}$ . In addition, we assume that  $\lambda$  is greater than the spatial extent of the cluster, i.e., the shoulders of all particles in the cluster overlap. For the continuum matter sphere this means  $\lambda > 2R$ . The energy of any particle in the discrete particle treatment is simply  $\epsilon/2$  times the number of shoulder overlaps with the other particles in the cluster,  $N - 1$ . Since, in the continuum treatment, the whole cluster, i.e., the whole sphere  $B_R(\mathbf{C})$  of radius  $R$  and centre at  $\mathbf{C}$ , is fully contained within a sphere of radius  $\lambda$  centred around any point inside  $B_R(\mathbf{C})$ , we obtain

$$e_{\mathcal{C}}^{\text{HC}}(\boldsymbol{\mu}) = \frac{\epsilon \rho_{\text{eff}}}{2} \int_{B_R(\mathbf{C}) \setminus B_{\sigma}(\boldsymbol{\mu})} d^3r. \quad (9.9)$$

The integral in this formula is the volume of the sphere  $B_R(\mathbf{C})$  representing the cluster, with a hole cut out by the sphere  $B_{\sigma}(\boldsymbol{\mu})$ . Clearly, this volume is *not* the same for all points  $\boldsymbol{\mu}$  in  $B_R(\mathbf{C})$ , it is larger for points  $\boldsymbol{\mu}$  at the surface of the sphere that represents the cluster. In other words, the physical reality that all particles have the same energy, irrespective of their position in the cluster, is not reflected by the CT when the energy assigned to a continuum matter point is given by equation (9.6). In fact, in the case discussed here we obtain the counterintuitive result, that points (i.e., particles) on the surface of the cluster sphere even have higher energy. Therefore we use a different way to derive the energy

assigned to a continuum matter point.

Consider an arbitrary arrangement of square–shoulder particles for which no hard core overlaps occur. Compare the energies of these particles with those of particles that are arranged exactly on the same positions, but interact via a penetrable sphere interaction [equation (2.11)] with the same shoulder parameters  $\lambda$  and  $\epsilon$ . Obviously, each particle has the *same* energy, no matter whether the interaction contains a hard core or not, because hard core overlaps are simply not allowed for the construction of the particle arrangement. As a consequence, we also demand the CT to provide consistent results for either interaction in the case of equal  $\hat{\rho}(\mathbf{r})$ .

But what are the differences between the square–shoulder and the penetrable sphere models, that the CT should also reflect? Obviously, the hard core is responsible for the exclusion of any configuration of the particles that would lead to an overlap of the cores. The CT cannot fully reproduce this phenomenon, since the exact information about particle positions in the aggregate is lost upon approximating the aggregate by the continuum matter. What is accounted for is the average density inside the aggregate,  $\rho_{\text{eff}}$ , as well as the aggregate’s shape. Therefore, the difference between the square–shoulder and the penetrable sphere model in the CT is, that the hard core delimits the effective density inside the aggregate, its maximum value is the density of close–packed hard spheres, i.e.,

$$0 < \rho_{\text{eff}} \leq \frac{\sqrt{2}}{\sigma^3} . \quad (9.10)$$

As long as this condition is met, the energies assigned to a point should be the same for SSM and PSM interactions, respectively<sup>3</sup>.

Let us therefore insert the PSM interaction [equation (2.11)] into equation (5.97),

$$e_C(\boldsymbol{\mu}) = \frac{\epsilon \rho_{\text{eff}}}{2} \int_{\mathbb{R}^3} \theta_C(\mathbf{r}) \theta(\lambda - |\mathbf{r} - \boldsymbol{\mu}|) d^3r - e_{\text{self}} = \frac{\epsilon \rho_{\text{eff}}}{2} \int_{B_\lambda(\boldsymbol{\mu})} \theta_C(\mathbf{r}) d^3r - e_{\text{self}} . \quad (9.11)$$

In the PSM there is an easy way to estimate the self–energy. Consider a particle positioned at  $\boldsymbol{\mu}$  and let there be  $N$  particles in total in a sphere of radius  $\lambda$  centred at  $\boldsymbol{\mu}$ , i.e.,

$$N = \sum_{\nu_i \in B_\lambda(\boldsymbol{\mu})} 1 \quad \longrightarrow \quad \rho_{\text{eff}} \int_{B_\lambda(\boldsymbol{\mu})} \theta_C(\mathbf{r}) d^3r , \quad (9.12)$$

with the integral being used as an approximation for  $N$  in the CT, see equations (5.92) and (5.93). Clearly, the energy of the particle at  $\boldsymbol{\mu}$  is, according to equation (5.95), given

---

<sup>3</sup>Of course there can be configurations for the PSM that satisfy equation (9.10) but violate the hard core condition. But as long as there exists a possible configuration for the SSM, we have to keep the corresponding  $\rho_{\text{eff}}$  under consideration.

by

$$e_{\boldsymbol{\mu}} = \frac{\epsilon}{2}(N - 1) \longrightarrow \frac{\epsilon\rho_{\text{eff}}}{2} \int_{B_{\lambda}(\boldsymbol{\mu})} \theta_C(\mathbf{r}) d^3r - \frac{\epsilon}{2}, \quad (9.13)$$

where  $N$  has been replaced by the CT approximation [equation (9.12)]. Comparison with equation (9.11) reveals, that the self-energy term for the PSM is simply

$$e_{\text{self}} = \frac{\epsilon}{2}, \quad (9.14)$$

reflecting the fact, that the integration over the whole interaction sphere yields one additional count of overlaps, the one with the reference particle itself.

In summary we obtain for the energy assigned to a point of continuum matter interacting via a square-shoulder potential

$$e_C(\boldsymbol{\mu}) = \frac{\epsilon}{2} \left( \rho_{\text{eff}} \int_{B_{\lambda}(\boldsymbol{\mu})} \theta_C(\mathbf{r}) d^3r - 1 \right), \quad (9.15a)$$

subject to the additional condition

$$0 < \rho_{\text{eff}} \leq \frac{\sqrt{2}}{\sigma^3}. \quad (9.15b)$$

This definition has the advantage of leading to the same energy for all points  $\boldsymbol{\mu}$  within a small, isolated cluster. At first glance we seem to get the drawback that, due to the subtraction in equation (9.15a), the energy for a purely repulsive interaction can become negative, which would also be an unphysical result. But taking a closer look we note, that this can only happen in two cases:

- For points belonging to a very small and isolated aggregate, which would correspond to an aggregate of less than one particle, where  $\int_{B_{\lambda}(\boldsymbol{\mu})} \theta_C(\mathbf{r}) d^3r$  is so small that  $\rho_{\text{eff}} \int_{B_{\lambda}(\boldsymbol{\mu})} \theta_C(\mathbf{r}) d^3r < 1$ , and
- for a very dilute continuum matter ( $\rho_{\text{eff}}^* \ll 1$ ), for which the corresponding PSM or SSM systems would most probably not be in equilibrium even for arbitrarily small pressure (at  $T = 0$ ),

both unphysical situations anyway.

Now we are ready to apply the CT to the four types of aggregate shapes (see section 5.8). To start with the simplest case, where calculations can be done analytically without further approximations, we first consider the homogeneous continuum matter, corresponding to compact phases. Symbolic calculations in the following sections were done with the aid of *Mathematica* [70].

### 9.3.2 Homogeneous Distribution

We first repeat the findings of section 5.8 for this case: The continuum matter is completely homogeneous,

$$\hat{\rho}(\mathbf{r}) \equiv \rho_{\text{eff}} \equiv \rho_c \iff \theta_c(\mathbf{r}) \equiv 1 \quad \forall \mathbf{r} \in \mathbb{R}^3, \quad (9.16a)$$

and the energies of all points in space are equal, hence

$$e_c = e_c(\mathbf{r}) \quad \forall \mathbf{r} \in \mathbb{R}^3. \quad (9.16b)$$

Inserting this into equation (9.15a), we obtain for the (average) continuum matter enthalpy, equation (5.101),

$$h_c = \epsilon \rho_{\text{eff}} \frac{2\pi}{3} \lambda^3 - \frac{\epsilon}{2} + \frac{P}{\rho_{\text{eff}}}. \quad (9.17)$$

$\epsilon$  and  $\lambda$  are the interaction parameters, and the ambient pressure  $P$  is the independent thermodynamic variable. The equilibrium continuum matter distribution is then found by minimising the enthalpy of equation (9.17) at given  $\epsilon$ ,  $\lambda$ , and  $P$  by varying  $\rho_{\text{eff}}$ , the only remaining variable there. Thus minimisation is easy, equation (9.17) has exactly one extremum which is a minimum in the range of positive real numbers, setting the first derivative to zero yields

$$\rho_{\text{eff}} = \sqrt{\frac{3P}{2\pi\epsilon\lambda^3}}. \quad (9.18)$$

Remember now, that we always have to satisfy the ‘‘hard core’’ condition of equation (9.15b) for the continuum matter. The strictly monotonous behaviour of equation (9.18) gives rise to a pressure threshold  $P_t$  above which always the close-packed structure ( $\rho_{\text{eff}}^* = \sqrt{2}$ ) is the equilibrium one:

$$P_t = \frac{4\pi}{3} \left(\frac{\lambda}{\sigma}\right)^3 \frac{\epsilon}{\sigma^3}. \quad (9.19)$$

In summary we obtain for a homogeneous continuum matter distribution, describing compact structures of the SSM:

	$e_c$	$\rho_c$	$h_c$	
$P < P_t$	$\sqrt{\frac{2\pi}{3}\lambda^3 P \epsilon - \frac{\epsilon}{2}}$	$\sqrt{\frac{3P}{2\pi\epsilon\lambda^3}}$	$2\sqrt{\frac{2\pi}{3}\lambda^3 P \epsilon - \frac{\epsilon}{2}}$	(9.20)
$P \geq P_t$	$\frac{2\pi}{3}\sqrt{2}\left(\frac{\lambda}{\sigma}\right)^3 \epsilon - \frac{\epsilon}{2}$	$\frac{\sqrt{2}}{\sigma^3}$	$\frac{2\pi}{3}\sqrt{2}\left(\frac{\lambda}{\sigma}\right)^3 \epsilon - \frac{\epsilon}{2} + \frac{P\sigma^3}{\sqrt{2}}$	

By introducing what we call shoulder-reduced quantities,

$$\check{P} = \frac{P\sigma^6}{\epsilon\lambda^3} = \frac{P^*}{\lambda^{*3}}, \quad (9.21a)$$

$$\check{e} = \frac{e^* + \frac{1}{2}}{\lambda^{*3}}, \quad (9.21b)$$

$$\check{h} = \frac{h^* + \frac{1}{2}}{\lambda^{*3}}, \text{ and} \quad (9.21c)$$

$$\check{\rho} = \rho^*, \quad (9.21d)$$

we can write equation (9.20) in a compact way:

	$\check{e}_c$	$\check{\rho}_c$	$\check{h}_c$
$\check{P} < \frac{4\pi}{3}$	$\sqrt{\frac{2\pi}{3}\check{P}}$	$\sqrt{\frac{3}{2\pi}\check{P}}$	$2\sqrt{\frac{2\pi}{3}\check{P}}$
$\check{P} \geq \frac{4\pi}{3}$	$\frac{2\pi}{3}\sqrt{2}$	$\sqrt{2}$	$\frac{2\pi}{3}\sqrt{2} + \frac{\check{P}}{\sqrt{2}}$

(9.22)

The main reason for the introduction of shoulder-reduced quantities is that, for all the expressions in equation (9.22), there appears no other variable than the shoulder-reduced pressure  $\check{P}$ . This means, the shoulder-reduced thermodynamic quantities, as functions of the shoulder-reduced pressure, are *independent* of both interaction potential parameters  $\epsilon$  and  $\lambda$ .<sup>4</sup> In graphical representations we will therefore use shoulder-reduced variables instead of the usual reduced ones from now on.

### 9.3.3 Planar Lamellae

We consider an infinite periodic array of parallel, planar lamellae of thickness  $D$ , separated by a distance  $L$  (see figure 9.8). Obviously,  $D < L$ . W.l.o.g. we put the origin of a Cartesian coordinate system into the centre of one lamella, with the  $x$ -axis perpendicular to the lamellar plane and the  $y$ - and  $z$ -axes parallel to this plane. The continuum matter density in this case can be written as

$$\hat{\rho}(\mathbf{r}) = \rho_{\text{eff}}\theta_c(\mathbf{r}) = \rho_{\text{eff}} \sum_{i=-\infty}^{\infty} \theta_{iL-\frac{D}{2}, iL+\frac{D}{2}}(x), \quad (9.23)$$

with  $x$  being the  $x$ -coordinate of  $\mathbf{r}$  and  $\theta_{a,b}(x)$  being an abbreviation for  $\theta(x-a)\theta(b-x)$ , which is nothing else than 1 if  $a < x < b$  and 0 otherwise. As discussed in section 5.8, the points of the segment obtained by intersecting a line orthogonal to the lamellae with one arbitrary lamella are *sufficient* to consider for calculating the average energy (exactly half the segment would be necessary *and* sufficient). Using  $B_\lambda(x)$  as an abbreviation for the

---

<sup>4</sup>They are of course also independent of  $\sigma$ , which was chosen to be the unit of measure for lengths. Therefore, to be precise, we should say the shoulder-reduced quantities are independent of  $\lambda^*$ .



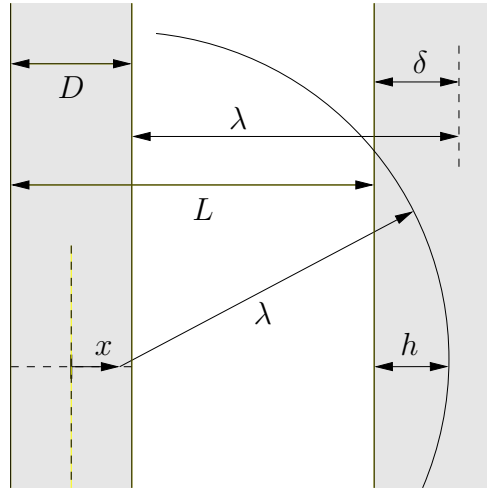


Figure 9.8: Cut through two of the periodically recurring lamellae of thickness  $D$  and distance  $L$ . Qualitatively different points are denoted by  $x$ . If  $L \gtrsim \lambda$ ,  $\delta$  and  $h$  can be defined as labelled.

sphere of radius  $\lambda$  with centre at  $(x, 0, 0)$ , we obtain

$$e_c = \frac{1}{D} \int_{-D/2}^{D/2} \frac{\epsilon}{2} \left( \rho_{\text{eff}} \int_{B_\lambda(x)} \theta_c(\mathbf{r}') d^3r' - 1 \right) dx. \quad (9.24)$$

This 4D integral can indeed be solved, the result is presented in appendix E. But when combining it with the pressure term using equation (5.104) to obtain the continuum matter enthalpy per particle  $h_c = e_c + P/\rho_c$ , minimising this complicated function simultaneously w.r.t.  $L$ ,  $D$ , and  $\rho_{\text{eff}}$  (the parameters describing the continuum matter) is a hopeless venture. Therefore we decided to investigate the lamellar energies only under some additional assumptions:

$$D, \sigma \ll \lambda \quad \text{and} \quad L \gtrsim \lambda. \quad (9.25)$$

They were motivated by results from the genetic algorithm (see section 9.2), where the assumptions (9.25) were satisfied for all lamellar MECs (except, of course,  $\sigma \ll \lambda$  in the case of short shoulder width). But we will show at the end of this section, that these assumptions are self-contained, i.e., they can be justified solely within the CT for the SSM without using any input from other theoretical or even experimental approaches.

To calculate the continuum matter energy per particle [equation (9.24)] under these assumptions we follow the idea of Glaser *et al.* [27] and split up this formula in the following way: Firstly into a contribution of the lamella that contains the origin (and hence the centres of all considered spheres  $B_\lambda(x)$  with  $x \in [-D/2, D/2]$ ) which we call  $e_{\text{intra}}$ , that also contains the self-energy correction. And secondly the contribution stemming from

overlaps of the considered spheres  $B_\lambda(x)$  with all other lamellae,

$$e_C = \underbrace{\frac{1}{D} \int_{-D/2}^{D/2} \frac{\epsilon}{2} \left( \rho_{\text{eff}} \int_{B_\lambda(x)} \theta_{-\frac{D}{2}, \frac{D}{2}}(x') d^3 r' - 1 \right) dx}_{e_{\text{intra}}} + \frac{1}{D} \int_{-D/2}^{D/2} \frac{\epsilon}{2} \rho_{\text{eff}} \int_{B_\lambda(x)} \sum_{i \neq 0} \theta_{iL - \frac{D}{2}, iL + \frac{D}{2}}(x) d^3 r' dx. \quad (9.26)$$

The second condition of equation (9.25) guarantees, that from the contributions of the other lamellae all but those of the next neighbours vanish. Therefore, for the second part it is convenient to first consider just 2 lamellae and to call the resulting continuum matter energy per particle which stems from inter-lamellar overlaps  $e_{\text{inter}}$ . Note, that this splitting now really demands for  $x$  to range over the entire segment  $[-D/2, D/2]$  as an integration region, since for the case of only two lamellae there is no inversion (or mirror) symmetry at the origin (inside one lamella), which originally reduced the set of qualitatively different points  $\mathcal{N}$  of one lamella to only half the segment, see section 5.8. In total we obtain

$$e_C = e_{\text{intra}} + 2e_{\text{inter}}. \quad (9.27)$$

We first deal with the intra-lamellar part. The integral over  $d^3 r'$  is descriptively the overlap volume of the sphere centred around  $(x, 0, 0)$  having radius  $\lambda$  and the central lamella (that contains the origin). Because of  $D \ll \lambda$  we calculate it only to first order in  $D/\lambda$ , giving  $\lambda^2 \pi D$  — the volume of a flat cylindrical disc, which is *independent* of  $x$ . Therefore the result from the outer integral over  $x$  simply cancels the prefactor of  $1/D$ , yielding

$$e_{\text{intra}} \simeq \frac{\epsilon}{2} (\rho_{\text{eff}} \lambda^2 \pi D - 1). \quad (9.28)$$

In order to calculate

$$e_{\text{inter}} = \frac{1}{D} \int_{-D/2}^{D/2} \frac{\epsilon}{2} \rho_{\text{eff}} \int_{B_\lambda(x)} \theta_{L - \frac{D}{2}, L + \frac{D}{2}}(x) d^3 r' dx \quad (9.29)$$

we introduce the overlap parameter  $\delta$  (see figure 9.8), defined as

$$\delta = D + \lambda - L. \quad (9.30)$$

The assumption  $L \gtrsim \lambda$  can be formulated more exactly using this overlap parameter,

$$\delta < D \quad \text{and} \quad \delta \ll \lambda. \quad (9.31a)$$

The integration over  $d^3 r'$  can again be understood in terms of overlaps of the involved structures, i.e., the spheres  $B_\lambda(x)$  and the neighbouring lamella. For  $\delta \leq 0$  there would be no overlap at all between points in adjacent lamellae, i.e.,  $e_{\text{inter}}$  would be zero. Hence, at arbitrarily small ambient pressure, a lamellar configuration with  $\delta \leq 0$  will always be

compressed until a small gain in inter-lamellar energy through an appropriate positive overlap stabilises the configuration, we can assume

$$0 < \delta . \quad (9.31b)$$

Thus, all spheres  $B_\lambda(x)$  with  $x \in (D/2 - \delta, D/2]$  have a nonzero overlap volume with the neighbouring lamella, that has the shape of a spherical segment<sup>5</sup>. The occurring segments are cut from a sphere of radius  $\lambda$  and have a height  $h$  ranging from 0 to  $\delta$ . As a consequence of the right inequality (9.31a) also  $h \ll \lambda$ , the overlap volume can thus be approximated by the lowest order expression in  $h/\lambda$ , given by  $\pi h^2 \lambda$ .

For  $x \in [-D/2, D/2 - \delta]$  the overlap volume is zero, which means we can restrict the  $x$ -integration regime in equation (9.29) to  $x \in (D/2 - \delta, D/2]$ . A transformation of variable from  $x$  to  $h = x + \delta - D/2$  results in an integration regime of  $(0, \delta]$  for  $h$ , the integral can easily be evaluated as  $\pi \delta^3 \lambda / 3$ . Collecting all prefactors from equation (9.29) this results in

$$e_{\text{inter}} \simeq \frac{\epsilon \pi \delta^3 \lambda \rho_{\text{eff}}}{6D} . \quad (9.32)$$

With equation (5.104) and equation (9.30) the pressure-term is

$$\frac{P}{\rho c} = \frac{P(D + \lambda - \delta)}{\rho_{\text{eff}} D} . \quad (9.33)$$

Note, that we must not just keep the leading term for small  $D/\lambda$  and  $\delta/\lambda$  in this case, because this would be  $P\lambda/\rho_{\text{eff}}D$  — completely independent of  $\delta$ . But it is clear, that the interplay between the opposing effects of a varying overlap parameter  $\delta$  on energy on one hand and the pressure-term on the other hand plays an important role when minimising the enthalpy. The increase in the average density for increasing  $\delta$  leads to a negative contribution to the pressure-term which is physically relevant and hence must not be dropped.

Equations (9.28), (9.32), and (9.33) lead to the following expression for the equivalent to the enthalpy per particle in the CT:

$$h_c = \frac{\epsilon}{2} (\rho_{\text{eff}} \lambda^2 \pi D - 1) + \frac{\epsilon \pi \delta^3 \lambda \rho_{\text{eff}}}{3D} + \frac{P(D + \lambda - \delta)}{\rho_{\text{eff}} D} . \quad (9.34)$$

To find the minimum of this function w.r.t. the three occurring lamellar continuum matter parameters  $D$ ,  $\delta$ , and  $\rho_{\text{eff}}$ , we first consider the effective density. Since  $h_c(\rho_{\text{eff}}) = c_1 + c_2 \rho_{\text{eff}} + c_3 / \rho_{\text{eff}}$  there is exactly one minimum in the range of positive real numbers which we obtain by setting the first derivative of  $h_c$  w.r.t.  $\rho_{\text{eff}}$  to 0:

$$\rho_{\text{eff}} = \sqrt{\frac{6P(D - \delta + \lambda)}{\pi \lambda \epsilon (2\delta^3 + 3D^2 \lambda)}} . \quad (9.35)$$

If we now insert this result in equation (9.34) we can plot  $h_c(D, \delta; P, \lambda)$  and  $\rho_{\text{eff}}(D, \delta; P, \lambda)$  simultaneously (see figure 9.9) for typical values of the parameters  $P$  and  $\lambda$ . We recognise,

<sup>5</sup>A portion of a sphere cut off by a plane; its curved surface is called spherical calotte. A spherical segment of height  $h$  of a sphere of radius  $r$  has a volume of  $\frac{\pi}{3} h^2 (3r - h)$ .

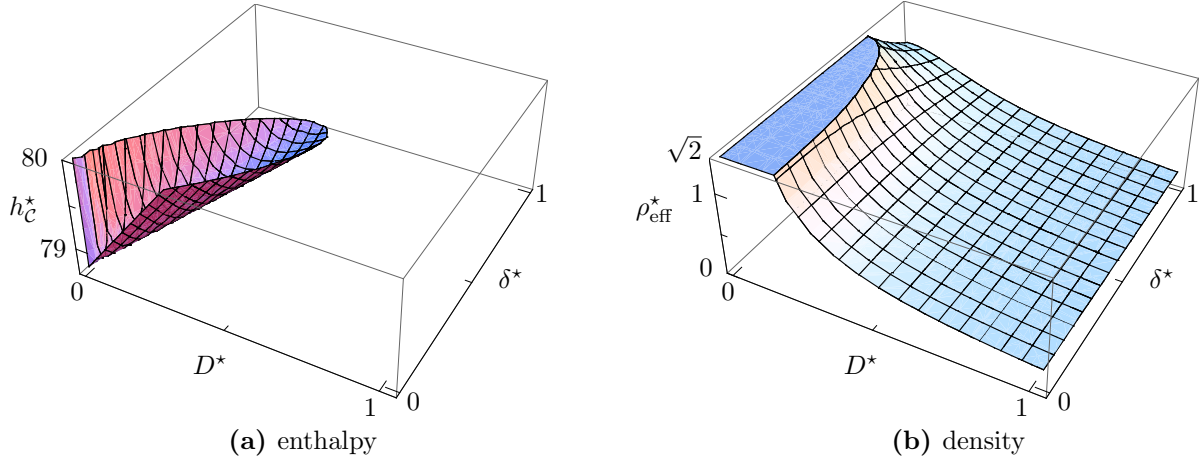


Figure 9.9: The reduced enthalpy of equation (9.34) in (a) and the reduced effective density of equation (9.35) in (b) as functions of the reduced thickness  $D^*$  of the lamellae and the reduced penetration depth  $\delta^*$ , for  $\check{P} = 1$  and  $\lambda^* = 10$ .

that the minimum of  $h_C$  lies inside the regime where  $\rho_{\text{eff}}$  is, according to equation (9.35), larger than  $\sqrt{2}/\sigma^3$  — which is not allowed due to equation (9.15b). Therefore we can set

$$\rho_{\text{eff}} \equiv \frac{\sqrt{2}}{\sigma^3}. \quad (9.36)$$

We will check whether there exists a pressure regime where this is not valid later on.

Using equation (9.36),  $h_C$  becomes a function of only two variables,  $\delta$  and  $D$ , and can easily be minimised. We obtain for the position of the minimum

$$D = \sigma \sqrt{\frac{P\sigma^3}{\pi\epsilon\lambda/\sigma} \left( 1 - \sqrt{\frac{2P\sigma^3}{9\pi\epsilon(\lambda/\sigma)^3}} \right)} \quad \text{and} \quad (9.37a)$$

$$\delta = \sigma \sqrt{\frac{P\sigma^3}{2\pi\epsilon\lambda/\sigma}}. \quad (9.37b)$$

Introducing  $\check{P}$  according to equation (9.21b) we can define a shoulder-reduced lamella thickness  $\check{D}$  and a shoulder-reduced overlap parameter  $\check{\delta}$ ,

$$\check{D} = \frac{D^*}{\lambda^*} = \frac{D}{\lambda} = \sqrt{\frac{\check{P}}{\pi} \left( 1 - \sqrt{\frac{2\check{P}}{9\pi}} \right)}, \quad \text{and} \quad (9.38a)$$

$$\check{\delta} = \frac{\delta^*}{\lambda^*} = \frac{\delta}{\lambda} = \sqrt{\frac{\check{P}}{2\pi}}; \quad (9.38b)$$

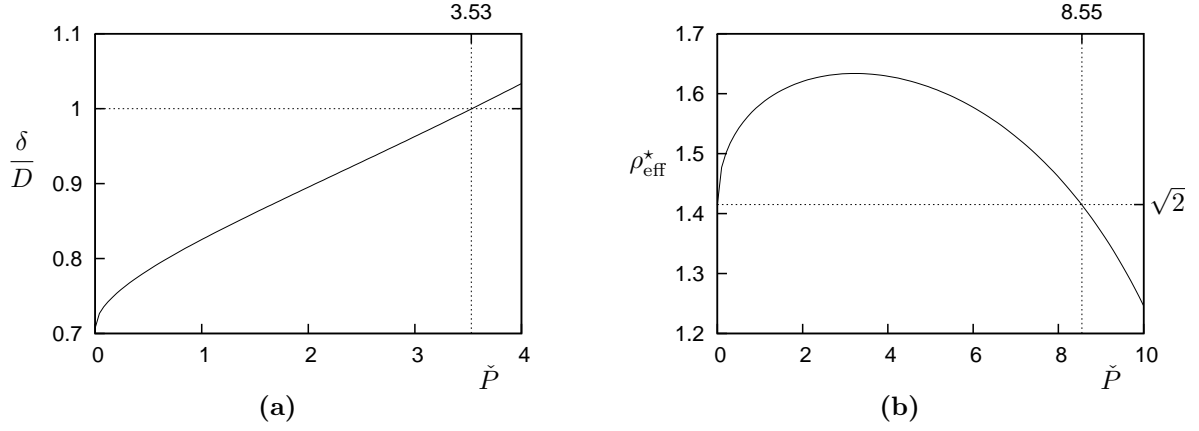


Figure 9.10: Relative penetration depth  $\delta/D$  in (a) and effective density of equation (9.35) with  $\delta$  and  $D$  from equation (9.37) in (b) versus  $\check{P}$ .

the resulting shoulder-reduced thermodynamic quantities are

$$\check{h}_c = \frac{\check{P}}{\sqrt{2}} + \frac{\pi^{\frac{1}{4}}}{\sqrt{3}} \sqrt{2\check{P} (3\sqrt{\pi} - \sqrt{2\check{P}})}, \quad (9.38c)$$

$$\check{\rho}_c = \rho_c^* = \frac{\sqrt{4\check{P} (3\sqrt{\pi} - \sqrt{2\check{P}})}}{\sqrt{6\pi\sqrt{\pi} - \sqrt{3\check{P}\sqrt{\pi}} + \sqrt{2\check{P} (3\sqrt{\pi} - \sqrt{2\check{P}})}}}, \text{ and} \quad (9.38d)$$

$$\check{e}_c = \frac{\pi^{\frac{1}{4}}}{2\sqrt{3}} \frac{3\sqrt{2\pi\check{P}} - \check{P}}{\sqrt{3\sqrt{\pi} - \sqrt{2\check{P}}}}. \quad (9.38e)$$

Now we check the pressure range for which  $\delta < D$  holds, and verify the usage of equation (9.36). Plotting  $\delta/D$  [see figure 9.10(a)] reveals that there is an upper limit for the pressure if we want to guarantee that  $\delta < D$ , our assumption (9.31a), is valid. This pressure limit can easily be calculated using equations (9.38a,b):

$$\frac{\delta}{D} = \frac{\check{\delta}}{\check{D}} = 1 \left/ \sqrt{2 - \frac{2}{3} \sqrt{\frac{2\check{P}}{\pi}}} \right., \quad (9.39)$$

which has to be equal to 1 for  $\check{P} = \check{P}_{\text{lam,max}}$ , leading to

$$\check{P}_{\text{lam,max}} = \frac{9\pi}{8} \simeq 3.53. \quad (9.40)$$

If, with  $\delta$  and  $D$  according to equations (9.37), the effective density of equation (9.35) is greater than the maximum value of  $\sqrt{2}/\sigma^3$ , then our assumption in equation (9.36) of

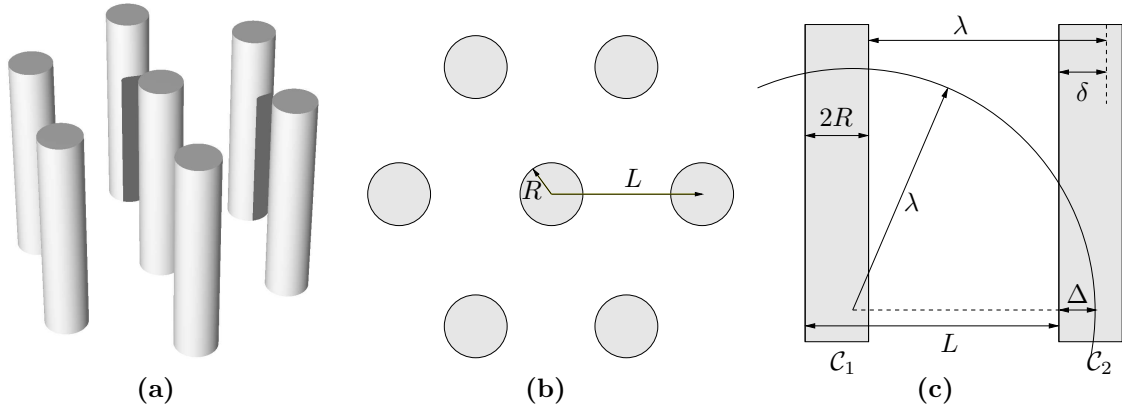


Figure 9.11: Cylindrical columns arranged on a 2D hexagonal lattice, in a 3D view (a), cut perpendicular to the column axes (b), and cut by a plane that contains two cylinder axes (c). Arrows indicate the lengths as labelled. In (c) one can see an example sphere of radius  $\lambda$  around a point of the cross section of one column having a penetration depth for the inter-columnar overlap volume of  $\Delta$ .

$\rho_{\text{eff}}$  having the highest possible value is valid. As shown in figure 9.10(b) this is indeed the case in the pressure regime  $\check{P} \leq \check{P}_{\text{lam,max}}$ ,  $\delta$  and  $D$  having the functional form of equation (9.37) would keep the effective density according to equation (9.35) above the close-packed one even up to  $\check{P} = \frac{49\pi}{18} \simeq 8.55$ .

### 9.3.4 Cylindrical Columns

Similar to the lamellar case we consider now cylindrical columns of radii  $R \ll \lambda$ , see figure 9.11(a). We arrange them on a 2D hexagonal lattice where they have a distance of  $L$  to the nearest neighbouring column, i.e.,

$$\hat{\rho}_c(\mathbf{r}) = \rho_{\text{eff}} \sum_{i,j=-\infty}^{\infty} \theta(R^2 - |i\mathbf{a} + j\mathbf{b} + \hat{\mathbf{z}} \cdot \mathbf{r} - \mathbf{r}|) , \quad (9.41)$$

with  $\mathbf{a}$  and  $\mathbf{b}$  being the primitive lattice vectors of the 2D hexagonal lattice lying in the  $x$ - $y$ -plane ( $|\mathbf{a}| = |\mathbf{b}| = L$  is a choice with shortest possible 2D primitive vectors, i.e., 2D MDP vectors), and  $\hat{\mathbf{z}}$  being the unit vector in  $z$ -direction. Again a penetration depth  $\delta$  is defined as

$$\delta = 2R + \lambda - L \quad (9.42)$$

[see figures 9.11(b) and 9.11(c)]. As discussed in section 5.8 the circular cross-section of one cylinder can be taken as integration regime to obtain the average continuum matter energy  $e_c$ . Assuming the origin of our coordinate system in the centre of the circular

cross-section of one cylinder we obtain

$$e_C = \frac{1}{R^2\pi} \int_{x^2+y^2 \leq R^2} \frac{\epsilon}{2} \left( \int_{B_\lambda(x,y)} \hat{\rho}_C(\mathbf{r}') d^3r' - 1 \right) dx dy, \quad (9.43)$$

where we used  $B_\lambda(x, y)$  as an abbreviation for the sphere of radius  $\lambda$  with centre at  $(x, y, 0)$ . Further, we make the following assumptions:

$$0 < \delta < 2R \ll \lambda. \quad (9.44)$$

Next we again split up the total energy per particle in an intra- and an inter-columnar part to facilitate calculations. Due to the six nearest neighbours in the 2D-hexagonal lattice

$$e_C = e_{\text{intra}} + 6e_{\text{inter}}. \quad (9.45)$$

First we consider

$$e_{\text{intra}} = \frac{1}{R^2\pi} \int_{x^2+y^2 \leq R^2} \frac{\epsilon}{2} \left( \rho_{\text{eff}} \int_{B_\lambda(x,y)} \theta(R^2 - (x'^2 + y'^2)) d^3r' - 1 \right) dx dy. \quad (9.46)$$

The integral over  $d^3r'$  can again be interpreted in terms of overlaps, i.e., of the spheres  $B_\lambda(x, y)$  with the central cylinder, defined by  $x'^2 + y'^2 \leq R^2$ . Since the radius of the cylinder,  $R$ , as well as the displacement between the cylinder axis and the centre of the sphere,  $\sqrt{x^2 + y^2}$ , are much smaller than the radius of the sphere,  $\lambda$ , this overlap volume can be approximated by  $R^2\pi \cdot 2\lambda$ , which is independent of  $x$  and  $y$ . The integral over  $dx dy$  therefore just cancels the prefactor of  $1/R^2\pi$ . Collecting the remaining prefactors the intra-columnar continuum matter energy per particle leads to

$$e_{\text{intra}} \simeq \frac{\epsilon}{2} (\rho_{\text{eff}} R^2 \pi 2\lambda - 1). \quad (9.47)$$

The inter-columnar energy per particle

$$e_{\text{inter}} = \frac{1}{R^2\pi} \int_{x^2+y^2 \leq R^2} \frac{\epsilon}{2} \rho_{\text{eff}} \int_{B_\lambda(x,y)} \theta(R^2 - [(x' - L)^2 + y'^2]) d^3r' dx dy \quad (9.48)$$

is much more complicated to evaluate. First we recognise, that the integral over  $d^3r'$  represents the overlap volume between a sphere  $B_\lambda(x, y)$ , having its centre at  $(x, y, 0)$  inside the cylinder  $\mathcal{C}_1$  containing the origin, and a parallel cylinder  $\mathcal{C}_2$  whose axis contains  $(L, 0, 0)$ , as depicted in figure 9.11(c). This figure also shows, that the overlap volume is a portion near the surface of the sphere, having an individual overlap parameter  $\Delta = x - R + \delta \leq \delta$ . Again applying the assumption (9.44) we can neglect the curvature of the sphere in the plane perpendicular to the cylinder axes for the calculation of the small overlap volume, i.e.,

we set this overlap volume to be equal to the one of the cylinder  $\mathcal{C}_2$  and another cylinder of radius  $\lambda$  and axis through  $(x, y, 0)$  pointing in  $\hat{\mathbf{y}}$ -direction — *perpendicular* to the axis of  $\mathcal{C}_2$ . The resulting overlap volume can be expressed via

$$V = \frac{16}{15}R^3 \sqrt{2\frac{\lambda}{R} \left(2 - \frac{\Delta}{R}\right)} \left\{ \left[4 - \frac{\Delta}{R} \left(2 - \frac{\Delta}{R}\right)\right] E\left(\frac{\Delta/R}{\Delta/R-2}\right) - \left[\frac{\Delta}{R} - 4\right] K\left(\frac{\Delta/R}{\Delta/R-2}\right) \right\}, \quad (9.49)$$

with  $E(x)$  and  $K(x)$  being the first and second kind elliptic integrals, respectively [121]<sup>6</sup>. To be able to use the known power series expansions for the elliptic integrals

$$E(x) = \pi \left( \frac{1}{2} - \frac{x}{8} - \frac{3x^2}{128} + \mathcal{O}(x^3) \right) \quad \text{and} \quad (9.50a)$$

$$K(x) = \pi \left( \frac{1}{2} + \frac{x}{8} + \frac{9x^2}{128} + \mathcal{O}(x^3) \right) \quad (9.50b)$$

in equation (9.49), the overlap parameter  $\Delta$ , varying between 0 and  $\delta$ , has to be considerably smaller than  $2R$ , where the argument  $\frac{\Delta}{R}/\frac{\Delta}{R} - 2$  of both elliptic functions diverges. At  $\delta \lesssim R$  the (absolute value of the) argument is smaller or of the order of 1, which would be acceptable. Therefore we assume  $\delta \lesssim R$ , of course this assumption will have to be checked for the final equilibrium columns. To lowest order in  $\Delta/R$  we obtain

$$V \simeq \frac{6}{5}\pi\Delta^2\sqrt{R\lambda}. \quad (9.51)$$

This volume is now independent of  $y$ , while  $x$  is hidden in  $\Delta$ . Thus we just multiply  $V$  by the factor of  $\sqrt{R^2 - x^2} = \sqrt{R^2 - (R - \delta + \Delta)^2} \simeq \sqrt{2R(\delta - \Delta)}$  to respect the  $y$ -integration. The integration over  $dx$  can be transformed to one over  $d\Delta$  from  $\Delta = 0$  to  $\Delta = \delta$ , the result for the CT equivalent of the inter-columnar energy per particle after collecting all the prefactors is

$$e_{\text{inter}} \simeq \frac{\rho_{\text{eff}}\epsilon 16\sqrt{2\delta^7\lambda}}{175R}. \quad (9.52)$$

To calculate the pressure term we need the average density which is, according to equation (5.103),  $\rho_{\mathcal{C}} = \rho_{\text{eff}}R^2\pi/\frac{\sqrt{3}}{2}L^2$ . Again we set  $\rho_{\text{eff}} = \sqrt{2}/\sigma^3$ , i.e., close-packed particles inside the columnar aggregate. We arrive at an approximate expression for the enthalpy per particle,

$$h_{\mathcal{C}} \simeq \frac{\epsilon}{2} \left( 2\sqrt{2}\pi \frac{R^2\lambda}{\sigma^3} - 1 \right) + \frac{192\epsilon\sqrt{\delta^7\lambda}}{175R\sigma^3} + \frac{\sqrt{3}P\sigma^3(\lambda + 2R - \delta)^2}{2\sqrt{2}\pi R^2}. \quad (9.53)$$

With the definitions  $\check{R} = R/\lambda$  and  $\check{\delta} = \delta/\lambda$ , the minimum w.r.t.  $\delta$  of this function is given by the root of

$$\frac{3 \cdot 2^{11}}{5^4} \pi^2 \check{R}^2 \check{\delta}^5 - \check{P}^2 \check{\delta}^2 + 2\check{P}^2 (1 + 2\check{R}) \check{\delta} - \check{P}^2 (1 + 4\check{R} + 4\check{R}^2) = 0, \quad (9.54)$$

<sup>6</sup>The exact, but much more complicated formula for the overlap volume of a sphere and a cylinder also contains elliptic integrals, see [122].



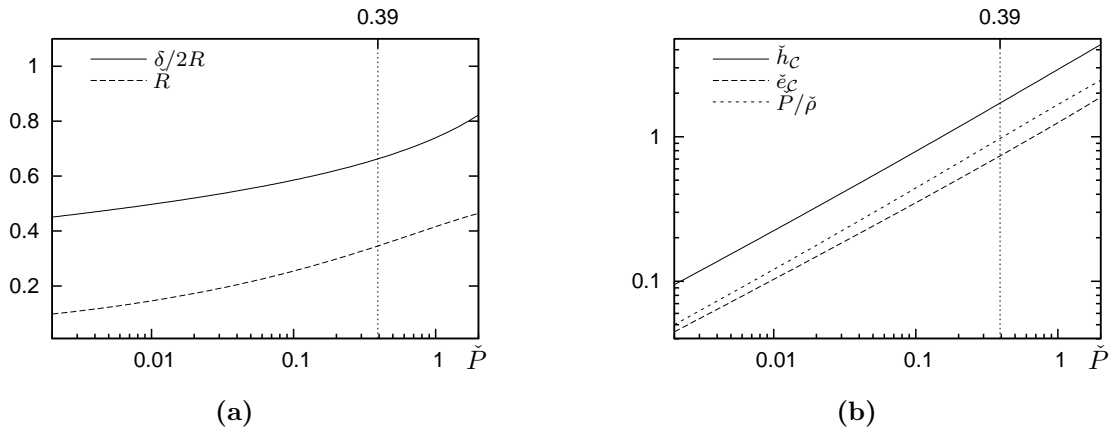


Figure 9.12: In (a) we plot the ratio of the penetration depth  $\delta$  over the column diameter  $2R$ , which has to be smaller than 1 for the approximate theory to be applicable. We also include the ratio  $\check{R} = R/\lambda$ , assumed to be  $\ll 1$  in our calculations, which is more or less the case.

(b) shows the shoulder-reduced enthalpy per particle and the respective contributions from the energy and pressure terms, in dependence of the shoulder-reduced pressure.

The dotted vertical lines indicate the upper limiting pressure, see later.

of which there exists only one real solution in the interesting pressure regime. Inserting back this solution into equation (9.53) and minimising w.r.t.  $R$  is not possible in an analytic way, which is why we have to do this numerically.

Similar to the homogeneous and lamellar cases all the shoulder-reduced quantities  $\check{\delta}$ ,  $\check{R}$ ,  $\check{\rho}_c$ ,  $\check{h}_c$ , and  $\check{e}_c$  for the equilibrium structure only depend, due to the approximation of  $R \ll \lambda$ , on the shoulder-reduced pressure  $\check{P}$ . Except for the effective density all these quantities are plotted in figure 9.12. As will be shown later, the columnar phase has only to be considered up to a certain limiting pressure, turning out to have the value of  $\check{P} \simeq 0.39$ . One can see that inside the pressure range where the columns have lower enthalpy than both the lamellae and the homogeneous distribution, all approximating assumptions are met:  $\delta/2R$  is always less than 1 [see figure 9.12(a)] and has its maximum value of  $\simeq 0.66$  at the transition pressure to the lamellar phase, and the maximum value of  $R/\lambda$  is  $\simeq 0.35$ , also at the transition pressure.

### 9.3.5 Spherical Clusters

Finally we consider spherical clusters of equal radius  $R$ , arranged on a 3D Bravais lattice, i.e.,

$$\hat{\rho}_c(\mathbf{r}) = \rho_{\text{eff}} \sum_{i,j,k=0}^{\infty} \theta(R - |\mathbf{r} - \mathbf{L}_{ijk}|) , \quad (9.55)$$

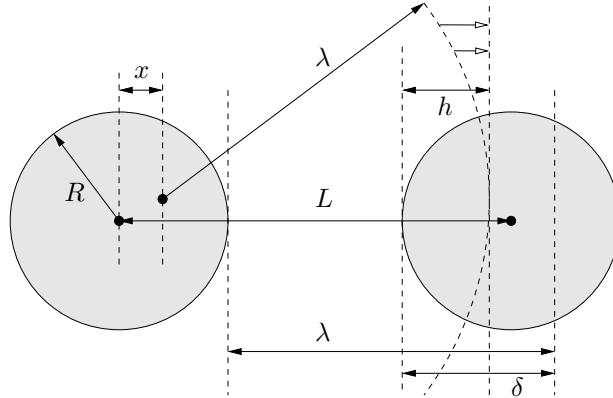


Figure 9.13: Two spherical clusters of Radius  $R$  and distance  $L$ . Open arrows indicate how the surface of a sphere of radius  $\lambda$  is approximated by a plane in the region of the other spherical cluster.  $\delta$  is the penetration depth,  $x$  the offset of an arbitrary point and  $h$  the height of the corresponding spherical segment.

with the lattice vectors  $\mathbf{L}_{ijk}$ , described in equation (5.2). Again we assume  $\check{R} = R/\lambda \ll 1$  and, as depicted in figure 9.13, define the penetration depth as

$$\delta = \lambda + 2R - L . \quad (9.56)$$

Of course, also  $0 < \delta$  and  $\check{\delta} = \delta/\lambda \ll 1$  shall hold.

As a first step we again calculate the intra- and inter-cluster continuum matter energies per particle. According to section 5.8, the integration regime  $\mathcal{N}$  in the formula for the CT energy per particle [equation (5.100)] is just the whole sphere representing the cluster, the intra-cluster continuum matter energy per particle is therefore

$$e_{\text{intra}} = \frac{1}{\frac{4\pi}{3}R^3} \int_{B_R(\mathbf{0})} \frac{\epsilon}{2} \left( \rho_{\text{eff}} \int_{B_\lambda(\mathbf{r})} \theta(R - |\mathbf{r}'|) d^3r' - 1 \right) d^3r . \quad (9.57)$$

The integral over  $d^3r'$  is the overlap volume between the spheres  $B_\lambda(\mathbf{r})$  [with  $\mathbf{r} \in B_R(\mathbf{0})$ ] and  $B_R(\mathbf{0})$ . Because of  $R \ll \lambda$  this is the same situation as discussed for the construction of the self-energy term in section 9.3.1, the smaller sphere is always contained inside the larger one. Therefore integration over  $d^3r'$  leads to the  $\mathbf{r}$ -independent result  $\frac{4\pi}{3}R^3$ , the integral over  $d^3r$  just cancels the prefactor of  $1/\frac{4\pi}{3}R^3$  and the intra-spherical energy per particle is given by

$$e_{\text{intra}} = \frac{\epsilon}{2} \left( \rho_{\text{eff}} \frac{4\pi}{3}R^3 - 1 \right) . \quad (9.58)$$

The inter-cluster continuum matter energy per particle is given by

$$e_{\text{inter}} = \frac{1}{\frac{4\pi}{3}R^3} \int_{B_R(\mathbf{0})} \frac{\epsilon}{2} \rho_{\text{eff}} \int_{B_\lambda(\mathbf{r})} \theta(R - |\mathbf{r}' - L\hat{\mathbf{x}}|) d^3r' d^3r , \quad (9.59)$$

for two clusters separated by the distance  $L$  along the  $x$ -axis ( $\hat{\mathbf{x}}$  is the unit vector in  $x$ -direction). As depicted in figure 9.13, due to  $R \ll \lambda$  the overlap volume of a sphere with radius  $\lambda$  centred at an arbitrary point inside one cluster with the neighbouring cluster [the integral over  $d^3r'$  in equation (9.59)] can be approximated by the spherical segment of height  $h = x + \delta - R$ , where  $x$  is the offset of the mid point of the  $\lambda$ -sphere from the first cluster in the direction of the other one (see figure 9.13). In this way we neglect the curvature of the  $\lambda$ -sphere in the region around its surface of the (much smaller)  $R$ -sphere. Through this approximation all points with equal offset have the same overlap volume of

$$V_s = \frac{\pi}{3} h^2 (3R - h), \quad (9.60)$$

the volume of the spherical segment. It is possible to evaluate now the inter-spherical energy per particle by multiplying  $V_s$  with the disc-like area  $\pi(R^2 - x^2)$  of points of equal offset  $x$  (the factor from the integration over  $dydz$ ) and integrating over  $x$  from  $R - \delta$  to  $R$  (where the overlap volume is non-zero). Multiplying by the remaining prefactors we obtain

$$e_{\text{inter}} = \frac{\rho_{\text{eff}} \epsilon \pi \delta^4 (30R^2 - 12R\delta + \delta^2)}{480R^3}. \quad (9.61)$$

To construct the pressure term, we need information about the crystal structure the spherical clusters are arranged on. In order to keep our considerations simple, we want to have just one parameter for the spatial extent of the crystal structure. Therefore we only consider the cubic Bravais lattices. Given the distance between next neighbours ( $L$ ), it is easy to calculate the volume per site,  $V_c$ , and hence the overall density according to equation (5.102) in dependence of  $L$ , the effective density  $\rho_{\text{eff}}$  of one cluster, and the cluster radius  $R$ :

	fcc	bcc	sc
$V_c$	$\frac{L^3}{\sqrt{2}}$	$\frac{4L^3}{\sqrt{27}}$	$L^3$
$\rho_c$	$\rho_{\text{eff}} \frac{4\pi\sqrt{2} R^3}{3 L^3}$	$\rho_{\text{eff}} \pi \sqrt{3} \frac{R^3}{L^3}$	$\rho_{\text{eff}} \frac{4\pi R^3}{3 L^3}$
$f$	$\frac{4\pi\sqrt{2}}{3} \simeq 5.92$	$\pi\sqrt{3} \simeq 5.44$	$\frac{4\pi}{3} \simeq 4.19$
$n_{\text{nn}}$	12	8	6

(9.62)

$n_{\text{nn}}$  is the number of next neighbours and  $f$  is the numerical prefactor occurring in the density relation, i.e.,  $\rho = \rho_{\text{eff}} f R^3 / L^3$ . With help of these parameters we can write the continuum matter enthalpy per particle for clusters arranged on cubic Bravais lattices as

$$h_c = \frac{\epsilon}{2} \left( \rho_{\text{eff}} \frac{4\pi}{3} R^3 - 1 \right) + n_{\text{nn}} \frac{\rho_{\text{eff}} \epsilon \pi \delta^4 (30R^2 - 12R\delta + \delta^2)}{480R^3} + \frac{P(\lambda + 2R - \delta)^3}{\rho_{\text{eff}} f R^3}. \quad (9.63)$$

In an effort to minimise this expression analytically, we have to introduce simplifying assumptions.

First, we again set the effective density to the close-packed one, which is in agreement with the findings in section 9.2. Next we consider the three terms occurring in the expression for  $e_{\text{inter}}$ , namely  $30R^2$ ,  $12R\delta$ , and  $\delta^2$ . As will be shown shortly,  $\delta/R \lesssim 0.5$  always holds in the relevant pressure regime, consequently the second term is at maximum 20% of the first one, the third hardly reaches 1%. Therefore we just consider the leading term, omitting the higher order corrections. This approximation still respects the fact, that with increasing overlap  $\delta$  the inter-cluster energy increases, too — it does so with the power of 4.

For the pressure term we also use  $\lambda \gg R \gtrsim 2\delta$ , but with some caution: We cannot just keep the highest (third) order in  $\lambda$ , because then we lose the information that the pressure term has to decrease with increasing overlap  $\delta$ , i.e., decreasing volume. Keeping also the second order terms in  $\lambda$  we take this fact into account and finally arrive at the approximation<sup>7</sup>

$$h_C \simeq \frac{\epsilon}{2} \left( \sqrt{2} \frac{4\pi}{3} \frac{R^3}{\sigma^3} - 1 \right) + n_{\text{nn}} \frac{\sqrt{2}\epsilon\pi\delta^4}{\sigma^3 16R} + \frac{P\sigma^3}{\sqrt{2}fR^3} (\lambda^3 + 3\lambda^2 (2R - \delta)) . \quad (9.64)$$

Minimising w.r.t.  $\delta$  leads to

$$\delta = \sigma \sqrt[3]{\frac{6P\sigma^3\lambda^2}{fn_{\text{nn}}\pi\epsilon R^2}} \Leftrightarrow \check{\delta} = \sqrt[3]{\frac{6\check{P}}{fn_{\text{nn}}\pi\check{R}^2}} , \quad (9.65)$$

and after inserting back into equation (9.64) and setting the first derivative w.r.t.  $R$  to be equal to 0, we obtain a twentieth order algebraic equation in  $R$  (more clearly laid out using shoulder-reduced quantities) for the position of the minimum of  $h_C$ :

$$\begin{aligned} & 3^4 11^3 \check{P}^4 - 2^5 3^3 f n_{\text{nn}} \pi \check{P}^3 \check{R}^2 - 2^7 3^4 f n_{\text{nn}} \pi \check{P}^3 \check{R}^3 - 2^9 3^4 f n_{\text{nn}} \pi \check{P}^3 \check{R}^4 - 2^{11} 3^3 f n_{\text{nn}} \pi \check{P}^3 \check{R}^5 + \\ & + 2^7 3^3 f^2 n_{\text{nn}} \pi^2 \check{P}^2 \check{R}^8 + 2^{10} 3^3 f^2 n_{\text{nn}} \pi^2 \check{P}^2 \check{R}^9 + 2^{11} 3^3 f^2 n_{\text{nn}} \pi^2 \check{P}^2 \check{R}^{10} - 2^9 3^2 f^3 n_{\text{nn}} \pi^3 \check{P} \check{R}^{14} + \\ & - 2^{11} 3^2 f^3 n_{\text{nn}} \pi^3 \check{P} \check{R}^{15} + 2^{11} f^4 n_{\text{nn}} \pi^4 \check{R}^{20} = 0 , \end{aligned} \quad (9.66)$$

which *Mathematica* can still treat in a semi-analytical way. The correct branch is easily identified through selecting the largest real root of the above equation.

We can insert now the proper values for  $f$  and  $n_{\text{nn}}$  from equation (9.62) to obtain the result for the different cubic lattices. For each lattice, we obtain an upper pressure value at which the clusters touch their next neighbours, namely  $\check{P}_{\text{max},\text{fcc}} \simeq 99.91$ ,  $\check{P}_{\text{max},\text{bcc}} \simeq 44.75$ , and  $\check{P}_{\text{max},\text{sc}} \simeq 20.53$ . In figure 9.14 we check the validity of our approximations up to these pressure values, which obviously cannot hold both at cluster contact. While  $\delta/R \lesssim 0.5$  is well met,  $R \ll \lambda$  is already poor for  $\check{P} \gtrsim 0.1$ , the ratio is  $R/\lambda \gtrsim 0.45$  for the fcc cluster

<sup>7</sup>A similar approximation was also tried for the columnar case, but did not work there, since it produced even negative energies. The reason we suspect is, that the columnar phases appear in a much higher pressure regime (nearly 2 orders of magnitude higher), resulting in considerable contributions from the pressure term of smallest order in  $\lambda$  compared to the inter-columnar part.

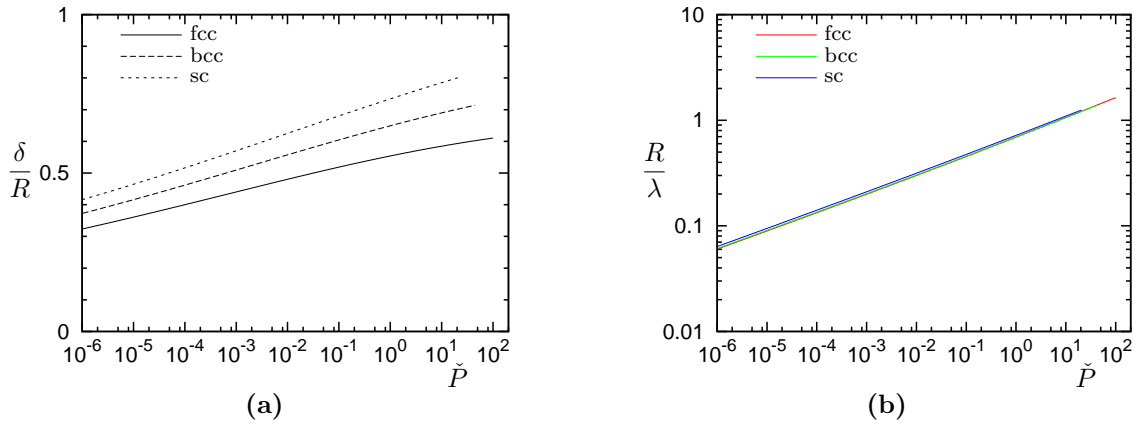


Figure 9.14: Graphical check for the validity of  $\delta/R \lesssim 0.5$  (a) and  $R \ll \lambda$  (b). While the first assumption is quite well met for all pressure values with non-touching clusters, the second one becomes poor for  $\check{P} \gtrsim 0.1$ .

phase there<sup>8</sup>. Nevertheless we made first order approximations that are reasonable for  $\check{P} \lesssim 0.1$ , which again result in  $\lambda$ -independent shoulder-reduced quantities, and it will turn out later, that the cluster phase has only to be considered up to a pressure of  $\check{P} \simeq 0.013$  anyway.

Now we compare the continuum matter enthalpies per particle of the three considered cluster lattices. As can be seen in figure 9.15 the shoulder-reduced enthalpies in dependence of the shoulder-reduced pressure are extremely close to each other. Since this is also the case for  $R/\lambda$  (see figure 9.14(b)) we conclude: When changing the Bravais lattice for the spherical clusters from fcc over bcc to sc (for constant  $\lambda$ ) at fixed pressure

- $n_{\text{nm}}$  decreases as well as  $f$  [see the table of expressions (9.62)], resulting in decreasing  $e_c$  and  $\rho_c$ ,
- the cluster radius  $R$  remains approximately constant [see figure 9.14(b)],
- the cluster overlap  $\delta$  increases [see figure 9.14(a)], causing also an increase in  $e_c$  and  $\rho_c$ , in a way that
- at the bottom line the CT enthalpy per particle remains approximately constant (see figure 9.15).

A closer investigation shows, that this mechanism is slightly overcompensating, i.e.,  $\delta$  is increased in such a way that the overall density in fact also increases (leading to a slight decrease in the pressure contribution to enthalpy); the same is true for the energy per particle.

<sup>8</sup>Note that for  $2R > \lambda$  equation (9.58) is no longer valid and needs increasingly significant corrections as  $2R/\lambda$  grows beyond 1.

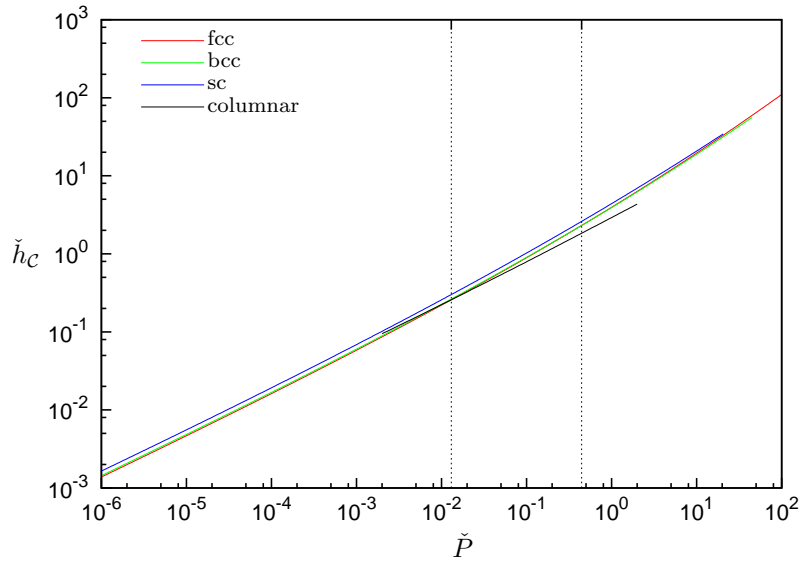


Figure 9.15: Shoulder-reduced enthalpy for the three considered cubic lattices and the columnar case as indicated in the legend. The transition pressure at  $\check{P} \simeq 0.444$  between fcc and bcc is visualised by a vertical dashed line, as well as the transition from fcc to the columnar phase at  $\check{P} \simeq 0.013$ .

It is nevertheless possible to recognise an ordering scheme of these three lattices with increasing pressure, if one is interested only in the lattice exhibiting the lowest  $h_c$ . Using the minimum enthalpy per particle-functions given by the above expressions, we find that at low pressures the fcc enthalpy per particle is the lowest one, above  $\check{P} \simeq 0.444$  the bcc lattice takes over until  $\check{P} \simeq 2.80 \cdot 10^3$ , above which the sc lattice provides the minimum enthalpy per particle. Of course, this transition to clusters on an sc lattice will never appear, since the maximum pressure values for the bcc and sc phases are given by  $\check{P}_{\max, \text{bcc}} \simeq 44.75$  and  $\check{P}_{\max, \text{sc}} \simeq 20.53$  (see above). But also the bcc phase will never represent the phase exhibiting the minimum enthalpy, since the columnar phase is always favoured to any cluster phase for  $\check{P} \gtrsim 0.013$  (see figure 9.15)<sup>9</sup>.

### 9.3.6 Summary and Comparison

We consider now the whole pressure regime, and the equilibrium continuum matter enthalpies per particle from the four aggregate shapes. The true equilibrium at given pressure is of course always the one that exhibits the overall minimum enthalpy, which means we have to find the lower hull of our four enthalpy curves.

Starting at nearly vanishing pressure we find, that first (fcc) clusters represent the

<sup>9</sup>The intersections of the bcc and the sc enthalpy curves with the columnar one are at  $\check{P} \simeq 0.0082$  and  $\check{P} \simeq 0.00029$ , respectively.

thermodynamically stable structure, i.e., the structure providing the lowest CT enthalpy per particle. Slowly increasing the pressure reveals, that there appears a transition from the cluster to the columnar phase, intersecting the corresponding enthalpy curves results in a transition pressure of

$$\check{P}_{\text{col,clu}} \simeq 0.013 , \quad (9.67)$$

also visualised in figure 9.15. As mentioned above this means, in our approximation the only relevant cubic lattice is the fcc structure when it comes to the overall minimum enthalpy configuration in the CT.

Further increasing the pressure we find a limiting pressure value above which the enthalpy per particle of the hexagonally arranged cylinders is greater than that of the lamellae and *vice versa* below:

$$\check{P}_{\text{lam,col}} \simeq 0.39 . \quad (9.68)$$

If we now also compare the enthalpies for the homogeneous and the lamellar phases we recognise, that the two curves intersect at a pressure value of

$$\check{P}_{\text{hom,lam}} = 4\pi \left( 5 - 2\sqrt{6} \right) \simeq 1.27 , \quad (9.69)$$

the lamellar enthalpy is less than the homogeneous one for  $\check{P} < \check{P}_{\text{hom,lam}}$ , and greater for  $\check{P} > \check{P}_{\text{hom,lam}}$ . This guarantees, that our assumptions for the three non-homogeneous phases,  $R \ll \lambda$  and  $\delta \lesssim R$  or  $D \ll \lambda$  and  $\delta < D$ , are satisfied for the respective pressure regimes where the different aggregate shapes are stable.

The final result is visualised in figure 9.16. The transition pressures, indicated by vertical lines, are of course just approximate values within the lowest order theory we presented in this section. The respective  $\check{h}_c$ -curves, that have to be intersected to obtain the transition pressure values, meet at extremely flat angles. Inclusion of even small higher order terms might lead to different values.

Nevertheless, the mean-field type CT confirms the sequence of aggregate shapes with increasing pressure,

cluster — columns — lamellae — compact structures,

that has been also identified in the GA-based search, see section 9.2. Also, the transition values for the pressure are represented in a qualitative way. This can be visualised by a combined plot of the CT results and the data (for  $h$ ,  $e$ , and  $\rho$ ) from section 9.2 for the three investigated shoulder widths. A combined plot of energy, density, and enthalpy versus pressure is given in figures 9.17, 9.18, and 9.19.

There appear several phenomena. As expected, the energy- and density-curves of CT and exact calculations (see section 9.2) are qualitatively different: the exact ones are step-functions while the CT-curves (for different aggregate types) are continuous, strictly monotonously increasing functions of pressure. But in general the agreement between CT and the exact results is reasonably well for intermediate and long shoulder width. Non-surprisingly, the resulting curves for the short shoulder width-example,  $\lambda^* = 1.5$ , which clearly does not obey  $\lambda^* \gg 1$  (assumed in the CT), deviates substantially from CT

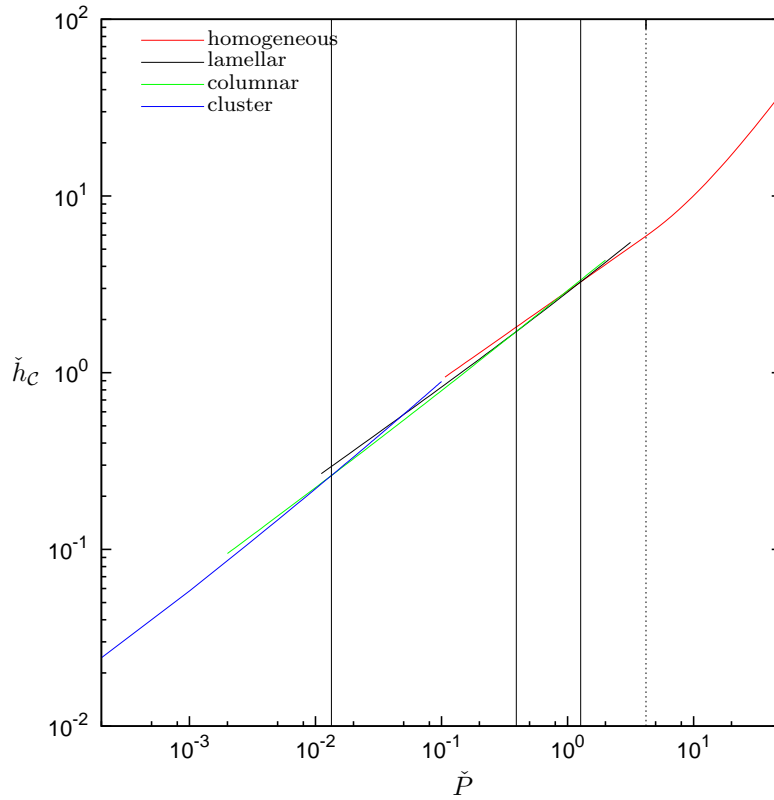


Figure 9.16: The shoulder-reduced enthalpy per particle for the four structural forms of the continuum matter as indicated in the legend versus shoulder-reduced pressure. Vertical solid lines separate (from left to right) pressure regions where the minimum enthalpy is achieved by the (fcc) cluster, columnar, lamellar, or homogeneous phase respectively, at  $\check{P} \simeq 0.013$ ,  $0.39$ , and  $1.27$ . The dashed vertical line indicates the pressure value of  $\check{P} \simeq 4.19$  above which the close-packed structure ( $\check{\rho} = \sqrt{2}$ ) is attained.

results (mind the logarithmic scales). Another issue are the stable pressure regimes of the respective aggregate types, which are not predicted very well. The reason is, as has been discussed before, the extremely flat intersection angles of the enthalpy-curves; figure 9.19 shows, that especially the exact curves in the columnar regime exhibit recognisable deviations from the CT curve even for large  $\lambda$ -values. This is on the one hand due to the drastic simplifications for the columnar phase in CT, which became necessary because of the highly complicated expression for the overlap volume that contained elliptic functions, and on the other hand caused by the assumption that  $\rho_{\text{eff}}^* = \sqrt{2}$  also for the columnar



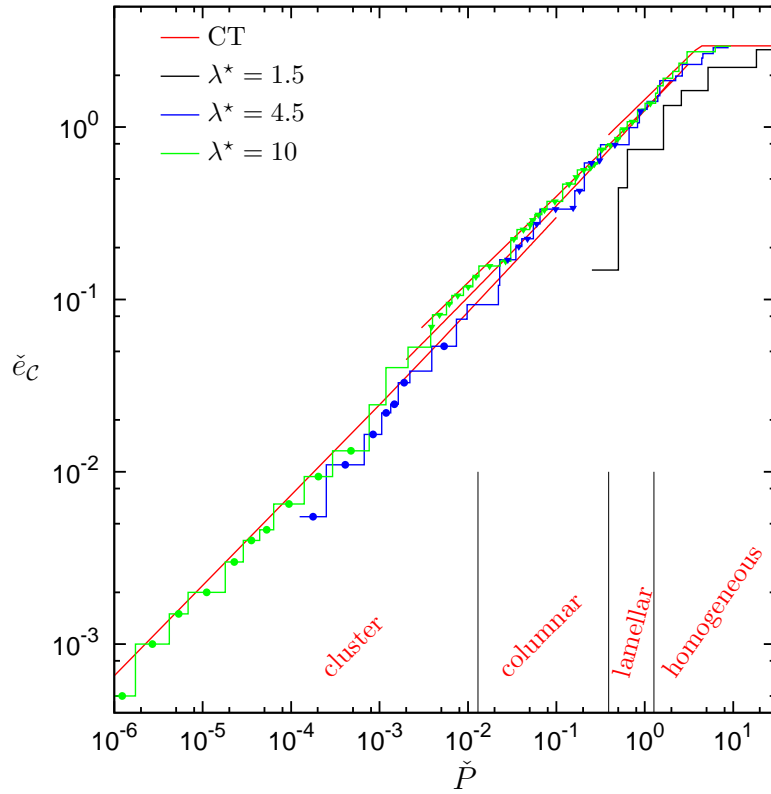


Figure 9.17: The shoulder-reduced energy per particle for the SSM within the CT and for three different shoulder widths, as indicated in the legend, versus shoulder-reduced pressure. Symbols refer to cluster (dots) and lamellar (triangles) structures for  $\lambda^* = 4.5$  and  $10$ . The pressure ranges for the different aggregate types within CT are given in the lower section of the graph.

phase, which is poorly met for  $\lambda^* = 10$  (see section 9.2).

Nevertheless, the numerical agreement between the exact enthalpy-, energy-, and density-values and the predictions from CT is astonishingly good. In addition, the CT also provides insight in the interplay between the thermodynamic variables of the SSM through leading to the definitions of shoulder-reduced quantities. Plotting shoulder-reduced quantities results in the curves for different  $\lambda$ -values to converge to the respective CT curve with increasing  $\lambda$ .

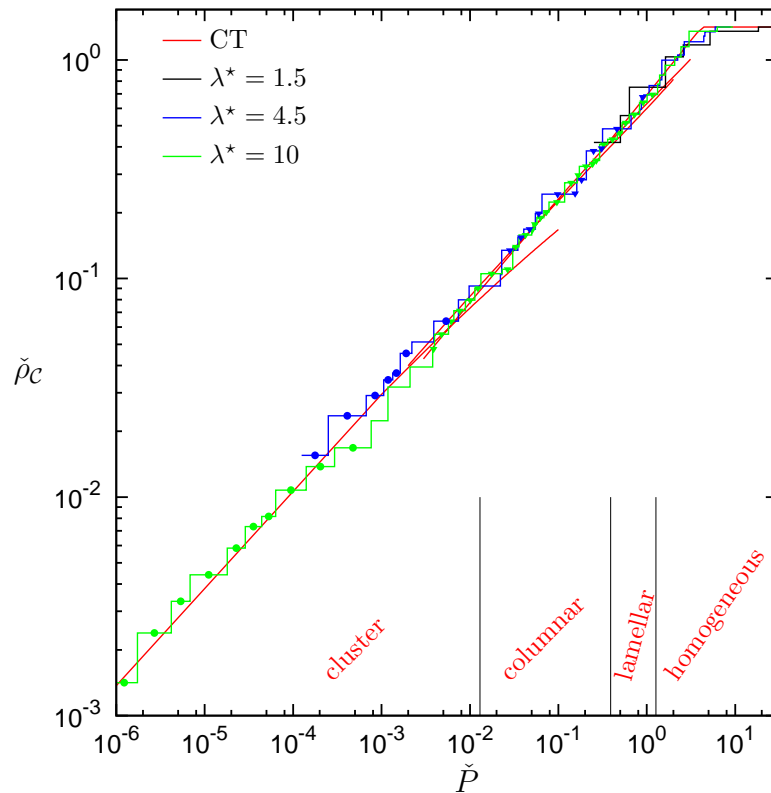


Figure 9.18: The (shoulder-reduced) density per particle for the SSM within the CT and for three different shoulder widths, as indicated in the legend, versus shoulder-reduced pressure. Symbols refer to cluster (dots) and lamellar (triangles) structures for  $\lambda^* = 4.5$  and 10. The pressure ranges for the different aggregate types within CT are given in the lower section of the graph.

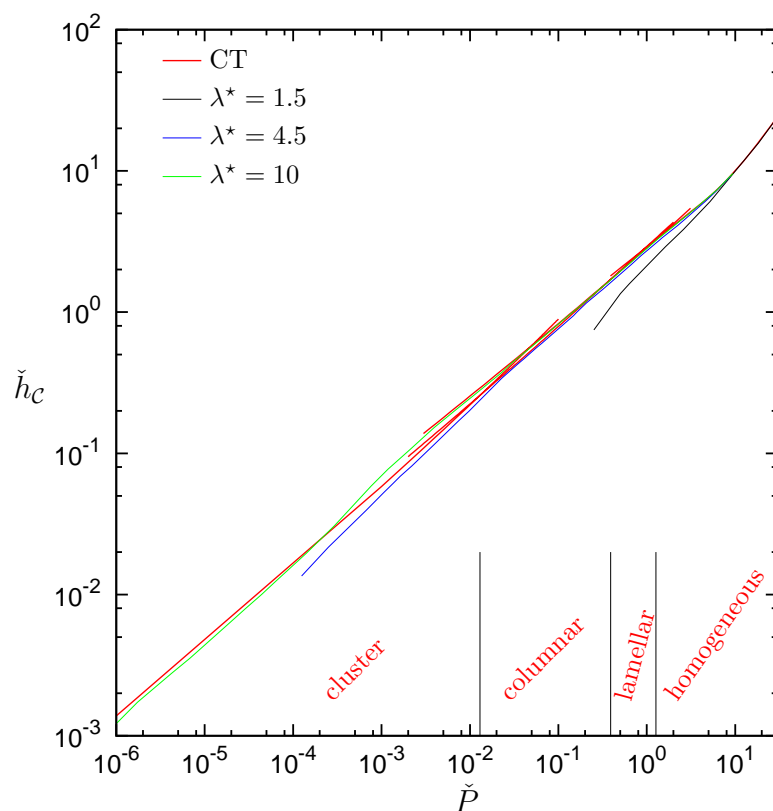


Figure 9.19: The shoulder-reduced enthalpy per particle for the SSM within the CT and for three different shoulder widths, as indicated in the legend, versus shoulder-reduced pressure. The pressure ranges for the different aggregate types within CT are given in the lower section of the graph.



# Chapter 10

## Hard Core Yukawa Model

In this chapter we investigate the phase behaviour at  $T = 0$  of the hard core Yukawa model [see equation (2.3)] with the methods described in section 5.7.5. Investigations of this model using computer simulations have been performed in [103–105] for finite temperatures, i.e.,  $T > 0$ . At zero temperature of course only solid crystals occur. We choose the cutoff-parameter  $\delta = 10^{-10}$ , see section 5.7.3. The influence on the phase diagram of this choice for the cutoff is discussed in appendix F.

First we applied the GA based search algorithm on a coarse  $P^*-\kappa^*$ -grid with up to three basis particles, although only configurations with one basis particle turned out to be the MECs (minimum enthalpy configurations). We found the expected bcc and fcc structures; with general scaling of these two candidate structures (see section 5.7.5) one can easily calculate the exact phase diagram for  $T = 0$  with bcc and fcc considered, see figure 10.1. Of course, one can also calculate the information of the corresponding packing fractions,  $\eta = \rho \frac{4\pi}{3} \left(\frac{\sigma}{2}\right)^3$ , at the coexistence pressure values. In the MC simulation data of [105] one can see the tendency with decreasing temperature of the bcc regime becoming broader and moving towards lower  $\kappa^*$ -values, while the fluid phase-region becomes continually smaller. Obviously the fluid phase finally has to vanish, as can be seen in the limiting case of our  $T = 0$  phase diagram (figure 10.2) in the  $\kappa^*-\eta$ -plane, which also matches a coarse extrapolation of the MC data to  $T = 0$ .

At  $T = 0$ , the maximum possible interaction range parameter  $\kappa$  to obtain a stable bcc phase at any pressure value, is  $\kappa_{\max}^* \simeq 1.874465$ ; the corresponding packing fraction of the delimiting point is the one for a bcc crystal with touching hard cores. Since the nearest neighbour distance is then exactly  $\sigma$ , we call this structure  $\text{bcc}_\sigma$ , its packing fraction is  $\eta_{\text{bcc}_\sigma} = \pi\sqrt{3}/8$ . Above  $\kappa_{\max}^*$  the equilibrium structure is always an fcc crystal (see figures 10.1 and 10.2).

For  $\kappa^* < \kappa_{\max}^*$  the upper bound in the  $\eta$ -range for the bcc region (see figure 10.2) remains of course the bcc packing where the hard cores touch each other,  $\eta_{\text{bcc}_\sigma}$ . The lower bounds in  $\eta$  as well as in pressure of the bcc region decrease with  $\kappa^*$  and finally have to become zero for  $\kappa^* = 0$ , where the hard core Coulomb system is attained. The difference in  $h^*$  between the bcc and fcc structures (with optimum scaling factor  $s_{\text{eq}}$ ) is visualised for one selected  $\kappa^*$ -value in figure 10.3(a). Below the first transition pressure

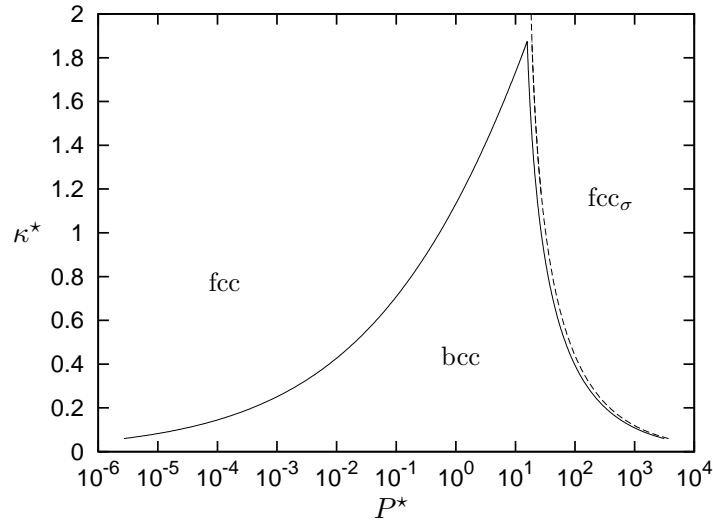


Figure 10.1: Phase diagram for the hard core Yukawa model in the  $\kappa^*$ - $P^*$ -plane at  $T = 0$ . Solid lines delimit the bcc region, the dashed line indicates the limiting pressure above which the particles are close-packed at the hard cores, indicated by the  $\sigma$ -subscript to the fcc crystal structure abbreviation. The  $bcc_\sigma$  regime is too narrow to be visible, it is located at the high-pressure bcc-delimiting line.

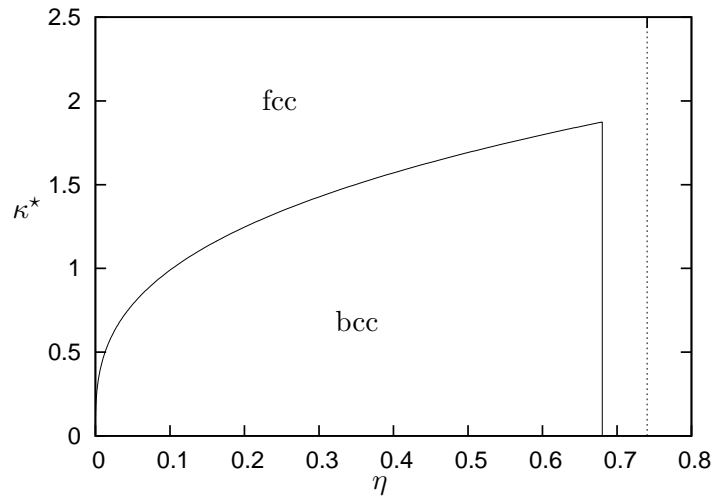


Figure 10.2: Phase diagram of the hard core Yukawa model at  $T = 0$  in the inverse screening length-packing fraction plane. The vertical broken line indicates the packing fraction of fcc $_\sigma$  ( $\pi/3\sqrt{2}$ ), i.e., the maximum possible value for  $\eta$ . The  $bcc_\sigma$  phase is stable along the vertical solid line at  $\eta = \pi\sqrt{3}/8$ , the coexistence region between  $bcc_\sigma$  and fcc is not visible.

the fcc phase is stable, then there occurs a first order phase transition to bcc. Note that the density (packing fraction) has a positive jump at the phase transition, the nearest neighbour distance decreases abruptly, as can be seen in figure 10.3(b), where the scaling

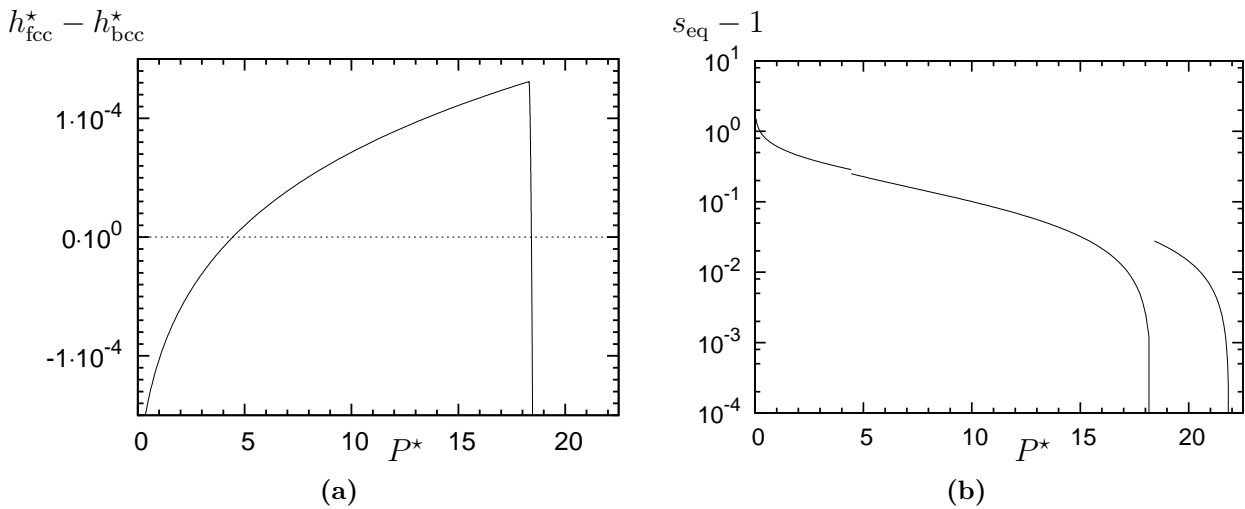


Figure 10.3: Enthalpy and scaling for  $\kappa^* = 1.5$  and  $T = 0$  in the hard core Yukawa model: (a) The difference between the reduced enthalpies per particles of the fcc and bcc structures versus reduced pressure. The pronounced kink at  $P^* \simeq 18.3$  appears because for  $P^* \gtrsim 18.3$  the particles in the bcc structure touch each other at the hard cores. In (b) the scaling factor, giving the nearest neighbour distance as  $s_{\text{eq}}\sigma$ , is plotted as  $s_{\text{eq}} - 1$  on a logarithmic scale versus pressure, to visualise the two first order phase transitions.

factor  $s_{\text{eq}}$  [see equation (5.87)] of the corresponding reference structure, either  $\mathcal{K}_0 = \text{fcc}_\sigma$  or  $\mathcal{K}_1 = \text{bcc}_\sigma$ , is plotted (note, that we always use the densest possible reference structure, i.e.,  $s_{\text{min}} = 1$ , see section 5.7.5). The bcc structure is stable up to the pressure where the hard spheres touch each other, where a second order phase transition to  $\text{bcc}_\sigma$  takes place. Only slightly above this pressure the next first order phase transition to fcc occurs, and of course we finally end up with another second order transition to  $\text{fcc}_\sigma$ , occurring at  $P^* \simeq 21.86$  (visible in figure 10.3(b)).

After having evaluated the full fcc–bcc–phase diagram, we launched our GA based search algorithm on the corresponding transition pressures and some intermediate values. While the lower transition remained unaltered, and also the intermediate values produced no new symmetry structures, we observed a change in the phase behaviour at the  $\text{bcc}_\sigma$ –fcc transition: a new phase emerged, one with only ct symmetry. Since the ct lattice has two independent parameters instead of just one like bcc or fcc, the simple method of a general scaling factor was not sufficient to cover all ct lattices and hence to calculate the phase diagram. Therefore, in addition to the scaling factor  $s$ , we used the parameter  $f$  [see equation (5.89)] as a second optimisation variable, describing the continuous transformation from bcc ( $f = 1$ ) to fcc ( $f = \sqrt{3/2}$ ) — a Bain transformation.

In figure 10.4 the enthalpy per particle of the ct structure in dependence of the parameter  $f$ , for  $\kappa^* = 0.6$  and five different pressure values (relative to the enthalpy per particle of the optimum fcc structure at the same pressure) is plotted. Curve A corresponds to the

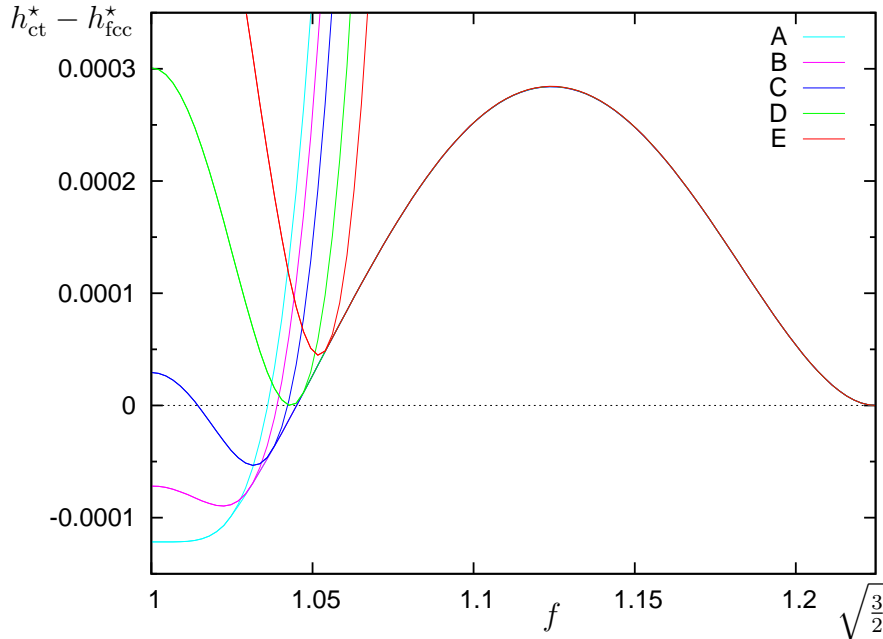


Figure 10.4: Reduced enthalpy per particle difference in the hard core Yukawa model between the ct and fcc structures for  $\kappa^* = 0.6$  in dependence of the Bain parameter  $f$ ;  $f = 1$  corresponds to the bcc and  $f = \sqrt{3/2}$  to the fcc structure. At five different pressure values the curves are plotted, labelled alphabetically with increasing values: A corresponds to the pressure where the ct structure starts to be the MEC, D is the threshold above which the fcc is stable.

Both the enthalpy per particle of the  $ct_\sigma$  structure (thin lines) and the ct structure with optimal scaling [ $s_{\text{eq}}$  according to equation (5.87), thick lines] are plotted, however they always lie exactly on top of each other for  $f$ -values between 1 and the position of the (local) minimum. Above the corresponding minima, the curves of the scaled ct structures for different pressure values quickly approach a common curve.

pressure value of  $P_2^* \simeq 52.53547$ , the largest pressure value where  $bcc_\sigma$  ( $f = 1$  for ct) is the preferred structure. When slightly increasing the pressure to  $P_3^* \simeq 52.59067$  (curve B)  $bcc_\sigma$  ( $f = 1$ ) would still be favoured to fcc ( $f = \sqrt{3/2}$ ), but the enthalpy per particle of the ct structure in dependence of  $f$  and  $s$  establishes a new minimum at  $f \simeq 1.02205$  and  $s = 1$ . The optimum structure remains a ct one even if the pressure exceeds  $P^* \simeq 52.64588$ , above which fcc would be favoured to  $bcc_\sigma$ ; The example value of  $P_4^* \simeq 52.66457$  is shown as line C in figure 10.4,  $f \simeq 1.03172$  and again  $s = 1$  characterise the ct structure with minimum enthalpy per particle in this case.

We have observed that when minimising  $h_{\text{ct}}^*$  w.r.t.  $f$  and  $s$ , the curves  $h_{\text{ct}}^*(f, s_{\text{eq}})$  and  $h_{\text{ct}}^*(f, s = 1)$  as functions of  $f$  are exactly on top of each other for  $f$ -values smaller than the position of the (local) minimum and only differ for larger values of  $f$ , of course always



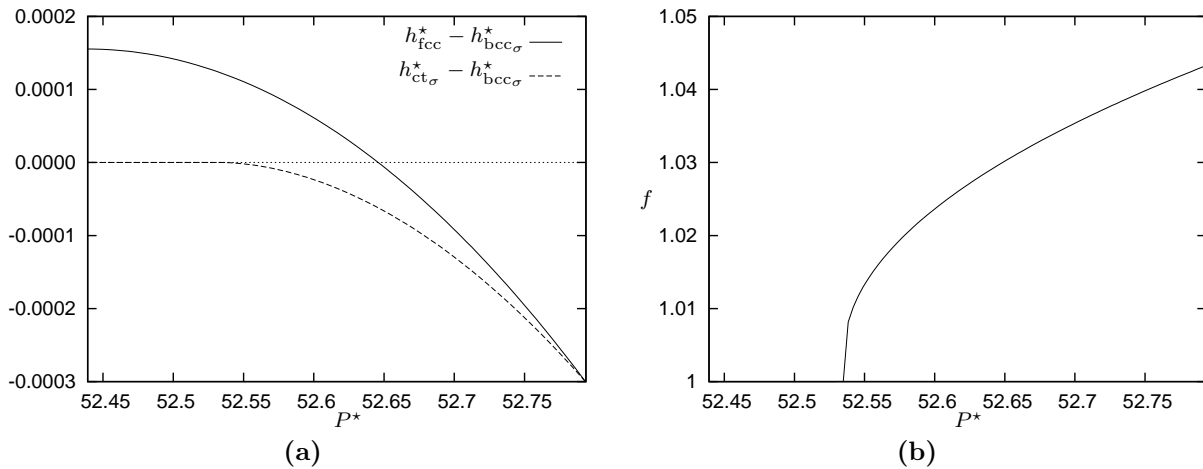


Figure 10.5: Curves for  $\kappa^* = 0.6$  in the hard core Yukawa model, considered in the pressure regime above  $P^* = 52.44$ , where the bcc structure starts to exhibit hard cores. In (a) the difference between the reduced enthalpies per particle of the fcc and  $\text{bcc}_\sigma$  as well as the  $\text{ct}_\sigma$  and  $\text{bcc}_\sigma$  structures versus reduced pressure are plotted. In (b) the parameter  $f$  of the corresponding  $\text{ct}_\sigma$  structure is plotted versus pressure. Due to numerical problems the exact transition pressure between  $\text{bcc}_\sigma$  and  $\text{ct}_\sigma$  is slightly overestimated.

satisfying  $h_{\text{ct}}^*(f, s_{\text{eq}}) \leq h_{\text{ct}}^*(f, s = 1)$ . This means that the equilibrium ct structure, if it exists at all, is a  $\text{ct}_\sigma$  structure where the nearest neighbours touch each other, i.e.,  $s_{\text{eq}} = 1$ . This observation drastically simplifies the numerical calculations, since we only need to find the minimum of a function of one variable,  $h_{\text{ct}_\sigma}^*(f)$ , the variable being the Bain transformation parameter  $f$ . This is the reason why the introduction of the parametrisation of all ct structures according to equation (5.89), where  $s = 1$  always results in a  $\text{ct}_\sigma$  structure for  $f \in [\sqrt{3}/2, \sqrt{3}/2]$ , is beneficial.

One can see in figure 10.4, that the minimum of the enthalpy per particle w.r.t.  $f$  shifts to larger  $f$ -values upon increasing pressure. However, the  $\text{ct}_\sigma$  structure is not the equilibrium lattice for all values of  $f$  up to  $f = \sqrt{3}/2$ , which would finally correspond to  $\text{fcc}_\sigma$ . In the  $\kappa^* = 0.6$  example there occurs a first order phase transition from  $\text{ct}_\sigma$  with  $f \simeq 1.0433$  to fcc (where  $s > 1$ ) already at  $P_5^* \simeq 52.79367$ .

The difference in  $h^*$  (and the corresponding parameter  $f$ ) of the stable  $\text{ct}_\sigma$  structure and the optimum  $\text{bcc}_\sigma$  structure in dependence of  $P^*$  for our example value of  $\kappa^* = 0.6$  is plotted in figure 10.5. Between the pressure values of  $P_1^* \simeq 52.43907$  and  $P_2^* \simeq 52.53547$ ,  $\text{bcc}_\sigma$  is the stable structure. The transition pressure for the second order phase transition between  $\text{bcc}_\sigma$  and  $\text{ct}_\sigma$ ,  $P_2^*$ , is difficult to determine numerically, because  $h_{\text{ct}_\sigma}^* - h_{\text{bcc}_\sigma}^*$  is a very flat curve at the transition. Since we set the transition pressure to the value where a difference in  $h^*$  of the  $\text{ct}_\sigma$  and  $\text{bcc}_\sigma$  structures is numerically detectable, this pressure is always slightly overestimated.

Figure 10.6 shows a close-up of the phase diagram region in the  $\kappa^* - P^*$ -plane where the

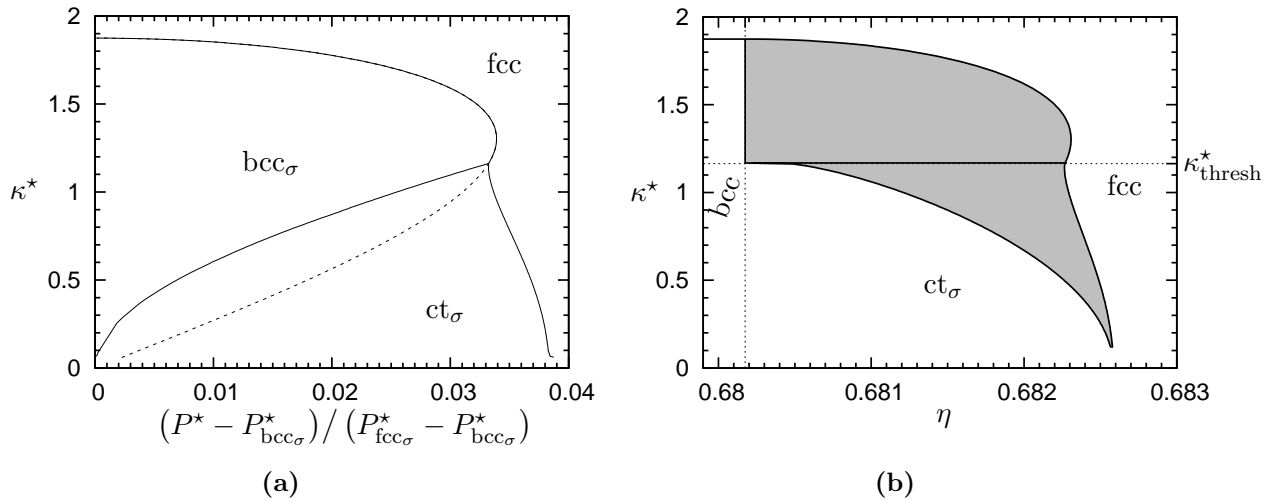


Figure 10.6: Close-up of the phase diagram region of the hard core Yukawa model above the pressure where the  $\text{bcc}_\sigma$  structure starts to exhibit touching hard cores ( $P_{\text{bcc}\sigma}^*$ ) in (a).  $P_{\text{fcc}\sigma}^*$  is the smallest pressure where  $\text{fcc}_\sigma$  is stable.  $\text{ct}_\sigma$  labels the region where a centred tetragonal structure with touching hard cores is the equilibrium one. The dashed line would be the threshold between the  $\text{bcc}_\sigma$  and  $\text{fcc}$  regions if no  $\text{ct}_\sigma$  structures were considered.

In (b) a close-up of the  $\kappa^*$ - $\eta$ -region where the  $\text{ct}_\sigma$  structure happens to be the MEC is visualised. The  $\text{ct}_\sigma$  region is bounded by the vertical line corresponding to the  $\text{bcc}_\sigma$  structure and the coexistence region (grey) between  $\text{ct}_\sigma$  and  $\text{fcc}$ .

$\text{ct}_\sigma$  structure occurs. For a better visualisation we use the (reduced) pressure relative to the smallest one where  $\text{bcc}_\sigma$  is stable,  $P_{\text{bcc}\sigma}^*$ , and in addition divide by the pressure difference between  $P_{\text{bcc}\sigma}^*$  and  $P_{\text{fcc}\sigma}^*$ , the smallest pressure for a stable  $\text{fcc}_\sigma$  structure. Thus, on the abscissa we plot the fraction of the tiny region between the dashed ( $\text{fcc}$ - $\text{fcc}_\sigma$  transition) and the close-by solid line ( $\text{bcc}_\sigma$ - $\text{fcc}$  transition) in figure 10.1. For the example value of  $\kappa^* = 0.6$  we have  $P_{\text{bcc}\sigma}^* = P_1^* \simeq 52.43907$  and  $P_{\text{fcc}\sigma}^* \simeq 62.22915$ ; both tend to infinity as  $\kappa^*$  approaches zero.

It is interesting to note, that between the largest  $\kappa^*$  value, above which only  $\text{fcc}_{(\sigma)}$  is stable,  $\kappa_{\text{max}}^* \simeq 1.874465$ , and another threshold value of  $\kappa_{\text{thresh}}^* \simeq 1.16$ , no  $\text{ct}_\sigma$  structure can be identified, a regime of stable  $\text{bcc}_\sigma$  has a phase boundary immediately with  $\text{fcc}$ . Below  $\kappa_{\text{thresh}}^*$  the  $\text{ct}_\sigma$  region starts to form, becoming broader with decreasing  $\kappa^*$ . Due to the numerical problems discussed above,  $\kappa_{\text{thresh}}^*$  is underestimated.

The high density region of the phase diagram can also be visualised in the  $\kappa^*$ - $\eta$ -plane, as is done in figure 10.6(b). The grey area depicted there is the coexistence region; below  $\kappa_{\text{thresh}}^*$  between the  $\text{fcc}$  phase and the  $\text{ct}_\sigma$  phase, above (up to  $\kappa_{\text{max}}^*$ ) between  $\text{bcc}_\sigma$  and  $\text{fcc}$ . The high density (large  $\eta$ ) delimiting line of the  $\text{ct}_\sigma$  region, beyond which the coexistence region is situated, moves to larger packing fractions the smaller  $\kappa^*$ . This means, since the density is strictly monotonously increasing with  $f$  for  $f \in [1, \sqrt{3/2}]$ , that  $f$  is maximal for

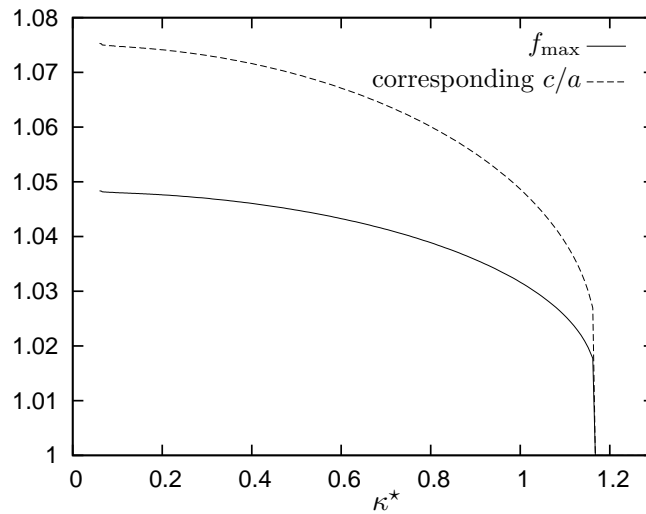


Figure 10.7: Maximum value of the parameter  $f$ , occurring at the transition between  $ct_\sigma$  and  $fcc$ , along with the corresponding value of the ratio of the edge lengths of the  $ct$  unit cell, versus  $\kappa^*$ , for the hard core Yukawa model.

the structure at the phase transition to  $fcc$ . This value is plotted in figure 10.7 along with the corresponding ratio between the longer and the shorter edge lengths of the  $ct$  unit cell. It is clearly visible that our numerical problems lead to a  $\kappa_{\text{thresh}}^*$ -value that is probably 5% too small, nevertheless it is obvious that  $\kappa_{\text{thresh}}^* < \kappa_{\text{max}}^*$ .

Thus, we have revealed the existence of stable  $ct$  structures at very high pressure values, where the  $bcc$  structure is known to exhibit touching hard cores, as long as the interaction range is not too short. They can be understood as “incomplete” Bain transformations from  $bcc$  to  $fcc$ , which resemble the more the  $bcc$  phase the smaller the pressure. However, the region where the  $ct$  structures are stable turned out to be extremely small, which will make it difficult to detect in experiments or simulations. Additionally it is also possible, that the  $ct$  stability region shrinks or even vanishes at higher temperatures.



# Chapter 11

## Conclusion and Outlook

This thesis has been dedicated to the investigation of the phase behaviour of various model systems, representing reasonable models for a variety of colloidal systems. All investigated systems have in common, that the constituting particles, the colloids, interact via a hard core plus varying potential tails.

The first focus has been laid on the critical behaviour of systems exhibiting long-range interactions. For the first representative, the charged Yukawa model, we developed a modified self-consistent Ornstein-Zernike approximation (mSCOZA) to be able to cope with the infinitely ranged Coulomb interaction, formerly preventing an application of SCOZA. In addition, we introduced a simple interpolation method for the exact location of the maximum of compressibility in dependence of density at given temperature, which improved the numerical results for the location of the critical point as well as for the various thermodynamic properties in its vicinity by orders of magnitude within the used theory.

With help of these methods we could detect, that a variation in the relative strength of the two competing tails of the charged Yukawa model, the Coulomb and the Yukawa interactions, does not change the critical exponents of the respective systems. However, the location of the critical point strongly depends on this relative strength, as does the *effective* critical behaviour: Effective critical exponents attain their respective non-mean field-values the closer to the critical point the stronger the long-ranged Coulomb contribution to the interaction potential is. Similar findings could be presented for the charged Kac model, which we were able to approximate in an adequate way by a charged Yukawa system, using high numerical accuracy calculations.

Further insight could be gained by verifying a relation between the relative strength-parameter  $\xi^2$  of the two potential tails of a Kac-Yukawa model and the critical exponent  $\gamma$  of the reference system, where particles just interact via the hard core Yukawa potential. This relation,  $\xi^2 \sim (T_c - T_c^{\text{ref}})^\gamma$ , thus provides additional means for the calculation of critical exponents of (in principle) arbitrary reference systems. Instead of investigating the divergence of the isothermal compressibility of the reference system at its critical point, one can determine the locations of the critical points of a series of systems with an additional Kac interaction, whose relative strength (compared to the tail of the reference system) is

tuned by the prefactor  $\xi^2$ .

The second main area of interest was the solid phase behaviour at  $T = 0$  of hard core systems with two different kinds of repulsive tails, the square-shoulder model and the hard core Yukawa model. For a successful, numerical investigation of the minimum enthalpy configurations at given pressure, we had to develop a new parametrisation of all crystal structures, which easily provides the exact knowledge of the smallest occurring distance between any points of the crystal lattice. For this so-called minimum distance parametrisation we could also provide a complete mapping of its variables to the conventional ones for Bravais lattices.

This tool provided high success rates in the search for equilibrium structures, i.e., minimum enthalpy configurations, using the genetic algorithm developed in our Soft Matter Theory group, the results were further refined by use of a Powell algorithm. After thorough investigations of possible close-packed structures, we were able to develop a systematic search strategy for all minimum enthalpy configurations of step-shaped, monotonously decreasing potential tails, strongly footing on the aforementioned methods. The square-shoulder model belongs to this class of systems and displayed an astonishing variety of equilibrium structures over the entire pressure regime. These minimum enthalpy configurations were found to appear in four types of aggregates. With increasing pressure we encountered clusters, columns, lamellae, and compact structures, a rule which turned out to be the more satisfied the larger the shoulder width was chosen compared to the hard core diameter. This sequence of structural archetypes for the square-shoulder model could also be predicted via a newly developed, mean-field type continuum theory, where the aggregates of particles are replaced by a continuum matter of equal average density, filling space in the respective shapes. Also, the continuum theory of equilibrium structures proved to give accurate numerical results for all considered thermodynamic variables and potentials. In addition, it provided further insight by giving rise to shoulder-reduced quantities, which lie, when plotted for systems of different shoulder widths, on common curves, as long as the shoulder width is not of comparable magnitude to the hard core diameter.

The systematic search strategy for step-shaped potential tails could also be extended to certain continuous tails via metric scaling, although only high-symmetry (cubic and centred tetragonal) structures were fully covered in this case. Since the hard core Yukawa model was formerly known to exhibit only solid phases with cubic symmetry (fcc and bcc) and fulfils the requirements of the extended search strategy, it has been a perfect test system for this method. Our work revealed the existence of another, centred tetragonal phase in the high density region of phase space. The region of stability for this new phase strongly depends on the interaction range of the Yukawa tail, at very short ranges only fcc is stable.

There are various possibilities for further extensions of the methods presented in this thesis. The most promising ones are probably:

- The application of the interpolation scheme, introduced around the maximum of

compressibility above the critical temperature, to the two compressibility maxima below this temperature for SCOZA and mSCOZA. This would give rise to highly improved boundary conditions and hence a more accurate shape of the spinodal and binodal lines. Critical exponents, when approaching the critical point from lower temperatures, would become assessable with similar accuracy like those from above the critical temperature.

- The implementation of other pair potentials and multiple components in our search algorithms for solid equilibrium structures. Thus, models having even more relevance to industrial applications (see introduction) could be investigated.
- The extension of the solid phase methods to finite temperatures.

The work presented in this thesis led to the original publications of [62] and the HPC–Europa scientific highlight<sup>1</sup> [114] concerning the investigations of criticality, and the *Soft Matter* hot article<sup>2</sup> [85] and [86] describing the findings for the square–shoulder model. The publications [87, 123, 124] were still under preparation during the conclusion of this thesis.

---

<sup>1</sup>[http://www.hpc-europa.org/index.php?section=Transnational&subsection=scientific\\_highlights](http://www.hpc-europa.org/index.php?section=Transnational&subsection=scientific_highlights)

<sup>2</sup><http://www.rsc.org/publishing/journals/SM/HotArticles.asp>





# Acknowledgements

Many thanks to:

- Gerhard Kahl for leading me into interesting, state of the art science, while at the same time giving me a large deal of freedom in exploring it.
- Martin Neumann, for his friendly acceptance to be my second referee and his thorough proof-reading.
- Jean-Michel Caillol, Jean-Jacques Weis, and Dominique Levesque, for their hospitality and aiding work.
- Julia Fornleitner, Dieter Gottwald, and Mario Kahn for helpful discussions and supporting work.
- Jürgen Köfinger, for introducing me into the SMT group.
- Other colleagues and friends for their support and company (in alphabetical order): Carlos Alvarez, Günther Doppelbauer, María José Fernaud Espinoza, Georg Falkinger, Michaela Jedinger, Florian Libisch, Christos Likos, Christiane Maria Losert-Valiente Kroon, Bianca Mladek, Alexander Paulsen, Dieter Schwanzer, Juan Antonio Valiente Kroon.
- All my extended family, especially my parents Gabriele and Josef Pauschenwein, for providing the social environment that gave me the opportunity to stride the path I have chosen.
- Martina Jedinger.

Financial support by the Austrian research fund (FWF), project numbers W004, P17823-N08, and P19890-N16, by the HPC-Europa project RII3-CT-2003-506079 (with the support of the European Community – Research Infrastructure Action under the FP6 “Structuring the European Research Area” Programme), and by the Vienna University of Technology (Förderungsstipendium) are gratefully acknowledged.



**Part V**  
**Appendix**



# Appendix A

## Coulomb Part of the Charged Yukawa Model

In this appendix we analytically calculate the contribution to the internal energy from the Coulomb interaction of the charged Yukawa model within the MSA. We follow the way described in [125] and define

$$D = 4\pi\beta\frac{q^2}{\varepsilon}, \quad (\text{A.1})$$

$$c^0(r) = c^C(r) + \beta\frac{q^2}{\varepsilon r}, \quad (\text{A.2})$$

$$S(r) = 2\pi \int_r^\infty tc^0(t) dt, \quad (\text{A.3})$$

$$C^0(k) = 2 \int_0^\infty \cos kr S(r) dr, \quad (\text{A.4})$$

$$J(r) = 2\pi \int_r^\infty th^C(t) dt, \quad \text{and} \quad (\text{A.5})$$

$$H(k) = 2 \int_0^\infty \cos kr J(r) dr. \quad (\text{A.6})$$

Comparing equation (A.2) with equation (4.6d) we see, that  $c^0(r) = 0$  for  $r > \sigma$ , and hence  $S(r)$  and  $C^0(k)$  exist. Equation (A.5) is strongly connected to the Coulomb energy per volume [equation (4.8)], considering equation (4.4b) we get

$$u^C = \frac{\rho^2 q^2}{\varepsilon} J(0). \quad (\text{A.7})$$

For physical reasons  $J(r)$  therefore exists, and so does  $H(k)$ . Our goal is now to determine  $J(0)$ .

Using

$$\phi^C(r) = \lim_{\mu \rightarrow 0} \frac{q^2}{\varepsilon r} e^{-\mu r} \quad (\text{A.8})$$

the Fourier transformation of the Coulomb–Ornstein–Zernike relation (4.3b) is

$$\lim_{\mu \rightarrow 0} (1 + \rho H(k)) \left( 1 - \rho \left( C^0(k) - D \frac{1}{k^2 + \mu^2} \right) \right) = 1 . \quad (\text{A.9})$$

Now we introduce the Baxter factorisation [126] for the second factor

$$1 - \rho \left( C^0(k) - D \frac{1}{k^2 + \mu^2} \right) = \tilde{Q}(k, \mu) \tilde{Q}(-k, \mu) \quad (\text{A.10})$$

with

$$\tilde{Q}(k, \mu) = 1 - \rho \int_0^\sigma e^{ikr} Q(r, \mu) dr + \rho A \int_\sigma^\infty e^{(ik-\mu)r} dr , \quad (\text{A.11})$$

where for  $r > \sigma$  the Ansatz

$$Q(r, \mu) = \sum_{i=1}^n d_i e^{-z_i r} , \quad r > \sigma \quad (\text{A.12})$$

for a linear combination of Yukawa tails outside the core with screening lengths  $z_i$  has been used ( $n = 1$ ,  $d_1 = -A$ ,  $z_1 = \mu$ ). Continuity of  $Q(r, \mu)$  at  $r = \sigma$  leads to

$$Q(\sigma, \mu) = -Ae^{-\mu\sigma} . \quad (\text{A.13})$$

Now consider the Fourier transformed Ornstein–Zernike relation (A.9) with the limit of  $\mu \rightarrow 0$  temporarily left out, replace the second factor on the left hand side by equation (A.10) and divide by  $\tilde{Q}(-k, \mu)$ :

$$(1 + \rho H(k)) \tilde{Q}(k, \mu) = \frac{1}{\tilde{Q}(-k, \mu)} . \quad (\text{A.14})$$

The inverse Fourier transformation of this equation gives for the left hand side

$$\begin{aligned}
& \int_{-\infty}^{\infty} dk e^{-kr} \tilde{Q}(k, \mu) + \rho \int_{-\infty}^{\infty} dk e^{-kr} H(k) \tilde{Q}(k, \mu) = \\
& = \int_{-\infty}^{\infty} dk e^{-kr} \left( 1 - \rho \int_0^{\infty} dr' e^{ikr'} Q(r', \mu) \right) + \\
& + \rho \int_{-\infty}^{\infty} dk e^{-kr} 2 \int_0^{\infty} dr' \frac{e^{ikr'} + e^{-ikr'}}{2} J(r') \cdot \left( 1 - \rho \int_0^{\infty} dr'' e^{ikr''} Q(r'', \mu) \right) = \\
& = \int_{-\infty}^{\infty} dk e^{-kr} - \rho \int_0^{\infty} dr' Q(r', \mu) \underbrace{\int_{-\infty}^{\infty} dk e^{ik(r'-r)}}_{=2\pi\delta(r-r')} + \\
& + \rho \int_{-\infty}^{\infty} dk e^{-kr} \int_{-\infty}^{\infty} dr' e^{ikr'} J(|r'|) \cdot \left( 1 - \rho \int_0^{\infty} dr'' e^{ikr''} Q(r'', \mu) \right) = \\
& = 2\pi\delta(r) - 2\pi\rho Q(r, \mu)\theta(r) + 2\pi\rho J(|r|) - \\
& - \rho^2 \int_{-\infty}^{\infty} dr' \int_0^{\infty} dr'' \underbrace{\int_{-\infty}^{\infty} dk e^{ik(r'+r''-r)} J(|r'|)}_{2\pi\delta(r'-(r-r''))} Q(r'', \mu) = \\
& = 2\pi\delta(r) - 2\pi\rho Q(r, \mu)\theta(r) + 2\pi\rho J(|r|) - 2\pi\rho^2 \int_0^{\infty} dr'' J(|r-r''|) Q(r'', \mu), \quad (\text{A.15})
\end{aligned}$$

with the usual Heaviside step function  $\theta(r)$ . The last term can be modified to

$$\begin{aligned}
& -2\pi\rho^2 \int_0^{\sigma} dr_1 J(|r-r_1|) Q(r_1, \mu) - 2\pi\rho^2 \int_{\sigma}^{\infty} dr'' J(|r-r''|) \left( -A e^{-\mu r''} \right) = \\
& = \left| \begin{array}{l} r-r'' = -r_1 \\ dr'' = dr_1 \end{array} \right| = -2\pi\rho^2 \int_0^{\sigma} dr_1 J(|r-r_1|) Q(r_1, \mu) + 2\pi\rho^2 \int_{\sigma-r}^{\infty} dr_1 J(|r_1|) A e^{-\mu(r+r_1)}.
\end{aligned}$$

For the right hand side we get using

$$\frac{1}{\tilde{Q}(-k, \mu)} = \frac{1}{1 - \rho \int_0^{\infty} e^{-ikr} Q(r, \mu) dr} = \sum_{n=0}^{\infty} \left( \rho \int_0^{\infty} e^{-ikr} Q(r, \mu) dr \right)^n \quad (\text{A.16})$$

for the Fourier transformation

$$\begin{aligned}
\int_{-\infty}^{\infty} \frac{e^{-ikr}}{\tilde{Q}(-k, \mu)} dk & = \int_{-\infty}^{\infty} e^{-ikr} dk + \rho \int_{-\infty}^{\infty} dk e^{-ikr} \int_0^{\infty} dr' e^{-ikr'} Q(r', \mu) + \dots \\
& = \int_{-\infty}^{\infty} e^{-ikr} dk + 2\pi\rho \int_0^{\infty} dr' \delta(r+r') Q(r', \mu) + \dots \\
& = 2\pi\delta(r), \quad \forall r > 0.
\end{aligned} \quad (\text{A.17})$$

By combining the left and right hand sides this leads (through division by  $2\pi\rho$ ) to

$$J(r) = Q(r, \mu) + \rho \int_0^{\sigma} dr_1 Q(r_1, \mu) J(|r-r_1|) - \rho e^{-\mu r} \int_{\sigma-r}^{\infty} dr_1 J(|r_1|) A e^{-\mu r_1}. \quad (\text{A.18})$$

Now we consider  $r < \sigma$ . Since  $h^C(t) = 0$  as long as  $t < \sigma$ , we get

$$J(r) = J(\sigma) =: J, \quad \forall r < \sigma. \quad (\text{A.19})$$

Equation (A.18) is therefore for  $r < \sigma$

$$J = Q(r, \mu) + \rho \int_0^\sigma dr_1 Q(r_1, \mu) J - A\rho e^{-\mu r} \int_{\sigma-r}^\infty dr_1 J(r_1) e^{-\mu r_1}. \quad (\text{A.20})$$

Using  $R = \sigma - r$  we transform the last integral via partial integration<sup>1</sup>:

$$\begin{aligned} \int_{\sigma-r}^\infty dr' J(r') e^{-\mu r'} &= 2\pi \int_R^\infty dr' e^{-\mu r'} \int_{r'}^\infty dt t h^C(t) = \\ &= -\frac{2\pi}{\mu} e^{-\mu r'} \int_{r'}^\infty dt t h^C(t) \Big|_R^\infty - \frac{2\pi}{\mu} \int_R^\infty dr' e^{-\mu r'} r' h^C(r') = \\ &= \frac{2\pi}{\mu} \int_R^\infty dt e^{-\mu R} t h^C(t) - \frac{2\pi}{\mu} \int_R^\infty dr' e^{-\mu r'} r' h^C(r') = \\ &= 2\pi \int_R^\infty dr' h^C(r') r' \frac{e^{-\mu R} - e^{-\mu r'}}{\mu} = \\ &= 2\pi \int_R^\infty dr' h^C(r') r' (r' - R + \mathcal{O}(\mu)) \\ &= 2\pi \int_\sigma^\infty dr' r'^2 h^C(r') - (\sigma - r) J + \mathcal{O}(\mu), \end{aligned} \quad (\text{A.21})$$

where in the last step  $R$  in the lower limit of the integral could be replaced by  $\sigma$  because  $R = \sigma - r < \sigma$  and the integrand is 0 for all  $r'$ -values smaller than  $\sigma$ .

Now we take the limit  $\mu \rightarrow 0$ . Through writing  $Q(r) := Q(r, 0)$  equation (A.20) becomes

$$J = Q(r) + \rho \int_0^\sigma dr_1 Q(r_1) J - 2\pi A\rho \int_\sigma^\infty dr' r'^2 h^C(r') + A\rho(\sigma - r) J. \quad (\text{A.22})$$

It can easily be seen that  $Q(r)$  is a 1<sup>st</sup> order polynomial in  $r$  for  $r < \sigma$ ,

$$Q(r) = a + br, \quad (\text{A.23})$$

which we can insert in equation (A.22), yielding

$$J = a + br + \rho J \left( a\sigma + b\frac{\sigma^2}{2} + A\sigma - Ar \right) - 2\pi\rho A \int_\sigma^\infty dr' r'^2 h^C(r'). \quad (\text{A.24})$$

In this equation we can collect the powers of  $r$ , giving

$$J = a + \rho J a \sigma + \rho J b \frac{\sigma^2}{2} + \rho J A \sigma - 2\pi\rho A \int_\sigma^\infty dr' r'^2 h^C(r') \quad \text{and} \quad (\text{A.25})$$

$$0 = b - \rho J A \quad \Rightarrow \quad b = \rho J A. \quad (\text{A.26})$$

<sup>1</sup>Also use  $\frac{\partial}{\partial x} \int_{a(x)}^{b(x)} f(x) dx = \int_{a(x)}^{b(x)} f'(x) dx + b'(x) f[b(x)] - a'(x) f[a(x)]$ .



From the continuity equation (A.13) it follows that  $a = -A - b\sigma$ , together with equation (A.26) we can therefore eliminate  $a$  and  $b$ , getting

$$J = -A - \rho J A \sigma - \rho^2 J^2 A \frac{\sigma^2}{2} - 2\pi\rho A \int_{\sigma}^{\infty} dr' r'^2 h^C(r'). \quad (\text{A.27})$$

The remaining integral can also be evaluated (remember that  $\rho_+ = \rho_- \equiv \rho/2$ ):

$$\begin{aligned} 2\pi\rho \int_0^{\infty} dr r^2 h^C(r) &= 2\pi\frac{\rho}{2} \int_0^{\infty} dr r^2 (h_{++} - h_{+-}) = \\ &= \frac{1}{2} \left( 4\pi\rho_+ \int_0^{\infty} dr r^2 g_{++}(r) - 4\pi\rho_- \int_0^{\infty} dr r^2 g_{+-}(r) \right) = \\ &= \frac{1}{2} (N_+ - 1 - N_-) = -\frac{1}{2}. \end{aligned}$$

This leads to the final equation for  $J$

$$2J + A(1 + \rho J\sigma)^2 = 0, \quad (\text{A.28})$$

with the solutions

$$J = \frac{-1 - A\rho\sigma \pm \sqrt{1 + 2A\rho\sigma}}{A\rho^2\sigma^2}. \quad (\text{A.29})$$

To derive the quantity  $A$  (which will turn out to depend only on  $D$  and  $\rho$ ) we need another equality in the Baxter formalism [126],

$$2\pi r c(r) = -Q'(r) + \rho \int_0^{\infty} Q(t) Q'(r+t) dt, \quad (\text{A.30})$$

which we evaluate for  $r \gg \sigma$ :

$$\begin{aligned} 2\pi r \left( -\frac{D}{4\pi r} \right) &= -\mu A e^{-\mu r} + \rho \int_0^{\sigma} (a + bt)(-\mu A) e^{-\mu(r+t)} dt + \rho \int_{\sigma}^{\infty} A e^{-\mu t} (-\mu A) e^{-\mu(r+t)} dt \\ &= \dots = -\frac{1}{2}\rho A^2 + \mathcal{O}(\mu). \end{aligned} \quad (\text{A.31})$$

This leads to  $(A\rho)^2 = D\rho \equiv \kappa^2$ , where  $\kappa$  is the Debye length.

To find out which of the two solutions is the physical one, we use the low density behaviour of the internal energy. First we recognise that  $D$  is density independent, so to explicitly get the density dependence of  $u^C$  [equation (A.7)] we use equation (A.29) with all appearances of  $A\rho$  replaced by  $\sqrt{D\rho}$ ,

$$u^C = \rho^2 \frac{q^2}{\epsilon} J = \frac{1}{4\pi\beta\sigma^2} \sqrt{D\rho} \left( -1 - \sigma\sqrt{D\rho} \pm \sqrt{1 + 2\sigma\sqrt{D\rho}} \right). \quad (\text{A.32})$$

To find out which sign we have to take, consider now not the excess internal energy per volume, but the total one, and expand the square root with the  $\pm$  sign in front of it in a

series for small  $\rho$ :

$$U^{\text{ex,C}} = \frac{NkT}{4\pi\sigma^2} \sqrt{\frac{D}{\rho}} \left( -1 - \sigma\sqrt{D\rho} \pm \left( 1 + \sigma\sqrt{D\rho} - \frac{1}{2}\sigma^2 D\rho \pm \dots \right) \right) \quad (\text{A.33})$$

$$\rightarrow \frac{NkT}{4\pi\sigma^2} \sqrt{D} \cdot \begin{cases} -\frac{1}{2}\sigma^2 D\sqrt{\rho} & (+) \\ -\frac{2}{\sqrt{\rho}} & (-) \end{cases} . \quad (\text{A.34})$$

$U^{\text{ex,C}}$  has to become zero as  $\rho$  goes to 0 while  $N$  remains finite. Therefore the solution with the + sign has to be the right one:

$$u^{\text{C}} = \frac{\kappa}{4\pi\beta\sigma^2} \left( -1 - \sigma\kappa + \sqrt{1 + 2\sigma\kappa} \right) , \quad (\text{A.35})$$

with

$$\kappa = \sqrt{4\pi\beta\rho\frac{q^2}{\varepsilon}} . \quad (\text{A.36})$$

# Appendix B

## 2D Lattices

### B.1 Two Dimensional Minimum Distance Parametrisation

In contrast to 3D, where all primitive unit cells have the same volume, in 2D they have the same area. The unification algorithm described in 5.1 therefore changes to

1. Calculate the circumference  $\Sigma^*$  of the primitive unit cell given by  $\mathbf{a}$  and  $\mathbf{b}$ .
2. Calculate the circumferences of the 4 primitive cells defined through

$$(\mathbf{a}, \mathbf{b} \pm \mathbf{a}), \quad (\mathbf{a} \pm \mathbf{b}, \mathbf{b}), \quad (\text{B.1})$$

and denote the smallest one by  $\tilde{\Sigma}$ .

3. If  $\tilde{\Sigma} < \Sigma^*$  then take the corresponding primitive vectors to  $\tilde{\Sigma}$  as the new values for  $\mathbf{a}$  and  $\mathbf{b}$  and start over again.

Another feature of the 2D case is, that if  $(\mathbf{a}, \mathbf{b})$  is the unit cell with the smallest circumference, there exists no lattice vector shorter than  $\mathbf{b}$ .

**Proof:** Assume to the contrary that there exists a lattice-vector  $\mathbf{c}$  which has length  $|\mathbf{c}| < |\mathbf{b}|$ . Now consider an arbitrary lattice point from which all three vectors  $\mathbf{a}$ ,  $\mathbf{b}$ ,  $\mathbf{c}$  point to another lattice point. It is obvious, that the cells  $(\mathbf{a}, \mathbf{c})$  and  $(\mathbf{b}, \mathbf{c})$  have smaller circumferences than  $(\mathbf{a}, \mathbf{b})$ , in contradiction to the assumption.  $\square$

Equation (B.1) can be reduced to even less possibilities. Firstly, since  $|\mathbf{a}| \geq |\mathbf{b}|$ , the circumference of  $(\mathbf{a} \pm \mathbf{b}, \mathbf{b})$  is always less or equal the circumference of  $(\mathbf{a}, \mathbf{a} \pm \mathbf{b})$ , which means only  $(\mathbf{a} \pm \mathbf{b}, \mathbf{b})$  have to be considered. Secondly, since the angle between  $\mathbf{a}$  and  $\mathbf{b}$  is restricted to values between 0 and  $\pi/2$ , we always have  $|\mathbf{a} + \mathbf{b}| \geq |\mathbf{a} - \mathbf{b}|$ . Hence, the only unit cell of equation (B.1) that has to be considered is

$$(\mathbf{a} - \mathbf{b}, \mathbf{b}). \quad (\text{B.2})$$

In the region where the unification algorithm does not lead to another unit cell the condition

$$|\mathbf{a} - \mathbf{b}| \geq a \quad (\text{B.3})$$

has therefore to be satisfied, inserting  $\mathbf{a} = a(1, 0)$  and  $\mathbf{b} = ax(\cos \varphi, \sin \varphi)$  leads to

$$\cos \varphi \leq \frac{x}{2}. \quad (\text{B.4})$$

This condition is not only necessary but also sufficient to describe the region that remains unchanged under the application of the unification algorithm. A derivation, that includes the rigorous proof that this region only incorporates lattices where  $\mathbf{b}$  is the smallest lattice vector (no “local minima”), is done in section 5.2.1.

## B.2 Fractal Parameter Space

We consider a 2D lattice with lattice vectors

$$\mathbf{a} = a \begin{pmatrix} 1 \\ 0 \end{pmatrix}, \quad \text{and} \quad \mathbf{b} = a \begin{pmatrix} x \cos \varphi \\ x \sin \varphi \end{pmatrix}, \quad (\text{B.5})$$

where

$$a > 0, \quad (\text{B.6a})$$

$$0 < x \leq 1, \quad \text{and} \quad (\text{B.6b})$$

$$0 < \varphi \leq \frac{\pi}{2}, \quad (\text{B.6c})$$

with one single particle in the basis (at the lattice sites). The area–number density is given as

$$\eta = \frac{1}{a^2 x \sin \varphi}. \quad (\text{B.7})$$

For constant  $\eta$  we can replace  $a$  by  $1/\sqrt{\eta x \sin \varphi}$  and the parameter space for the possible lattices becomes 2D ( $x$  and  $\varphi$ ). For the next steps we have to make a simple variable transformation to

$$b_x = x \cos \varphi \quad \text{and} \quad (\text{B.8a})$$

$$b_y = x \sin \varphi, \quad (\text{B.8b})$$

resulting in

$$b_x \geq 0, \quad b_y > 0, \quad \text{with } b_x^2 + b_y^2 \leq 1, \quad \text{and} \quad (\text{B.9})$$

$$a = 1/\sqrt{\eta b_y}. \quad (\text{B.10})$$

Now we take the hard core of the basis particle into account, which has a diameter of  $\sigma$ . The condition, that all possible distances between lattice points have to be at least  $\sigma$

can, due to the translational symmetry, be formulated just for the central lattice point — all lattice vectors have to be longer than  $\sigma$ :

$$(n\mathbf{a} - m\mathbf{b})^2 > \sigma^2, \quad (\text{B.11})$$

with  $n, m \in \mathbb{Z}$ . The reason why we use a minus instead of a plus in front of  $m$  will be explained later. Obviously it does not make any difference. Inserting equation (B.5) and equation (B.8) yields

$$n^2 a^2 - 2nma^2 b_x + m^2 a^2 (b_x^2 + b_y^2) > \sigma^2, \quad (\text{B.12})$$

which, after division by  $a^2$  and usage of equation (B.10), results in

$$n^2 - 2nmb_x + m^2 (b_x^2 + b_y^2) > \sigma^2 \eta b_y. \quad (\text{B.13})$$

We define as usual  $\eta^* = \eta\sigma^2$ . The case  $m = 0$  gives  $b_y \leq |n|/\eta^*$ , always fulfilled for  $n \geq 2$ . The case  $n = 0$  is unphysical (the distance of the origin from itself needs not be greater than  $\sigma$ ), which is why  $n = m = 0$  has to be excluded. We therefore just keep in mind that

$$b_y \leq 1/\eta^*, \quad (\text{B.14})$$

which is only relevant for large densities. Therefore we consider now  $m \in \mathbb{Z} \setminus \{0\}$ .

The integers  $n$  and  $m$  only occur squared or as a product in equation (B.13), which means that w.l.o.g. we can restrict one of them to be non-negative — we choose

$$n \in \mathbb{N}_0. \quad (\text{B.15})$$

After dividing by  $m^2$  ( $m \neq 0$ , see above) we can therefore construct whole-square expressions for  $b_x$  and  $b_y$  and put what remains to the other side of the inequality, resulting in

$$\left(b_x - \frac{n}{m}\right)^2 + \left(b_y - \frac{\eta^*}{2m^2}\right)^2 > \left(\frac{\eta^*}{2m^2}\right)^2. \quad (\text{B.16})$$

This inequality has an easy geometrical interpretation: It excludes the disks (but keeps their rims) with midpoints at  $M = \left(\frac{n}{m}, \frac{\eta^*}{2m^2}\right)$  and radii of  $R = \frac{\eta^*}{2m^2}$  for all possible combinations of  $m$  and  $n$  from the quarter-disk-like parameter space defined in equation (B.9).

The possible, or better to say relevant values of  $n$  and  $m$  can still be narrowed down. Let us first consider the case where  $n > m > 0$ . The abscissa coordinate of the corresponding midpoint is therefore greater than 1, and we can formulate a necessary condition for the disk to be relevant. Its radius must have at least such a value, that it overlaps with the  $[0, 1] \times [0, 1]$  square in parameter space to have a chance to overlap with the parameter space defined in equation (B.9), i.e.,  $\frac{\eta^*}{2m^2} \geq \frac{n}{m} - 1$ , and after multiplication with  $2m^2$

$$\eta^* \geq 2 \underbrace{m}_{\geq 1} \underbrace{(n - m)}_{\geq 1} \geq 2. \quad (\text{B.17})$$

Since  $\eta_{\max}^* = 2/\sqrt{3}$  this is impossible, which means  $n \leq m$  for  $m > 0$ .

If we consider  $m < 0$  we get in a similar way  $\eta^* \geq 2n|m| \geq 2$ , never true except for  $n = 0$ . But for  $n = 0$  equation (B.16) is insensitive to the sign of  $m$ , which means all possibilities are covered within the case  $m > 0$ . This explains why we chose the minus sign in equation (B.11), because now we have  $m \in \mathbb{N}$ .

Next consider all cases for one fixed rational number  $q = \frac{n}{m} (\leq 1)$ . This means, the abscissa of the midpoint of every corresponding disk remains fixed, while its ordinate and radius (which are always the same) can change with  $m$ . As a matter of fact, all these disks touch the abscissa in the same point  $(q, 0)$  (from the same side), simple geometry tells that all these disks are included in the one with the largest radius, i.e., smallest  $m$ . The smallest possible  $m$  for fixed  $q = \frac{n}{m}$  is obtained for the case where  $m$  and  $n$  are coprime.

Finally we check the disk at  $M = (0, \eta^*/2)$ , more precisely the intersection of its (circular) rim with the boundary of the parameter space defined in equation (B.9). For  $\eta^* \leq 1$  we get two intersection points at  $(0, 0)$  and  $(0, \eta^*)$ , resulting in a complete half-disk to be excluded. But for  $\eta^* > 1$  the second intersection point is at the circular rim of the parameter space defined in equation (B.9) at  $(\sqrt{1 - \frac{1}{\eta^{*2}}}, \frac{1}{\eta^*})$ , which then is at the same time the point with the highest  $b_y$ -value. This means, equation (B.14) is always satisfied.

In summary we get for the set of allowed parameters

$$\tilde{S} = \{(b_x, b_y) \in \mathbb{R}^2 | 0 \leq b_x, 0 < b_y, b_x^2 + b_y^2 \leq 1\} \setminus \bigcup_M D_R(M) , \quad (\text{B.18a})$$

where  $D_R(M)$  is the disk of radius  $R = \frac{\eta^*}{2m^2}$  around the midpoint  $M = (\frac{n}{m}, \frac{\eta^*}{2m^2})$  and

$$m \in \mathbb{N} \quad \wedge \quad n \in \mathbb{N}_0 \quad \wedge \quad n \leq m \quad \wedge \quad m, n \text{ coprime.} \quad (\text{B.18b})$$

Obviously this set includes only the irrational numbers on the abscissa itself, a typical fractal behaviour. This can also be seen in figure B.1, where we plot the allowed region in  $b_x$ - $b_y$ - as well as in  $x$ - $\varphi$ -space.

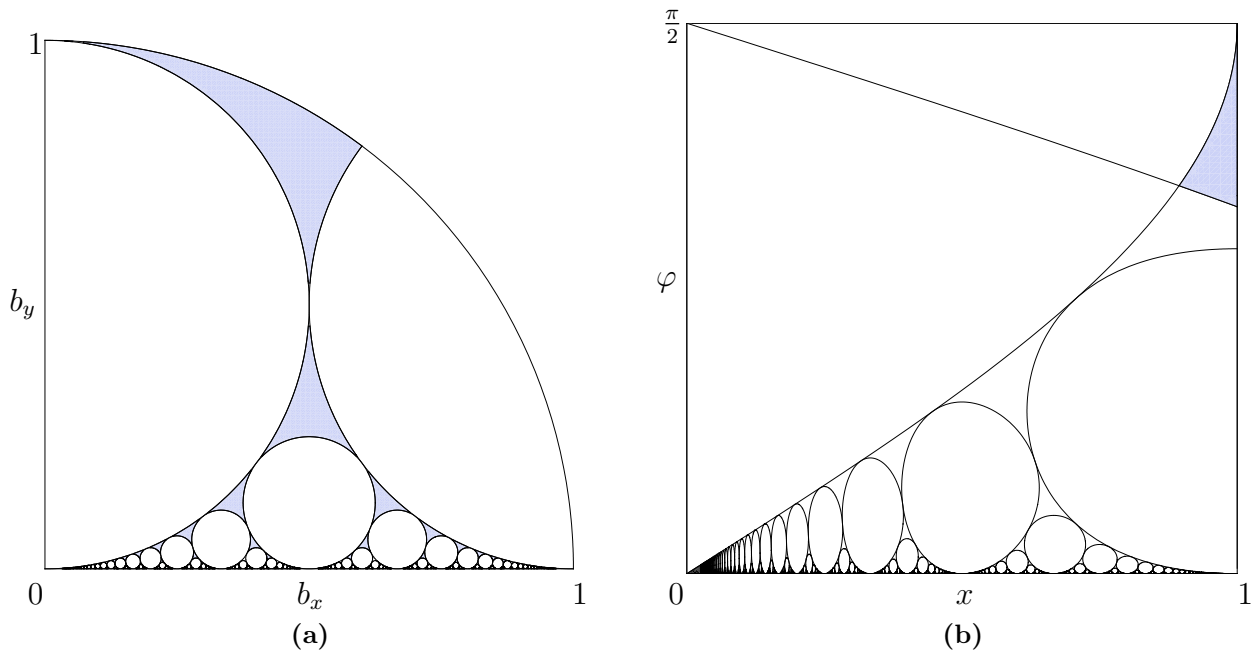


Figure B.1: In (a) the allowed region in  $b_x$ - $b_y$ -space is plotted for the special case of  $\eta^* = 1$ , where the rims of the excluded disks are just exactly the so called Ford circles. The region is then a superset of the Apollonian gasket, a fractal of dimension  $\simeq 1.3057$ . For different values of  $\eta^*$  the disks change their radii while still touching the abscissa and excluding all rational values of  $b_x$  there.

In (b) we map the region back to  $x$ - $\varphi$ -space. We additionally include the line  $\cos \varphi = x/2$ , above which the minimum distance configurations lie; the remaining region is coloured blue.





# Appendix C

## 3D Symmetries in the MDP

### C.1 Mapping from the BCO MDP to the Conventional Parameters

In this section we give the back-transformation formulas to obtain the conventional bco Bravais lattice parameters for given MDP parameters, to complete the discussion of the bco lattices of section 5.3. Similar to there, we distinguish three cases:

1.  $\tilde{d}/2$  is the smallest distance in the bco lattice, the MDP parameters are [see equation (5.53a)]

$$x = 1 \wedge 0 < \cos \varphi < \frac{1}{2} \wedge -\frac{1}{2} \leq \xi \leq -\frac{1}{2} + \cos \varphi \wedge \eta, \zeta \text{ maximal} . \quad (\text{C.1})$$

The three corresponding MDP vectors can be envisaged as three linearly independent vectors pointing from the centred position of the bco unit cell to three corners. Due to the restrictions of equation (C.1) for  $\mathbf{b}$  and  $\mathbf{c}$  we know, that they point to three corners of one face of the bco unit cell. Hence the distances between the apices of the three position vectors represent two edge lengths of the bco unit cell along with its diagonal, and the distance from  $-\mathbf{c}$  to  $\mathbf{b}$  and  $\mathbf{a}$  result in another diagonal and the third edge length. To know which distances to drop to get rid of the diagonal lengths, one just has to check which resulting vectors are pairwise orthogonal to each other. We obtain three candidate lengths

$$l_1 = a\sqrt{2}\sqrt{1 - \cos \varphi} , \quad l_2 = a\sqrt{2}\sqrt{\cos \varphi - \xi} , \quad \text{and} \quad l_3 = a\sqrt{2}\sqrt{1 + \xi} . \quad (\text{C.2})$$

If we want to know exactly which of these  $l_i$  are the conventional unit cell parameters ordered by magnitude ( $\tilde{c} < \tilde{b} < \tilde{a}$ ), we have to consider the following cases:

- $0 < \cos \varphi \leq \frac{1}{4}$ :  $\tilde{a} = l_1$ 
  - ★  $-\frac{1}{2} \leq \xi \leq -\frac{1}{2} + \frac{1}{2} \cos \varphi$ :  $\tilde{b} = l_2, \tilde{c} = l_3$
  - ★  $-\frac{1}{2} + \frac{1}{2} \cos \varphi < \xi \leq -\frac{1}{2} + \cos \varphi$ :  $\tilde{b} = l_3, \tilde{c} = l_2$

- $\frac{1}{4} \leq \cos \varphi \leq \frac{1}{3}$ :
  - ★  $-\frac{1}{2} \leq \xi \leq 2 \cos \varphi - 1$ :  $\tilde{a} = l_2, \tilde{b} = l_1, \tilde{c} = l_3$
  - ★  $2 \cos \varphi - 1 < \xi \leq -\frac{1}{2} + \frac{1}{2} \cos \varphi$ :  $\tilde{a} = l_1, \tilde{b} = l_2, \tilde{c} = l_3$
  - ★  $-\frac{1}{2} + \frac{1}{2} \cos \varphi < \xi \leq -\cos \varphi$ :  $\tilde{a} = l_1, \tilde{b} = l_3, \tilde{c} = l_2$
  - ★  $-\cos \varphi < \xi \leq -\frac{1}{2} + \cos \varphi$ :  $\tilde{a} = l_3, \tilde{b} = l_1, \tilde{c} = l_2$
- $\frac{1}{3} < \cos \varphi < \frac{1}{2}$ :
  - ★  $-\frac{1}{2} \leq \xi \leq -\cos \varphi$ :  $\tilde{a} = l_2, \tilde{b} = l_1, \tilde{c} = l_3$
  - ★  $-\cos \varphi < \xi \leq -\frac{1}{2} + \frac{1}{2} \cos \varphi$ :  $\tilde{a} = l_2, \tilde{b} = l_3, \tilde{c} = l_1$
  - ★  $-\frac{1}{2} + \frac{1}{2} \cos \varphi < \xi \leq 2 \cos \varphi - 1$ :  $\tilde{a} = l_3, \tilde{b} = l_2, \tilde{c} = l_1$
  - ★  $2 \cos \varphi - 1 < \xi \leq -\frac{1}{2} + \cos \varphi$ :  $\tilde{a} = l_3, \tilde{b} = l_1, \tilde{c} = l_2$

2.  $\tilde{c} < \tilde{d}/2 < \tilde{b}$  with the conditions of equation (5.53b). Let the origin be the centre of the bco unit cell. Then the two MDP vectors  $\mathbf{a}$  and  $\mathbf{b}$  point to two corner points which can either be the delimiting points for an edge of length  $\tilde{a}$  or  $\tilde{b}$ , or for a diagonal of a face having  $\tilde{c}$  as an edge length. The two cases can be distinguished by the sign of  $\xi$ : If  $\xi > 0$  then  $\mathbf{b} - \mathbf{a}$  is a lattice vector along an edge of the unit cell, if  $\xi < 0$  it is a lattice vector along a face diagonal. In any case  $\tilde{c} = c$ , we differentiate them:

- $\xi < 0$ :  $\tilde{c} = a\sqrt{-2\xi}, \tilde{b} = a\sqrt{2}\sqrt{1 - \cos \varphi + \xi}$ , and  $\tilde{a} = a\sqrt{2}\sqrt{1 + \cos \varphi}$ .
- $\xi > 0$ :  $\tilde{c} = a\sqrt{2\xi}$ 
  - ★  $0 < \cos \varphi \leq \frac{1}{4}$  and  $\xi > 2 \cos \varphi$ :  
 $\tilde{b} = a\sqrt{2}\sqrt{1 + \cos \varphi - \xi}$  and  $\tilde{a} = a\sqrt{2}\sqrt{1 - \cos \varphi}$ ,
  - ★ else  $\tilde{b} = a\sqrt{2}\sqrt{1 - \cos \varphi}$  and  $\tilde{a} = a\sqrt{2}\sqrt{1 + \cos \varphi - \xi}$ .

3. The case  $\tilde{c} < \tilde{b} < \tilde{d}/2$  has already been completely discussed in section 5.3.

## C.2 Minimum Distances in the SFCM Lattice

See section 5.3 for an explanation of the symbols. To find out whether a given set of minimum distance vectors  $\mathbf{a}$ ,  $\mathbf{b}$ , and  $\mathbf{c}$  correspond to a sfcmlattice, proceed in the following way:

Distinguish between:

1. The  $\tilde{d}/2$  point lies at  $\mathbf{a}'/2$ . Candidate lengths are:

- $b', c', \tilde{d}/2$ , which can appear in the following orders of increasing length:
  - ★  $b' \rightarrow c' \rightarrow \tilde{d}/2$

Check whether the minimum vectors  $\mathbf{b}'$  and  $\mathbf{a}'$  form a centred rectangular 2D-lattice of kind 5.9(d). Then, check whether  $\mathbf{c}' \perp \mathbf{b}'$ . The result is:

$$\tilde{\mathbf{a}} = 2\mathbf{a}' \pm \mathbf{b}' \quad (\tilde{\mathbf{a}} \perp \mathbf{b}') \quad \tilde{\mathbf{b}} = \mathbf{c}' \quad \tilde{\mathbf{c}} = \mathbf{b}' \quad (\text{C.3})$$

$$\star b' \rightarrow \tilde{d}/2 \rightarrow c'$$

Only possible if  $\tilde{d}/2 = c'$ , otherwise  $\tilde{d}/2$  would have been chosen twice (see next item). Do the same as in the previous item, but exchange the roles of  $\mathbf{a}'$  and  $\mathbf{b}'$ .

$$\star b' \rightarrow \tilde{d}/2 \rightarrow \tilde{d}/2$$

Check whether  $\mathbf{b}'$  and  $\mathbf{a}'$  form a centred rectangular 2D lattice of kind 5.9(c). Then check  $\mathbf{c}' \perp (\mathbf{a}' \pm \mathbf{b}')$  and obtain:

$$\tilde{\mathbf{a}} = \mathbf{a}' \mp \mathbf{b}' \quad \tilde{\mathbf{b}} = \mathbf{c}' \quad \tilde{\mathbf{c}} = \mathbf{a}' \pm \mathbf{b}' \quad (\text{C.4})$$

$$\star \tilde{d}/2 \rightarrow b' \rightarrow c'$$

Only possible if  $\tilde{d}/2 = b' = c'$ , else see next item. Check whether  $\mathbf{a}'$  and  $\mathbf{c}'$  form a centred rectangular 2D lattice of kind 5.9(d) with equal lengths (which is equal to 5.9(a)). Then check whether  $\mathbf{b}' \perp \mathbf{a}'$

$$\tilde{\mathbf{a}} = 2\mathbf{c}' \pm \mathbf{a}' \quad (\tilde{\mathbf{a}} \perp \mathbf{a}') \quad \tilde{\mathbf{b}} = \mathbf{b}' \quad \tilde{\mathbf{c}} = \mathbf{a}' \quad (\text{C.5})$$

$$\star \tilde{d}/2 \rightarrow \tilde{d}/2 \rightarrow b'$$

Check whether  $\mathbf{c}'$  and  $\mathbf{b}'$  form a centred rectangular 2D lattice of kind 5.9(c). Then check  $\mathbf{a}' \perp (\mathbf{c}' \pm \mathbf{b}')$  and obtain:

$$\tilde{\mathbf{a}} = \mathbf{c}' \mp \mathbf{b}' \quad \tilde{\mathbf{b}} = \mathbf{a}' \quad \tilde{\mathbf{c}} = \mathbf{c}' \pm \mathbf{b}' \quad (\text{C.6})$$

$$\star \tilde{d}/2 \rightarrow b' \rightarrow \tilde{d}/2$$

Only possible if  $\tilde{d}/2 = b'$ . Check whether  $\mathbf{c}'$  and  $\mathbf{a}'$  form a centred rectangular 2D lattice of kind 5.9(c). Then check  $\mathbf{b}' \perp (\mathbf{c}' \pm \mathbf{a}')$  and obtain:

$$\tilde{\mathbf{a}} = \mathbf{c}' \mp \mathbf{a}' \quad \tilde{\mathbf{b}} = \mathbf{b}' \quad \tilde{\mathbf{c}} = \mathbf{c}' \pm \mathbf{a}' \quad (\text{C.7})$$

$$\star c' \rightarrow b' \rightarrow \tilde{d}/2$$

Check whether  $\mathbf{c}'$  and  $\mathbf{a}'$  form a centred rectangular 2D lattice of kind 5.9(d). Then check  $\mathbf{b}' \perp \mathbf{c}'$ , result:

$$\tilde{\mathbf{a}} = 2\mathbf{a}' \pm \mathbf{c}' \quad \tilde{\mathbf{b}} = \mathbf{b}' \quad \tilde{\mathbf{c}} = \mathbf{c}' \quad (\text{C.8})$$

$$\star c' \rightarrow \tilde{d}/2 \rightarrow b'$$

Check whether  $\mathbf{c}'$  and  $\mathbf{b}'$  form a centred rectangular 2D lattice of kind 5.9(d). Then check  $\mathbf{a}' \perp \mathbf{c}'$ , result:

$$\tilde{\mathbf{a}} = 2\mathbf{b}' \pm \mathbf{c}' \quad \tilde{\mathbf{b}} = \mathbf{a}' \quad \tilde{\mathbf{c}} = \mathbf{c}' \quad (\text{C.9})$$

$$\star \tilde{d}/2 \rightarrow c' \rightarrow b'$$

Only possible if  $\tilde{d}/2 = c'$ . Check whether  $\mathbf{b}'$  and  $\mathbf{c}'$  form a centred rectangular 2D lattice of kind 5.9(d) or the one of equation (5.9(a)). Then check  $\mathbf{b}' \perp \mathbf{c}'$ , result:

$$\tilde{\mathbf{a}} = 2\mathbf{c}' \pm \mathbf{b}' \quad \tilde{\mathbf{b}} = \mathbf{a}' \quad \tilde{\mathbf{c}} = \mathbf{b}' \quad (\text{C.10})$$

- $a', b', \tilde{d}/2$

- ★  $b' \rightarrow a' \rightarrow \tilde{d}/2$

Check whether  $\mathbf{b}'$  and  $\mathbf{a}'$  form a centred rectangular 2D lattice of kind 5.9(d). Then check  $\mathbf{c}' \perp (2\mathbf{a}' \pm \mathbf{b}')$  and obtain:

$$\tilde{\mathbf{a}} = \mathbf{b}' \quad \tilde{\mathbf{b}} = \mathbf{c}' \quad \tilde{\mathbf{c}} = 2\mathbf{a}' \pm \mathbf{b}' \quad (\text{C.11})$$

- ★  $b' \rightarrow \tilde{d}/2 \rightarrow a'$

Only possible if  $\tilde{d}/2 = a'$ . Check whether  $\mathbf{a}'$  and  $\mathbf{b}'$  form a centred rectangular 2D lattice of kind 5.9(d). Then check  $\mathbf{c}' \perp (2\mathbf{b}' \pm \mathbf{a}')$ , remember sign for result:

$$\tilde{\mathbf{a}} = \mathbf{a}' \quad \tilde{\mathbf{b}} = \mathbf{c}' \quad \tilde{\mathbf{c}} = 2\mathbf{b}' \pm \mathbf{a}' \quad (\text{C.12})$$

- ★  $\tilde{d}/2 \rightarrow b' \rightarrow a'$

Only possible if  $\tilde{d}/2 = b' = a'$ . Check whether  $\mathbf{a}'$  and  $\mathbf{c}'$  form a centred rectangular 2D lattice of kind 5.9(d). Then check  $\mathbf{b}' \perp (2\mathbf{c}' \pm \mathbf{a}')$ , remember sign for result:

$$\tilde{\mathbf{a}} = \mathbf{a}' \quad \tilde{\mathbf{b}} = \mathbf{b}' \quad \tilde{\mathbf{c}} = 2\mathbf{c}' \pm \mathbf{a}' \quad (\text{C.13})$$

- ★  $a' \rightarrow b' \rightarrow \tilde{d}/2$

$a' = b'$ . Check whether  $\mathbf{c}'$  and  $\mathbf{a}'$  form a centred rectangular 2D lattice of kind 5.9(d). Then check  $\mathbf{b}' \perp (2\mathbf{a}' \pm \mathbf{c}')$ , remember sign for result:

$$\tilde{\mathbf{a}} = \mathbf{c}' \quad \tilde{\mathbf{b}} = \mathbf{b}' \quad \tilde{\mathbf{c}} = 2\mathbf{a}' \pm \mathbf{c}' \quad (\text{C.14})$$

- ★  $a' \rightarrow \tilde{d}/2 \rightarrow b'$

$a' = \tilde{d}/2 = b'$ . Check whether  $\mathbf{c}'$  and  $\mathbf{b}'$  form a centred rectangular 2D lattice of kind 5.9(d). Then check  $\mathbf{a}' \perp (2\mathbf{b}' \pm \mathbf{c}')$ , remember sign for result:

$$\tilde{\mathbf{a}} = \mathbf{c}' \quad \tilde{\mathbf{b}} = \mathbf{a}' \quad \tilde{\mathbf{c}} = 2\mathbf{b}' \pm \mathbf{c}' \quad (\text{C.15})$$

- ★  $\tilde{d}/2 \rightarrow a' \rightarrow b'$

$\tilde{d}/2 = a' = b'$ . Check whether  $\mathbf{b}'$  and  $\mathbf{c}'$  form a centred rectangular 2D lattice of kind 5.9(d). Then check  $\mathbf{a}' \perp (2\mathbf{c}' \pm \mathbf{b}')$ , remember sign for result:

$$\tilde{\mathbf{a}} = \mathbf{b}' \quad \tilde{\mathbf{b}} = \mathbf{a}' \quad \tilde{\mathbf{c}} = 2\mathbf{c}' \pm \mathbf{b}' \quad (\text{C.16})$$

- $a', f, \tilde{d}/2$

- ★  $a' \rightarrow \tilde{d}/2 \rightarrow f, \tilde{d}/2 \rightarrow a' \rightarrow f, \tilde{d}/2 \rightarrow f \rightarrow a'$

$$b' = a' = \tilde{d}/2 \wedge b' \geq f \frac{4}{3}$$

- ★  $\tilde{d}/2 \rightarrow \tilde{d}/2 \rightarrow f$

Check whether  $\mathbf{b}'$  and  $\mathbf{c}'$  form a centred rectangular 2D lattice of kind 5.9(c). Whichever vector of

$$\mathbf{b}' + \mathbf{c}' \quad \mathbf{b}' - \mathbf{c}' \quad (\text{C.17})$$

is shorter represents  $\tilde{\mathbf{c}}$ , the other one is  $\tilde{\mathbf{a}}$  (if they are equal only a centred tetragonal configuration is possible, see Fig. 5.28).

Now check which two of the following conditions are met:

$$\mathbf{a}' \pm \mathbf{b}' \perp \tilde{\mathbf{c}} \quad \mathbf{a}' \pm \mathbf{c}' \perp \tilde{\mathbf{c}} \quad (\text{C.18})$$

the smaller one being  $(\pm)\tilde{\mathbf{b}}$ , see Fig. 5.28.

- $b', f, \tilde{d}/2$

There is no way to combine these in an allowed way.

- $c', f, \tilde{d}/2$

- ★  $c' \rightarrow \tilde{d}/2 \rightarrow f$

Check whether  $\mathbf{c}'$  and  $\mathbf{b}'$  form a centred rectangular 2D lattice of kind 5.9(d),  $\tilde{\mathbf{c}} = \mathbf{c}'$ . Then,  $\tilde{\mathbf{a}} = 2\mathbf{b}' \pm \tilde{\mathbf{c}}$ , whichever is perpendicular to  $\tilde{\mathbf{c}}$ . Set  $\mathbf{v} = \mathbf{b}' \pm \tilde{\mathbf{c}}$ , whichever has equal length to  $\mathbf{b}'$ . Now, like above, check which two of the following conditions are met:

$$\mathbf{a}' \pm \mathbf{b}' \perp \tilde{\mathbf{c}} \quad \mathbf{a}' \pm \mathbf{v} \perp \tilde{\mathbf{c}} \quad (\text{C.19})$$

the smaller one being  $(\pm)\tilde{\mathbf{b}}$ .

- ★  $\tilde{d}/2 \rightarrow c' \rightarrow f$

Only possible for  $c' = \tilde{d}/2$ . Proceed as in the previous item with exchanged roles of  $\mathbf{b}'$  and  $\mathbf{c}'$ .

2. The  $\tilde{d}/2$  point lies at  $\mathbf{b}'/2$

We know that  $\tilde{d}^2 = b'^2 + c'^2$ .

- $a', b', \tilde{d}/2$

- ★  $b' \rightarrow a' \rightarrow \tilde{d}/2$

Check whether  $\mathbf{c}'$  and  $\mathbf{a}'$  form a centred rectangular 2D lattice of kind 5.9(d),  $\tilde{\mathbf{b}} = \mathbf{c}'$ . Then,  $\tilde{\mathbf{c}} = 2\mathbf{a}' \pm \tilde{\mathbf{b}}$ , whichever is perpendicular to  $\tilde{\mathbf{b}}$ . Finally check  $\tilde{\mathbf{a}} = \mathbf{b}' \perp \tilde{\mathbf{c}}$ .

- ★  $\tilde{b} \rightarrow \tilde{d}/2 \rightarrow \tilde{a}$

Check whether  $\mathbf{c}'$  and  $\mathbf{b}'$  form a centred rectangular 2D lattice of kind 5.9(d),  $\tilde{\mathbf{b}} = \mathbf{c}'$ . Then,  $\tilde{\mathbf{c}} = 2\mathbf{b}' \pm \tilde{\mathbf{b}}$ , whichever is perpendicular to  $\tilde{\mathbf{b}}$ . Finally check  $\tilde{\mathbf{a}} = \mathbf{a}' \perp \tilde{\mathbf{c}}$ .

- ★  $\tilde{d}/2 \rightarrow b' \rightarrow a'$

Only possible if  $b' = \tilde{d}/2$ . Check whether  $\mathbf{b}'$  and  $\mathbf{c}'$  form a centred rectangular 2D lattice of kind 5.9(d),  $\tilde{\mathbf{b}} = \mathbf{b}'$ . Then,  $\tilde{\mathbf{c}} = 2\mathbf{c}' \pm \tilde{\mathbf{b}}$ , whichever is perpendicular to  $\tilde{\mathbf{b}}$ . Finally check  $\tilde{\mathbf{a}} = \mathbf{a}' \perp \tilde{\mathbf{c}}$ .

- ★  $\tilde{d}/2 \rightarrow \tilde{d}/2 \rightarrow a'$

Check whether  $\mathbf{b}'$  and  $\mathbf{c}'$  form a centred rectangular 2D lattice of kind 5.9(c),  $\tilde{\mathbf{c}} = \mathbf{b}' \pm \mathbf{a}'$ , whichever is perpendicular to  $\tilde{\mathbf{a}} = \mathbf{a}'$ . Then,  $\tilde{\mathbf{b}} = \mathbf{b}' \mp \mathbf{a}'$ .

- ★  $a' \rightarrow b' \rightarrow \tilde{d}/2$   
Only possible if  $a' = b'$ . Check whether  $\mathbf{b}'$  and  $\mathbf{a}'$  form a centred rectangular 2D lattice of kind 5.9(d),  $\tilde{\mathbf{b}} = \mathbf{b}'$ . Then,  $\tilde{\mathbf{c}} = 2\mathbf{a}' \pm \tilde{\mathbf{b}}$ , whichever is perpendicular to  $\tilde{\mathbf{b}}$ . Finally check  $\tilde{\mathbf{a}} = \mathbf{c}' \perp \tilde{\mathbf{c}}$ .
- ★  $a' \rightarrow \tilde{d}/2 \rightarrow b'$   
Only possible if  $a' = \tilde{d}/2 = b'$ . Check whether  $\mathbf{a}'$  and  $\mathbf{b}'$  form a centred rectangular 2D lattice of kind 5.9(d),  $\tilde{\mathbf{b}} = \mathbf{a}'$ . Then,  $\tilde{\mathbf{c}} = 2\mathbf{b}' \pm \tilde{\mathbf{b}}$ , whichever is perpendicular to  $\tilde{\mathbf{b}}$ . Finally check  $\tilde{\mathbf{a}} = \mathbf{c}' \perp \tilde{\mathbf{c}}$ .
- ★  $a' \rightarrow \tilde{d}/2 \rightarrow \tilde{d}/2$   
Only possible if  $a' = b' = \tilde{d}/2$ . Check whether  $\mathbf{b}'$  and  $\mathbf{a}'$  form a centred rectangular 2D lattice of kind 5.9(c),  $\tilde{\mathbf{c}} = \mathbf{b}' \pm \mathbf{a}'$ , whichever is perpendicular to  $\tilde{\mathbf{a}} = \mathbf{c}'$ . Then,  $\tilde{\mathbf{b}} = \mathbf{b}' \mp \mathbf{a}'$ .
- ★  $\tilde{d}/2 \rightarrow a' \rightarrow b'$   
Only possible if  $a' = b' = \tilde{d}/2$ . Check whether  $\mathbf{a}'$  and  $\mathbf{c}'$  form a centred rectangular 2D lattice of kind 5.9(d),  $\tilde{\mathbf{b}} = \mathbf{a}'$ . Then,  $\tilde{\mathbf{c}} = 2\mathbf{c}' \pm \tilde{\mathbf{b}}$ , whichever is perpendicular to  $\tilde{\mathbf{b}}$ . Finally check  $\tilde{\mathbf{a}} = \mathbf{b}' \perp \tilde{\mathbf{c}}$ .
- $a', c', \tilde{d}/2$ 
  - ★  $a' \rightarrow c' \rightarrow \tilde{d}/2$   
Check whether  $\mathbf{b}'$  and  $\mathbf{c}'$  form a centred rectangular 2D lattice of kind 5.9(d),  $\tilde{\mathbf{c}} = \mathbf{b}'$ ,  $\tilde{\mathbf{b}} = 2\mathbf{c}' \pm \tilde{\mathbf{c}}$ , whichever is perpendicular to  $\tilde{\mathbf{c}}$ . Then, check  $\tilde{\mathbf{a}} = \mathbf{c}' \perp \tilde{\mathbf{c}}$ .

Shuffled sequences of these vectors often only appear when certain vectors have equal lengths. Anyway, the checking of the 2D centred rectangular symmetry and the other conditions as in the previous item are performed completely analogously.

- ★  $a' \rightarrow \tilde{d}/2 \rightarrow c', \tilde{d}/2 = c'$ .
- ★  $\tilde{d}/2 \rightarrow a' \rightarrow c', \tilde{d}/2 = a' = c'$ .
- ★  $c' \rightarrow a' \rightarrow \tilde{d}/2$ .
- ★  $c' \rightarrow \tilde{d}/2 \rightarrow a'$ .
- ★  $\tilde{d}/2 \rightarrow c' \rightarrow a', \tilde{d}/2 = c'$ .
- $b', f, \tilde{d}/2$ 
  - ★  $\tilde{d}/2 \rightarrow \tilde{d}/2 \rightarrow f$   
Check whether  $\mathbf{c}'$  and  $\mathbf{b}'$  form a centred rectangular structure of kind 5.9(c).  $\tilde{\mathbf{c}} = \mathbf{c}' \pm \mathbf{b}'$  (whichever is smaller),  $\tilde{\mathbf{b}}$  is the other one. The smallest of the four vectors  $\mathbf{a}' \pm \mathbf{b}'$ ,  $\mathbf{a}' \pm \mathbf{c}'$  being perpendicular to  $\tilde{\mathbf{c}}$  is  $(\pm)\tilde{\mathbf{a}}$ .
- $a', f, \tilde{d}/2$   
Since always  $f > \tilde{d}/2$ , if we also encounter  $a' < f$ ,  $a'$  together with two times  $\tilde{d}/2$  will constitute the length–sequence of the MDP vectors. If  $a' = f$  we will have either  $\tilde{d}/2 \rightarrow \tilde{d}/2 \rightarrow a'$  or  $\tilde{d}/2 \rightarrow \tilde{d}/2 \rightarrow f$ , the latter being the only remaining possibility for  $a' > f$ .

- $c', f, \tilde{d}/2$ 
  - ★  $c' \rightarrow \tilde{d}/2 \rightarrow f$   
Check whether  $\mathbf{c}'$  and  $\mathbf{b}'$  form a centred rectangular 2D lattice of kind 5.9(d),  $\tilde{\mathbf{c}} = \mathbf{c}'$ ,  $\tilde{\mathbf{b}} = 2\mathbf{b}' \pm \tilde{\mathbf{c}}$ , whichever is perpendicular to  $\tilde{\mathbf{c}}$ . Set  $\mathbf{v} = \mathbf{b}' \pm \tilde{\mathbf{c}}$ , whichever has equal length to  $\mathbf{b}'$ . The smallest of the four vectors  $\mathbf{a}' \pm \mathbf{b}'$ ,  $\mathbf{a}' \pm \mathbf{v}$  being perpendicular to  $\tilde{\mathbf{c}}$  is  $(\pm)\tilde{\mathbf{a}}$ .
  - ★  $\tilde{d}/2 \rightarrow c' \rightarrow f$   
Only possible if  $\tilde{d}/2 = c'$ . Like above with  $\mathbf{b}' \leftrightarrow \mathbf{c}'$ .

3. The  $\tilde{d}/2$  point lies at  $(-\mathbf{a}' + \mathbf{b}')/2$

Distances:

$$\frac{\tilde{d}^2}{4} = \frac{a'^2 + b'^2 + c'^2}{4} - \frac{1}{2}a'b' \cos \alpha' \quad (\text{C.20})$$

$$f = \frac{a'^2 + b'^2 + c'^2}{4} + \frac{1}{2}a'b' \cos \alpha' \quad (\text{C.21})$$

Resulting again in  $f \geq \tilde{d}/2$ , where the equality holds only for  $\cos \alpha' = 0$ , which corresponds to a sfc structure. Therefore we can take  $f > \tilde{d}/2$  for granted in the sfc case. We construct the possible combinations:

- $a', b', \tilde{d}/2$ 
  - ★  $b' \rightarrow a' \rightarrow \tilde{d}/2$   
 $\tilde{\mathbf{b}} = \mathbf{c}'$  and  $\tilde{\mathbf{a}} = \mathbf{b}'$ . Construct  $\mathbf{n} = \tilde{\mathbf{a}} \times \tilde{\mathbf{b}}$  and  $\mathbf{v} = \mathbf{a}' \cdot \mathbf{n}_0$ , this results (possibly) in  $\tilde{\mathbf{c}} = 2\mathbf{v}$ . To *verify* the sfc structure construct the projection of  $\mathbf{a}'$  onto the  $(\tilde{\mathbf{a}}, \tilde{\mathbf{b}})$ -plane:  $\mathbf{w} = \mathbf{a}' - \mathbf{v}$ . Then one of the four equalities  $\tilde{\mathbf{b}} \pm 2\mathbf{w} = \pm\tilde{\mathbf{a}}$  has to be met.
  - ★  $b' \rightarrow \tilde{d}/2 \rightarrow a'$ . Only if  $a' = \tilde{d}/2$ . Like the first item with  $\mathbf{b}' \leftrightarrow \mathbf{a}'$ .
  - ★  $b' \rightarrow \tilde{d}/2 \rightarrow \tilde{d}/2$   
 $\tilde{\mathbf{b}} = \mathbf{c}'$ . Check whether  $\mathbf{b}'$  and  $\mathbf{a}'$  form a centred rectangular structure of kind 5.9(c).  $\tilde{\mathbf{c}} = \mathbf{b}' \pm \mathbf{a}'$  whichever is perpendicular to  $\tilde{\mathbf{b}}$ .  $\tilde{\mathbf{a}}$  can be found through checking the angle between the candidates and  $\tilde{\mathbf{b}}$ , but this is not necessary.
  - ★  $\tilde{d}/2 \rightarrow b' \rightarrow a'$   
Only if  $\tilde{d}/2 = b' = a'$ . Like the first item with cyclic exchange of vectors.
  - ★  $\tilde{d}/2 \rightarrow \tilde{d}/2 \rightarrow b'$ . Like the third item with  $\mathbf{c}' \leftrightarrow \mathbf{a}'$ .
  - ★  $a' \rightarrow b' \rightarrow \tilde{d}/2$ . Only if  $a' = b'$ , like first item.
  - ★  $a' \rightarrow \tilde{d}/2 \rightarrow b'$ . Only if  $a' = b' = \tilde{d}/2$ , like first.
  - ★  $\tilde{d}/2 \rightarrow a' \rightarrow b'$ . Only if  $a' = b' = \tilde{d}/2$ , like first.
  - ★  $\tilde{d}/2 \rightarrow \tilde{d}/2 \rightarrow a'$ . Only if  $a' = b'$ , like third item.
- $b', c', \tilde{d}/2$

- ★  $b' \rightarrow c' \rightarrow \tilde{d}/2$   
 $\tilde{\mathbf{b}} = \mathbf{c}'$  and  $\tilde{\mathbf{c}} = \mathbf{b}'$ . Check whether  $\tilde{\mathbf{c}}$  and  $\mathbf{a}'$  form a centred rectangular 2D lattice of kind 5.9(d) and whether  $\tilde{\mathbf{b}} \perp \tilde{\mathbf{c}}$ .  $\tilde{\mathbf{a}} = 2\mathbf{a}' \pm \tilde{\mathbf{c}} (\perp \tilde{\mathbf{c}})$ .

Again, for the shuffled sequences, the identification is performed analogously, with the possible necessity of certain length–equalities:

- ★  $b' \rightarrow \tilde{d}/2 \rightarrow c', \tilde{d}/2 = c'$ .
- ★  $\tilde{d}/2 \rightarrow b' \rightarrow c', \tilde{d}/2 = c' = b'$ .
- ★  $c' \rightarrow b' \rightarrow \tilde{d}/2$ .
- ★  $c' \rightarrow \tilde{d}/2 \rightarrow b'$ .
- ★  $\tilde{d}/2 \rightarrow c' \rightarrow b', \tilde{d}/2 = c'$ .
- $a', c', \tilde{d}/2$   
 Obviously  $a' = b'$ .  $a' = b' = \tilde{d}/2 \Rightarrow c' = a' \sqrt{2(1 + \cos \alpha')}$ . Since a distinction between  $\mathbf{a}'$  and  $\mathbf{b}'$  is not necessary,
  - ★  $c' \rightarrow \tilde{d}/2 \rightarrow a'$ , see  $c' \rightarrow \tilde{d}/2 \rightarrow b'$ ,
  - ★  $\tilde{d}/2 \rightarrow c' \rightarrow a'$ , see  $\tilde{d}/2 \rightarrow c' \rightarrow b'$ .
- $f$ 
  - ★  $\tilde{d}/2 \rightarrow \tilde{d}/2 \rightarrow f$   
 Check whether  $\mathbf{c}'$  and  $\mathbf{b}'$  form a centred rectangular structure of kind 5.9(c).  $\tilde{\mathbf{c}} = \mathbf{c}' \pm \mathbf{b}'$  (whichever is smaller),  $\tilde{\mathbf{a}}'$  is the other one. The smallest of the four vectors  $\mathbf{a}' \pm \mathbf{b}'$ ,  $\mathbf{a}' \pm \mathbf{c}'$  being perpendicular to  $\tilde{\mathbf{c}}$  is  $(\pm)\tilde{\mathbf{b}}$ .
  - ★  $c' \rightarrow \tilde{d}/2 \rightarrow f$   
 Check whether  $\mathbf{c}'$  and  $\mathbf{b}'$  form a centred rectangular 2D lattice of kind 5.9(d),  $\tilde{\mathbf{c}} = \mathbf{c}'$ ,  $\tilde{\mathbf{a}} = 2\mathbf{b}' \pm \tilde{\mathbf{c}}$ , whichever is perpendicular to  $\tilde{\mathbf{c}}$ . Set  $\mathbf{v} = \mathbf{b}' \pm \tilde{\mathbf{c}}$ , whichever has equal length to  $\mathbf{b}'$ . The smallest of the four vectors  $\mathbf{a}' \pm \mathbf{b}'$ ,  $\mathbf{a}' \pm \mathbf{v}$  being perpendicular to  $\tilde{\mathbf{c}}$  is  $(\pm)\tilde{\mathbf{b}}$ .
  - ★  $\tilde{d}/2 \rightarrow c' \rightarrow f$   
 Only possible if  $\tilde{d}/2 = c'$ . Like above with  $\mathbf{b}' \leftrightarrow \mathbf{c}'$ .



# Appendix D

## Complete List of Minimum Enthalpy Configurations for the Square–Shoulder Model with $\lambda = 4.5\sigma$

This appendix is dedicated to the detailed, analytical, geometric analysis of the 33 occurring MECs at  $T = 0$  for the square–shoulder model with shoulder width  $\lambda = 4.5\sigma$ . The complete list of MECs can be found in table 9.3 and figure 9.5, which we will refer to repeatedly. The MECs will be labelled with their (unambiguous) energy per particle  $e$ , starting at the high density/pressure limiting case. We will also use the abbreviations for the Bravais lattices listed in table G.3.

- $e = 236\epsilon$ . The stable structure at very high pressures is the hcp structure, see figure 9.5(33). The hexagonal unit cell is given by  $\tilde{a} = \sigma$ ,  $\tilde{c} = 2\sigma\sqrt{2/3}$ , and w.l.o.g.,  $\tilde{\mathbf{a}} = \tilde{a}\hat{\mathbf{x}}$  and  $\tilde{\mathbf{b}} = \tilde{a}(1/2\hat{\mathbf{x}} + \sqrt{3}/2\hat{\mathbf{y}})$ . The second basis particle is positioned at  $\mathbf{v}_2 = \sigma/2\hat{\mathbf{x}} + \sigma/(2\sqrt{3})\hat{\mathbf{y}} + \tilde{c}/2\hat{\mathbf{z}}$ . An fcc structure with nearest neighbours touching at the hard cores has an energy per particle of  $277\epsilon$ .
- $e = 243\epsilon$ . The first different structure when lowering the pressure is a ct one, where the squared base area has an edge length of  $\tilde{a} = \sigma$  and the centred particle, painted red in figure 9.5(32), touches the surrounding corner particles at the hard core. This gives  $\tilde{c} = \sqrt{2}\sigma$ .
- $e = 229\epsilon$ . Next we obtain an fcc structure [see figure 9.5(31)] where actually *no spheres touch* each other at the hard core: The structure is stabilised by touching shoulders,

$$\left| 3\tilde{a}\hat{\mathbf{x}} + \frac{\tilde{a}}{2}\hat{\mathbf{y}} + \frac{\tilde{a}}{2}\hat{\mathbf{z}} \right| = \lambda. \quad (\text{D.1})$$

Therefore the length of the unit cell is  $a = \lambda\sqrt{\frac{2}{19}} \simeq 1.46\sigma$  ( $\simeq 1.03\sqrt{2}\sigma$ ).

- $e = 210$ . This sfcm structure has also no touching cores, although it looks as if it was the case at first sight: The face centred particle [red in figure 9.5(30)] seems to touch

the surrounding corner particles, and also the lattice vector from one face centred plane to another, in our description called  $\tilde{\mathbf{b}}$  (see figure 5.27), seems to have length  $\sigma$ . But as a matter of fact the structure is determined by the following conditions derived from touching shoulders (we use  $\mathbf{w} = (\tilde{\mathbf{a}} + \tilde{\mathbf{c}})/2$  as short notation for the centred particle position)

$$\begin{aligned} \left| -\tilde{\mathbf{a}} + 5\tilde{\mathbf{b}} + \tilde{\mathbf{c}} \right| &= \left| -2\tilde{\mathbf{a}} + 5\tilde{\mathbf{b}} - 2\tilde{\mathbf{c}} + \mathbf{w} \right| = \\ &= \left| -3\tilde{\mathbf{a}} + 5\tilde{\mathbf{b}} - 2\tilde{\mathbf{c}} + \mathbf{w} \right| = \left| -2\tilde{\mathbf{a}} + 4\tilde{\mathbf{b}} - 3\tilde{\mathbf{c}} + \mathbf{w} \right| = \lambda, \end{aligned} \quad (\text{D.2})$$

leading to the only solution with positive lengths of

$$\tilde{\mathbf{a}} = \sqrt{\frac{5}{38}}\lambda \hat{\mathbf{x}} \quad \tilde{\mathbf{b}} = \frac{\lambda}{95} \left( \sqrt{2} \hat{\mathbf{x}} + \sqrt{3} \hat{\mathbf{z}} \right) \quad \tilde{\mathbf{c}} = \sqrt{\frac{3}{38}}\lambda \hat{\mathbf{y}}. \quad (\text{D.3})$$

Since  $\lambda = 4.5\sigma$ ,  $\tilde{\mathbf{b}}$  as well as  $\mathbf{w}$  have a length which is approximately 3% larger than  $\sigma$ .

- **$e = 180\epsilon$ .** With the ansatz for a ct structure  $\tilde{\mathbf{a}} = \tilde{a} \hat{\mathbf{x}}$ ,  $\tilde{\mathbf{b}} = \tilde{a} \hat{\mathbf{y}}$ ,  $\tilde{\mathbf{c}} = \tilde{c} \hat{\mathbf{z}}$ ,  $\mathbf{w} = (\tilde{\mathbf{a}} + \tilde{\mathbf{b}} + \tilde{\mathbf{c}})/2$  and the conditions

$$|4\tilde{\mathbf{a}} + \tilde{\mathbf{c}}| = |-3\tilde{\mathbf{c}} + \mathbf{w}| = \lambda \quad (\text{D.4})$$

we get  $\tilde{a} = \sqrt{\frac{21}{389}}\lambda \simeq 1.03\sigma$ ,  $\tilde{c} = \sqrt{\frac{31}{199}}\lambda \simeq 1.78\sigma$ , resulting also in  $|\mathbf{w}| \simeq 1.15\sigma$ . [See figure 9.5(29).]

- **$e = 169\epsilon$ .** At this energy we find a bcc structure [see figure 9.5(28)], stabilised by touching shoulders:

$$\left| 3\tilde{a} \hat{\mathbf{x}} + \frac{\tilde{a}}{2}(\hat{\mathbf{x}} + \hat{\mathbf{y}} + \hat{\mathbf{z}}) \right| = \lambda \quad \Rightarrow \quad \tilde{a} = \frac{2}{\sqrt{51}}\lambda, \quad (\text{D.5})$$

resulting in a nearest neighbour distance of  $\simeq 1.09\sigma$ .

- **$e = 138\epsilon$ .** Again there are no touching cores, the appearing hex structure [see figure 9.5(27)] is determined through

$$4\tilde{a} = 4\tilde{c} = \lambda \quad \Rightarrow \quad \tilde{a} = \tilde{c} = \frac{1}{4}\lambda = 1.125\sigma. \quad (\text{D.6})$$

- **$e = 128\epsilon$ .** This sc structure [see figure 9.5(26)] is determined through

$$|4\tilde{a} \hat{\mathbf{x}} + \tilde{a} \hat{\mathbf{y}}| = \lambda \quad \Rightarrow \quad \tilde{a} = \frac{1}{\sqrt{17}}\lambda \simeq 1.09\sigma. \quad (\text{D.7})$$

- $e = 115\epsilon$ . At this energy per particle we find a trig structure [see figure 9.5(25)] with basis vectors given by equation (5.47) From the conditions

$$|-4\tilde{\mathbf{a}} + \tilde{\mathbf{b}} + 2\tilde{\mathbf{c}}| = |-4\tilde{\mathbf{a}} + \tilde{\mathbf{c}}| = \lambda \quad (\text{D.8})$$

we obtain  $\cos \tilde{\alpha} = \frac{1}{3}$  and  $\tilde{a} = \sqrt{\frac{3}{43}}\lambda \simeq 1.19\sigma$ .

- $e = 112.3\epsilon$ . This three-layer lamellar structure consists of an underlying tric structure [see figure 9.5(24)]. It is easier to consider the layers first and then their stacking, therefore we set here

$$\tilde{\mathbf{b}} = \tilde{b} \hat{\mathbf{y}}, \quad \tilde{\mathbf{c}} = \tilde{c} \cos \alpha \hat{\mathbf{y}} + \tilde{c} \sin \alpha \hat{\mathbf{z}}, \quad \tilde{\mathbf{a}} = a_x \hat{\mathbf{x}} + a_y \hat{\mathbf{y}} + a_z \hat{\mathbf{z}}. \quad (\text{D.9})$$

A single-layer is built up by  $\tilde{\mathbf{b}}$  and  $\tilde{\mathbf{c}}$ . From  $\tilde{b} = \tilde{c} = \sigma$  and  $|\tilde{\mathbf{b}} + \tilde{\mathbf{c}}| = \lambda$  we obtain

$$\tilde{\mathbf{b}} = \sigma \hat{\mathbf{y}}, \quad (\text{D.10a})$$

$$\begin{aligned} \tilde{\mathbf{c}} &= \frac{\lambda^2 - 18\sigma^2}{18\sigma} \hat{\mathbf{y}} + \sigma \sqrt{1 - \frac{(\lambda^2 - 18\sigma^2)^2}{324\sigma^4}} \hat{\mathbf{z}} = \\ &= \frac{\sigma}{8} \hat{\mathbf{y}} + \frac{3\sqrt{7}\sigma}{8} \hat{\mathbf{z}} \simeq 0.125\sigma \hat{\mathbf{y}} + 0.99\sigma \hat{\mathbf{z}} \end{aligned} \quad (\text{D.10b})$$

Now we concern ourselves with the stacking of such layers inside one lamella. The next layer is determined by the second basis vector which satisfies

$$|\tilde{\mathbf{v}}_2| = \sigma, \quad |\tilde{\mathbf{v}}_2 + 4\tilde{\mathbf{c}}| = \lambda, \quad |\tilde{\mathbf{v}}_2 - 4\tilde{\mathbf{b}}| = \lambda, \quad (\text{D.11})$$

leading to

$$\begin{aligned} \tilde{\mathbf{v}}_2 &= \frac{1}{4} \sqrt{\frac{9\lambda^4 - 290\lambda^2\sigma^2 + 2025\sigma^4}{\lambda^2 - 36\sigma^2}} \hat{\mathbf{x}} - \left( \frac{\lambda^2}{8\sigma} - \frac{17\sigma}{8} \right) \hat{\mathbf{y}} + \frac{(\lambda^2 - 17\sigma^2) \sqrt{-\lambda^4 + 36\lambda^2\sigma^2}}{8\sigma(36\sigma^2 - \lambda^2)} \hat{\mathbf{z}} = \\ &= \frac{3}{8} \sqrt{\frac{31}{7}} \sigma \hat{\mathbf{x}} - \frac{13}{32} \sigma \hat{\mathbf{y}} + \frac{351}{16} \frac{\sigma}{18\sqrt{7}} \hat{\mathbf{z}} \simeq 0.79\sigma \hat{\mathbf{x}} - 0.41\sigma \hat{\mathbf{y}} + 0.46\sigma \hat{\mathbf{z}}. \end{aligned} \quad (\text{D.12})$$

The third layer, described by the third basis vector, follows from

$$|\tilde{\mathbf{v}}_3 - \tilde{\mathbf{v}}_2| = \sigma, \quad |\tilde{\mathbf{v}}_3 - \tilde{\mathbf{v}}_2 \pm 4\tilde{\mathbf{c}}| = \lambda, \quad (\text{D.13})$$

giving

$$\tilde{\mathbf{v}}_3 = \frac{1}{2} \sqrt{\frac{9\lambda^4 - 290\lambda^2\sigma^2 + 2025\sigma^4}{\lambda^2 - 36\sigma^2}} \hat{\mathbf{x}} = \frac{3}{2} \sqrt{\frac{31}{7}} \sigma \hat{\mathbf{x}} \simeq 1.58\sigma \hat{\mathbf{x}}. \quad (\text{D.14})$$

To obtain the lamellar arrangement of these triple-layers we need the third unit cell vector  $\tilde{\mathbf{a}}$ . It is defined through

$$|\tilde{\mathbf{a}}| = \lambda, \quad |\tilde{\mathbf{a}} + 3\tilde{\mathbf{b}} - \tilde{\mathbf{v}}_3| = \lambda, \quad |\tilde{\mathbf{a}} + \tilde{\mathbf{v}}_2 + 2\tilde{\mathbf{c}} - 2\tilde{\mathbf{b}} - \tilde{\mathbf{v}}_3| = \lambda. \quad (\text{D.15})$$

These equations yield quite long expressions in  $\sigma$  and  $\lambda$ , if we immediately replace  $\lambda$  by  $\frac{9}{2}\sigma$  we obtain

$$\begin{aligned}\tilde{\mathbf{a}} &= \frac{(180947 + 9338\sqrt{403})\sigma}{5616\sqrt{217}}\hat{\mathbf{x}} + \frac{(-17173 + 1334\sqrt{403})\sigma}{22464}\hat{\mathbf{y}} - \frac{(10373 - 406\sqrt{403})\sigma}{1728\sqrt{7}}\hat{\mathbf{z}} \\ &\simeq 4.45\sigma\hat{\mathbf{x}} + 0.43\sigma\hat{\mathbf{y}} - 0.49\sigma\hat{\mathbf{z}}.\end{aligned}\quad (\text{D.16})$$

There are no overlaps between particles of one layer and the same layer in the next lamella.

- $e = 96\epsilon$ . With the same ansatz like above ( $\tilde{\mathbf{a}} = \tilde{a}\hat{\mathbf{x}}$ ,  $\tilde{\mathbf{b}} = \tilde{a}\hat{\mathbf{y}}$ ,  $\tilde{\mathbf{c}} = \tilde{c}\hat{\mathbf{z}}$ ,  $\mathbf{w} = (\tilde{\mathbf{a}} + \tilde{\mathbf{b}} + \tilde{\mathbf{c}})/2$ ) and the conditions

$$|\tilde{\mathbf{a}} + 2\tilde{\mathbf{c}}| = |\tilde{\mathbf{a}} + 3\tilde{\mathbf{b}} + \tilde{\mathbf{c}}| = \lambda \quad (\text{D.17})$$

we obtain  $\tilde{a} = \frac{\lambda}{\sqrt{13}} \simeq 1.25\sigma$ ,  $\tilde{c} = \sqrt{\frac{3}{13}}\lambda \simeq 2.16\sigma$  for this ct structure [see figure 9.5(23)].

- $e = 90\epsilon$ . At this energy we obtain a bco structure [see figure 9.5(22)], stabilised by touching shoulders through

$$|2\tilde{\mathbf{a}} + \tilde{\mathbf{b}} + \mathbf{w}| = \lambda, \quad (\text{D.18})$$

leading to  $\tilde{a} = \frac{2}{\sqrt{35}}\lambda \simeq 1.52\sigma$ .

- $e = 71.5\epsilon$ . This structure consists of double layers in a lamellar arrangement [see figure 9.5(21)]; it is a fco structure, where the following conditions lead to its stabilisation ( $\tilde{\mathbf{a}} = \tilde{a}\hat{\mathbf{x}}$ ,  $\tilde{\mathbf{b}} = \tilde{b}\hat{\mathbf{y}}$ ,  $\tilde{\mathbf{c}} = \tilde{c}\hat{\mathbf{z}}$ ,  $\tilde{\mathbf{v}}_2 = v_x\hat{\mathbf{x}} + v_y\hat{\mathbf{y}}$ ):

$$\begin{aligned}\left|2\tilde{\mathbf{b}} + \frac{\tilde{\mathbf{b}} + \tilde{\mathbf{c}}}{2} - \tilde{\mathbf{c}}\right| &= \left|\frac{\tilde{\mathbf{a}} + \tilde{\mathbf{c}}}{2} + \tilde{\mathbf{v}}_2 - \tilde{\mathbf{a}} - 2\tilde{\mathbf{b}}\right| = \left|\frac{\tilde{\mathbf{a}} + \tilde{\mathbf{c}}}{2}\right| = \\ &= \left|\frac{\tilde{\mathbf{a}} + \tilde{\mathbf{c}}}{2} + \tilde{\mathbf{b}} + \tilde{\mathbf{v}}_2 - \tilde{\mathbf{a}}\right| = \left|2\tilde{\mathbf{c}} + \frac{\tilde{\mathbf{a}} + \tilde{\mathbf{b}}}{2} + \tilde{\mathbf{v}}_2 - \tilde{\mathbf{a}}\right| = \lambda.\end{aligned}\quad (\text{D.19})$$

The resulting lattice parameters are  $\tilde{a} = 5\sqrt{3/19}\lambda$ ,  $\tilde{b} = \sqrt{3/19}\lambda$ ,  $\tilde{c} = \lambda/\sqrt{19}$ ,  $v_x = v_y = \tilde{b}/2$ . The particles in one layer form a 2D hexagonal structure with 2D lattice constant equal to the third bco edge length  $\tilde{c} \simeq 1.03\sigma$ , the particles of the second layer in the same lamella occupy the sites that are shifted about  $\frac{\tilde{c}}{2}\hat{\mathbf{z}}$  and have a distance from the two closest particles of the first layer of  $\tilde{c}$ .

The reason why we do not describe the structure as a hexagonal one is, that one would need then four instead of two basis particles, since the next lamella is again shifted about  $\frac{\tilde{c}}{2}\hat{\mathbf{z}}$ , which means that the lamellae face each other with (relatively) non-shifted layers.

- $e = 58\epsilon$ . In figure 9.5(20) we have an sm structure with one extra basis particle. One layer is described by the SM unit cell vectors  $\tilde{\mathbf{b}} = b_x \hat{\mathbf{x}} + b_y \hat{\mathbf{y}}$  and  $\tilde{\mathbf{c}} = \tilde{c} \hat{\mathbf{x}}$ , ( $\tilde{\mathbf{b}} \perp \tilde{\mathbf{c}}$  and  $\tilde{\mathbf{a}} \perp \tilde{\mathbf{c}}$ ), having lengths

$$\tilde{c} = \sigma, \quad \tilde{b} = \frac{\lambda}{4}. \quad (\text{D.20})$$

The other layer is described by the extra basis particle ( $\tilde{\mathbf{v}}_2 = v_x \hat{\mathbf{x}} + v_y \hat{\mathbf{y}} + v_z \hat{\mathbf{z}}$ ), which touches the four particles of the rectangle spanned by  $\tilde{\mathbf{b}}$  and  $\tilde{\mathbf{c}}$  at the hard core. The determining conditions are

$$|\tilde{\mathbf{v}}_2| = |\tilde{\mathbf{v}}_2 - \tilde{\mathbf{c}}| = |\tilde{\mathbf{v}}_2 - \tilde{\mathbf{b}}| = \sigma, \quad (\text{D.21})$$

and for the arrangement of the next lamella we have to satisfy

$$|\tilde{\mathbf{v}}_2 + \tilde{\mathbf{a}} + \tilde{\mathbf{b}} + \tilde{\mathbf{c}}| = \tilde{a} = \lambda. \quad (\text{D.22})$$

These equations lead to

$$b_x = \frac{(-1593 + \sqrt{2970249}) \sigma}{4480}, \quad (\text{D.23})$$

$$b_y = \frac{\sqrt{\frac{1}{2}(13879 - 3\sqrt{2970249})} (5301 + \sqrt{2970249}) \sigma}{412160}, \quad (\text{D.24})$$

$$v_x = -\frac{(3481 + 3\sqrt{2970249}) \sigma}{13440}, \quad (\text{D.25})$$

$$v_y = \frac{59\sqrt{\frac{1}{2}(13879 - 3\sqrt{2970249})} \sigma}{6720}, \quad (\text{D.26})$$

$$v_z = \frac{\sigma}{2}. \quad (\text{D.27})$$

Layers of the same colour in figure 9.5(20) have no overlapping particle shoulders. Differently coloured particles of ascending layers can only overlap their shoulders if they are “facing” each other [e.g. the red layer of the left lamella and the green layer of the right one in figure 9.5(20)]. There are 14 such inter-lamellar overlaps.

- $e = 56\epsilon$ . The layers of this lamellar structure [see figure 9.5(19)] are identical to the ones of the previous case, but their arrangement is different:  $\mathbf{b}$  and  $\tilde{\mathbf{c}}$  from the previous structure “exchange” their roles (the layers are slanted around the longer of the two vectors instead of around the shorter one)

$$\tilde{\mathbf{b}} = \sigma \hat{\mathbf{y}}, \quad \tilde{\mathbf{c}} = \frac{\lambda}{4} \hat{\mathbf{z}}, \quad \tilde{\mathbf{v}}_2 = \frac{\sqrt{48\sigma^2 - \lambda^2}}{8} \hat{\mathbf{x}} + \frac{\sigma}{2} \hat{\mathbf{y}} + \frac{\lambda}{8} \hat{\mathbf{z}}. \quad (\text{D.28})$$

For the vector  $\tilde{\mathbf{a}}$  we make the ansatz  $\tilde{\mathbf{a}} = a_x \hat{\mathbf{x}} + a_y \hat{\mathbf{y}}$  leading to the coordinates of the centred particle of this sfc structure of  $\mathbf{w} = \tilde{\mathbf{a}} + \tilde{\mathbf{c}}/2$ . The components of  $\tilde{\mathbf{a}}$  are

determined through

$$\lambda = \left| \mathbf{w} + \tilde{\mathbf{c}} + 2\tilde{\mathbf{b}} - \tilde{\mathbf{v}}_2 \right| = \left| \mathbf{w} - 2\tilde{\mathbf{b}} - \tilde{\mathbf{v}}_2 \right| \quad (\text{D.29})$$

$\Downarrow$

$$a_x = \frac{1}{4}\sqrt{48\sigma^2 - \lambda^2} + \frac{1}{64\sigma}\sqrt{-\lambda^4 + 15872\sigma^2\lambda^2 - 65536\sigma^4} \simeq 9.21\sigma \quad (\text{D.30})$$

$$a_y = \sigma - \frac{\lambda^2}{64\sigma} \simeq 0.68\sigma \quad (\text{D.31})$$

Again, only particles of adjacent (or the same) layers can intersect, i.e., the blue ones in the central lamella of figure 9.5(19) have overlaps with other particles of the same lamella (102 in total each) and green ones of the right lamella (10). In the figure the  $\hat{\mathbf{y}}$ -vector points in the direction of the lines of touching particles of equal colour ( $\simeq$ up), the  $\hat{\mathbf{z}}$ -vector points along the lines of equally coloured particles from back to front, and the  $\hat{\mathbf{x}}$ -vector is chosen to complete a right-handed system.  $\tilde{\mathbf{a}}$  points e.g. from the lowermost green particle of the left lamella to the lowermost one of the right lamella.

- **$e = 38.5\epsilon$ .** This ct structure [see figure 9.5(18)] has two basis particles and contains no touching cores. Its dimensions are

$$\tilde{a} = \frac{1}{2}\sqrt{\frac{\sqrt{457} - 17}{14}}\lambda \simeq 1.26\sigma, \quad \tilde{c} = \frac{24 + \sqrt{457}}{14}\sqrt{\frac{537 - 25\sqrt{457}}{7}}\lambda \simeq 8.82\sigma \quad (\text{D.32})$$

with  $\tilde{\mathbf{a}} = \tilde{a}\hat{\mathbf{x}}$ ,  $\tilde{\mathbf{b}} = \tilde{a}\hat{\mathbf{y}}$ ,  $\tilde{\mathbf{c}} = \tilde{c}\hat{\mathbf{z}}$ ,  $\mathbf{w} = (\tilde{\mathbf{a}} + \tilde{\mathbf{b}} + \tilde{\mathbf{c}})/2$ , and the extra particle is positioned at

$$\tilde{\mathbf{v}}_2 = \frac{\tilde{a}}{2}\hat{\mathbf{x}} + \frac{\tilde{a}}{2}\hat{\mathbf{y}} + \frac{1}{4}\sqrt{\frac{537 - 25\sqrt{457}}{7}}\lambda\hat{\mathbf{z}}. \quad (\text{D.33})$$

This follows from the conditions for the extra particle position ( $\tilde{\mathbf{v}}_2 = \frac{\tilde{a}}{2}\hat{\mathbf{x}} + \frac{\tilde{a}}{2}\hat{\mathbf{y}} + h\hat{\mathbf{z}}$ ) of

$$|\mathbf{w}| = \left| -\tilde{\mathbf{a}} + 3\tilde{\mathbf{b}} + \tilde{\mathbf{v}}_2 \right| = \left| 2\tilde{\mathbf{b}} - \mathbf{w} + \tilde{\mathbf{v}}_2 \right| = \lambda. \quad (\text{D.34})$$

There are 9 inter-lamellar overlaps [again, particles of layers that “face” each other in figure 9.5(18)].

- **$e = 30.5\epsilon$ .** This trig structure [figure 9.5(17)] has also two basis particles. Since  $\tilde{a}$  is very small, we see very clearly the hexagonal layers built by  $\mathbf{p} = \tilde{\mathbf{b}} - \tilde{\mathbf{a}}$  and  $\mathbf{q} = \tilde{\mathbf{c}} - \tilde{\mathbf{a}}$ . These layers are completely determined by the fact, that its 2D basis vectors satisfy  $|3\mathbf{p} + 2\mathbf{q}| = \lambda$ , leading to a layer-(and hence lamellar-)internal energy per particle of  $30\epsilon$ . This means the nearest neighbour distance is  $\lambda/\sqrt{19} \simeq 1.03\sigma$ .

Now these lamellae are stacked in a way, that, first, one pair of adjacent lamellae are above each other like in a 3D-hexagonal lattice, with exactly one overlap between

particles of different lamellae. This is visualised in figure 9.5(17), where the middle and the right lamellae are stacked in this way. The single overlap is visualised by the yellow particles which touch each other (if belonging to different lamellae), whence the green particle, surrounded by six yellow ones in the right lamella, exhibits a shoulder overlap with the yellow particle of the central lamella.

The next layer has no overlaps with the previous one, it is not stacked in the previous hexagonally, but in a trigonal way, so that the layer is packed as closely as possible under these conditions. This is again visualised in figure 9.5(17), where the yellow particles of the left lamella touch the yellow particle of the central lamella at the shoulder.

For completeness we present the lattice and basis vectors:

$$\tilde{\mathbf{a}} = \tilde{a} \hat{\mathbf{x}}, \quad \tilde{\mathbf{b}} = \tilde{a}(\cos \alpha \hat{\mathbf{x}} + \sin \alpha \hat{\mathbf{y}}), \quad \tilde{\mathbf{c}} = \tilde{a} \left( \cos \alpha \hat{\mathbf{x}} + \frac{\cos \alpha \sin \alpha}{1 + \cos \alpha} \hat{\mathbf{y}} + \sqrt{\frac{\cos \alpha - \cos 2\alpha}{1 + \cos \alpha}} \hat{\mathbf{z}} \right), \quad (\text{D.35a})$$

$$\tilde{a} = 5 \sqrt{\frac{19 + 4\sqrt{21}}{589 - 76\sqrt{21}}} \lambda \simeq 8.86\sigma, \quad \cos \alpha = \frac{13 + 8\sqrt{21}}{50} \simeq 0.993 \quad (\text{D.35b})$$

$$\tilde{\mathbf{v}}_2 = \frac{5}{2} \sqrt{\frac{19 + 4\sqrt{21}}{589 - 76\sqrt{21}}} \lambda \hat{\mathbf{x}} + \frac{5}{2(63 + 8\sqrt{21})} \sqrt{\frac{1281 - 4\sqrt{21}}{589 - 76\sqrt{21}}} \lambda \hat{\mathbf{y}} + 2 \frac{11 + \sqrt{21}}{19 + 4\sqrt{21}} \sqrt{\frac{506 + 96\sqrt{21}}{24339 - 76\sqrt{21}}} \lambda \hat{\mathbf{z}} \quad (\text{D.35c})$$

$$\simeq 4.43\sigma \hat{\mathbf{x}} + 0.26\sigma \hat{\mathbf{y}} + 0.75\sigma \hat{\mathbf{z}}. \quad (\text{D.35d})$$

- $\mathbf{e} = 30\epsilon$ . This trig structure represents a stacking of exactly the same layers like in the previous case, but now there are no overlaps between layers. To stack them as closely as possible under this condition leads to

$$\tilde{a} = \lambda, \quad \cos \alpha = \frac{37}{38} \simeq 0.974, \quad (\text{D.36})$$

with no extra basis particles, see figure 9.5(16).

- $\mathbf{e} = 24.5\epsilon$ . This tric structure [see figure 9.5(15)] with two basis particles consists of single-layer lamellae which again consist of double stripes. Particles of different lamellae do not overlap, the stripes are built up by a sequence of particles touching at the cores ( $\tilde{c} = \sigma$ ). The 2D layer lattice is determined through  $\tilde{\mathbf{c}} = \sigma \hat{\mathbf{z}}$ ,  $\tilde{\mathbf{b}} = b_x \hat{\mathbf{x}} + b_y \hat{\mathbf{y}}$  and the conditions  $2\tilde{b} = \lambda$  and  $|\tilde{\mathbf{b}} - 4\tilde{\mathbf{c}}| = \lambda$ .

The extra particle is positioned in the  $\tilde{\mathbf{b}}\text{-}\tilde{\mathbf{c}}$ -plane and satisfies  $|\tilde{\mathbf{v}}_2| = \sigma$  and  $|\tilde{\mathbf{v}}_2 + 4\tilde{\mathbf{c}}| = \lambda$ . The layers are then stacked according to  $|\tilde{\mathbf{v}}_2 - \tilde{\mathbf{a}} - \tilde{\mathbf{c}}| = |\tilde{\mathbf{v}}_2 + \tilde{\mathbf{a}} - \tilde{\mathbf{b}}| = \lambda$ , and

$|\tilde{\mathbf{v}}_2 + \tilde{\mathbf{a}} - \tilde{\mathbf{b}} + \tilde{\mathbf{c}}| = \lambda$ , finally leading to

$$\begin{aligned} \tilde{\mathbf{a}} &= -\frac{103}{128}\sigma \hat{\mathbf{x}} + 3\frac{13468\sqrt{95}+26185\sqrt{3311}}{3591040}\sigma \hat{\mathbf{y}} - \frac{3}{44888\sqrt{10}}\sqrt{40241621573 + 8080691\sqrt{314545}}\sigma \hat{\mathbf{z}} \\ &\simeq -0.80\sigma \hat{\mathbf{x}} + 1.37\sigma \hat{\mathbf{y}} - 4.47\sigma \hat{\mathbf{z}} \end{aligned} \quad (\text{D.37a})$$

$$\tilde{\mathbf{b}} = \left(2\sigma - \frac{3\lambda^2}{32\sigma}\right) \hat{\mathbf{x}} + \frac{1}{32}\sqrt{640\lambda^2 - \frac{9\lambda^4}{\sigma^2} - 4096\sigma^2} \hat{\mathbf{y}} \simeq 0.10\sigma \hat{\mathbf{x}} + 2.25\sigma \hat{\mathbf{y}} \quad (\text{D.37b})$$

$$\tilde{\mathbf{c}} = \sigma \hat{\mathbf{z}} \quad (\text{D.37c})$$

$$\tilde{\mathbf{v}}_2 = \frac{\lambda^2 - 17\sigma^2}{8\sigma} \hat{\mathbf{x}} + \frac{1}{8}\sqrt{34\lambda^2 - \frac{\lambda^4}{\sigma^2} - 225\sigma^2} \hat{\mathbf{y}} \simeq 0.41\sigma \hat{\mathbf{x}} + 0.91\sigma \hat{\mathbf{y}}, \quad (\text{D.37d})$$

where we have again replaced  $\lambda$  by  $\frac{9}{2}\sigma$  in the expressions for the components of  $\tilde{\mathbf{a}}$ , because the full expressions are quite long and non-instructive.

- $\mathbf{e} = 20\epsilon$ . This tric structure with one basis particle consist of single-layer lamellae (spanned by  $\tilde{\mathbf{b}}$  and  $\tilde{\mathbf{c}}$ ) where all overlaps occur inside each lamella [see figure 9.5(14)]. The three unit vectors obey

$$|\tilde{\mathbf{a}}| = |-\tilde{\mathbf{a}} + \tilde{\mathbf{b}}| = |-\tilde{\mathbf{a}} + \tilde{\mathbf{b}} - \tilde{\mathbf{c}}| = |2\tilde{\mathbf{b}} + 3\tilde{\mathbf{c}}| = |3\tilde{\mathbf{b}} + 2\tilde{\mathbf{c}}| = |3\tilde{\mathbf{b}} - 3\tilde{\mathbf{c}}| = \lambda, \quad (\text{D.38})$$

leading to

$$\tilde{\mathbf{a}} = \lambda \hat{\mathbf{x}} = 4.5\sigma \hat{\mathbf{x}}, \quad (\text{D.39a})$$

$$\tilde{\mathbf{b}} = \frac{\lambda}{30} \left( \hat{\mathbf{x}} + \sqrt{59} \hat{\mathbf{y}} \right) \simeq 0.15\sigma \hat{\mathbf{x}} + 1.15\sigma \hat{\mathbf{y}}, \quad (\text{D.39b})$$

$$\tilde{\mathbf{c}} = \frac{\lambda}{45} \left( -\hat{\mathbf{x}} + \frac{16}{\sqrt{59}} \hat{\mathbf{y}} + 15\sqrt{\frac{34}{59}} \hat{\mathbf{z}} \right) \simeq -0.1\sigma \hat{\mathbf{x}} + 0.21\sigma \hat{\mathbf{y}} + 1.14\sigma \hat{\mathbf{z}}. \quad (\text{D.39c})$$

- $\mathbf{e} = 18\epsilon$ . The hexagonal single-layer lamellae of this trig structure [see figure 9.5(13)] are predetermined by the condition, that the long diagonal of the primitive, hexagonal 2D unit cell is  $\lambda/2$ , leading to an energy per particle of  $18\epsilon$  inside one lamella. To get the smallest distance between layers so that there are no extra overlaps we simply have to set  $\tilde{a} = \lambda$ . The angle between the trigonal unit cell vectors is given by  $\cos \alpha = 23/24 \simeq 0.958$ .
- $\mathbf{e} = 15\epsilon$ . An energy per particle of  $15\epsilon$  has the bco structure visualised in figure 9.5(12), where the conditions

$$\left| \frac{\tilde{\mathbf{a}} + \tilde{\mathbf{b}} + \tilde{\mathbf{c}}}{2} \right| = 3\tilde{b} = 4\tilde{c} = \lambda \quad (\text{D.40})$$

are met. The resulting bco parameters are given by

$$\tilde{a} = \frac{\sqrt{551}}{12}\lambda \simeq 8.80\sigma, \quad \tilde{b} = \frac{1}{3}\lambda = 1.5\sigma, \quad \tilde{c} = \frac{1}{4}\lambda = 1.125\sigma. \quad (\text{D.41})$$



- $\mathbf{e} = 10.5\epsilon$ . This tric structure [see figure 9.5(11)] consist of columns that are built by close-packed double lines:

$$\tilde{\mathbf{c}} = \sigma \hat{\mathbf{z}}, \quad \tilde{\mathbf{v}}_2 = \sigma \frac{\sqrt{3}}{2} \hat{\mathbf{y}} + \frac{\sigma}{2} \hat{\mathbf{z}}. \quad (\text{D.42})$$

Parallel to the double-line-plane, the adjacent double lines are close-packed at the shoulders so that  $\tilde{a} = |\tilde{\mathbf{a}} - \tilde{\mathbf{c}}| = |\tilde{\mathbf{a}} - \tilde{\mathbf{v}}_2| = \lambda$ , i.e.,

$$\tilde{\mathbf{a}} = \sqrt{\lambda^2 - \frac{\sigma^2}{3}} \hat{\mathbf{x}} + \frac{\sigma}{2\sqrt{3}} \hat{\mathbf{y}} + \frac{\sigma}{2} \hat{\mathbf{z}} \simeq 4.46\sigma \hat{\mathbf{x}} + 0.29\sigma \hat{\mathbf{y}} + 0.5\hat{\mathbf{z}} \quad (\text{D.43})$$

To determine the last unit cell vector we have to solve  $\tilde{\mathbf{b}} = |\tilde{\mathbf{b}} - \tilde{\mathbf{c}}| = |\tilde{\mathbf{b}} - (\tilde{\mathbf{a}} + \tilde{\mathbf{v}}_2)| = \lambda$ , leading to

$$\begin{aligned} \tilde{\mathbf{b}} = & \sqrt{9\lambda^2 - 3\sigma^2} \frac{3\lambda^4 + 2\lambda^2\sigma^2 - \sigma^4 - 2\sigma\sqrt{9\lambda^6 - 7\lambda^2\sigma^4 + 2\sigma^6}}{6(3\lambda^4 + 2\lambda^2\sigma^2 - \sigma^4)} \hat{\mathbf{x}} + \\ & + \frac{2\lambda^2\sigma + 2\sigma^2 + \sqrt{9\lambda^6 - 7\lambda^2\sigma^4 + 2\sigma^6}}{2\sqrt{3}(\lambda^2 + \sigma^2)} \hat{\mathbf{y}} + \frac{\sigma}{2} \hat{\mathbf{z}} \end{aligned} \quad (\text{D.44a})$$

$$\simeq 1.27\sigma \hat{\mathbf{x}} + 4.29\sigma \hat{\mathbf{y}} + 0.5\sigma \hat{\mathbf{z}}. \quad (\text{D.44b})$$

- $\mathbf{e} = 8\epsilon$ . Here we encounter close-packed double lines forming columns, that are arranged on an sm lattice to have no inter-columnar overlaps [see figure 9.5(10)]. One possible parametrisation is

$$\tilde{\mathbf{c}} = \sigma \hat{\mathbf{z}} \quad (\text{D.45a})$$

$$\tilde{\mathbf{v}}_2 = -\frac{\sqrt{3}}{2}\sigma \hat{\mathbf{x}} + \frac{\sigma}{2} \hat{\mathbf{z}} \simeq -0.87 \hat{\mathbf{x}} + 0.5 \hat{\mathbf{z}} \quad (\text{D.45b})$$

$$\tilde{\mathbf{a}} = \frac{3\lambda^2 + 4\lambda\sigma - \sigma^2}{2\sqrt{3}\lambda} \hat{\mathbf{x}} + \frac{\lambda - \sigma}{2\sqrt{3}\lambda} \sqrt{3\lambda^2 - \sigma^2} \hat{\mathbf{y}} \simeq 4.99\sigma \hat{\mathbf{x}} + 1.74\sigma \hat{\mathbf{y}} \quad (\text{D.45c})$$

$$\tilde{\mathbf{b}} = \frac{3\lambda^2 + 2\lambda\sigma - \sigma^2}{2\sqrt{3}\lambda} \hat{\mathbf{x}} - \frac{\lambda + \sigma}{2\sqrt{3}\lambda} \sqrt{3\lambda^2 - \sigma^2} \hat{\mathbf{y}} \simeq 4.41\sigma \hat{\mathbf{x}} - 2.73\sigma \hat{\mathbf{y}}. \quad (\text{D.45d})$$

- $\mathbf{e} = 6.5\epsilon$ . Again we get double lines [see figure 9.5(9)], but now the particles along one line do not touch at the hard core, but the shoulders of a particle and the 4<sup>th</sup> one in either direction along the line touch each other. Particles of the second line each touch one of the first line at the hard core, summing up to a total of 13 overlaps in

one double line per particle.

$$\tilde{\mathbf{c}} = \frac{\lambda}{4} \hat{\mathbf{z}} = 1.125\sigma \hat{\mathbf{z}} \quad (\text{D.46a})$$

$$\tilde{\mathbf{v}}_2 = \frac{1}{2} \sqrt{4\sigma^2 - \frac{\sigma^4}{\lambda^2}} \hat{\mathbf{x}} + \frac{\sigma^2}{2\lambda} \hat{\mathbf{z}} \simeq 0.99\sigma \hat{\mathbf{x}} + 0.11\sigma \hat{\mathbf{z}} \quad (\text{D.46b})$$

$$\tilde{\mathbf{b}} = \frac{7\lambda\sqrt{4\lambda^2\sigma^2 - \sigma^4}}{32\lambda^2 - 8\sigma^2} \hat{\mathbf{x}} - \frac{\sqrt{7}}{4} \sqrt{\frac{9\lambda^4 - 4\lambda^2\sigma^2}{4\lambda^2 - \sigma^2}} \hat{\mathbf{y}} + \frac{\lambda}{8} \hat{\mathbf{z}} \simeq 0.44\sigma \hat{\mathbf{x}} - 4.44\sigma \hat{\mathbf{y}} + 0.56\sigma \hat{\mathbf{z}} \quad (\text{D.46c})$$

$$\begin{aligned} \tilde{\mathbf{a}} = & \frac{63\sigma^2\sqrt{4\lambda^2\sigma^2 - \sigma^4} - 4\lambda^2(49\sqrt{4\lambda^2\sigma^2 - \sigma^4} + \sqrt{329}\sqrt{36\lambda^4 - 25\lambda^2\sigma^2 + 4\sigma^4})}{126(4\lambda^3 - \lambda\sigma^2)} \hat{\mathbf{x}} + \\ & - \frac{\sqrt{36\lambda^6 - 25\lambda^4\sigma^2 + 4\lambda^2\sigma^4} 72\sqrt{7}\lambda^2 + \sigma(-32\sqrt{7}\sigma + 7\sqrt{47}\sqrt{9\lambda^2 - 4\sigma^2})}{63(36\lambda^4 - 25\lambda^2\sigma^2 + 4\sigma^4)} \hat{\mathbf{y}} + \\ & - \frac{\sigma^2}{2\lambda} \hat{\mathbf{z}} \simeq -4.64\sigma \hat{\mathbf{x}} - 2.64\sigma \hat{\mathbf{y}} - 0.11\sigma \hat{\mathbf{z}}. \end{aligned} \quad (\text{D.46d})$$

- $\mathbf{e} = 4.375\epsilon$ . This bco structure has clusters of 8 particles at each lattice site [see figure 9.5(8)]. Inside each cluster all shoulders overlap (28), and there are additional overlaps between the centred cluster and the one in  $(\tilde{\mathbf{a}} + \tilde{\mathbf{b}} + \tilde{\mathbf{c}})/2$  direction (4) and the one in  $(-\tilde{\mathbf{a}} + \tilde{\mathbf{b}} + \tilde{\mathbf{c}})/2$  direction (3). This gives an energy per particle of  $35\epsilon/8 = 4.375\epsilon$ . An exact, geometric interpretation has not been possible so far, due to the large number of basis particles and hence determining equations.
- $\mathbf{e} = 3\epsilon$ . The lines of this columnar bco structure [see figure 9.5(7)] are beaded by the smallest unit cell vector. There are only overlaps inside each line, the lengths are:

$$\tilde{a} = \frac{\sqrt{47}}{4} \lambda \simeq 7.71\sigma, \quad \tilde{b} = \lambda = 4.5\sigma, \quad \tilde{c} = \frac{\lambda}{4} = 1.125\sigma. \quad (\text{D.47})$$

- $\mathbf{e} = 2.5\epsilon$ . Here we have clusters of six particles arranged on a tric lattice [see figure 9.5(6)]. Overlaps only occur inside a cluster, giving an energy per particle of  $\frac{6.5}{2}\epsilon/6 = 2.5\epsilon$ . The 6-cluster can be understood as built up by parts of two close-packed hexagonal layers: from one layer take four particles forming a close-packed rhombus, and from the next layer take two touching particles of which one occupies the tetrahedral site of three of the rhombus particles and the other one touches in

total three particles. This gives

$$\tilde{\mathbf{v}}_2 = \frac{\sigma}{2} \hat{\mathbf{x}} + \sigma \frac{\sqrt{3}}{2} \hat{\mathbf{y}} \quad (\text{D.48a})$$

$$\tilde{\mathbf{v}}_3 = -\frac{\sigma}{2} \hat{\mathbf{x}} + \sigma \frac{\sqrt{3}}{2} \hat{\mathbf{y}} \quad (\text{D.48b})$$

$$\tilde{\mathbf{v}}_4 = \sigma \sqrt{3} \hat{\mathbf{y}} \quad (\text{D.48c})$$

$$\tilde{\mathbf{v}}_5 = \frac{\sigma}{\sqrt{3}} \hat{\mathbf{y}} - \sqrt{\frac{2}{3}} \sigma \hat{\mathbf{z}} \quad (\text{D.48d})$$

$$\tilde{\mathbf{v}}_6 = \frac{5\sigma}{2\sqrt{3}} \hat{\mathbf{y}} - \sqrt{\frac{2}{3}} \sigma \hat{\mathbf{z}}. \quad (\text{D.48e})$$

To stack these clusters as closely as possible without inter-cluster overlaps, satisfy

$$|\tilde{\mathbf{c}} + \tilde{\mathbf{v}}_5 - \tilde{\mathbf{v}}_2| = |\tilde{\mathbf{c}} + \tilde{\mathbf{v}}_6 - \tilde{\mathbf{v}}_2| = |\tilde{\mathbf{c}} + \tilde{\mathbf{v}}_3 - \tilde{\mathbf{v}}_2| = \quad (\text{D.49a})$$

$$= |\mathbf{b} - \tilde{\mathbf{v}}_4| = |\tilde{\mathbf{b}} - \tilde{\mathbf{v}}_6| = |\tilde{\mathbf{b}} - \tilde{\mathbf{c}} - \tilde{\mathbf{v}}_6| = \quad (\text{D.49b})$$

$$= |\tilde{\mathbf{a}} + \tilde{\mathbf{v}}_3 - \tilde{\mathbf{v}}_6| = |\tilde{\mathbf{a}} + \tilde{\mathbf{v}}_4 - \tilde{\mathbf{b}} - \tilde{\mathbf{v}}_5| = |\tilde{\mathbf{a}} + \tilde{\mathbf{v}}_3 - \tilde{\mathbf{c}} - \tilde{\mathbf{v}}_6| = \lambda. \quad (\text{D.49c})$$

The resulting analytic expressions are very lengthy, numerically we get

$$\tilde{\mathbf{a}} \simeq 4.94\sigma \hat{\mathbf{x}} - 1.00\sigma \hat{\mathbf{y}} - 2.30\sigma \hat{\mathbf{z}}, \quad (\text{D.50a})$$

$$\tilde{\mathbf{b}} \simeq 3.90\sigma \hat{\mathbf{x}} + 1.08\sigma \hat{\mathbf{y}} + 3.70\sigma \hat{\mathbf{z}}, \quad (\text{D.50b})$$

$$\tilde{\mathbf{c}} \simeq 3.64\sigma \hat{\mathbf{x}} - 2.10\sigma \hat{\mathbf{y}} + 2.97\sigma \hat{\mathbf{z}}. \quad (\text{D.50c})$$

- **$e = 1.75\epsilon$ .** On this tric lattice there are clusters of four particles, arranged in a rhombus with touching hard cores [see figure 9.5(5)]. Overlaps are inside each cluster (6), and in the direction of the long diagonal of the rhombus, along which the next rhombus is positioned, there is one extra overlap. The plane of the rhombus is defined as the  $\tilde{\mathbf{a}}\text{--}\tilde{\mathbf{b}}$ -plane, the vectors are

$$\tilde{\mathbf{v}}_2 = \sigma \hat{\mathbf{y}}, \quad \tilde{\mathbf{v}}_3 = -\frac{\sigma}{2} \hat{\mathbf{x}} + \frac{\sqrt{3}}{2} \sigma \hat{\mathbf{y}}, \quad \tilde{\mathbf{v}}_4 = -\frac{\sigma}{2} \hat{\mathbf{x}} - \frac{\sqrt{3}}{2} \sigma \hat{\mathbf{y}}, \quad (\text{D.51a})$$

$$\tilde{\mathbf{a}} = \frac{\sqrt{3}\sigma + \sqrt{4\lambda^2 - \sigma^2}}{2} \hat{\mathbf{x}} \simeq 5.34\sigma \hat{\mathbf{x}}, \quad (\text{D.51b})$$

$$\tilde{\mathbf{b}} = \frac{\sqrt{3}\sigma + \sqrt{4\lambda^2 - \sigma^2}}{4} \hat{\mathbf{x}} + \frac{3\sigma + \sqrt{3}\sqrt{4\lambda^2 - \sigma^2}}{4} \hat{\mathbf{y}} \simeq 2.67\sigma \hat{\mathbf{x}} + 4.62\sigma \hat{\mathbf{y}}, \quad (\text{D.51c})$$

$$\tilde{\mathbf{c}} = \frac{\lambda^2(5\sqrt{3}\sigma + 3\sqrt{4\lambda^2 - \sigma^2}) - \sigma^2(3\sqrt{3}\sigma + 5\sqrt{4\lambda^2 - \sigma^2})}{12\lambda^2 - 4\sigma^2} \hat{\mathbf{x}} + \frac{(\lambda^2 + \sigma^2)(\sigma + \sqrt{12\lambda^2 - 3\sigma^2})}{12\lambda^2 - 4\sigma^2} \hat{\mathbf{y}} + \quad (\text{D.51d})$$

$$+ \frac{\sqrt{12\lambda^6 + 5\lambda^4\sigma(-7\sigma + \sqrt{12\lambda^2 - 3\sigma^2}) - 3\sigma^5(\sigma + \sqrt{12\lambda^2 - 3\sigma^2}) + 2\lambda^2\sigma^3(7\sigma + \sqrt{12\lambda^2 - 3\sigma^2})}}{\sqrt{2}(3\lambda^2 - \sigma^2)} \hat{\mathbf{z}} \simeq$$

$$\simeq 2.80\sigma \hat{\mathbf{x}} + 1.47\sigma \hat{\mathbf{y}} + 4.06\sigma \hat{\mathbf{z}}. \quad (\text{D.51e})$$

- **$e = 1.5\epsilon$ .** One needs eight basis particles to describe this structure of two different kinds of 4-clusters, with no overlaps between particles of different clusters, arranged on a *triclinic* lattice [see figure 9.5(4)]. Again, the large number of eight basis particles prevents an exact, analytic investigation.

- $\mathbf{e} = \boldsymbol{\epsilon}$ . Disjoint 3-clusters are the basis for this sfc structure [see figure 9.5(3)]. The clusters form equilateral triangles with touching hard cores, the slanting of the clusters and the unit cell, strongly connected, has not been solved yet.
- $\mathbf{e} = 0.5\boldsymbol{\epsilon}$ . On this sm lattice there are disjoint dimers on the lattice sites. The two particles forming the dimer touch each other at the hard core, the packing of the dimers is determined by

$$\begin{aligned} |\tilde{\mathbf{a}} + \tilde{\mathbf{c}} + \tilde{\mathbf{v}}_2| &= |\tilde{\mathbf{a}} - \tilde{\mathbf{b}} + \tilde{\mathbf{c}} + \tilde{\mathbf{v}}_2| = |\tilde{\mathbf{c}} + \tilde{\mathbf{v}}_2| = \\ |\tilde{\mathbf{c}}| = |\tilde{\mathbf{b}}| &= |-\tilde{\mathbf{b}} + \tilde{\mathbf{v}}_2| = |-\tilde{\mathbf{b}} + \tilde{\mathbf{c}} + \tilde{\mathbf{v}}_2| = |\tilde{\mathbf{a}} + \tilde{\mathbf{v}}_2| = \lambda, \end{aligned} \quad (\text{D.52})$$

leading to

$$\begin{aligned} \tilde{\mathbf{a}} &= \frac{10\lambda^6\sigma^4 - 7\lambda^4\sigma^6 + \lambda^2\sigma^8 + 2\lambda^2\sigma^3\sqrt{(2\lambda^2 - \sigma^2)^3(3\lambda^2 - \sigma^2)(\lambda^2 + \sigma^2)}}{3\sigma^4(16\lambda^6 - 6\lambda^4\sigma^2 - 3\lambda^2\sigma^4 + \sigma^6)} \\ &\cdot \sqrt{\frac{72\lambda^8\sigma^2 + 39\lambda^6\sigma^4 - 30\lambda^4\sigma^6 + 3\lambda^2\sigma^8 - 6\lambda^2\sigma^3\sqrt{(2\lambda^2 - \sigma^2)^3(3\lambda^2 - \sigma^2)(\lambda^2 + \sigma^2)}}{3\lambda^8 + 2\lambda^6\sigma^2 - \lambda^4\sigma^4}} \hat{\mathbf{x}} \\ &\simeq 5.23\sigma \hat{\mathbf{x}}, \end{aligned} \quad (\text{D.53a})$$

$$\tilde{\mathbf{b}} = \lambda \hat{\mathbf{y}} = 4.5\sigma \hat{\mathbf{y}}, \quad (\text{D.53b})$$

$$\begin{aligned} \tilde{\mathbf{c}} &= \frac{6\lambda^6\sigma + \lambda^4\sigma^3 - 4\lambda^2\sigma^5 + \sigma^7 - 2\lambda^2\sqrt{(2\lambda^2 - \sigma^2)^3(3\lambda^2 - \sigma^2)(\lambda^2 + \sigma^2)}}{6\sigma(16\lambda^6 - 6\lambda^4\sigma^2 - 3\lambda^2\sigma^4 + \sigma^6)} \\ &\cdot \sqrt{\frac{72\lambda^8\sigma^2 + 39\lambda^6\sigma^4 - 30\lambda^4\sigma^6 + 3\lambda^2\sigma^8 - 6\lambda^2\sigma^3\sqrt{(2\lambda^2 - \sigma^2)^3(3\lambda^2 - \sigma^2)(\lambda^2 + \sigma^2)}}{3\lambda^8 + 2\lambda^6\sigma^2 - \lambda^4\sigma^4}} \hat{\mathbf{x}} + \\ &+ \frac{\lambda^2 - \sigma^2}{2\lambda} \hat{\mathbf{y}} + \frac{\sqrt{3\lambda^4 + 2\lambda^2\sigma^2 - \sigma^4 + \sigma\sqrt{6\lambda^6 + \lambda^4\sigma^2 - 4\lambda^2\sigma^4 + \sigma^6}}}{\sqrt{6}\lambda} \hat{\mathbf{z}} = \\ &\simeq -1.83\sigma \hat{\mathbf{x}} + 2.14\sigma \hat{\mathbf{x}} + 3.51\sigma \hat{\mathbf{z}}, \end{aligned} \quad (\text{D.53c})$$

$$\begin{aligned} \tilde{\mathbf{v}}_2 &= -\frac{1}{2} \sqrt{\frac{24\lambda^6\sigma^2 + 13\lambda^4\sigma^4 - 10\lambda^2\sigma^6 + \sigma^8 - 2\sigma^3\sqrt{(2\lambda^2 - \sigma^2)^3(3\lambda^2 - \sigma^2)(\lambda^2 + \sigma^2)}}{9\lambda^6 + 6\lambda^4\sigma^2 - 3\lambda^2\sigma^4}} \hat{\mathbf{x}} + \\ &+ \frac{\sigma^2}{2\lambda} \hat{\mathbf{y}} + \\ &- \frac{1}{\sqrt{6}} \sqrt{\frac{6\lambda^6\sigma^2 + \lambda^4\sigma^4 - 4\lambda^2\sigma^6 + \sigma^8 + \sqrt{(2\lambda^2 - \sigma^2)^3(3\lambda^2 - \sigma^2)(\lambda^2 + \sigma^2)}}{\lambda^2(3\lambda^2 - \sigma^2)(\lambda^2 + \sigma^2)}} \\ &\simeq -0.78\sigma \hat{\mathbf{x}} + 0.11\sigma \hat{\mathbf{y}} - 0.62\sigma \hat{\mathbf{z}}. \end{aligned} \quad (\text{D.53d})$$

- $\mathbf{e} = \mathbf{0}$ . At very low pressure there occurs again a close-packing at the shoulders, as an example the corresponding fcc lattice is drawn in figure 9.5(1).  $\tilde{\mathbf{a}} = \sqrt{2}\lambda$ .

# Appendix E

## Selected Analytic Expressions in Continuum Theory

For the calculation of the lamellar energy in the square-shoulder model we split up the internal energy per particle of equation (9.24) into intra- and inter-lamellar contributions (see 9.3.3) and get

$$\frac{e_{\text{intra}}}{\varepsilon} = -\frac{1}{2} + \frac{\pi\rho_{\text{eff}}}{2} \cdot \begin{cases} D\lambda^2 - \frac{D^3}{6} & D \leq \lambda \\ \frac{4}{3}\lambda^3 - \frac{\lambda^4}{2D} & D > \lambda \end{cases}, \quad (\text{E.1})$$

plotted in figure E.1 ( $D$  is the lamella thickness, see figure E.1). One can see, that the linear approximation used in section 9.3.3 is quite good for  $D \lesssim \lambda/2$ , the error is less than 5%.

For the interaction energy between two different layers having distance  $\ell$  we get

$$e_{\text{inter}}(\ell) = \frac{\varepsilon\pi\rho_{\text{eff}}}{24D} \cdot \begin{cases} -D^4 + 4D^3\ell - 6D^2(\ell^2 - \lambda^2) + 4D(\ell - \lambda)^2(\ell + 2\lambda)^2 + (\ell - \lambda)^3(\ell + 3\lambda) & \ell < \lambda \\ (D - \ell - 3\lambda)(D - \ell + \lambda)^3 & \ell \geq \lambda \end{cases}. \quad (\text{E.2})$$

The total energy per particle is therefore the sum of  $e_{\text{intra}}$  and all possible inter lamellar interactions, determined by the interaction range  $\lambda$ . The possible lamellae distances are  $\ell = nL$  ( $L$  being the nearest lamellar distance and  $n \in \mathbb{N}$ ), those contributing to the interaction energy are the ones satisfying  $\ell < D + \lambda$ , which results in the maximum value of  $n$  as

$$N = \left\lfloor \frac{D + \lambda}{L} \right\rfloor, \quad (\text{E.3})$$

where  $\lfloor \cdot \rfloor$  denotes the Gaussian floor function. With this we finally get

$$e = e_{\text{intra}} + 2 \sum_{n=1}^N e_{\text{inter}}(nL). \quad (\text{E.4})$$

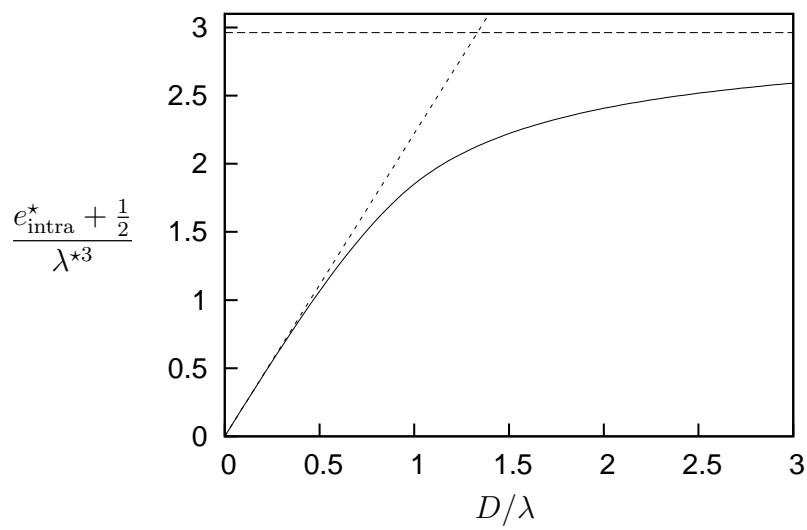


Figure E.1:  $(e_{\text{intra}}^* + \frac{1}{2}) / \lambda^{*3}$  (red) for a lamella with effective density  $\rho_{\text{eff}}^* = \sqrt{2}$  in dependence of the ratio  $D/\lambda$ . The dashed green line is the asymptote for large values of  $D/\lambda$  ( $2\sqrt{2}\pi/3 \simeq 2.96$ , the value for the homogeneous distribution), the dashed blue one is the linearised function for small values.

# Appendix F

## Influence of a Cutoff on the Hard Core Yukawa Model

To rule out the influence of the chosen cutoff radius in chapter 10 we further investigated the low pressure/packing fraction regime. It is clear that at very low pressure the particles, that are already in an fcc phase, will adjust the nearest neighbour distance in a way to become exactly equal to the cutoff radius  $r_{\text{cut}}$  (the structure is termed  $\text{fcc}_{\text{cut}}$ ). In this way the interaction energies between all particles vanish, the remaining contribution to the enthalpy being the volume term. Since the density is constant,  $\rho_{\text{cut}} = \sqrt{2}/r_{\text{cut}}^3$ ,  $h^*$  is just a straight line in the  $h^*-P^*$ -diagram; we obtain an *unphysical* second order phase transition between  $\text{fcc}_{\text{cut}}$  and fcc. The regime where this transition occurs is visualised in figure F.1. As can be seen there, the  $\text{fcc}_{\text{cut}}$ -phase only occurs below packing fractions

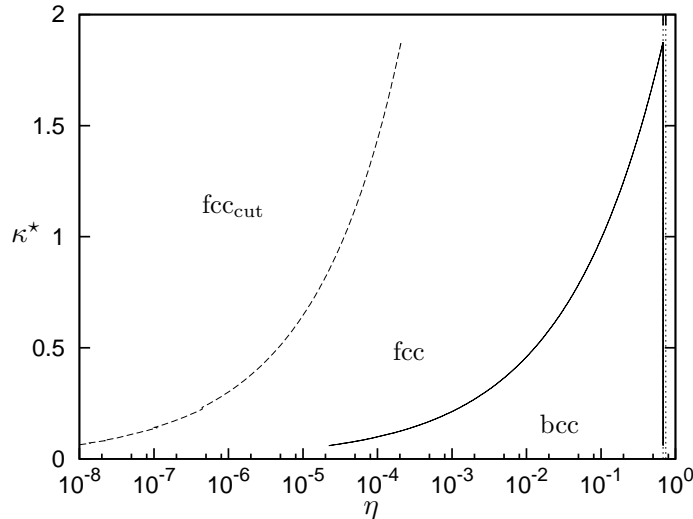


Figure F.1: The  $T = 0$  phase diagram as in figure 10.2, but with a logarithmic scale on the packing fraction-axis. The dashed line indicates the limit below which we just obtain an fcc structure with nearest neighbour distance being equal to the pair potential cutoff  $r_{\text{cut}}$ .

which are three to four orders of magnitude smaller than the first order fcc–bcc–transition packing fractions (note that the difference in  $\eta_{\text{fcc}}$  and  $\eta_{\text{bcc}}$  at the transition is too small to be visible in either figure 10.2 or figure F.1). Therefore we can assume, that the cutoff distance has no significant influence on the results for the other phase transitions.



# Appendix G

## Tables

Table G.1: Critical point location ( $\rho_c^*$  and  $T_{c,\text{RPM}}^*$ ) and fitted critical exponent  $\beta$  for various values of  $\xi^2$  and  $\alpha^*$  for the charged Kac model (chapter 7). For  $\xi^2 < 0.1$  the fitted data for  $\beta$  tends to be unreliable.

$\xi^2$	$\alpha^*$	$\rho_c^*$	$T_{c,\text{RPM}}^*$	$\beta$
100.	1.8	0.314445	65.2809	0.402347
	0.5	0.25857	107.189	0.455282
	0.2	0.25075	112.192	0.487867
	0.15	0.25004	112.633	0.492727
	0.14	0.24992	112.706	0.49385
	0.1	0.249525	112.95	0.496725
	0.01	0.249	113.306	0.499831
11.1	1.8	0.31358	7.2724	0.402147
	0.5	0.258205	11.9303	0.458607
	0.1	0.2492	12.5707	0.498284
	0.01	0.248795	12.5988	0.497799
1.	1.8	0.299915	0.678068	0.407351
	0.5	0.25156	1.10175	0.464236
	0.1	0.243085	1.16016	0.497945
	0.01	0.245	1.16723	0.499645
0.6	1.8	0.28944	0.417367	0.410648
	0.5	0.24631	0.673785	0.465365
	0.1	0.23822	0.70923	0.497732
	0.01	0.23785	0.710791	0.497532
0.36	1.8	0.27159	0.261159	0.411219
	0.5	0.23748	0.417098	0.465964
	0.1	0.23004	0.438768	0.496376
	0.01	0.22	0.443552	0.499275

0.25	1.8	0.251165	0.189923	0.412711
	0.5	0.22772	0.299591	0.472473
	0.1	0.221025	0.314937	0.498725
	0.01	0.22	0.323474	0.494371
0.16	1.8	0.21023	0.132612	0.420454
	1.	0.217574	0.178782	0.432193
	0.5	0.20959	0.203843	0.461918
	0.4	0.20787	0.207481	0.478158
	0.3	0.20635	0.210442	0.487022
	0.2	0.20515	0.212634	0.495717
	0.17	0.20486	0.213131	0.497272
	0.16	0.20478	0.213279	0.497793
	0.155	0.20474	0.21335	0.497941
	0.15	0.2047	0.213419	0.496929
	0.1	0.20436	0.213986	0.499349
	0.05	0.204158	0.214331	0.498864
	0.01	0.204089	0.214442	0.49998
0.125	1.8	0.17388	0.111322	0.416685
	0.5	0.19524	0.166978	0.473493
	0.1	0.19129	0.175065	0.497302
	0.01	0.190728	0.175661	0.490538
0.1	1.8	0.124975	0.0974366	0.417448
	0.5	0.17843	0.141048	0.472271
	0.1	0.176125	0.147629	0.49581
	0.01	0.1788	0.14795	0.49751
0.075	1.8	0.0475	0.0874404	0.482061
	0.5	0.149	0.116013	0.473831
	0.1	0.150085	0.121007	0.490675
	0.01	0.1496	0.121242	0.487587
0.06	1.8	0.028575	0.0843423	0.524375
	0.5	0.11785	0.102144	0.47329
	0.1	0.12291	0.106031	0.489163
	0.01	0.124	0.106218	0.467265
0.05	1.8	0.023315	0.0828916	0.523741
	0.5	0.08537	0.0941456	0.467864
	0.1	0.09489	0.0970958	0.481766
	0.01	0.09592	0.0972545	0.485004
0.04	1.8	0.02011	0.0817199	0.519083
	0.5	0.048255	0.0882476	0.487491
	0.1	0.05781	0.0899971	0.480583

	0.01	0.058	0.0900909	0.456845
0.03	1.8	0.018	0.0807444	0.586359
	0.5	0.0295	0.0845853	0.551899
	0.1	0.033	0.0854693	0.530362
	0.01	0.0328229	0.0855167	0.515019
0.02	0.01	0.0225402	0.0825501	0.525541
0.01	1.8	0.01532	0.0791961	0.515201
	0.5	0.01714	0.0801528	0.525892
	0.1	0.0174975	0.0803368	0.528195
	0.01	0.0175	0.0803464	0.53093

Table G.2: CP data of the Kac–Yukawa model (chapter 8) for three different values of  $\alpha^*$  and a sequence of approximately logarithmically decreasing values of  $\xi^2$ . The CPs are given relative to the CP of the reference system,  $\rho_c^{*,\text{ref}} \simeq 0.314496596966$  and  $T_{c,Y}^{*,\text{ref}} \simeq 1.21869174843$ .

$\xi^2$	$\alpha^* = 0.1$		$\alpha^* = 0.01$		$\alpha^* = 0.0001$	
	$\rho_c^* - \rho_c^{*,\text{ref}}$	$T_{c,Y}^* - T_{c,Y}^{*,\text{ref}}$	$\rho_c^* - \rho_c^{*,\text{ref}}$	$T_{c,Y}^* - T_{c,Y}^{*,\text{ref}}$	$\rho_c^* - \rho_c^{*,\text{ref}}$	$T_{c,Y}^* - T_{c,Y}^{*,\text{ref}}$
100.	-0.0648714	683.285	-0.0652806	684.815	-0.0652835	684.831
60.	-0.0647966	409.989	-0.0652012	410.907	-0.0652034	410.916
30.	-0.0646309	205.016	-0.065055	205.476	-0.0650642	205.48
20.	-0.0644901	136.692	-0.064895	136.999	-0.0648971	137.002
10.	-0.064012	68.3679	-0.064418	68.5215	-0.0644224	68.523
6.	-0.0634088	41.0382	-0.0638136	41.1306	-0.063817	41.1315
3.	-0.0619711	20.5408	-0.0623789	20.5873	-0.062382	20.5878
2.	-0.0605822	13.7082	-0.0609867	13.7394	-0.060989	13.7398
1.	-0.0567923	6.87532	-0.0571936	6.89127	-0.0571957	6.89143
0.6	-0.0524863	4.14167	-0.052885	4.15151	-0.0528874	4.15161
0.3	-0.0442885	2.09017	-0.0446784	2.09545	-0.0446814	2.09551
0.2	-0.0384683	1.40522	-0.0388163	1.409	-0.0388199	1.40904
0.1	-0.0279289	0.717649	-0.0282894	0.719961	-0.0282913	0.719984
0.06	-0.0207861	0.440149	-0.0211007	0.441895	-0.0211024	0.441913
0.03	-0.0129946	0.228779	-0.0132933	0.230142	-0.0132949	0.230156
0.02	-0.00959185	0.156731	-0.00988317	0.15799	-0.00988515	0.158004
0.01	—	—	-0.00574965	0.0838376	-0.00575821	0.0838508
0.006	-0.00354341	0.0517463	-0.00378895	0.0529604	-0.0037905	0.0529743
0.005	-0.0030154	0.0438013	—	—	—	—
0.004	-0.00247368	0.0357202	—	—	—	—
0.003	-0.00187178	0.0274542	-0.00209814	0.0286958	-0.00209961	0.0287117
0.002	-0.00129957	0.0189216	-0.00148375	0.020165	-0.00148592	0.0201825
0.001	-0.000652268	0.00994844	-0.000793683	0.0111399	-0.000795359	0.0111608
0.0006	-0.000388833	0.00614903	-0.000494333	0.00724959	-0.000496114	0.00727367
0.0003	-0.000190937	0.00316584	-0.000256705	0.0040876	-0.000266882	0.00411676
0.0002	-0.00012589	0.00213565	-0.000172315	0.00293739	-0.000181582	0.00296995
0.0001	-6.19833·10 <sup>-5</sup>	0.00108206	-7.9269·10 <sup>-5</sup>	0.00167985	-8.8507·10 <sup>-5</sup>	0.00171875
6·10 <sup>-5</sup>	-3.69059·10 <sup>-5</sup>	0.000653143	-4.22832·10 <sup>-5</sup>	0.00111568	-3.98476·10 <sup>-5</sup>	0.00115938
3·10 <sup>-5</sup>	-1.83324·10 <sup>-5</sup>	0.000328206	-1.57087·10 <sup>-5</sup>	0.000638829	-7.58478·10 <sup>-6</sup>	0.000688355
2·10 <sup>-5</sup>	-1.21929·10 <sup>-5</sup>	0.000219248	-7.54543·10 <sup>-6</sup>	0.000458973	-2.65197·10 <sup>-6</sup>	0.000511003
1·10 <sup>-5</sup>	-6.07735·10 <sup>-6</sup>	0.000109884	-7.62248·10 <sup>-7</sup>	0.000257024	1.65887·10 <sup>-6</sup>	0.000310781
6·10 <sup>-6</sup>	-3.64512·10 <sup>-6</sup>	6.61426·10 <sup>-5</sup>	9.43259·10 <sup>-7</sup>	0.000165146	3.05862·10 <sup>-6</sup>	0.000217663
3·10 <sup>-6</sup>	-1.82099·10 <sup>-6</sup>	3.32468·10 <sup>-5</sup>	1.31365·10 <sup>-6</sup>	8.85016·10 <sup>-5</sup>	3.74044·10 <sup>-6</sup>	0.000136055
2·10 <sup>-6</sup>	-1.21357·10 <sup>-6</sup>	2.22746·10 <sup>-5</sup>	1.13475·10 <sup>-6</sup>	6.0756·10 <sup>-5</sup>	3.79045·10 <sup>-6</sup>	0.000104112
1·10 <sup>-6</sup>	-6.02284·10 <sup>-7</sup>	1.12276·10 <sup>-5</sup>	7.264·10 <sup>-7</sup>	3.14344·10 <sup>-5</sup>	3.60201·10 <sup>-6</sup>	6.66448·10 <sup>-5</sup>
6·10 <sup>-7</sup>	-3.6368·10 <sup>-7</sup>	6.90756·10 <sup>-6</sup>	4.78904·10 <sup>-7</sup>	1.92849·10 <sup>-5</sup>	3.36429·10 <sup>-6</sup>	4.85224·10 <sup>-5</sup>
3·10 <sup>-7</sup>	-1.81643·10 <sup>-7</sup>	3.61375·10 <sup>-6</sup>	2.57422·10 <sup>-7</sup>	9.90556·10 <sup>-6</sup>	3.01371·10 <sup>-6</sup>	3.19096·10 <sup>-5</sup>
2·10 <sup>-7</sup>	-1.2097·10 <sup>-7</sup>	2.51574·10 <sup>-6</sup>	1.75894·10 <sup>-7</sup>	6.73405·10 <sup>-6</sup>	2.83855·10 <sup>-6</sup>	2.51353·10 <sup>-5</sup>
1·10 <sup>-7</sup>	-5.88214·10 <sup>-8</sup>	1.35468·10 <sup>-6</sup>	9.17152·10 <sup>-8</sup>	3.47597·10 <sup>-6</sup>	2.54197·10 <sup>-6</sup>	1.68278·10 <sup>-5</sup>
6·10 <sup>-8</sup>	-3.60338·10 <sup>-8</sup>	9.78465·10 <sup>-7</sup>	5.48238·10 <sup>-8</sup>	2.25417·10 <sup>-6</sup>	2.35006·10 <sup>-6</sup>	1.26999·10 <sup>-5</sup>
3·10 <sup>-8</sup>	-1.78339·10 <sup>-8</sup>	6.4904·10 <sup>-7</sup>	2.77908·10 <sup>-8</sup>	1.28801·10 <sup>-6</sup>	2.11001·10 <sup>-6</sup>	8.70324·10 <sup>-6</sup>
2·10 <sup>-8</sup>	-1.17674·10 <sup>-8</sup>	5.39231·10 <sup>-7</sup>	1.86872·10 <sup>-8</sup>	9.65465·10 <sup>-7</sup>	1.94655·10 <sup>-6</sup>	7.0047·10 <sup>-6</sup>
1·10 <sup>-8</sup>	-4.22122·10 <sup>-9</sup>	3.66405·10 <sup>-7</sup>	1.10194·10 <sup>-8</sup>	5.79658·10 <sup>-7</sup>	1.6212·10 <sup>-6</sup>	4.79046·10 <sup>-6</sup>
6·10 <sup>-9</sup>	-3.27422·10 <sup>-9</sup>	3.85498·10 <sup>-7</sup>	5.88572·10 <sup>-9</sup>	5.13466·10 <sup>-7</sup>	1.25431·10 <sup>-6</sup>	3.70725·10 <sup>-6</sup>
3·10 <sup>-9</sup>	-1.45426·10 <sup>-9</sup>	3.52556·10 <sup>-7</sup>	3.12768·10 <sup>-9</sup>	4.1655·10 <sup>-7</sup>	7.04709·10 <sup>-7</sup>	2.56286·10 <sup>-6</sup>
2·10 <sup>-9</sup>	-8.47615·10 <sup>-10</sup>	3.41575·10 <sup>-7</sup>	2.20746·10 <sup>-9</sup>	3.8424·10 <sup>-7</sup>	4.55198·10 <sup>-7</sup>	2.05677·10 <sup>-6</sup>
1·10 <sup>-9</sup>	1.23866·10 <sup>-9</sup>	2.67576·10 <sup>-7</sup>	2.76642·10 <sup>-9</sup>	2.8891·10 <sup>-7</sup>	2.17568·10 <sup>-7</sup>	1.33878·10 <sup>-6</sup>

Table G.3: Standard abbreviations for the 14 Bravais lattices used in this thesis. The seven crystal systems are separated by double lines.

Bravais lattice	abbreviation
<i>simple cubic</i>	<i>sc</i>
<i>body centred cubic</i>	<i>bcc</i>
<i>face centred cubic</i>	<i>fcc</i>
<i>hexagonal</i>	<i>hex</i>
<i>trigonal (rhombohedral)</i>	<i>trig</i>
<i>simple tetragonal</i>	<i>st</i>
<i>centred tetragonal</i>	<i>ct</i>
<i>simple orthorhombic</i>	<i>so</i>
<i>single face centred orthorhombic</i>	<i>sfco</i>
<i>body centred orthorhombic</i>	<i>bco</i>
<i>face centred orthorhombic</i>	<i>fco</i>
<i>simple monoclinic</i>	<i>sm</i>
<i>single face centred monoclinic</i>	<i>sfcm</i>
<i>triclinic</i>	<i>tric</i>

Table G.4: Stable crystal structures for  $\lambda^* = 1.5$  in the SSM (see section 9.2.1). For abbreviations of Bravais lattices see table G.3, lattice parameters are explained in section 5.3.  $n_b$  is the number of particles in the basis, the first one is always located at  $(0, 0, 0)$ , i.e., the lattice point. The general shape is indicated by the abbreviations for cluster, columnar, lamellar, and compact structures. Energy per particle, number density, enthalpy per particle, and pressure are given in standard reduced units (see section 2.8).

structure							stable up to	
lattice		$n_b$	additional basis vectors	shape	$e^*$	$\rho^*$	$h^*$	$P^*$
fcc	$\tilde{a}^* = 2.12132$	1	—	clu	0	0.419026	1.4673	0.022722
bco	$\tilde{a}^* = 2.3979$ $\tilde{b}^* = 1.5000$ $\tilde{c}^* = 14$	1	—	col	1	0.556038	4.87251	2.15327
fco	$\tilde{a}^* = 2.6105$ $\tilde{b}^* = 2.5855$ $\tilde{c}^* = 1.5811$	2	(0.65264, -0.64639, 0.39528)	com	2	0.749611	9.41777	5.56044
hex	$\tilde{a}^* = 1.0000$ $\tilde{c}^* = 1.1251$	1	—	lam	4	1.02633	13.4373	9.68586
sfco	$\tilde{a}^* = 3.0907$ $\tilde{b}^* = 1.1285$ $\tilde{c}^* = 1.0009$	2	(0.65750, -0.56323, 0.50046)	com	5	1.14798	18.2397	15.1988
bco	$\tilde{a}^* = 1.3229$ $\tilde{b}^* = 1.1180$ $\tilde{c}^* = 14$	1	—	com	7	1.35225	52.6443	61.7223
fcc	$\tilde{a}^* = 1.41421$	1	—	com	9	1.41421	$\infty$	$\infty$

Table G.5: Stable crystal structures for  $\lambda^* = 4.5$  in the SSM (see section 9.2.2). For abbreviations of Bravais lattices see table G.3, lattice parameters are explained in section 5.3 (hcp, the last structure, is not a Bravais lattice but the hexagonal close-packed structure, see section 5.5).  $n_b$  is the number of particles in the basis, the first one is always located at  $(0, 0, 0)$ , i.e., the lattice point. The general shape is indicated by the abbreviations for cluster, columnar, lamellar, and compact structures. Energy per particle, number density, enthalpy per particle, and pressure are given in standard reduced units (see section 2.8); cf. table 9.3 and appendix D for more explanations.

structure							stable up to	
lattice	$n_b$	additional basis vectors	shape	$e^*$	$\rho^*$	$h^*$	$P^*$	
fcc	$\tilde{a}^* = 6.36396$	1	—	clu	0	0.015519	1.4673	0.022722
tric	$\tilde{a}^* = 5.3194$ $\tilde{b}^* = 4.5252$ $\tilde{c}^* = 4.5252$ $\tilde{\varphi}^* = 89.6^\circ$ $\tilde{\psi}^* = 131.1^\circ$ $\tilde{\vartheta}^* = 51.3^\circ$	2	$(-0.81024, 0.10954, -0.66177)$	clu	1/2	0.0235413	3.10122	0.0612361
sfc	$\tilde{a}^* = 8.8652$ $\tilde{b}^* = 4.9539$ $\tilde{c}^* = 5.43622$ $\tilde{\alpha}^* = 59.7^\circ$	3	$(-0.53066, 0.86848, -0.12650)$ $(-0.28185, 0.31369, -0.95327)$	clu	1	0.0291432	4.30468	0.0963088
tric	$\tilde{a}^* = 8.9400$ $\tilde{b}^* = 5.5029$ $\tilde{c}^* = 5.4349$ $\tilde{\varphi}^* = 84.3^\circ$ $\tilde{\psi}^* = 88.5^\circ$ $\tilde{\vartheta}^* = 61.1^\circ$	8	$( 3.70338, 2.09473, 1.46530)$ $(-0.50698, -0.31596, -0.87883)$ $( 4.08308, -2.64192, 1.64060)$ $( 3.59316, 0.34289, -2.68731)$ $(-1.01266, 0.31558, -0.12157)$ $( 4.25481, -0.80332, -2.47722)$ $(-0.83304, -0.71614, 0.10106)$	clu	3/2	0.0343386	5.04542	0.121745
tric	$\tilde{a}^* = 5.3938$ $\tilde{b}^* = 5.3938$ $\tilde{c}^* = 5.0506$ $\tilde{\varphi}^* = 61.0^\circ$ $\tilde{\psi}^* = 30.0^\circ$ $\tilde{\vartheta}^* = 57.4^\circ$	4	$(-0.87634, -0.53172, 0.02374)$ $(-0.02621, 1.03954, -0.14489)$ $(-0.93725, 0.57784, -0.23493)$	clu	7/4	0.0369436	5.76683	0.148396
tric	$\tilde{a}^* = 5.5623$ $\tilde{b}^* = 5.5623$ $\tilde{c}^* = 5.5337$ $\tilde{\varphi}^* = 69.8^\circ$ $\tilde{\psi}^* = 29.2^\circ$ $\tilde{\vartheta}^* = 55.3^\circ$	6	$(1.02837, -0.68225, -0.45641)$ $(0.94629, 0.31420, -0.64168)$ $(0.14898, 0.99795, -0.05266)$ $(1.09183, 0.38183, 0.34536)$ $(0.81156, -0.56895, 0.51702)$	clu	5/2	0.0454251	6.92969	0.201219
sfc	$\tilde{a}^* = 7.7998$ $\tilde{b}^* = 1.1250$ $\tilde{c}^* = 4.5$ $\tilde{\alpha}^* = 81.6^\circ$	1	—	col	3	0.0512049	9.94791	0.355767
bco	$\tilde{a}^* = 6.5090$ $\tilde{b}^* = 6.3750$ $\tilde{c}^* = 64$	8	$( 0.18886, -0.76927, 0.77087)$ $( 1.08823, -0.80489, 1.41865)$ $( 0.31751, 0.87410, 0.80528)$ $( 0.39066, -0.03966, 1.55730)$ $(-0.38677, 0.03757, 0.93309)$ $( 1.07127, 0.74535, 1.53852)$ $( 0.96906, 0.00302, 0.70122)$	clu	35/8	0.0638386	14.9456	0.674811

tric	$\tilde{a}^* = 5.4310$ $\tilde{b}^* = 4.5000$ $\tilde{c}^* = 1.1250$ $\tilde{\varphi}^* = 65.9^\circ$ $\tilde{\psi}^* = 110.6^\circ$ $\tilde{\vartheta}^* = 85.7^\circ$	2	$(-0.87315, 0.51230, -0.01753)$	col	13/2	0.0799011	17.6651	0.892101
tric	$\tilde{a}^* = 5.2539$ $\tilde{b}^* = 4.5852$ $\tilde{c}^* = 1.0000$ $\tilde{\varphi}^* = 64.5^\circ$ $\tilde{\psi}^* = 113.0^\circ$ $\tilde{\vartheta}^* = 85.0^\circ$	2	$(-0.76073, 0.33613, -0.55526)$	col	8	0.0923016	29.7823	2.01054
tric	$\tilde{a}^* = 4.5000$ $\tilde{b}^* = 4.5000$ $\tilde{c}^* = 1.0000$ $\tilde{\varphi}^* = 71.9^\circ$ $\tilde{\psi}^* = 115.3^\circ$ $\tilde{\vartheta}^* = 85.2^\circ$	2	$(0.00617, 0.97025, 0.41969)$	col	21/2	0.104269	30.4709	2.08234
bco	$\tilde{a}^* = 8.8025$ $\tilde{b}^* = 1.5000$ $\tilde{c}^* = 14$	1	—	col(lam)	15	0.134597	38.5818	3.17405
trig	$\tilde{a}^* = 4.5000$ $\tilde{\alpha}^* = 16.6^\circ$	1	—	lam	18	0.154216	41.9457	3.69282
tric	$\tilde{a}^* = 4.5000$ $\tilde{b}^* = 1.1634$ $\tilde{c}^* = 1.1609$ $\tilde{\varphi}^* = 83.8^\circ$ $\tilde{\psi}^* = 106.3^\circ$ $\tilde{\vartheta}^* = 79.6^\circ$	1	—	lam	20	0.168271	49.7316	5.00296
tric	$\tilde{a}^* = 4.6008$ $\tilde{b}^* = 2.2500$ $\tilde{c}^* = 1.0000$ $\tilde{\varphi}^* = 78.9^\circ$ $\tilde{\psi}^* = 146.5^\circ$ $\tilde{\vartheta}^* = 83.2^\circ$	2	$(0.13009, 0.92388, 0.36113)$	lam(col)	49/2	0.198281	54.4411	5.93677
trig	$\tilde{a}^* = 4.5000$ $\tilde{\alpha}^* = 13.2^\circ$	1	—	lam	30	0.242901	85.4955	13.4799
trig	$\tilde{a}^* = 8.8604$ $\tilde{\alpha}^* = 6.7^\circ$	2	$(-4.37006, -0.25502, -0.14757)$	lam	61/2	0.245109	90.5729	14.7244
ct	$\tilde{a}^* = 1.2656$ $\tilde{c}^* = 8.8202$	2	$(-0.62117, 0.62295, -0.62661)$	lam	77/2	0.282765	105.305	18.8902
sfc	$\tilde{a}^* = 9.2996$ $\tilde{b}^* = 1.0000$ $\tilde{c}^* = 1.125$ $\tilde{\alpha}^* = 86.3^\circ$	2	$(0.69634, 0.45321, 0.56157)$	lam	56	0.383128	127.765	27.4952
sm	$\tilde{a}^* = 4.5125$ $\tilde{b}^* = 1.1286$ $\tilde{c}^* = 1.0000$ $\tilde{\alpha}^* = 86.8^\circ$	2	$(-0.74521, -0.50455, -0.47822)$	lam	58	0.394111	130.992	28.767
fco	$\tilde{a}^* = 8.9675$ $\tilde{b}^* = 1.7891$ $\tilde{c}^* = 1.0330$	2	$(-0.89248, 0.00270, -0.51646)$	lam	143/2	0.483543	196.917	60.6447
bcc	$\tilde{a}^* = 1.5220$	1	—	com	90	0.567211	223.299	75.6087
ct	$\tilde{a}^* = 1.2481$ $\tilde{c}^* = 2.1617$	1	—	com	96	0.593946	229.183	79.1032
tric	$\tilde{a}^* = 4.5054$ $\tilde{b}^* = 1.0029$ $\tilde{c}^* = 1.0010$ $\tilde{\varphi}^* = 84.7^\circ$ $\tilde{\psi}^* = 121.6^\circ$ $\tilde{\vartheta}^* = 79.7^\circ$	3	$(-1.56283, 0.14388, -0.17068)$ $(-0.69498, 0.45863, -0.55764)$	lam	337/3	0.676968	236.852	84.2951

trig	$\tilde{a}^* = 1.1887$ $\tilde{\alpha}^* = 70.5^\circ$	1	—	com	115	0.691783	255.127	96.9377
sc	$\tilde{a}^* = 1.0946$	1	—	com	128	0.762525	295.358	127.615
hex	$\tilde{a}^* = 1.1250$ $\tilde{c}^* = 1.1250$	1	—	com	138	0.810983	304.219	134.801
bcc	$\tilde{a}^* = 1.2612$	1	—	com	169	0.996907	372.935	203.304
ct	$\tilde{a}^* = 1.0336$ $\tilde{c}^* = 1.7765$	1	—	com	180	1.05374	410.006	242.368
sfc	$\tilde{a}^* = 1.6323$ $\tilde{b}^* = 1.0324$ $\tilde{c}^* = 1.26439$ $\tilde{\alpha}^* = 50.8^\circ$	1	—	com	210	1.2118	542.216	402.58
fcc	$\tilde{a}^* = 1.4600$	1	—	com	229	1.28531	550.261	412.919
ct	$\tilde{a}^* = 1.0607$ $\tilde{c}^* = 1.3229$	1	—	com	243	1.34387	645.109	540.383
hcp	$\tilde{a}^* = 1.41421$	1	—	com	263	1.41421	$\infty$	$\infty$



Table G.6: Stable crystal structures for  $\lambda^* = 10$  in the SSM (see section 9.2.3). For abbreviations of Bravais lattices see table G.3, lattice parameters are explained in section 5.3.  $n_b$  is the number of particles in the basis, the first one is always located at  $(0, 0, 0)$ , i.e., the lattice point. The general shape is indicated by the abbreviations for cluster, columnar, lamellar, and compact structures. Energy per particle, number density, enthalpy per particle, and pressure are given in standard reduced units (see section 2.8).

		structure					stable up to	
	lattice	$n_b$	additional basis vectors	shape	$e^*$	$\rho^*$	$h^*$	$P^*$
fcc	$\tilde{a}^* = 14.1421$	1	—	clu	0	0.00141421	1.2271	0.00173538
tric	$\tilde{a}^* = 10.9382$ $\tilde{b}^* = 10.0478$ $\tilde{c}^* = 10.0478$ $\tilde{\varphi}^* = 63.1^\circ$ $\tilde{\psi}^* = 29.0^\circ$ $\tilde{\vartheta}^* = 58.3^\circ$	2	$(0.91005, -0.36001, -0.26719)$	clu	1/2	0.00238672	2.25868	0.00419747
tric	$\tilde{a}^* = 10.7998$ $\tilde{b}^* = 10.7998$ $\tilde{c}^* = 10.5292$ $\tilde{\varphi}^* = 60.3^\circ$ $\tilde{\psi}^* = 24.8^\circ$ $\tilde{\vartheta}^* = 57.5^\circ$	3	$(-0.81767, 0.51135, -0.30929)$ $(-0.77857, -0.47770, 0.40698)$	clu	1	0.00333482	3.0507	0.0068387
fcc	$\tilde{a}^* = 15.3659$	4	$(0.48070, 0.62031, -0.61979)$ $(-0.07602, 1.18268, 0.00645)$ $(0.55650, 0.62573, 0.56315)$	clu	3/2	0.00441009	5.58967	0.0180358
tric	$\tilde{a}^* = 11.2657$ $\tilde{b}^* = 11.0332$ $\tilde{c}^* = 11.0196$ $\tilde{\varphi}^* = 60.7^\circ$ $\tilde{\psi}^* = 90.0^\circ$ $\tilde{\vartheta}^* = 59.4^\circ$	6	$(0.57717, 0.65987, -0.57059)$ $(0.25561, -0.33266, -0.96606)$ $(1.23585, 0.03277, -0.06596)$ $(1.32367, -0.36376, -1.01186)$ $(0.32746, 0.53230, -1.59208)$	clu	5/2	0.00583745	7.43354	0.0287993
tric	$\tilde{a}^* = 11.4788$ $\tilde{b}^* = 11.2096$ $\tilde{c}^* = 11.0512$ $\tilde{\varphi}^* = 64.2^\circ$ $\tilde{\psi}^* = 24.7^\circ$ $\tilde{\vartheta}^* = 58.6^\circ$	8	$(-0.72659, 0.82808, -1.11119)$ $(-0.59459, -0.73681, 0.36437)$ $(0.07109, -0.82039, -1.08788)$ $(-0.67155, -0.18649, -0.79050)$ $(0.22541, 0.26625, -1.13579)$ $(0.27800, -0.97247, -0.09709)$ $(-1.22806, 0.50112, -0.28383)$	clu	7/2	0.00732147	9.52129	0.0440847
tric	$\tilde{a}^* = 11.8731$ $\tilde{b}^* = 11.2962$ $\tilde{c}^* = 10.9053$ $\tilde{\varphi}^* = 64.3^\circ$ $\tilde{\psi}^* = 94.8^\circ$ $\tilde{\vartheta}^* = 56.9^\circ$	9	$(0.82474, 0.95319, -0.12807)$ $(1.44922, 0.46266, -0.75872)$ $(1.72420, 0.64955, 0.18621)$ $(0.88737, -0.40089, -0.22773)$ $(0.16289, 1.42436, -0.97000)$ $(1.38441, -0.20856, 0.66999)$ $(1.88014, -0.28258, -0.24801)$ $(0.46096, 0.47088, -0.92498)$	clu	37/9	0.00814847	11.9036	0.0634965

sfc	$\tilde{a}^* = 19.2684$ $\tilde{b}^* = 15.7988$ $\tilde{c}^* = 12.7306$ $\tilde{\alpha}^* = 38.6^\circ$	13	(0.44755, 0.91801, -0.11148) (1.48971, -0.84034, 0.51235) (1.26925, 0.38519, 0.32560) (0.50674, -0.72028, 0.78984) (0.94630, -0.87813, -1.43206) (0.99028, 0.00000, 1.33712) (0.92942, -1.27158, -0.49641) (1.40687, -0.36286, -0.37622) (1.14382, 0.59344, -0.77968) (0.02512, -1.12245, -0.02828) (0.50846, -0.20473, -0.83640) (0.31345, 0.50670, 0.80312)	clu	6	0.0107556	19.0931	0.140824
tric	$\tilde{a}^* = 11.9793$ $\tilde{b}^* = 11.7424$ $\tilde{c}^* = 11.6522$ $\tilde{\varphi}^* = 82.5^\circ$ $\tilde{\psi}^* = 136.4^\circ$ $\tilde{\vartheta}^* = 49.3^\circ$	17	(-1.02532, -0.19210, 0.00573) (-1.19948, 0.31935, -1.52332) (-0.55120, 0.18007, 0.81471) ( 0.70664, 0.73255, 0.36108) ( 0.91136, -0.41257, -0.06429) ( 1.35125, 0.96258, -0.89366) (-0.31342, 0.27567, -1.05693) (-0.04768, 0.93504, -0.35263) (-0.57891, -0.80934, 0.66850) ( 0.52824, -0.69801, -0.94550) (-0.47050, -0.68437, -0.82459) ( 0.35283, 0.94461, -1.43816) (-1.40967, -0.69228, -1.16808) ( 0.62834, 0.29371, -0.72043) ( 0.32264, -0.29913, 0.89808) (-1.09468, 0.75042, -0.56192)	clu	151/17	0.0137918	30.2684	0.294953
tric	$\tilde{a}^* = 11.9429$ $\tilde{b}^* = 11.9410$ $\tilde{c}^* = 11.6799$ $\tilde{\varphi}^* = 76.3^\circ$ $\tilde{\psi}^* = 137.2^\circ$ $\tilde{\vartheta}^* = 53.9^\circ$	22	( 0.16829, -1.29092, 1.11928) ( 0.89924, 0.51697, -0.01372) ( 0.98247, -1.51476, -0.00191) ( 0.78242, 0.27645, 1.93716) (-0.24968, -0.98180, 2.16378) ( 1.82481, 0.12528, -0.15331) ( 2.03967, 0.64811, 1.24421) ( 1.80364, -0.91620, -0.02214) ( 0.49318, -1.65921, 2.30030) ( 0.63087, -1.09566, -0.85722) ( 1.70121, -0.86973, 1.77734) (-0.16829, 0.82686, 0.56432) ( 1.49755, -1.65492, 2.44415) ( 1.07711, 0.45955, 0.98359) (-0.14167, -1.07789, -0.19995) ( 0.70893, -0.73539, 1.94083) ( 1.20547, -1.55321, 1.16854) (-0.63886, -0.85711, 0.65633) ( 0.80111, -0.51790, 0.94303) ( 1.79210, -0.28737, 0.91699) ( 0.88172, -0.49542, -0.07884)	clu	140/11	0.0168149	58.1688	0.764095
sm	$\tilde{a}^* = 11.6873$ $\tilde{b}^* = 10.5914$ $\tilde{c}^* = 1.1981$ $\tilde{\alpha}^* = 64.8^\circ$	3	( 0.71942, -0.55992, 0.50170) (-1.01569, 0.37010, -0.39868)	col	24	0.0223623	76.7725	1.18012
tric	$\tilde{a}^* = 11.0943$ $\tilde{b}^* = 10.9843$ $\tilde{c}^* = 2.9682$ $\tilde{\varphi}^* = 60.3^\circ$ $\tilde{\psi}^* = 0.0^\circ$ $\tilde{\vartheta}^* = 88.3^\circ$	10	(2.94230, 0.15290, 0.57067) (1.46475, -0.10908, 0.09824) (2.14261, -0.09525, 1.15847) (1.48017, 0.62451, -1.18756) (0.69154, 1.20078, 0.25053) (2.52663, 0.46006, -1.02081) (0.44980, 1.03103, -0.85863) (1.78629, 1.18333, 0.16047) (0.67062, 0.00018, -0.77257)	col	397/10	0.0318327	105.805	2.10431

sfc	$\tilde{a}^* = 23.1794$ $\tilde{b}^* = 19.2350$ $\tilde{c}^* = 1.37171$ $\tilde{\alpha}^* = 30.0^\circ$	6	$(0.10953, 2.05299, 0.51490)$ $(0.96675, -0.86729, 0.58831)$ $(1.69475, 1.84061, 0.23270)$ $(0.86732, 0.91697, -0.54288)$ $(1.79105, 0.04499, -0.02499)$	col	157/3	0.0393535	148.417	3.78122
tric	$\tilde{a}^* = 29.8942$ $\tilde{b}^* = 1.4759$ $\tilde{c}^* = 1.4759$ $\tilde{\varphi}^* = 89.7^\circ$ $\tilde{\psi}^* = 94.5^\circ$ $\tilde{\vartheta}^* = 75.4^\circ$	3	$(-9.97579, -0.45598, 0.52507)$ $(9.96995, 0.68872, -0.35462)$	lam	69	0.0476124	152.359	3.96891
trig	$\tilde{a}^* = 30.0115$ $\tilde{\alpha}^* = 2.8^\circ$	3	$(10.00770, 0.72392, -0.13835)$ $(-9.94949, -0.72392, -0.69538)$	lam	81	0.0556191	183.754	5.71507
tric	$\tilde{a}^* = 10.0000$ $\tilde{b}^* = 1.2594$ $\tilde{c}^* = 1.2594$ $\tilde{\varphi}^* = 88.4^\circ$ $\tilde{\psi}^* = 115.5^\circ$ $\tilde{\vartheta}^* = 82.1^\circ$	1	—	lam	94	0.063675	197.396	6.58375
tric	$\tilde{a}^* = 10.0000$ $\tilde{b}^* = 1.2666$ $\tilde{c}^* = 1.1270$ $\tilde{\varphi}^* = 87.2^\circ$ $\tilde{\psi}^* = 106.8^\circ$ $\tilde{\vartheta}^* = 79.8^\circ$	1	—	lam	105	0.0712557	229.988	8.90612
sfc	$\tilde{a}^* = 2.2513$ $\tilde{b}^* = 10.0961$ $\tilde{c}^* = 1.1198$ $\tilde{\alpha}^* = 81.1^\circ$	1	—	lam	118	0.0795273	260.823	11.3583
sfc	$\tilde{a}^* = 1.8840$ $\tilde{b}^* = 10.0000$ $\tilde{c}^* = 1.17851$ $\tilde{\alpha}^* = 86.2^\circ$	1	—	lam	135	0.0902723	282.394	13.3056
sfc	$\tilde{a}^* = 1.8157$ $\tilde{b}^* = 29.9511$ $\tilde{c}^* = 1.04828$ $\tilde{\alpha}^* = 88.8^\circ$	3	$(-0.30261, -9.98167, -0.52414)$ $(-0.30261, 9.98167, -0.52414)$	lam	156	0.105271	376.348	23.1962
sfc	$\tilde{a}^* = 1.6842$ $\tilde{b}^* = 29.9659$ $\tilde{c}^* = 1.07873$ $\tilde{\alpha}^* = 88.1^\circ$	3	$(0.24831, -9.98244, 0.53861)$ $(0.15551, 9.98448, 0.53785)$	lam	166	0.110275	442.171	30.4549
tric	$\tilde{a}^* = 10.0400$ $\tilde{b}^* = 1.4306$ $\tilde{c}^* = 1.0000$ $\tilde{\varphi}^* = 87.6^\circ$ $\tilde{\psi}^* = 48.5^\circ$ $\tilde{\vartheta}^* = 86.8^\circ$	2	$(0.53211, -0.71035, 0.48726)$	lam	224	0.139592	480.973	35.8712
sfco	$\tilde{a}^* = 21.1473$ $\tilde{b}^* = 1.1926$ $\tilde{c}^* = 1.0035$	2	$(0.63187, -0.59497, 0.50169)$	lam	254	0.158042	569.811	49.9115
bco	$\tilde{a}^* = 19.9519$ $\tilde{b}^* = 1.2034$ $\tilde{c}^* = 14$	2	$(0.67334, 0.59193, 0.46974)$	lam	541/2	0.166754	579.6	51.5438
tric	$\tilde{a}^* = 10.1338$ $\tilde{b}^* = 1.1166$ $\tilde{c}^* = 1.0027$ $\tilde{\varphi}^* = 87.2^\circ$ $\tilde{\psi}^* = 82.3^\circ$ $\tilde{\vartheta}^* = 85.4^\circ$	2	$(-0.71571, -0.48050, 0.50683)$	lam	577/2	0.177065	610.643	57.0405

sfc	$\tilde{a}^* = 1.5362$ $\tilde{b}^* = 10.3331$ $\tilde{c}^* = 1.33063$ $\tilde{\alpha}^* = 85.9^\circ$	2	$(-0.01688, 0.76715, -0.66358)$	lam	310	0.189728	671.757	68.6354
sfc	$\tilde{a}^* = 1.8166$ $\tilde{b}^* = 20.9036$ $\tilde{c}^* = 1.04883$ $\tilde{\alpha}^* = 88.2^\circ$	4	$(0.36886, -10.00320, 0.25749)$ $(0.41713, -8.95333, 0.24496)$ $(0.05043, 1.04733, -0.00454)$	lam	1323/4	0.201273	720.713	78.4889
tric	$\tilde{a}^* = 10.0150$ $\tilde{b}^* = 1.0004$ $\tilde{c}^* = 1.0004$ $\tilde{\varphi}^* = 87.6^\circ$ $\tilde{\psi}^* = 83.6^\circ$ $\tilde{\vartheta}^* = 63.2^\circ$	2	$(0.78038, -0.52974, -0.33224)$	lam	370	0.223798	896.562	117.844
sfc	$\tilde{a}^* = 1.5284$ $\tilde{b}^* = 10.7833$ $\tilde{c}^* = 1.33064$ $\tilde{\alpha}^* = 86.5^\circ$	3	$(-0.04424, -0.78253, -0.66286)$ $(-0.04357, 0.76287, 0.66490)$	lam	1400/3	0.274122	1064.19	163.795
tric	$\tilde{a}^* = 10.8326$ $\tilde{b}^* = 1.0212$ $\tilde{c}^* = 1.0021$ $\tilde{\varphi}^* = 87.6^\circ$ $\tilde{\psi}^* = 90.8^\circ$ $\tilde{\vartheta}^* = 66.0^\circ$	3	$(0.84700, 0.43518, -0.31251)$ $(-0.83454, 0.17346, -0.52499)$	lam	1538/3	0.296985	1092.93	172.329
sfc	$\tilde{a}^* = 1.7384$ $\tilde{b}^* = 10.6935$ $\tilde{c}^* = 1.00364$ $\tilde{\alpha}^* = 86.9^\circ$	3	$(-0.30041, 0.83415, 0.48144)$ $(0.27907, -0.83761, 0.48239)$	lam	1691/3	0.325603	1309.48	242.84
hex	$\tilde{a}^* = 1.0000$ $\tilde{c}^* = 10.3631$	3	$(-0.03918, -0.55348, -0.83315)$ $(0.48765, -0.26251, 0.83412)$	lam	584	0.334728	1318.8	245.957
sfc	$\tilde{a}^* = 1.7321$ $\tilde{b}^* = 10.0298$ $\tilde{c}^* = 1$ $\tilde{\alpha}^* = 84.7^\circ$	3	$(0.20810, 0.90662, -0.37256)$ $(-0.28868, -0.81888, 0.49975)$	lam	1829/3	0.346844	1454.34	292.97
tric	$\tilde{a}^* = 10.7391$ $\tilde{b}^* = 1.0082$ $\tilde{c}^* = 1.0000$ $\tilde{\varphi}^* = 87.9^\circ$ $\tilde{\psi}^* = 84.3^\circ$ $\tilde{\vartheta}^* = 64.3^\circ$	4	$(0.82080, -0.51066, -0.25637)$ $(-1.83105, -0.10682, 0.08345)$ $(-0.84078, 0.12547, -0.52808)$	lam	2961/4	0.41027	1619.37	360.676
sfc	$\tilde{a}^* = 1.7325$ $\tilde{b}^* = 10.7097$ $\tilde{c}^* = 1.00026$ $\tilde{\alpha}^* = 84.4^\circ$	4	$(-0.04638, -0.90004, -0.44012)$ $(0.53847, 0.85487, -0.00735)$ $(0.13599, 1.72489, -0.33990)$	lam	3147/4	0.433182	1855.18	462.825
trig	$\tilde{a}^* = 10.0061$ $\tilde{\alpha}^* = 5.7^\circ$	4	$(-0.88681, -0.49292, 0.24717)$ $(0.89793, 0.43402, 0.08106)$ $(-1.79042, 0.20013, -0.17545)$	lam	1709/2	0.462511	1987.26	523.915
tric	$\tilde{a}^* = 10.7241$ $\tilde{b}^* = 1.0299$ $\tilde{c}^* = 1.0051$ $\tilde{\varphi}^* = 88.8^\circ$ $\tilde{\psi}^* = 88.4^\circ$ $\tilde{\vartheta}^* = 60.8^\circ$	5	$(0.89821, -0.42417, 0.19397)$ $(1.74685, 0.04932, -0.08573)$ $(-0.84984, 0.35880, -0.38605)$ $(-1.76301, 0.40938, 0.01837)$	lam	4861/5	0.51614	2198.95	633.175
tric	$\tilde{a}^* = 10.2614$ $\tilde{b}^* = 1.0000$ $\tilde{c}^* = 1.0000$ $\tilde{\varphi}^* = 89.0^\circ$ $\tilde{\psi}^* = 87.0^\circ$ $\tilde{\vartheta}^* = 60.0^\circ$	5	$(-1.85235, 0.20014, 0.28491)$ $(-2.75370, -0.17014, 0.04770)$ $(-0.93578, 0.20525, -0.28667)$ $(0.87877, -0.51321, -0.07651)$	lam	1074	0.562847	2542.46	826.516

tric	$\tilde{a}^* = 10.6968$ $\tilde{b}^* = 1.0028$ $\tilde{c}^* = 1.0017$ $\tilde{\varphi}^* = 87.3^\circ$ $\tilde{\psi}^* = 85.8^\circ$ $\tilde{\vartheta}^* = 61.0^\circ$	6	$(-3.85697, 0.02173, 0.43799)$ $(-1.99446, 0.56669, 0.07387)$ $(-2.92166, 0.20578, -0.24926)$ $(-1.15187, -0.19189, -0.40894)$ $(-4.87233, 0.27444, 0.18639)$	lam	2499/2	0.639245	2827.04	1008.44
tric	$\tilde{a}^* = 9.9906$ $\tilde{b}^* = 1.0000$ $\tilde{c}^* = 1.0000$ $\tilde{\varphi}^* = 88.5^\circ$ $\tilde{\psi}^* = 88.8^\circ$ $\tilde{\vartheta}^* = 60.0^\circ$	6	$(-3.85440, -0.08768, 0.42100)$ $(0.91163, 0.02133, 0.48209)$ $(-1.85083, -0.02566, 0.09628)$ $(-0.91956, 0.46710, -0.04917)$ $(-2.95541, 0.43216, 0.20464)$	lam	4120/3	0.693699	3283.51	1325.09
fcc	$\tilde{a}^* = 1.7277$	1	—	com	1575	0.775581	3377.76	1398.18
ct	$\tilde{a}^* = 1.4064$ $\tilde{c}^* = 1.1876$	1	—	com	1736	0.851639	3630.32	1613.28
sfc	$\tilde{a}^* = 1.2830$ $\tilde{b}^* = 1.1111$ $\tilde{c}^* = 1.81737$ $\tilde{\alpha}^* = 54.8^\circ$	1	—	com	1922	0.944364	4112.56	2068.69
fcc	$\tilde{a}^* = 1.5714$	1	—	com	2106	1.03096	4471.26	2438.49
ct	$\tilde{a}^* = 1.2480$ $\tilde{c}^* = 1.1168$	1	—	com	2350	1.14955	4964.88	3005.94
fcc	$\tilde{a}^* = 1.4359$	1	—	com	2740	1.35105	7374.94	6262.05
fcc	$\tilde{a}^* = 1$	2	—	com	2947	1.41421	$\infty$	$\infty$



# Bibliography

- [1] P.-G. de Gennes, "Soft matter," *Rev. Mod. Phys.*, **64**, 645 (1992).
- [2] P.-G. de Gennes, "Soft matter (Nobel lecture)," *Angew. Chem. Int. Edit.*, **31**, 842 (1992).
- [3] T. D. McCarthy, P. Karellas, S. A. Henderson, M. Giannis, D. F. O'Keefe, G. Heery, J. R. A. Paull, B. R. Matthews, and G. Holan, "Dendrimers as drugs: Discovery and preclinical and clinical development of dendrimer-based microbicides for HIV and STI prevention," *Mol. Pharmaceutics*, **2**, 312 (2005).
- [4] C. C. Lee, J. A. MacKay, J. M. J. Frechet, and F. C. Szoka, "Designing dendrimers for biological applications," *Nat. Biotechnol.*, **23**, 1517 (2005).
- [5] I. W. Hamley, "Nanotechnology with soft materials," *Angew. Chem. Int. Edit.*, **42**, 1692 (2003).
- [6] WIKIPEDIA, "Colloid." <http://en.wikipedia.org/wiki/Colloid>
- [7] E.R. Weeks, "Video microscopy of colloidal suspensions and colloidal crystals," *Current Opinion in Colloid and Interface Science*, **7**, 196 (2002).
- [8] D. G. Grier, "A revolution in optical manipulation," *Nature*, **424**, 810 (2003).
- [9] C. N. Likos, "Effective interactions in soft condensed matter physics," *Phys. Rep.*, **348**, 267 (2001).
- [10] E. J. Sambriski and M. G. Guenza, "Theoretical coarse-graining approach to bridge length scales in diblock copolymer liquids," *Phys. Rev. E*, **76**, 051801 (2007).
- [11] P. N. Pusey and W. van Megen, "Phase behaviour of concentrated suspensions of nearly hard colloidal spheres," *Nature*, **320**, 340 (1986).
- [12] M. Dijkstra, R. van Roij, and R. Evans, "Phase diagram of highly asymmetric binary hard-sphere mixtures," *Phys. Rev. E*, **59**, 5744 (1999).
- [13] A. Yethiraj and A. van Blaaderen, "A colloidal model system with an interaction tunable from hard sphere to soft and dipolar," *Nature*, **421**, 531 (2003).

- [14] M. E. Leunissen, C. G. Christova, A.-P. Hynninen, C. P. Royall, A. I. Campbell, A. Imhof, M. Dijkstra, R. van Roij, and A. van Blaaderen, "Ionic colloidal crystals of oppositely charged particles," *Nature*, **437**, 235 (2005).
- [15] A.-P. Hynninen, M. E. Leunissen, A. van Blaaderen, and M. Dijkstra, "CuAu structure in the restricted primitive model and oppositely charged colloids," *Phys. Rev. Lett.*, **96**, 18303 (2006).
- [16] I. Borukhov and L. Leibler, "Enthalpic stabilization of brush-coated particles in a polymer melt," *Macromolecules*, **35**, 5171 (2002).
- [17] Y. Norizoe and T. Kawakatsu, "Monte Carlo simulation of string-like colloidal assembly," *Europhys. Lett.*, **72**, 583 (2005).
- [18] J. S. Høye, J. L. Lebowitz, and G. Stell, "Generalized mean spherical approximations for polar and ionic fluids," *J. Chem. Phys.*, **61**, 3253 (1974).
- [19] J. S. Høye and G. Stell, "Ornstein-Zernike equation for a two-Yukawa  $c(r)$  with core condition," *Mol. Phys.*, **52**, 1071 (1984).
- [20] D. Pini, G. Stell, and N. B. Wilding, "A liquid-state theory that remains successful in the critical region," *Mol. Phys.*, **95**, 483 (1998).
- [21] J. Maddox, "Crystals from first principles," *Nature*, **335**, 201 (1988).
- [22] J. Holland, *Adaption in Natural and Artificial Systems*. Ann Arbor: The University of Michigan Press (1975).
- [23] D. Gottwald, C. N. Likos, G. Kahl, and H. Löwen, "Phase behavior of ionic microgels," *Phys. Rev. Lett.*, **92**, 068301 (2004).
- [24] B. M. Mladek, D. Gottwald, G. Kahl, M. Neumann, and C. N. Likos, "Formation of polymorphic cluster phases for a class of models of purely repulsive soft spheres," *Phys. Rev. Lett.*, **96**, 045701 (2006).
- [25] B. Mladek, D. Gottwald, G. Kahl, M. Neumann, and C. N. Likos, "Erratum: Formation of polymorphic cluster phases for a class of models of purely repulsive soft spheres [Phys. Rev. Lett. 96, 045701 (2006)]," *Phys. Rev. Lett.*, **97**, 019901 (2006).
- [26] J. Fornleitner, F. Lo Verso, G. Kahl, and C. N. Likos, "Genetic algorithms predict formation of exotic configurations for two-component dipolar monolayers," *Soft Matter*, **4**, 480 (2008).
- [27] M. Glaser, G. Grason, R. Kamien, A. Košmrlj, C. Santangelo, and P. Ziherl, "Soft spheres make more mesophases," *Europhys. Lett.*, **78**, 46004 (2007).
- [28] G. Stell, "Criticality and phase transitions in ionic fluids," *J. Stat. Phys.*, **78**, 197 (1995).



- [29] Y. Levin and M. E. Fisher, “Criticality in the hard–sphere ionic fluid,” *Physica A*, **225**, 164 (1996).
- [30] J.-M. Caillol, “New mean-field theories for the liquid–vapour transition of charged hard spheres,” *Mol. Phys.*, **103**, 1271 (2005).
- [31] B. V. Derjaguin and L. Landau, “Theory of the stability of strongly charged lyophobic sols and of the adhesion of strongly charged particles in solution of electrolytes,” *Acta Physicochim.*, **14**, 633 (1941).
- [32] E. J. W. Verwey, J. T. G. Overbeek, and K. van Nes, *Theory of the stability of lyophobic colloids*. New York: Elsevier (1948).
- [33] M. Kac, “On the partition function of a one-dimensional gas,” *Phys. Fluids*, **2**, 8 (1959).
- [34] T. Kristóf, D. Boda, J. Liszi, D. Henderson, and E. Carlson, “Vapour–liquid equilibrium of the charged Yukawa fluid from Gibbs ensemble Monte Carlo simulations and the mean spherical approximation,” *Mol. Phys.*, **101**, 1611 (2003).
- [35] P. Ziherl and R. Kamien, “Maximizing entropy by minimizing area: Towards a new principle of self-organization,” *J. Phys. Chem. B*, **105**, 10147 (2001).
- [36] E. Jagla, “Minimum energy configurations of repelling particles in two dimensions,” *J. Chem. Phys.*, **110**, 451 (1999).
- [37] Z. Yan, S. V. Buldyrev, N. Giovambattista, P. G. Debenedetti, and H. E. Stanley, “Family of tunable spherically symmetric potentials that span the range from hard spheres to waterlike behavior,” *Phys. Rev. E*, **73**, 051204 (2006).
- [38] J. Fornleitner and G. Kahl, “Lane formation vs. cluster formation in two dimensional square-shoulder systems - a genetic algorithm approach,” *Europhys. Lett.*, **82**, 18001 (2008).
- [39] T. Dauxois, S. Ruffo, E. Arimondo, and M. Wilkens, *Dynamics and Thermodynamics of Systems with Long-range Interactions*. Berlin, New York: Springer (2002).
- [40] K. Huang, *Statistical Mechanics*. New York: John Wiley and Sons (1963).
- [41] F. Schwabl, *Statistical Mechanics*. Springer (2002).
- [42] H. E. Stanley, *Introduction to Phase Transitions and Critical Phenomena*. Oxford: Clarendon Press (1971).
- [43] J.-P. Hansen and I. R. McDonald, *Theory of Simple Liquids*. London: Academic Press, 3<sup>rd</sup> ed. (2006).

- [44] B. Widom, "Surface tension and molecular correlations near the critical point," *J. Chem. Phys.*, **43**, 3892 (1965).
- [45] B. Widom, "Equation of state in the neighborhood of the critical point," *J. Chem. Phys.*, **43**, 3989 (1965).
- [46] J. M. Yeomans, *Statistical Mechanics of Phase Transitions*. Oxford: Clarendon Press (1992).
- [47] J. S. Høye, D. Pini, and G. Stell, "SCOZA critical exponents and scaling in three dimensions," *Physica A*, **279**, 213 (2000).
- [48] R. A. Sack, "Pressure-dependent partition functions," *Mol. Phys.*, **2**, 8 (1959).
- [49] J. L. Yarnell, M. J. Katz, and R. G. Wenzel, "Structure factor and radial distribution function for liquid argon at 85K," *Phys. Rev. A*, **7**, 2130 (1973).
- [50] L. S. Ornstein and F. Zernike *Proc. Akad. Sci. (Amsterdam)*, **17**, 793 (1914).
- [51] J. M. J. van Leeuwen, J. Groeneveld, and J. de Boer, "New method for the calculation of the pair correlation function. I," *Physica*, **25**, 792 (1959).
- [52] F. H. Stillinger and R. Lovett, "Ion-pair theory of concentrated electrolytes," *J. Chem. Phys.*, **48**, 3858 (1968).
- [53] E. Waisman, "The radial distribution function for a fluid of hard spheres at high densities. Mean spherical integral equation approach," *Mol. Phys.*, **25**, 45 (1973).
- [54] N. F. Carnahan and K. E. Starling, "Equation of state for nonattracting rigid spheres," *J. Chem. Phys.*, **51**, 635 (1969).
- [55] J. S. Høye, G. Stell, and E. Waisman, "Ornstein-Zernike equation for a two-Yukawa  $c(r)$  with core condition," *Mol. Phys.*, **32**, 209 (1976).
- [56] G. Stell and S. F. Sun, "Generalized mean spherical approximation for charged hard spheres: The electrolyte regime," *J. Chem. Phys.*, **63**, 5333 (1975).
- [57] G. Stell and J.-J. Weis, "Pair correlation in simple polar liquids," *Phys. Rev. A*, **16**, 757 (1977).
- [58] J. S. Høye and G. Stell, "Thermodynamics of the MSA for simple fluids," *J. Chem. Phys.*, **67**, 439 (1977).
- [59] E. Arrieta, C. Jedrzejek, and K. N. Marsh, "Mean spherical approximation algorithm for multicomponent multi-Yukawa fluid mixtures: Study of vapor-liquid, liquid-liquid, and fluid-glass transitions," *J. Chem. Phys.*, **95**, 6806 (1991).

- [60] E. Schöll-Paschinger, *Phase Behavior of Simple Fluids and their Mixtures*. PhD thesis, Institut für Theoretische Physik, TU Wien (2002).
- [61] J.-P. Hansen and C. Pearson, “Athermal models for diblock copolymer self-assembly,” *Mol. Phys.*, **104**, 3389 (2006).
- [62] G. J. Pauschenwein, J.-M. Caillol, D. Levesque, J.-J. Weis, E. Schöll-Paschinger, and G. Kahl, “Liquid-vapor transition of systems with mean field universality class,” *J. Chem. Phys.*, **126**, 14501 (2007).
- [63] E. Waisman and J. L. Lebowitz, “Mean spherical model integral equation for charged hard spheres I. Method of solution,” *J. Chem. Phys.*, **56**, 3086 (1972).
- [64] E. Waisman and J. L. Lebowitz, “Mean spherical model integral equation for charged hard spheres. II. Results,” *J. Chem. Phys.*, **56**, 3093 (1972).
- [65] W. F. Ames, *Numerical Methods for Partial Differential Equations*. New York: Academic Press (1977).
- [66] D. Pini, G. Stell, and R. Dickman, “Thermodynamically self-consistent theory of structure for three-dimensional lattice gases,” *Phys. Rev. E*, **57**, 2862 (1998).
- [67] N. W. Ashcroft and N. D. Mermin, *Solid State Physics*. Fort Worth, Philadelphia, San Diego, New York, Orlando, Austin, San Antonio, Toronto, Montreal, London, Sydney, Tokyo: Saunders College Publishing, Harcourt Brace College Publishers (1976).
- [68] D. Gottwald, *Genetic Algorithms in Condensed Matter Theory*. PhD thesis, Institut für Theoretische Physik, TU Wien (2005).
- [69] D. Gottwald, G. Kahl, and C. N. Likos, “Predicting equilibrium structures in freezing processes,” *J. Chem. Phys.*, **122**, 204503 (2005).
- [70] Wolfram Research, Inc., *Mathematica*. Champaign, Illinois: Version 6 (2007).
- [71] M. W. Deem and J. M. Newsam, “Determination of 4-connected framework crystal structures by simulated annealing,” *Nature*, **342**, 260 (1989).
- [72] J. Pannetier, J. Bassasalsina, J. Rodriguez-Carvajal, and V. Caignaert, “Prediction of crystal structures from crystal chemistry rules by simulated annealing,” *Nature*, **346**, 343 (1990).
- [73] M. B. Boisen, Jr., G. V. Gibbs, and M. S. T. Bukowinski, “Framework silica structures generated using simulated annealing with a potential energy function based on an  $\text{H}_6\text{Si}_2\text{O}_7$  molecule,” *Phys. Chem. Miner.*, **21**, 269 (1995).

- [74] J. C. Schön and M. Jansen, "First step towards planning of syntheses in solid-state chemistry: Determination of promising structure candidates by global optimization," *Angew. Chem. Int. Edit.*, **35**, 1286 (1996).
- [75] S. Goedecker, "Minima hopping: An efficient search method for the global minimum of the potential energy surface of complex molecular systems," *J. Chem. Phys.*, **120**, 9911 (2004).
- [76] R. Martoňák, A. Laio, and M. Parrinello, "Predicting crystal structures: The parrinello-rahman method revisited," *Phys. Rev. Lett.*, **90**, 075503 (2003).
- [77] R. Martoňák, A. Laio, M. Bernasconi, C. Ceriani, P. Raiteri, F. Zipoli, and M. Parrinello, "Simulation of structural phase transitions by metadynamics," *Z. Kristallogr.*, **220**, 489 (2005).
- [78] R. Martoňák, D. Donadio, A. R. Oganov, and M. Parrinello, "Crystal structure transformations in SiO<sub>2</sub> from classical and *ab initio* metadynamics," *Nat. Mater.*, **5**, 623 (2006).
- [79] A. Assion, T. Baumert, M. Bergt, T. Brixner, B. Kiefer, V. Seyfried, M. Strehle, and G. Gerber, "Control of chemical reactions by feedback-optimized phase-shaped femtosecond laser pulses," *Science*, **282**, 919 (1998).
- [80] W. P. C. Stemmer, "Rapid evolution of a protein in vitro by DNA shuffling," *Nature*, **370**, 389 (1994).
- [81] D. M. Deaven and K. M. Ho, "Molecular geometry optimization with a genetic algorithm," *Phys. Rev. Lett.*, **75**, 288 (1995).
- [82] S. M. Woodley, P. D. Battle, J. D. Gale, and C. R. A. Catlow, "The prediction of inorganic crystal structures using a genetic algorithm and energy minimisation," *Phys. Chem. Chem. Phys.*, **1**, 2535 (1999).
- [83] A. R. Oganov and C. W. Glass, "Crystal structure prediction using *ab initio* evolutionary techniques: Principles and applications," *J. Chem. Phys.*, **124**, 244704 (2006).
- [84] A. R. Oganov and C. W. Glass, "Evolutionary crystal structure prediction as a tool in materials design," *J. Phys.: Condens. Mat.*, **20**, 064210 (2008).
- [85] G. J. Pauschenwein and G. Kahl, "Clusters, columns, and lamellae - minimum energy configurations in core softened potentials," *Soft Matter*, **4**, 1396 (2008).
- [86] G. J. Pauschenwein and G. Kahl, "Zero temperature phase diagram of the square-shoulder system," *accepted by J. Chem. Phys.* (2008).

- [87] G. J. Pauschenwein and G. Kahl, “Stable centered tetragonal phases in the hard core Yukawa model,” *to be published* (2008).
- [88] J. Fornleitner. PhD thesis, Institut für Theoretische Physik, TU Wien (to be published).
- [89] M. J. D. Powell, “An efficient method for finding the minimum of a function of several variables without calculating derivatives,” *Comput. J.*, **7**, 152 (1964).
- [90] F. S. Acton, *Numerical Methods That Work*. Washington: Mathematical Association of America, 1990, corrected ed. (1970).
- [91] W. H. Press, S. A. Teukolsky, W. T. Vetterling, and B. P. Flannery, *Numerical Recipes in FORTRAN: The Art of Scientific Computing*. Cambridge: Cambridge University Press, 2<sup>nd</sup> ed. (1992).
- [92] M. A. Miller and W. P. Reinhardt, “Efficient free energy calculations by variationally optimized metric scaling: Concepts and applications to the volume dependence of cluster free energies and to solid–solid phase transitions,” *J. Chem. Phys.*, **113**, 7035 (2000).
- [93] E. C. Bain, “The nature of martensite,” *Trans. AIME*, **70**, 25 (1924).
- [94] Z. Nishiyama, M. E. Fine, M. Meshii, and C. M. Wayman, *Martensitic Transformation*. Academic Press (1978).
- [95] P. Beauchamp and J. Villain, “Computer study of the bcc  $\leftrightarrow$  fcc structure change by homogeneous deformations,” *J. Phys. France*, **44**, 1117 (1983).
- [96] F. Milstein, H. E. Fang, and J. Marschall, “Mechanics and energetics of the Bain transformation,” *Philos. Mag.*, **70**, 621 (1994).
- [97] G. H. Olsen and W. A. Jesser, “The f.c.c.-b.c.c. transformation in iron deposits on copper,” *Acta Metall. Mater.*, **19**, 1009 (1971).
- [98] G. H. Olsen and W. A. Jesser, “The effect of applied stress on the f.c.c.-b.c.c. transformation in thin iron films,” *Acta Metall. Mater.*, **19**, 1299 (1971).
- [99] B. R. Cuenya, M. Doi, S. Löbus, R. Courths, and W. Keune, “Observation of the fcc-to-bcc Bain transformation in epitaxial Fe ultrathin films on Cu<sub>3</sub>Au(0 0 1),” *Surf. Sci.*, **493**, 338 (2001).
- [100] T. Suzuki, M. Shimono, and S. Kajiwara, “On the mechanism for martensitic transformation from fcc to bcc,” *Mat. Sci. Eng. A-Struct.*, **312**, 104 (2001).
- [101] C. Engin and H. M. Urbassek, “Molecular-dynamics investigation of the fcc  $\rightarrow$  bcc phase transformation in Fe,” *Comp. Mater. Sci.*, **41**, 297 (2008).

- [102] Y.-Y. Huang, J.-Y. Hsu, H.-L. Chen, and T. Hashimoto, "Precursor-driven bcc-fcc order-order transition of sphere-forming block copolymer/homopolymer blend," *Macromolecules*, **40**, 3700 (2007).
- [103] E. J. Meijer and F. E. Azhar, "Novel procedure to determine coexistence lines by computer simulation. Application to hard-core Yukawa model for charge-stabilized colloids," *J. Chem. Phys.*, **106**, 4678 (1997).
- [104] F. E. Azhar, M. Baus, J.-P. Ryckaert, and E. J. Meijer, "Line of triple points for the hard-core Yukawa model: A computer simulation study," *J. Chem. Phys.*, **112**, 5121 (2000).
- [105] A.-P. Hynninen and M. Dijkstra, "Phase diagrams of hard-core repulsive Yukawa particles," *Phys. Rev. E*, **68**, 021407 (2003).
- [106] D. Henderson, E. Waisman, J. L. Lebowitz, and L. Blum, "Equation of state of a hard-core fluid with a Yukawa tail," *Mol. Phys.*, **35**, 241 (1978).
- [107] J.-M. Caillol, D. Levesque, and J.-J. Weis, "Critical behavior of the restricted primitive model revisited," *J. Chem. Phys.*, **116**, 10794 (2002).
- [108] E. Luijten, M. E. Fisher, and A. Z. Panagiotopoulos, "Universality class of criticality in the restricted primitive model electrolyte," *Phys. Rev. Lett.*, **88**, 185701 (2002).
- [109] A. Z. Panagiotopoulos, "Critical parameters of the restricted primitive model," *J. Chem. Phys.*, **116**, 3007 (2002).
- [110] Y. C. Kim and M. E. Fisher, "Singular coexistence-curve diameters: Experiments and simulations," *Chem. Phys. Lett.*, **414**, 185 (2005).
- [111] J.-M. Caillol, "Non-perturbative renormalization group for simple fluids," *Mol. Phys.*, **104**, 1931 (2006).
- [112] N. D. Goldenfeld, *Lectures on Phase Transitions and the Renormalisation Group*. New York: Addison-Wesley (1992).
- [113] D. M. Smith, "Algorithm 693: A FORTRAN package for floating-point multiple-precision arithmetic," *ACM T. Math. Software*, **17**, 273 (1991).
- [114] G. J. Pauschenwein, "Critical behavior of hard sphere systems with long-range interactions," in *Science and Supercomputing in Europe* (P. Alberigo, G. Erbacci, F. Garofalo, and S. Monfardini, eds.), ch. Physics, 1048, CINECA Consorzio Interuniversitario (2007).
- [115] C. N. Likos, M. Watzlawek, and H. Löwen, "Freezing and clustering transitions for penetrable spheres," *Phys. Rev. E*, **58**, 3135 (1998).

- [116] C. N. Likos, A. Lang, M. Watzlawek, and H. Löwen, “Criterion for determining clustering versus reentrant melting behavior for bounded interaction potentials,” *Phys. Rev. E*, **63**, 31206 (2001).
- [117] G. Falkinger, B. Mladek, D. Gottwald, and G. Kahl *submitted to J. Phys.: Condens. Mat.* (2008).
- [118] C. N. Likos, B. M. Mladek, D. Gottwald, and G. Kahl, “Why do ultrasoft repulsive particles cluster and crystallize? Analytical results from density functional theory,” *J. Chem. Phys.*, **126**, 224502 (2007).
- [119] B. M. Mladek, D. Gottwald, G. Kahl, M. Neumann, and C. N. Likos, “Clustering in the absence of attractions: Density functional theory and computer simulations,” *J. Phys. Chem. B*, **111**, 12799 (2008).
- [120] A. Campbell, V. Anderson, J. van Duijneveldt, and P. Bartlett, “Dynamical arrest in attractive colloids: The effect of long-range repulsion,” *Phys. Rev. Lett.*, **94**, 208301 (2005).
- [121] F. Bowman, *Introduction to Elliptic Functions, with Applications*. New York: Dover (1961).
- [122] F. Lamarche and C. Leroy, “Evaluation of the volume of intersection of a sphere with a cylinder by elliptic integrals,” *Comput. Phys. Commun.*, **59**, 359 (1990).
- [123] G. J. Pauschenwein and G. Kahl, “The minimum distance parametrisation,” *to be published* (2008).
- [124] G. J. Pauschenwein, G. Kahl, P. Zihlerl, *et al.*, “A continuum theory for the square-shoulder model,” *to be published* (2008).
- [125] L. Blum, “Mean spherical model for asymmetric electrolytes,” *Mol. Phys.*, **30**, 1529 (1975).
- [126] R. J. Baxter, “Ornstein-Zernike relation for a disordered fluid,” *Aust. J. Phys.*, **21**, 563 (1968).
- [127] S. Asakura and F. Oosawa, “On interaction between two bodies immersed in a solution of macromolecules,” *J. Chem. Phys.*, **22**, 1255 (1954).





# Gernot Pauschenwein – Curriculum Vitae

Full Name: Dipl.-Ing. Gernot Josef Pauschenwein  
Contacts: Web: [tph.tuwien.ac.at/smt/](http://tph.tuwien.ac.at/smt/)  
Email: [pauschenwein@cmt.tuwien.ac.at](mailto:pauschenwein@cmt.tuwien.ac.at)  
Inst. f. Theoretische Physik,  
Wiedner Hauptstr. 8–10, A–1040 Vienna  
Date of Birth: October 24<sup>th</sup>, 1977  
Place of Birth: Eisenstadt, Austria  
Nationality: Austrian



## Basic Education

---

1984 – 1988 Volksschule Wiesen  
1988 – 1996 Bundesrealgymnasium Mattersburg  
1992 – 1996 Participation at the Austrian Mathematics and Physics Olympiads  
1996 Matura passed with distinction, “Honourable mention” at the 27<sup>th</sup> International Physics Olympiad in Oslo

## Higher Education

---

1997 – 2004 Studies in Technical Physics at the Vienna University of Technology,  
Projects in: quantum field theory, string theory, general relativity,  
chaotic systems  
Sept. 1999 First diploma exam passed with distinction  
Oct. 2004 Second diploma exam passed with distinction  
Diploma thesis: “Electrodynamics on the Möbius Strip”  
2004 – 2008 PhD Student at the Institute for Theoretical Physics, Soft Matter  
Theory and the CMS (Center for Computational Materials Science)  
PhD thesis: “Phase Behaviour of Colloidal Systems”  
Oct. 2008 Rigorosum

## Work Experience

---

1996 – 1997 Civil service as paramedic and ambulance driver at the Red Cross  
1997 – 1999 Voluntary paramedic and ambulance driver at the Red Cross  
1999 – 2005 Tutor for the lectures “Methods of Theoretical Physics”, “Quantum  
Theory”, “Electrodynamics and Special Relativity”, and “Statistical  
Mechanics”  
July/Aug. 2000 Industrial placement at the Austrian Research Centers Seibersdorf  
July/Aug. 2001 Industrial placement at the Siemens AG Österreich, PSE (Optical  
& Transport Network)  
July/Aug. 2002 Collaborator at the CP violation experiment NA48 at CERN, Geneva  
2005 – 2008 Project assistant at the Institute for Theoretical Physics, Vienna Uni-  
versity of Technology through an FWF (Austrian research fund) fel-  
lowship  
May 2007 Visit to the Université Paris Sud through the HPC-EUROPA project  
(RII3-CT-2003-506079), with the support of the European Commu-  
nity – Research Infrastructure Action under the FP6 “Structuring the  
European Research Area” Programme.